IntechOpen

Cosmic Rays

Edited by Zbigniew Szadkowski

COSMIC RAYS

Edited by **Zbigniew Szadkowski**

Cosmic Rays
http://dx.doi.org/10.5772/intechopen.72533
Edited by Zbigniew Szadkowski

Contributors

Jorge Perez-Peraza, Juan Carlos Marquez Adame, Julia Tjus, Mehmet Guenduez, Björn Eichmann, Francis Halzen, Francesco Riggi, Domenico Lo Presti, Paola La Rocca, William R Webber, Svetlana Veretenenko, Maxim Ogurtsov, Markus Lindholm, Risto Jalkanen, Agnieszka Janiuk, Konstantinos Sapountzis, Zbigniew Piotr Szadkowski

© The Editor(s) and the Author(s) 2018
The rights of the editor(s) and the author(s) have been asserted in accordance with the Copyright, Designs and Patents Act 1988. All rights to the book as a whole are reserved by INTECHOPEN LIMITED. The book as a whole (compilation) cannot be reproduced, distributed or used for commercial or non-commercial purposes without INTECHOPEN LIMITED's written permission. Enquiries concerning the use of the book should be directed to INTECHOPEN LIMITED rights and permissions department (permissions@intechopen.com).
Violations are liable to prosecution under the governing Copyright Law.

Individual chapters of this publication are distributed under the terms of the Creative Commons Attribution 3.0 Unported License which permits commercial use, distribution and reproduction of the individual chapters, provided the original author(s) and source publication are appropriately acknowledged. If so indicated, certain images may not be included under the Creative Commons license. In such cases users will need to obtain permission from the license holder to reproduce the material. More details and guidelines concerning content reuse and adaptation can be foundat http://www.intechopen.com/copyright-policy.html.

Notice

Statements and opinions expressed in the chapters are these of the individual contributors and not necessarily those of the editors or publisher. No responsibility is accepted for the accuracy of information contained in the published chapters. The publisher assumes no responsibility for any damage or injury to persons or property arising out of the use of any materials, instructions, methods or ideas contained in the book.

First published in London, United Kingdom, 2018 by IntechOpen
eBook (PDF) Published by IntechOpen, 2019
IntechOpen is the global imprint of INTECHOPEN LIMITED, registered in England and Wales, registration number: 11086078, The Shard, 25th floor, 32 London Bridge Street
London, SE19SG – United Kingdom
Printed in Croatia

British Library Cataloguing-in-Publication Data
A catalogue record for this book is available from the British Library

Additional hard and PDF copies can be obtained from orders@intechopen.com

Cosmic Rays
Edited by Zbigniew Szadkowski

p. cm.

Print ISBN 978-1-78923-592-0

Online ISBN 978-1-78923-593-7

eBook (PDF) ISBN 978-1-83881-699-5

We are IntechOpen, the world's leading publisher of Open Access books

Built by scientists, for scientists

3,650+
Open access books available

114,000+
International authors and editors

119M+
Downloads

151
Countries delivered to

Our authors are among the
Top 1%
most cited scientists

12.2%
Contributors from top 500 universities

CLARIVATE ANALYTICS
BOOK CITATION INDEX
INDEXED

WEB OF SCIENCE™

Selection of our books indexed in the Book Citation Index
in Web of Science™ Core Collection (BKCI)

Interested in publishing with us?
Contact book.department@intechopen.com

Numbers displayed above are based on latest data collected.
For more information visit www.intechopen.com

Meet the editor

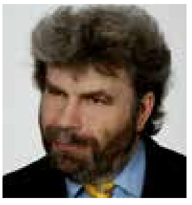

Zbigniew Szadkowski obtained his Doctorate degree in theoretical physics with the thesis "Quarks mixing in the chiral SU4 x SU4 and SU6 x SU6 symmetries" from the University of Łódź.
In 2007, he obtained his DSci degree in experimental physics with the habilitation thesis "Triggers in the Pierre Auger Observatory – Designs, Implementation and the Impact on the Experimental Results" from the University of Łódź.
Since 2012, he has been the head of the Department in High-Energy Astrophysics at the University of Łódź.
Since 1999, he has worked in the Pierre Auger Observatory, where he developed the Second Level Trigger for the Fluorescence Detector, the First Level Trigger implemented in 1660 surface detectors, as well as many advanced algorithms for surface and radio detectors based on the discrete cosine transform, artificial neural networks, wavelets, linear predictions, etc.

Contents

Preface

Dear Readers,

We present you with a set of essays on cosmic rays with a particular focus on galactic and extragalactic phenomena. The book is divided into two sections related to:

A. Extragalactic Cosmic Rays:

1. Introductory Chapter: Ultrahigh-Energy Cosmic Ray
2. Gamma Ray Bursts: Progenitors, Accretion in the Central Engine, Jet Acceleration Mechanisms

B. Galactic Cosmic Rays:

1. Cosmic Ray Muons as Penetrating Probes to Explore the World Around Us
2. Galactic Cosmic Rays from 1 MeV to 1 GeV as Measured by Voyager beyond the Heliopause
3. Galactic Cosmic Rays and Low Clouds: Possible Reasons for Correlation Reversal
4. Cosmic Ray Cradles in the Galaxy
5. Exploration of Solar Cosmic Ray Sources by Means of Particle Energy Spectra

This book contains works on both theoretical principles as well as results from experimental researches crucial for understanding the origin of cosmic rays.

The editors believe that this book will be interesting to both theorists and scientists working in modern experiments.

Interdisciplinarity is a strong theme of this book. We believe that cosmic rays are not separated from other scientific fields but form one of the crucial bases of modern astrophysics especially because the theoretical researches on the origin of cosmic rays are leading to a number of puzzling observations that indicate a much more complex astrophysical scenario, which we are far from understanding.

Zbigniew Szadkowski
Faculty of Physics and Applied Informatics
Department of High-Energy Astrophysics
University of Łódź, Poland

Section 1

Extragalactic Cosmic Rays

Chapter 1

Introductory Chapter: Ultrahigh-Energy Cosmic Rays

Zbigniew Szadkowski

Additional information is available at the end of the chapter

http://dx.doi.org/10.5772/intechopen.79535

1. Introduction

In 1938, Pierre Auger recorded coincidences by particle detectors separated by large distances at ground level. The source was ultrahigh energy cosmic rays (UHECRs) generating in the atmosphere extensive air showers (EAS). The energy of UHECRs reached up to 10^{15} eV [1, 2]. In this time energy of particles produced in laboratories was at the level of 10^{7} eV. In 1962, Linsley at Volcano Ranch recorded an air shower from a cosmic ray with giant energy higher than 10^{20} eV [3]. In 1965, Penzias and Wilson discovered the cosmic microwave background (CMB) radiation. This discovery overshadowed Linsley's experiment, the fantastically huge cosmic ray energy did not receive any attention that it deserved. Just after CMB discovery, **G**reisen, **Z**atsepin, and **K**uzmin (GZK) [4, 5] predicted that photo-pion production by the CMB photons reduces the path length for protons of UHECRs. In the rest frame of proton, the CMB is a beam of very energetic photons. The GZK threshold is the cosmic ray energy at which a Lorentz-boosted CMB photon has energy equal to the pion rest energy. The Planck distribution of CMB photons causes pion photo-production energy loss for protons with energies above approximately 7×10^{19} eV. The effect predicts that the spectrum from distributed homogeneous sources in the universe is suppressed above the GZK threshold at least one order of magnitude compared to the flux without the GZK effect.

If one assumes that the sources accelerate nuclei to a maximum energy above the energy threshold for photo-disintegration on CMB photons, the light elements could then be fragments of heavier nuclei that disintegrated during propagation. Candidate air shower primary particles all suffer severe propagation losses that should produce an effective cut-off at $\leq 10^{20}$ eV in experiments so far, assuming only that high-energy cosmic rays are normal particles that are produced in sources throughout the universe.

At the moment, the UHECRs remain a puzzle. Reliable conclusions from measurements of the energy spectrum, composition, and anisotropy and the proposed models cannot be obtained without a significant improvement in the observations.

IntechOpen

© 2018 The Author(s). Licensee IntechOpen. This chapter is distributed under the terms of the Creative Commons Attribution License (http://creativecommons.org/licenses/by/3.0), which permits unrestricted use, distribution, and reproduction in any medium, provided the original work is properly cited.

The statistics of registered events with energy about 10^{20} eV is definitely insufficient due to extremely low flux estimated less than 0.5 event per km^2 per century per steradian. So that only detectors of a huge size will be able to observe a sufficient number of events, which may be a fundament of a new physics.

Cosmic rays are high-speed particles traveling throughout our Galaxy, including the Solar System. Some of these particles originate from the Sun, but most come from sources outside the Solar System and are known as galactic cosmic rays (GCRs). The origin of the highest energy cosmic rays is expected to be extragalactic. Simple considerations about the confinement of particles in the Galaxy and Galactic halo strongly suggest that most of the highest-energy CR must have an extragalactic origin (unless their charge is unexpectedly large, which is also not favored by the observations). CR particles arriving at the top of the Earth's atmosphere are called primaries; their collisions with atmospheric nuclei give rise to secondaries.

Several experiments have been investigating ultrahigh-energy cosmic rays with energies reported beyond 10^{20}, but their origin is still unknown. For the current physics, astronomy and cosmology, it is a great challenge. In the 1990s, the largest experiments, AGASA and HiRes (both located in the Northern hemisphere), reported a discrepancy in the energy spectrum and clustering of cosmic ray arrival directions near the GZK energy threshold. This fact showed clearly that we require much more accurate and large-scale experiments to investigate this question without any doubts.

At 10^{15} eV, GCRs consist mostly of protons (nuclei of hydrogen atoms) and alpha particles (helium nuclei). The remainders are electrons and nuclei of heavier atoms. The composition changes with energy. At present, we believe that UHECRs consist mostly of charged nuclei. Gamma rays have been observed with energies as high as ~10^{12} eV. EAS generated by photons would be almost purely electromagnetic.

Because most cosmic ray primaries are strongly influenced by the solar magnetic field, most of those detected near the Earth have kinetic energies in excess of about 0.1 GeV. The number of particles decreases dramatically with increasing energy, but individual particles with the estimated energies above 10^{20} eV have also been recorded.

Due to magnetic fields, primary GCRs that are deflected in the space and arrive at the top of the Earth's atmosphere are nearly uniform from all directions. Thus, identification of UHECR sources based on arrival directions must be excluded. We have to deduce by other ways like, that is, the charge spectrum compared to spectroscopy data of stars and interstellar regions. The abundances of different elements have been well studied for particles with energies from roughly 100 MeV to several hundreds of GeV.

UHECRs are observed in an energy range from 10^9 eV to above 10^{20} eV. Over this range, the flux of cosmic rays appears to follow an approximate single power law ~$E^{-2.7}$, with sharper steepness ~$E^{-3.0}$ between so-called knee and ankle (see **Figure 1**) corresponding to 10^{15} eV and 10^{18} eV, respectively.

Cosmic rays with energies above ~10^{19} eV, known as ultra-high energy cosmic rays (UHECRs) are microscopic particles with a macroscopic amount of energy about a joule or more. The existence of such energetic particles, the mechanism of the acceleration to such extreme energies, the regions of their creation and the composition remains still a mystery.

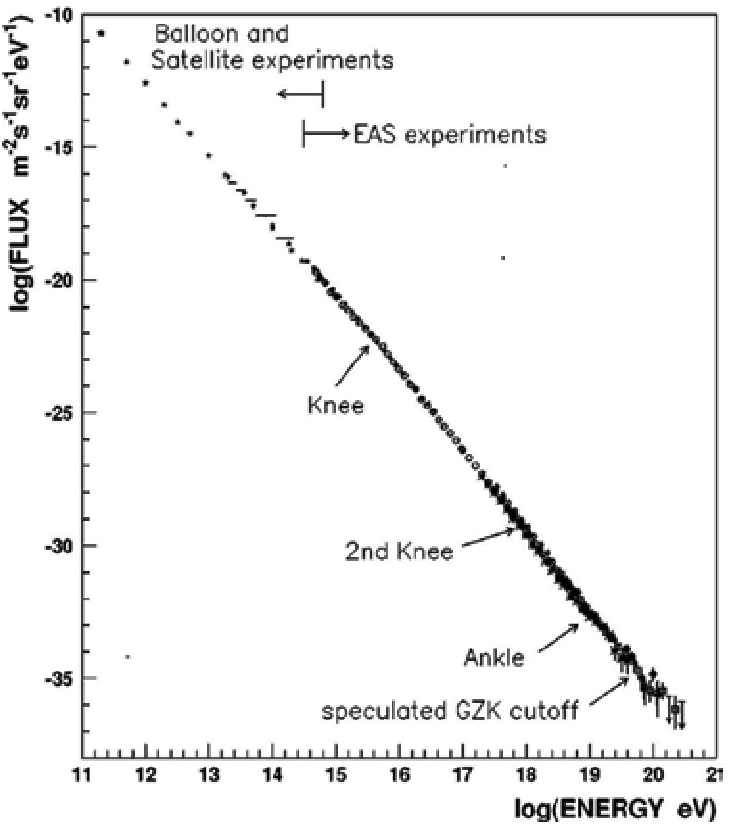

Figure 1. Observed energy spectrum of primary cosmic rays. The spectrum is expressed by a power law from 10^{11} to 10^{20} eV with a slight change of slopes around $10^{15.5}$ eV (knee), $10^{17.8}$ eV (second knee), and 10^{19} eV (ankle) [6].

The acceleration mechanism is still not clear and the study requires very careful measurements of the energy spectrum of UHECR to compare to the predictions from different acceleration models. Arrival directions of UHECRs are the second topic requiring a careful attention, and the third is both small- and large-scale anisotropies in their distribution. The fourth: the composition is one of the most difficult measurements because UHECRs cannot be detected directly using conventional particle detectors. Consequently, the composition as well as energy spectrum and arrival directions must be inferred from auxiliary measurements.

2. Extensive air showers

The cosmic rays with energies greater than 10^{14} eV have been investigated by using the Earth's atmosphere itself as part of the detection equipment. The interaction between high-energy cosmic rays and the air produces avalanches of secondary particles.

The process begins with the collision of the primary cosmic ray with a nucleus near the top of the atmosphere. This first collision produces typically several tens of secondary particles (depending on initial energy), mainly pions. The charged pions, as relatively long-lived, collide with another nucleus. The subsequent collisions are similar in nature to the primary collision. This process then leads to a cascade of particles, known as hadronic shower.

About 33% of pions, created in collisions, are neutral. They are very short-lived and decay very fast into a pair of photons before a next interaction with nuclei in the atmosphere. Next, photons interacting with the nuclei in the air create electron-positron pairs, which thus produce bremsstrahlung photons. This cascading process forms an electromagnetic avalanche. The hadronic shower itself permanently produces neutral pions and thus is developing secondary electromagnetic cascades along its path.

With an EAS development into the atmosphere, the number of generated particles successively increases (**Figure 2**). However, the process of multiplication is continued until the average energy of the shower particles is insufficient to produce more particles in subsequent collisions. Some part of energy is also leaking to the atmosphere due to ionization processes. Finally, the number of the particles traveling in the shower starts to decrease. This point of the EAS development is known as shower maximum. Beyond the maximum, the shower particles are gradually absorbed with an attenuation length of ~200 g/cm^2. The depth of shower maximum ($\boldsymbol{X}_{\mathbf{max}}$) is a function of energy. With a value of about 500 g/cm^2 at 10^{15} eV, the average X_{max} for showers increases by 60–70 g/cm^2 for every decade of energy [7]. The measured value of X_{max} can also be used to estimate the composition of the primary cosmic ray. Hadronic interaction length in air for protons is about 70 g/cm^2, and shorter for heavier nuclei. This means EAS are generated by heavier elements higher in the atmosphere.

More muons and fewer electromagnetic particles are produced by heavy primary particles rather than do lighter primaries, of the same primary energy. Iron and proton showers can be distinguished using surface detector data alone through the ratio of muons to electromagnetic particles, as well as through the arrival time distribution of particles in the shower front.

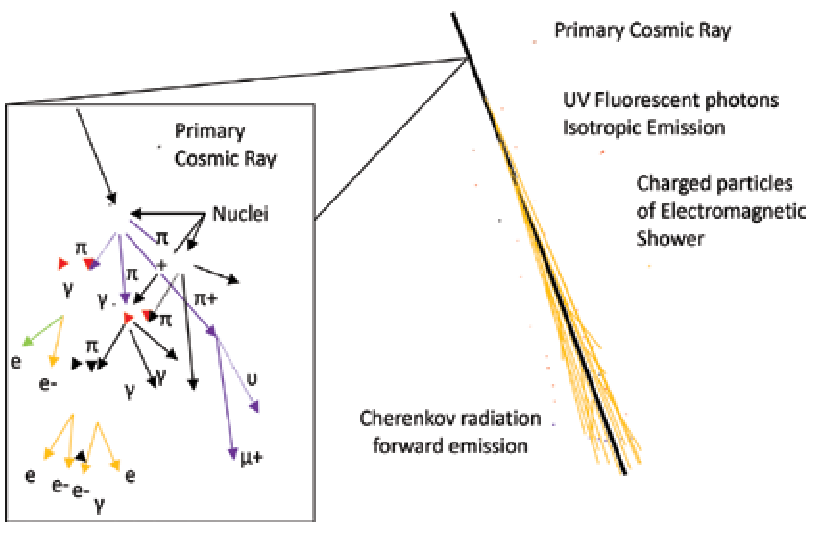

Figure 2. The schematic of the hadronic and electromagnetic components generation in the EAS development.

Particles scatter from the region of the shower axis throughout their development. The shower core effectively acts as a moving point source of both fluorescence photons and particles, which make their way to detectors far from the core. The shower front itself is slightly curved, resembling a cone. Particles far from the core will arrive behind the shower plane due to simple geometry. Electromagnetic component diffuses away from the shower axis throughout the shower development. It is wider in comparison to the hadronic one. Thus, far from the core particles are spread in time, with the time spread roughly proportional to the distance from the axis. This time spread helps to distinguish distant large showers from nearby small showers, and is thus useful in triggering the surface array. The time spread becomes greater as the depth of shower maximum increases.

Fluctuations in shower development distinguish detected signals. One of the most important sources of fluctuations is the depth and characteristics of the first few interactions. Fluctuations in later interactions are averaged over a large number of particles and are not important.

3. The GZK cut-off

We do not know the composition of the UHECRs. However, the set of stable particles as candidates for the UHECRs, which can trespass cosmological distances saving their energy, is quite limited: heavy or light atomic nuclei, photons and neutrinos. No any standard, electromagnetic mechanism can be responsible for photons and neutrinos (as neutral) acceleration. They can only be a product of the interaction of a still higher energy-charged particle. Therefore, in the framework of conventional astrophysics, we believe that light and heavy nuclei are probably the best candidates for the UHECR.

There is experimental evidence that the Universe was created some ~14 billion years ago from some singularity in a giant explosion known as the "Big Bang." Perhaps the most conclusive evidence for the Big Bang is the existence of the isotropic, with Planck distribution T = 2.73 K radiation permeating the entire Universe known as the **c**osmic **m**icrowave **b**ackground (CMB). Shortly after the CMB discovery, Greisen and independently Zatsepin and Kuzmin predicted that at very high energies, the universe should become opaque to light or heavy nuclei due to the following reactions:

$$\begin{aligned} p + \gamma_{CMB} &\rightarrow N + \pi & E_p &\geq 1.1 \times 10^{20}\ \text{eV} \\ p + \gamma_{CMB} &\rightarrow \Delta \rightarrow N + \pi & E_N &\geq 2.5 \times 10^{20}\ \text{eV}, \end{aligned} \tag{1}$$

where E_N is the energy of nucleon being disintegrated.

The energy budget in the center-mass-frame, for an average CMB energy 6.34×10^{-4} eV and protons with energy above 110 EeV, is sufficient for pion-production, during inelastic collisions with CMB photons.

Since in each such inelastic collision, protons leave a large part of their energy (of the order of 13% on average), their energy goes below 10 EeV (EeV = 10^{18} eV) after a few tens of Mpc.

As an example, if the largest energy cosmic ray ever detected 320 EeV (it is more than 50 J) were a proton produced with an initial energy of 10 ZeV (ZeV = 10^{21} eV), the distance of its source should be less than 50 Mpc (**Figure 3**). The same effect is expected for heavy nuclei. Nucleons will be stripped off from the nucleus due to inelastic collisions with most of all infrared background and also with CMB. Thus, the highest energy cosmic rays cannot originate at distances larger than a few tens of Mpc.

3.1. "Bottom-up" production

In order to accelerate charge particles to energies above 10^{20} eV, extremely powerful electromagnetic fields should exist. However, we did not register any stable region with so large potential, which could assure such an extremely energy in a single shot process. One of the earliest theories on the acceleration of cosmic rays proposed was the second order Fermi mechanism [9], where plasma clouds can be treated as a magnetic mirror. A particle trespassing a cloud from the front can be kicked back, like a tennis ball hit by a racket, with energy larger than its initial value. In this way, particles gain energy over many collisions. However, this mechanism is also too slow and too inefficient to account for the observed UHECR.

A more efficient and faster process is acceleration by crossing shock fronts generated in explosive phenomena (first-order Fermi mechanism - $\Delta E > 0$) [10, 11]. However that approach meets difficulties. Let us consider some hypothetical cosmic accelerator. The energy of accelerating

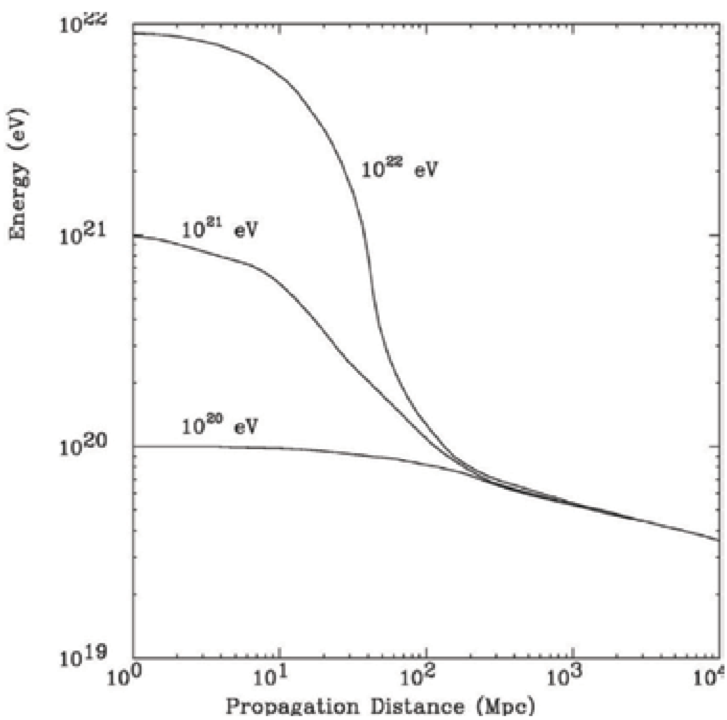

Figure 3. Energy degradation for nucleons as a function of distance to the observer for three different injection energies [8].

particles depends on the value and the size of the magnetic field and is limited by the Larmor radius related to their confinement. If the Larmor radius of the particle exceeds the size of the "accelerator," then the particles escape from it. Candidates of astrophysical object, which possesses such a large BR factor, are given on the Hillas plot [12].

$$E_{\max} = qBRc \tag{2}$$

where $E_{\max}$ is the maximal energy of particles confined in the magnetic field (J), q is the electric charge (C), B is the induction of the magnetic field (T), R is the radius of the confined trajectory (m), and c is the speed of light (m/s).

Many theories and models propose either sophisticated explanations or require some new physics. One of the models explores ultra-relativistic shock acceleration such as in hot spots of powerful radio galaxies and gamma-ray bursts (GRB) [13]. In the first case, relativistic jets are produced perpendicular to the accretion disk around a supermassive black hole in the central part of an active galactic nucleus. The shock on a jet, several hundred kpc from the central engine, due to collision with the intergalactic medium is considered as being able to accelerate particles up to the highest energies. This hypothesis, however, requires some additional assumptions. Such powerful galaxies are rather rare objects and should be clearly visible in the 50 Mpc distance.

The second model corresponds to the UHECR another astrophysical puzzle: the gamma-ray bursts. The emission of huge amounts of energies (typically a nonnegligible fraction of the mass energy of the Sun) is observed over a very short time (minutes), as gamma rays but with, in some cases, X-ray and optical contributions. Their distribution is cosmological and uniform. GRB happen relatively frequently: 2–3 per day. However, their distribution within the "GZK sphere" rather does not agree with the UHECRs observations. Other objects are also proposed as potential sources of UHECRs, such as rapidly rotating compact objects (young black holes, neutron stars or "magnetars"), which possibly are the sources of the most intense magnetic fields in the universe. The 10^{21} eV energies in such systems are rather difficult to reach.

3.2. "Top-down" production

If we have difficulties to imagine reliable mechanism accelerating particles from low to high energies, let us inverse the situation. Many theories propose top-down mechanism, decay of super-heavy, super-symmetric or Grand Unified Theories (GUT) particles [14]. The only problem is a justification of their existence or their surviving after the Big Bang. They could have survived up to now by some yet unknown mechanism (a very weakly violated quantum number, particles trapped inside huge potential walls called topological defects and released via spontaneous symmetry breaking mechanism). Their decay into a huge number of secondary particles (mainly pions) by hadronization of quark-antiquark pairs could produce the ZeV energies we expect, however they would decay mainly into photons (decays of neutral pions) and neutrinos (decays of charged pions). The current flux limits rule out or strongly disfavor that top-down models can account for a significant part of the observed UHECR flux. The bounds are reliable as the photon flux limits depend only on the simulation of electromagnetic showers and, hence, are very robust against assumptions on hadronic interactions at very high energy [15]. The photon flux limits have further far-reaching consequences by providing important constraints on theories of quantum gravity involving violation of Lorentz invariance (LIV) [16–19]. And, observing a single photon shower at ultra-high energy would imply very strong limits on another set of parameters of LIV theories [20, 21].

Author details

Zbigniew Szadkowski

Address all correspondence to: zbigniew.szadkowski@fis.uni.lodz.pl

Department of High-Energy Astrophysics, Faculty of Physics and Applied Informatics, University of Łódź, Poland

References

[1] Auger P et al. Etude d’un appareil a grand pouvoir de resolution pour rayons cosmiques. Comptes Rendus. 1938;**206**:1721

[2] Auger P. Extensive Cosmic-Ray Showers. Reviews of Modern Physics. 1939;**11**:288

[3] Linsley J. Evidence for a primary cosmic-ray particle with energy 10^{20} eV. Physical Review Letters. 1963;**10**:146

[4] Zatsepin GT, Kuźmin VA. Upper limit of the spectrum of cosmic rays. JETP Letters. 1966;**4**:78

[5] Greisen K. End to the cosmic-ray spectrum? Physical Review Letters. 1966;**16**:748

[6] Nagano M, Watson AA. Observations and implications of the ultrahigh-energy cosmic rays. Reviews of Modern Physics. 2000;**72**:689

[7] Fomin YA et al. Proc. 20th ICRC, vol. 6; Moscow: USSR; 1987. p. 110

[8] Cronin JW. Summary of the workshop. Nuclear Physics. 1992;**213**:2130. 28B (Proc. Supp.)

[9] Fermi E. On the Origin of the Cosmic Radiation. Physics Review. 1949;**75**:1169

[10] Krymsky GF. A regular mechanism for the acceleration of charged particles on the front of a shock wave. Doklady Akademii Nauk SSSR. 1977;**234**:1306

[11] Blandford RD, Ostriker JP. Particle acceleration by astrophysical shocks. The Astrophysical Journal. 1978;**221**:L29

[12] Hillas AM. The Origin of Ultra-High-Energy Cosmic Rays. Annual Review of Astronomy and Astrophysics. 1984;**22**:425

[13] Meszaros P. Theories of Gamma-Ray Bursts. Astro-ph/0111170

[14] Sigl G. Particle and Astrophysics Aspects of UHECR. Astro-ph/0008364

[15] Risse M, Homola P. Search for ultra-high energy photons using air showers. Modern Physics Letters A. 2007;**A22**:749 astro-ph/0702632

[16] Galaverni M, Sigl G. Lorentz Violation and Ultrahigh-Energy Photons. Physics Review. 2008;**D78**:063003. arXiv:0807.1210

[17] Galaverni M, Sigl G. Lorentz Violation for Photons and Ultra-High Energy Cosmic Rays. Physical Review Letters. 2008;**100**:021102 arXiv:0708.1737. 2015

[18] Liberati S, Maccione L. Quantum gravity phenomenology: achievements and challenges. Journal of Physics Conference Series. 2011;**314**:012007 arXiv:1105.6234

[19] Horvat R, Kekez D, Trampetic J. Spacetime noncommutativity and ultra-high energy cosmic ray experiments. Physics Review. 2011;**D83**:065013 arXiv:1005.3209

[20] Klinkhamer F. Potential sensitivities to Lorentz violation from nonbirefringent modified Maxwell theory of Auger, HESS, and CTA. Physics Review. 2010;**D82**:105024 arXiv:1008.1967

[21] Girelli F, Hinterleitner F, Major S. Loop Quantum Gravity Phenomenology: Linking Loops to Observational Physics. SIGMA. 2012;**8**:098 arXiv:1210.1485

Chapter 2

Gamma Ray Bursts: Progenitors, Accretion in the Central Engine, Jet Acceleration Mechanisms

Agnieszka Janiuk and Konstantinos Sapountzis

Additional information is available at the end of the chapter

http://dx.doi.org/10.5772/intechopen.76283

Abstract

The collapsar model was proposed to explain the long-duration gamma ray bursts (GRBs), while the short GRBs are associated with the mergers of compact objects. In the first case, mainly the energetics of the events is consistent with the proposed progenitor models, while the duration, time variability, as well as the afterglow emission may shed some light on the detailed properties of the collapsing massive stars. In the latter case, the recent discovery of the binary neutron star (NS-NS) merger in the gravitational wave observation made by LIGO (GW170817) and the detection of associated electromagnetic counterparts, for the first time, gave a direct proof of the NS-NS merger being a progenitor of a short GRB. In general, all GRBs are believed to be powered by accretion through a rotationally supported torus, or by fast rotation of a compact object. For long ones, the rotation of the progenitor star is a key property in order to support accretion over relatively long activity periods and also to sustain the rotation of the black hole itself. The latter is responsible for ejection of the relativistic jets, which are powered due to the extraction of the BH rotational energy, mitigated by the accretion torus, and magnetic fields. The jets must break through the stellar envelope though, which poses a question on the efficiency of this process. Similar mechanisms of powering the jet ejection may act in short GRBs, which in this case may freely propagate through the interstellar medium. The power of the jets launched from the rotating black hole is at first associated mostly with the magnetic Poynting flux, and then, at large distances it is transferred to the kinetic and finally radiative energy of the expanding shells. Beyond the radiative processes expected to take place in the jet propagation phase after the stellar envelope crossing, the significant fraction of the jet acceleration is expected to take place inside the stellar envelope and just right after it in the case of a significant decrease of the exterior pressure support. The implications of the hot cocoon formed during the penetration of the stellar body and the interaction of the outflow with the surrounding material are crucial not only for the outflow collimation but also provide specific observational imprints with most notorious observed panchromatic break in the afterglow lightcurves. Thus a significant number of models have been developed for both matter and Poynting dominated otuflows. In this chapter, we discuss these processes from the theoretical point of view and we highlight

IntechOpen

© 2018 The Author(s). Licensee IntechOpen. This chapter is distributed under the terms of the Creative Commons Attribution License (http://creativecommons.org/licenses/by/3.0), which permits unrestricted use, distribution, and reproduction in any medium, provided the original work is properly cited.

the mechanisms responsible for the ultimate production of electromagnetic transients called GRBs. We also speculate on the possible GRB-GW associacion scenarios. Finally, in the context of the recently discovered short GRB and its extended multiwalength emission, we present a model that connects the neutron-rich ejecta launched from the accreting torus in the GRB engine with the production of the unstable heavy isotopes produced in the so-called r-process. The radioactive decay of these isotopes is the source of additional emission observed in optical/infrared wavelengths and was confirmed to be found in a number of sources.

Keywords: gamma ray burst: general, black hole physics, accretion, accretion disks, gravitational waves, neutrinos, nuclear reactions, nucleosynthesis, abundances

1. Introduction

Gamma ray bursts are single, transient, short-lasting events (from a fraction of a second up to around a thousand seconds), and detected on the gamma ray sky. They are typically in the range between 10 keV and 20 MeV and are isotropically distributed on the celestial sphere, while they can occur at random directions, even a few times per day [1]. They are also often accompanied by an optical counterpart, late time X-ray signal, and the afterglow, which lasts for many days after the prompt phase and are detected in lower energies, down to the radio band.

The observed properties and energetics of gamma ray bursts has proven that at their hearts there is a cosmic explosion of an enormous power, which is definitely connected with the birth of compact stars. The newly born black hole is swallowing an extremely large amount of matter in a very short time. The accompanying process of ejection of rarefied and fast streams of plasma, which expand in the interstellar medium with a velocity close to the speed of light, is responsible for the gamma ray emission.

1.1. History of GRBs observations

Gamma ray bursts have been first detected in the 1960s. The original measurement was by chance made by the US military service that operated the satellite Vela. The discovery was published in the Astrophysical Journal much later [2]. The authors of this work refer to the old hypothesis [3] that the supernova explosions should be accompanied by the gamma and X-ray emission. Nevertheless, for the confirmation of the supernova-GRB connection, astronomers had to wait more than 30 years more. Since 1970s, it was already known that GRBs are cosmic events, so that they have been studied by research satellites. The main break through was made in 1990s, when the BATSE satellite confirmed the isotropic distribution of GRBs on the sky. This was a strong argument for their extragalactic origin, and thus GRBs being one of the brightest sources of radiation in the universe. Another achievement of the BATSE mission was to establish two classes of bursts, which statistically cluster around the long ($t > 2$ s) and short ($t < 2$ s) events [4]. Here, the time $t = T_{90}$ measures the 90% of counts detected by the counter.

Until 1997, there were no GRB counterparts found in the lower energy bands. For the first time, the Italian-Dutch satellite BeppoSAX detected the position of a GRB precisely enough, so that

http://dx.doi.org/10.5772/intechopen.76283

the localisation of an optical afterglow was possible for GRB970228 [5]. Here, the name of the GRB identifies the date of its observation, in the format *rrmmdd*. In May 1997, the first redshift of a GRB was estimated. The GRB970508, with $0.83 < z < 2.3$ [6], confirmed that the events are observed from cosmological distances. Typically, the optical afterglow of a GRB is of 19^{th} magnitude and can be observed from a couple weeks up to months after the burst. Its luminosity decrease with time has a power-law dependence. In addition, the X-ray afterglows can be observed, a few hours after the prompt phase. In some GRBs (like GRB991216), the emission lines have been reported in the Chandra, XMM-Newton, ASCA, and BeppoSAX data. Moreover, about half of the localized GRBs exhibits also the radio afterglows, seen about 1 day after the burst.

The host galaxies of GRBs have been identified based on their precise localisations, thanks to *Hubble Space Telescope* (GRB970228, Sahu et al. [7]). For a long time, this was possible only in the case of long GRBs. It was found that their hosts are statistically bluer and more actively starforming and are also only moderately metal-rich, or even metal-poor [8, 9]. The redshifts measured for a sample of GRBs were clustered around $z = 1$, and the redshift distribution was fitted well by the star formation rate dependence proposed by Porciani and Madau [10]. The local density of the GRBs derived from the luminosity function was about 0.44 $Gpc^3 yr^{-1}$. In the case of short GRBs, their space distribution was found to be more 'local' than for the long ones, with $V/V_{max} = 0.39$, and 0.28, respectively, while the local density was found about 1.7 bursts per Gpc^3 per year [11]. These were just rough estimates, taking into account the fact that the short GRBs were missing the redshift data at that time. The number density of bursts should also be corrected by a beaming factor.

The important discovery which confirmed the origin of GRBs was the detection of emission lines, characteristic for supernova explosion, in the optical afterglows spectra (e.g., GRB030329). Hence, a very strong support was found for the idea of massive star's explosions being the progenitors of these events [12, 13]. The supernova connection was proposed earlier, since in some of the optical afterglow lightcurves the characteristic red bumps were detected, a few weeks after the GRB [14]. A new era in the GRB studies was opened with the launch of the *Swift* satellite in 2004. It found, for the first time, the afterglows of short GRBs. It occured, that contrary to long bursts, the short GRBs do not originate from the starburst galaxies neither the supernova explosions. A good candidate for their progenitor is a merger event, during which two compact objects collide, such as a binary neutron star meger. The *Swift* satellite detected GRBs at higher redshifts, e.g., GRB090423 at $z = 8.1$ [15]. It occurred that a simple star formation law does not fit to the GRB distribution [16, 17]. It was found possible that the bursts are concentrating in the regions of specific value of metallicity.

In 2008, another high-energy mission was launched, *Fermi*. The detector GBM (gamma ray burst monitor) was placed onboard to detect gamma rays from cosmic transients. The burst GRB130427 was the most energetic event found to date and the energy of photons exceeded 90 GeV. The most recent achievements of the Fermi mission were connected with searching for high-energy electromagnetic counterparts to the gravitational wave events, discovered by LIGO interferometer.

1.2. Models of GRBs origin

The gamma ray emission originates at rather large distances from the base of the jet. Therefore, the central engine driving the jets and forming its base are hidden from the observer and any studies of its structure must be grounded on the indirect analysis. The signal which would be emitted from the engine could be produced either in gravitational waves or in the neutrinos of MeV energies. Such neutrinos are rather impossible to be detected from cosmological distances. Much more promissing are neutrinos produced in the GRB jets which have energies in the order of GeV [18–20].

The constraints which are based on the observed isotropic equivalent energy of the bursts suggested that the total energy released during the explosion is in the order of the binding energy of a compact object with a stellar mass:

$$E = \frac{GM^2}{R} \approx 3 \times 10^{54}\ \mathrm{erg} \tag{1}$$

The burst durations are, however, much longer than the dynamical time, over which the matter can free fall onto such a star. The extended duration of the event must therefore be driven by a viscous process. The most plausible is the disk accretion process, which in addition provides a required collimation of the burst stream along the disk rotation axis. The appearance of a large amount of matter in the vicinity of a black hole, to be accreted with a few tens-hundreds of a second, implies an extremely violent process, most probably a birth of a new black hole.

The scenario of a compact object merger [21] was able to explain the energies required for a detection of the event from a cosmological distance [22]. It was thought first that this scenario could be universal for all the types of GRBs; however, the observations of the GRB host galaxies, their active star formation rates in some cases, and the discoveries of GRB-supernova connection led to a different scenario for the long bursts. The currently accepted scenario for the long GRB progenitor is the *collapsar*, or *hypernova* model [23, 24]. In this model, the massive iron core of a rapidly rotating, evolved massive star (typically, the Wolf-Rayet type of star) quickly collapses to form a black hole. Most of the stellar envelope is expelled, but the remaining part is slowed down by the backward shocks and fall back. The material which posseses large angular momentum is concentrating in the equatorial plane of the star and forms an accretion disk. The non-rotating matter is falling radially along the axis of rotation into the black hole and the empty funnel forms there, to help collimate the subsequenltly launched jets [25]. They have to break out the stellar envelope, and accelerate up to ultrarelativistic velocities, with Lorentz factors in the order of $\Gamma \sim 100$.

The hypernovae connected with long GRBs are a subgroup of the supernovae type I b/c (which do not exhibit neither hydrogen nor helium lines in their spectra) and constitute about 10% of this class [26]. Statistically, this should agree with the estimated rate of GRBs. Their occurrence rate is about 10^{-3} of the supernova rate per galaxy per year [27]. The reason why not all the supernovae type I b/c (the core collapse supernovae) produce GRBs is most probably connected with the extremely low metallicities and rotation of the pre-SN star [28].

Among the models proposed to explain the short GRB population, the compact object merger model is most favored. Here, the duration of the event is limited by a much smaller size of the accretion disk, which forms after the remnant matter is left from the disrupted neutron star. The short bursts occur mostly in old, elliptical galaxies and within the regions of low star formation rate [29]. The most probable progenitor configuration is the NS-NS binary; the BH-NS was also studied, see. e.g., Narayan et al. [30]. Alternatively, also the magnetars, being extremely magnetized neutron stars when rotational energy is dissipated on the scale of seconds, may be able to produce Poynting dominated jets and power the GRBs [31].

2. Accretion onto a black hole as a driving engine of a GRB

The accretion tori surrounding black holes are ubiquitous in the universe. They occupy centers of galaxies, or reside in binary systems composed of stellar mass black holes and main sequence stars, being a source of power for their ultraviolet or X-ray emission. In these kinds of objects, frequently the black hole accretion is accompanied with the ejection of jets, launched along the accretion disk axis. Such sources are then observed as the radio-loud quasars, driven by the action of supermassive black holes, or the 'microquasars', which are driven by the stellar mass black holes. The jets of plasma are accelerated up to the relativistic speeds, and emit the high-energy radiation, measured over the entire energy spectrum.

Similarly, in the case of ultrarelativistic jets that are sources of gamma rays in GRBs, the driving engine is supposedly the stellar mass black hole surrounded by an accretion disk. However, since the GRB events are transients that last only up to several hundred seconds, and not for thousands, or millions of years, the accretion process should not be persistent and last not too long. The limiting time of the GRB engine activity is governed by the amount of matter available for accretion, and by the rate of this process (**Figure 1**).

From the computational point of view, the numerical model of any black hole accretion disk is based on standard equations of hydrodynamics (or MHD, if the magnetic fields are taken into account). The global parameters that enter the equations and act as scaling factors are the black hole mass, M_{BH}, its angular momentum (called spin, a), and accretion rate, $\dot{M}$.

2.1. Chemical composition of the accretion disk in GRB engine and the equation of state

The temperature and density in the accretion disk feeding the gamma ray busts are governed by a huge accretion rate. The physical conditions make the disk undergo onset of nuclear reactions, since $\rho \sim 10^{10} - 10^{12}\mathrm{g\ cm}^{-3}$ and $T \sim 10^9 - 10^{11}\mathrm{K}$. The disk is composed from the free protons, electrons and neutrons, and its electron fraction, defined as the ratio of protons to baryons, which is typically less than $Y_e = 0.5$. This is because of the neutronisation reactions, which are established by the condition of β-equilibrium, and greatly reduce the number density of free protons (balanced by electrons to satisfy the charge neutrality), in the cost of increasing the neutron number density.

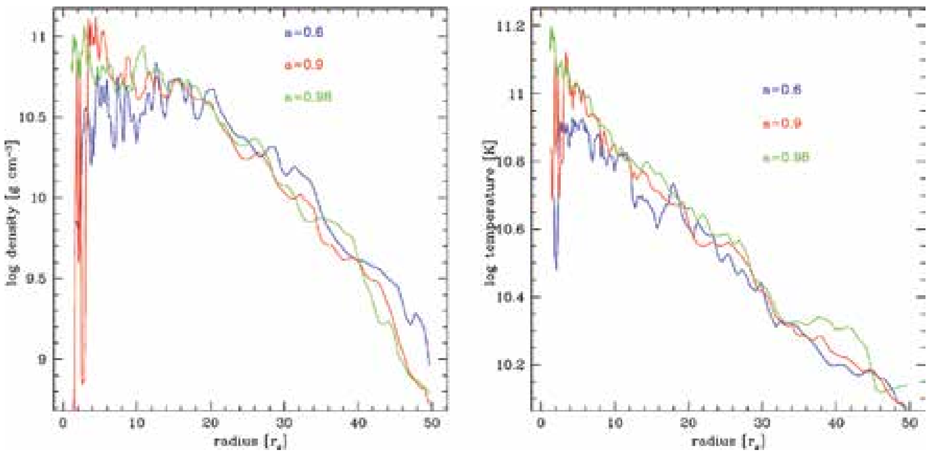

Figure 1. The structure of the black hole accretion disk in the GRB central engine. Three values of the BH spin, $a = 0.6, 0.9$, and $a = 0.98$, are shown with blue, red, and green lines, respectively. The black hole mass is equal to $3M_{\odot}$. The model is computed for the mass of the disk equal to about $0.1M_{\odot}$. The mass accretion rate is varying, and is about $0.2 - 0.3M_{\odot}s^{-1}$. Profiles show radial distribution of density and temperature in the disk equatorial plane.

Because the plasma may contain a certain number of positrons, which are also a product of the weak processes, the net value of the electron fraction must account for them, and is defined as:

$$Y_e = \frac{n_p}{n_p + n_n} = \frac{n_{e^-} - n_{e^+}}{n_b} \tag{2}$$

2.2. Neutrino cooling

The neutrino cooling in the GRB central engine is the most efficient mechanism of reducing the thermal energy of the plasma. The radiative processes involving photons are negligibly inefficient due to extremely large optical depths, such that the photons are completely trapped in the plasma.

The neutrino emission results from the following nuclear reactions:

$$\begin{aligned} p + e^- &\to n + v_e \\ n + v_e &\to p + e^- \\ p + \overline{v}_e &\to n + e_+ \\ n + e_+ &\to p + \overline{v}_e \\ p + e^- + \overline{v}^e &\to n \\ n &\to p + e^- + \overline{v}_e \end{aligned} \tag{3}$$

and in certain large parts of the disk these processes lead to a fairly large neutrino emissivities. The equation of state is based on the equilibrium of nuclear reactions, which leads to establishing the balance between the rates of forward and backward processes, and on the ratio of number densities of protons to neutrons [32].

The species in general are relativistic and may have an arbitrary degeneracy level (given by their chemical potential). They are therefore subject to the Fermi-Dirac statistics, as follows from the kinetic theory of gas, and hence the relations between pressure, density, temperature, and entropy in the gas will not obey the ideal gas equation of state. Typically, these quantities are computed numerically and stored in the EOS tables (**Figure 2**).

2.3. Accretion physics in general relativistic MHD framework

The initial conditions for the structure of accretion disk should be specified in the fixed grid and the background metric most appropriate for the GRB problem is the Kerr spacetime. This is because the black hole is rapidly spinning. The initial condition evolves according to the continuity equation and the energy-momentum conservation equation:

$$\left(\rho u_{\mu}\right)_{;\nu} = 0 \tag{4}$$

$$T^{\mu}_{\nu;\mu} = 0 \tag{5}$$

If the magnetic fields are taken into account, the energy tensor contains matter parts and electro-magnetic parts:

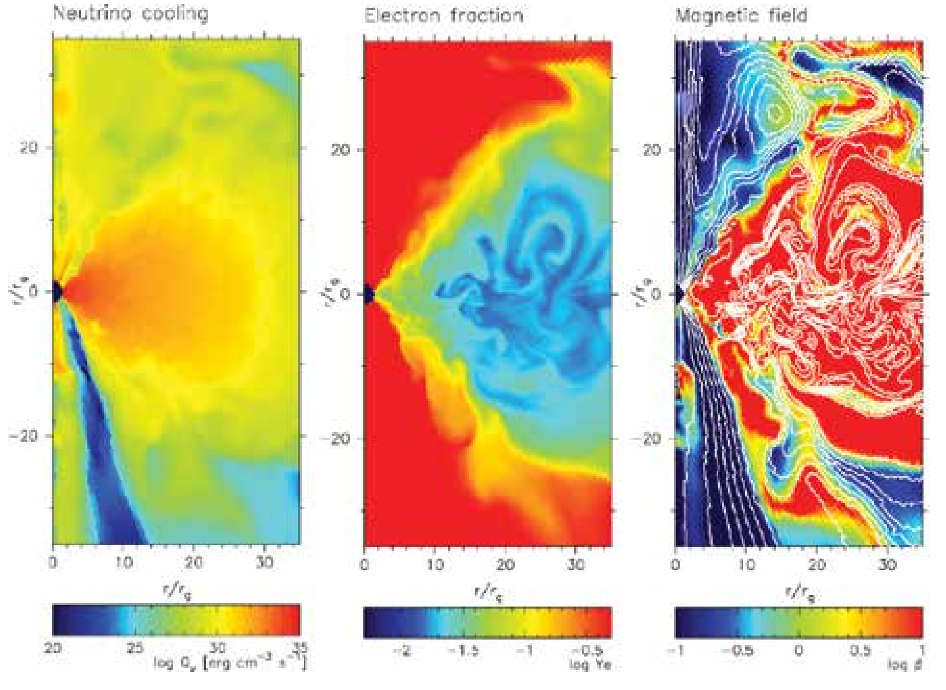

Figure 2. Neutrino emissivity (left), electron fraction (middle), and gas to magnetic pressure ratio (right) in the 2-dimensional simulation of the innermost parts of accretion flow around black hole in the GRB central engine. Contours show the magnetic field configuration. Parameters of the model are black hole spin $a = 0.98$, black hole mass $M = 3M_{\odot}$, and disk mass $M_d = 0.1M_{\odot}$.

$$T^{\mu\nu} = T^{\mu\nu}_{gas} + T^{\mu\nu}_{EM} \tag{6}$$

where

$$T^{\mu\nu}_{gas} = \rho h u^{\mu} u^{\nu} + p g^{\mu\nu} = (\rho + u + p) u^{\mu} u^{\nu} + p g^{\mu\nu} \tag{7}$$

$$T^{\mu\nu}_{EM} = b^2 u^{\mu} u^{\nu} + \frac{1}{2} b^2 g^{\mu\nu} - b^{\mu} b^{\nu}; \;\; b^{\mu} = u_{\nu} F^{\mu\nu} \tag{8}$$

where equation of state of gas in the adiabatic form, $p = K\rho^{\gamma} = (\gamma - 1)u$, does not hold for the dense and hot plasma in the GRB flows. The EOS has to be therefore substituted with the Fermi gas.

2.4. Nucleosynthesis of heavy isotopes in GRB engines

The subsequent isotopes after Helium are created in the outer layers of the accretion disk body, as well as in its ejecta. Synthesis of heavy isotopes can be computed by means of the thermonuclear reaction network simulations [33]. The code and reaction data (http://webnucleo.org) can be adopted to read the input data in the form of density, temperature, and electron fraction distribution along the distance radial coordinate in the accretion disk [34]. The numerical methods and algorithms in the network computations under the nuclear statistical equilibrium were described in Hix and Meyer [35] (see also Meyer [36] for a review of the r-process nucleosynthesis theory) (**Figure 3**).

The analysis of the integrated mass fraction distribution allows establishing the role of global parameters of the accretion flow model, such as the black hole mass and its spin, in forming the disk composition. We show here the resulting distribution of certain chosen isotopes synthesized

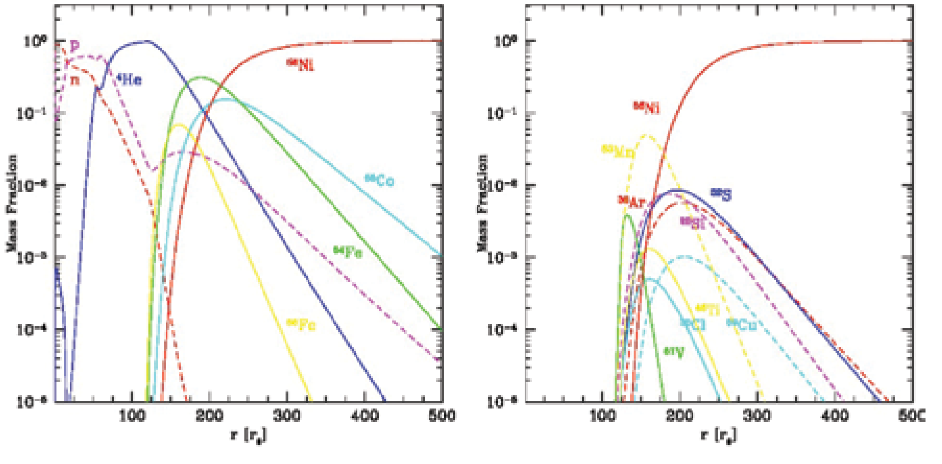

Figure 3. Profiles of the relative, height integrated mass fractions of the most abundant isotopes produced in the body of the accretion torus in GRB engine. The accretion rate is equal to about $0.1 M_{\odot} s^{-1}$. The black hole parameters are $M = 3M_{\odot}$, and $a = 0.98$. Nucleosynthesis computations were based on the NSE condition.

in the nearest vicinity of the accreting black hole (up to $500R_g$). The computations were performed via postprocessing of the results of the accretion disk structure, as computed for the spinning stellar mass black hole in the collapsar center [34]. As was also shown by Banerjee & Mukhopadhyay [37], many new isotopes of titanium, copper, zinc, etc., are present in the outflows. Emission lines of many of these heavy elements have been observed in the X-ray afterglows of several GRBs by Chandra, BeppoSAX, XMM-Newton; however Swift seems to have not yet detected these lines. In principle, the evolution of the isotope distribution can be traced along the trajectories of the winds ejected from the disk surface to large distances. Such situation is more appropriate for ejecta launched from disks feeding short GRBS, which forms in addition to the dynamical ejecta from the NS-NS merger [38]. If the accretion disk wind is expanding faster than the preceeding ejecta, the signatures of heavy elements might be observable via their radioactive decay and subsequent optical and infrared emission [39] called a 'kilonova' (see review by Tanaka [40]). Theoretically, this problem was studied in the first computations by Janiuk [32] and also by Siegel and Metzger [41].

3. Numerical simulations

The modeling of the emerging outflows in both types of GRBs is in general a very difficult task. Beyond the challenges of the various microphysical process participating and the general relativistic frameworks, it involves a wide range of spatial scales. For example, a simulation aimed to describe the whole extent of a jet originating from compact binaries needs a fine resolution of $\sim 10^2$ points for a typical 10 km of NS radius, or even an order of magnitude shorter, in order to properly resolve hydromagnetic phenomena like turbulence, Kelvin-Helmholtz instability (see Zrake & MacFadyen [42]; Kiuchi et al. [43]), and the magnetorotational instability (see Hawley et al. [44] and references therein). However, it must be able to reach radial distances up to the $\left(10^2 - 10^6\right)r_g$ where the terminating Lorentz factor might be achieved (e.g., Tchekhovskoy et al. [45]). An even more extended scale regime occurs in the long GRBs counterpart since the spatial scales involve the stellar envelope penetration phase and the propagation to the surrounding space (10^{10}–10^{13} cm). It is thus apparent that building a global simulation describing the whole outflow evolution is much beyond the present calculating capabilities and every specific effort is able to describe accurately a particular phase of the evolution, more or less extended depending on the use of adaptive mesh refinement techniques or a clever mesh selection.

3.1. Full GRMHD scheme

The merging phase of the compact object binaries has to be performed by fully relativistic schema, that is, ones that beyond capturing the essential of the hydro- and magneto-hydrodynamic aspects of the accretion evolves also the space-time. At present, the ambiguity for the precise nature of the members consisting the binary has not been clarified and the dominant research effort is oriented toward the BH-NS, NS-NS candidates. As a result, a number of codes were developed to solve the underlying equations for both types of progenitors, every of which presenting its own approximations and limitations (see Paschalidis [46] for a list on the codes and a more detailed review on the full GR findings).

Assuming the driving object of the burst is a black hole—torus system simulations must accomplish two challenges: create a viable disk that feeds the system for the burst duration and launch a jet which able to reach the Lorentz factor $\gamma_f \geq 100$ that satifies the fireball model requirements. None of these tasks are trivial to be obtained. Back of the envelope estimates for the accretion rate is $\dot{M} \sim \left(\varepsilon c^2\right)$, where ε is the efficiency of converting the disk accretion to the observed γ-photons luminosity, for the typical values of the sGRB medium value duration $t \sim 0.3s$ [4] and energy of 10^{51} erg result to a disk of $\sim 0.015 M_{\odot}$. Foucart [47] examined a number of unmagnetized BHNS simulation and proposed the fit:

$$\frac{M_{disk}}{M_{NS}} = 0.42 q^{1/3}(1-2C) - 0.148\frac{R_{ISCO}}{R_{NS}} \quad , \quad q = \frac{M_{BH}}{M_{NS}} \quad C = \frac{M_{NS}}{R_{NS}} \tag{9}$$

which is applicable on $a \leq 0.9$ [48], while a similar relationship has been proposed for the NS-NS and in the framework of the hydro simulations [49], but contrary to the one above the estimation is now EOS-dependent. Inspection of the above expression for a fixed value of q and assumed value of the compaction C provides the remnant disk mass as a function of the BH spin. The results of Foucart [47] and Lovelace et al. [48] point toward high initial values of the BH spin, if a massive disk is to be created.

Although the launch of jets was naturally obtained in the fixed space time simulations long before, that task proved to be non-trivial for the full GR ones. The NS-NS simulations by Rezzolla et al. [50] were until recently the only ones that demonstrated the emerging of a jet, while most of the simulations did not show a collimated outflow. For example, the BHNS of Kiuchi et al. [51], a wind was found, but for the NS-NS model of the pressure of the fall back material was so strong preventing even the launching of the wind.

All the above indicates that the magnetic field topology close to the vicinity of the black hole is of crucial importance and no matter of what process (Blandford and Payne [52]) is the one that drives the outflow acceleration and the resulting jet, a large scale poloidal component is crucial to drive the energy outflow outwards. But in the simulations, the field remaining outside the black hole is wounded to a toroidal configuration, while the poloidal component had an alternating orientation. Finally, the launching of the jets in the BHNS framework was achieved once a more realistic bipolar initial configuration was adopted [53]. The realization of such a configuration is a difficult task mostly because of the low density of the exterior medium. By adopting a specific set of initial condition to overcome code limitations on this regime, the authors managed to produce a configuration of enhanced magnetic field over the BH poles because of the magnetic winding. The field strength increased from 10^{13} to 10^{15} G, which is a crucial value for the BZ process (see below), resulted in the launch of a 100 ms jet, a relatively short duration. A similar evolution was also obtained for the NS-NS framework, where once again the importance of the exterior magnetic field seems to be of crucial importance [54]. As a result, previous GRMHD results of Rezzolla et al. [50] have been confirmed, while in consistency with Kiuchi et al. [51], the jet was launched only after the density of the fall back material above the BH has decreased.

4. Ejection and acceleration of jets in gamma ray bursts

In both frameworks of the bursts, the plausible central engine refers to hyperaccreting solar mass black holes surrounded by a massive disk $(0.1-1)M_{\odot}$, while the energy released and the prompt phase duration points to high accretion rates of order $(0.01-10)M_{\odot}s^{-1}$. The high-energy non-thermal photons received by the observers point for an ultrarelativistic outflow $\gamma \geq 100$, most likely in jet geometry, that in turn implies baryon-clean outflow. Building a launching mechanism for such a jet is not trivial and beyond the Blandford Znajek proccess [55]. Therefore, an another type of mechanism namely the neutrino pair annihilation was proposed.

But beyond the enormous energetic constrains, our mechanism has to face another major challenge, namely, the great variability of the prompt emission lightcurves. Although long debated, two of the most widely accepted models for the origin of the γ-radiation, the internal shocks and the photospheric emission link the rapid variability directly with the properties of the central engine (see, however, Morsony et al. [56] and Zhang & Yan [57] for a source of additional variability due to the propagation inside the star and the effects of amplified local turbulence). As a consequence, the determination of the minimum time variability by the observational data is of primary importance, but that proves to be challenging since the corresponding time scales have power densities very close to the data noise. Nevertheless, some typical values can be obtained and MacLachlan et al. [58] using a method based on wavelets proved that both types of bursts present variability in the order of a few to few tenths of milliseconds, with the long GRBs exhibiting a longer time variability than the short bursts.

4.1. Jet launching

The high density and temperature of the accreting flow result in a photon optically thick disk that cannot cool by radiation efficiently. On the other hand, the high temperature and density result in the intense neutrino emission from the inner parts of the disk, called NDAF (neutrino dominated accretion flow). The effects of neutrino outflow, if it is capable to produce a highly relativistic jet and what implications it imposes when it is combined with the Blandford-Znajek process, is a matter of intense debate, presently inconclusive. There exist two critical values of the accretion rate, $\dot{M}_{ign}$ and $\dot{M}_{trapped}$, that determine the efficient neutrino cooling. If the accretion rate is lower, the temperature is not high enough to initiate the neutrino emission. If the accretion rate is higher, the disk becomes optically thick to neutrinos. Assuming an α-viscosity in the disk [59], the values of the critical rates depend on both α and the spin of black hole a. For example, the calculation by Chen and Beloborodov [60] provided the fit:

$$\dot{M}_{ign} = K_{ign}\left(\frac{\alpha}{0.1}\right)^{5/3} \quad \dot{M}_{trap} = K_{trap}\left(\frac{\alpha}{0.1}\right)^{1/3} \tag{10}$$

where K_{ign}, K_{trap} depend on the black hole's spin. For $a=0$, $K_{ign}=0.071M_{\odot}s^{-1}$, $K_{trap}=9.3M_{\odot}s^{-1}$, while for $a=0.95$, $K_{ign}=0.021M_{\odot}s^{-1}$, $K_{trap}=1.8M_{\odot}s^{-1}$.

The total energy ejected in neutrinos was calculated by Zalamea and Beloborodov [61] and in principle can reproduce the GRB energies, but for the higher accretion rates $\dot{M} > 0.1 M_{\odot}\,\mathrm{s}^{-1}$ [62, 63], making the association with the longest duration bursts $t > 30s$ is problematic [64]. Recent hydrodynamic simulations of Just et al. [65] assuming a black hole and torus accretion system gave negative conclusion for the neutrino annihilation applicability on the merger type progenitors. Specifically, the NS-NS merger tends to create heavier baryon loaded environments. Moreover, the efficiency of the mechanism is crucially depend on the fastly rotating central object which might be difficult to obtain in the case of the NS-NS mergers. The situation is more improved for the BH-NS progenitor, providing $E^{ISO}_{\gamma>100} \sim 2 \times 10^{50}$erg, in a half cone opening around the axis $\theta_{\gamma>100} > 8^{o}$ which is only an order of magnitude lower than the medium of the observed GRBs [66]. Thus, the neutrino annihilation process can be applicable to the less energetic GRBS, but we still can exclude the case of its partial contribution to the rest class of short bursts (see, however, Levinson and Globus [67]).

The other mechanism that accounts for the launch of a low baryon loaded jet is the Blandford-Znajek process that might be resembled with a Penrose proccess of an ideally conducting plasma in the force free limit. According to it, the plasma is pushed via accretion to the ergospheric negative energy orbits, while the magnetic twist results in an outward propagating electromagnetic jet (see Komissarov [68] for an excellent explanation).

In general, the rotational energy of a black hole is

$$E_{rot} = 1.8 \times 10^{54} f(a) \frac{M}{M_{\odot}} erg \quad , \quad \mathrm{f(a)} = 1 - \sqrt{\frac{1+\sqrt{1-a^2}}{2}} \tag{11}$$

where $f(a) = 0.29$ for a maximally rotating BH ($a = 1$). The rotational energy of the BH can be extracted through the lines threading the horizon forming a Poynting dominated jet of power

$$\dot{E}_{BZ} = 10^{50} a^2 \left(\frac{M}{M_{\odot}}\right)^2 F(a) \left(\frac{B}{10^{15} G}\right)^2 \mathrm{ergs}^{-1} \tag{12}$$

where the spin dependent function is properly obtained under full GR framework. A familiar analytical approximation obtained by Lee et al. [69] and Wang et al. [70] is:

$$F(a) = \frac{1+q^2}{q^2}\left(\frac{1+q^2}{q^2}\arctan q - 1\right) \quad , \quad \mathrm{q} = \frac{\mathrm{a}}{1+\sqrt{1-\mathrm{a}^2}} \tag{13}$$

where $2/3 \geq F(a) \geq (\pi - 2)$ for $0 \geq a \geq 1$. A numerical investigation of the above estimation performed by Tchekhovskoy and McKinney [71] shows only small deviations at the very high rotation factors [72].

In the simulations under the fixed Kerr spacetime [71, 73], the central object is fed with a relatively large magnetic flux, that is, more than what the accreting plasma can push inside the horizon. The excessing part of the magnetic flow remains outside the horizon and forms a magnetic barrier [74, 75], saturating accretion and forming a baryon-clean funnel around the axis of rotation (MAD, magnetically-arrested disk). Moreover in some specific initial configuration assumed, the time averaged power of the jet outflow efficiency $\dot{E}_{\rm BZ}$ exceeded the accretion one $\dot{M}c^2$, demonstrating the extraction of the rotational energy of the central object. As a conclusion, the high values of the emitted energy combined with the low baryon load currently set the BZ as the favorable mechanism applying on the GRB. Nevertheless, as mentioned before the whole picture is still incomplete and it will probably remain so, as long as the neutrino effects will not be taken into account in a self-consistent manner.

4.2. Collimation mechanisms

The effects of the surrounding to the jet material are crucial for the dynamic evolution of the jet affecting both its acceleration and collimation. The build up of a large scale toroidal component in a magnetic dominated jet results to hoop stress that contributes to the jet collimation [76]. Nevertheless, this contribution proves to be less efficient in the relativistic regime and turns to be insufficient even for the cases where a very fast rotation is induced [77–79]. As a result, the contribution of the exterior environment pressure plays a fundamental role in the GRB outflow evolution for the merging binaries and core-collapsing bursts.

In the long GRB framework, the outflow penetrates the stellar envelope, most likely a Wolf-Rayet star, and continues its propagation to the interstellar space. The propagation of the jet's head in the dense environment results to sideway motion of the stellar material and to the formation of a hot cocoon surrounding the jet. The accurate description of such a system is cyclic and both jet and stellar material must be described self consistently. The jet velocity depends crucially on the jet cross section, while it determines the amount of energy injected in the cocoon that in its turn defines the supporting exterior pressure of the jet. As a result, there exists a number of numerical simulations investigating the evolution of this phase both of hydrodynamic (e.g., Mizuta and Aloy [80]; Lazzati et al. [81]) as also of magnetic dominated outflows [82]. In addition, theoretical and semi-analytical models have also been developed to interpret the underlying processes (e.g., Bromberg et al. [83]; Globus & Levinson [84]).

The initial propagation, close to the launching point, is similar to the two extreme case of a hydro or Poynting dominated jet since the outflows internal pressure much exceeds the cocoon's one. The outflow's freely expansion is up to the collimation point defined by the equality of the above quantities, while after it the outflow evolution differs accordingly to its magnetic context (see Granot et al. [85] for a review). The Poynting dominated outflows result in a faster drilling breakout time in an order of magnitude 0.1 to ~10 s. Bromberg et al. [86] proposed a criterion to identify t_b so that the burst T_{90} duration is directly correlated with the central engine activity. As a result, there expected a plateau at the long GRB duration distribution for times lower than the break out one. Surprisingly, the analysis of the observational data from the three most dedicated satellites (BATSE, Swift, and Fermi) provided values that are in favor of the hydrodynamic propagation scenario. If the hydrodynamic launching mechanism is to be excluded for the above reasons, a process that dissipates the outflow energy inside the star has to be found. Lately, the progress has been made by the investigation of the 'kink instability' [82]. As a result, a typical Poynting dominated collapsar jet is able to achieve the equipartition between thermal and magnetic energy at the so-called recollimation point ($\sim 10^8 cm$ in the specific simulations) without being disrupted by the instability. Such a jet propagates more or less as a hydrodynamic jet [85].

5. Radiative processes in jets: emission of gamma rays

Although rich in models, the dynamics of the phase after the jet break out, that is, at the place where the prompt radiation is being produced, is still not well understood. Among the two models assuming matter or Poynting flux dominance, the hot fireball [22, 87] is the older and more widely used one. The matter dominated fireball is mainly constituted by baryons and radiation, with the latter being significantly larger by at least two orders of magnitude. The adiabatic expansion of the fireball accelerates the baryons to high Lorentz factor, while a fraction of this thermal energy is being radiated when the flow becomes transparent to the electron-positron pair creation, providing the so-called photospheric emission. In even higher distances, the outflow inhomogeneities endure mutual collisions leading to the formation of internal shocks that accelerate electrons and produce the non-thermal part of the observed radiation.

The location of the photospheric radius R_{ph}, when we assume that acceleration has effectively completed (saturation radius) before the flow becomes transparent, was calculated by the number of models. Following, for example, Hascoët et al. [88] and references therein,

$$R_{ph} \simeq \frac{\kappa \dot{M}}{8\pi c \gamma^2} \sim 2.9 \times 10^{13} cm \left(\frac{k}{0.2cm^2/g}\right)(1+\sigma)^{-1}\left(\frac{\gamma}{100}\right)^{-3}\left(\frac{\dot{E}_{iso}}{10^{53} erg/s}\right) \tag{14}$$

where σ is the magnetization parameter at the saturation radius. The corresponding observed temperature and luminosity are:

$$T_{ph} \approx \frac{T_0}{1+z}\left(\frac{R_{ph}}{\gamma R_0}\right)^{-2/3} \quad L_{ph} = 4\pi R_0^2 \sigma_T T_0^4 \left(\frac{R_{ph}}{\gamma R_0}\right)^{-2/3} \tag{15}$$

where z is the redshift and T_0 is the temperature at the initial radius R_0. The emerging radiation is called a modified black body [87] with the lower energy Raleigh-Jeans tail having a photon index of 0.4 instead of 1 in the usual black body lower energy limit, because of relativistic geometric effects. It is worth to mention here that if some sub-photospheric dissipation occurs before the photospheric radius then the above scaling does not hold and the low energy part of the spectrum will be modified (see, for example, Thompson [89] and Giannios and Spruit [90] for the reconnection implications).

Beyond the photospheric emission, the interpretation of the non-thermal prompt emission is much more challenging. Up to day, there is no definite answer for the precise place that the γ-radiation emerge, but the most popular model is the internal shock model [91]. This model provides a natural way to dissipate the bulk kinetic of the outflow by assuming the mutual collision of inhomogeneities existing at the main body of the outflow. One of the great advantage of this model is its simplicity, while back of the envelope calculations exhibits the beauty and the essentials of the process.

Lets assume two cells with Lorentz factors $\gamma_1, \gamma_2 \gg 1$ and masses m_1, m_2, respectively, emitted with a time difference δt. As long as the latter is propagating faster, their mutual collision will occur at a distance

$$R_{int} = \frac{2\gamma_1^2\gamma_2^2}{\gamma_2^2 - \gamma_1^2} c\delta t \sim 2\gamma_{avg}^2 c\delta t \tag{16}$$

where γ_{avg} is the average Lorentz factor of the outflow. Using the conservation of the 4-momentum, we can model a plastic collision that will provide a single cell propagating

$$\gamma_f = \frac{m_1\gamma_1 + m_2\gamma_2}{\sqrt{m_1^2 + m_2^2 + 2m_1m_2\gamma_r}} \tag{17}$$

where $\gamma_r = \gamma_1\gamma_2(1 - u_1u_2/c^2)$ is the Lorentz factor of the relative motion; in reality the collision results in a pair of shocks that propagate at the slower and faster cell, respectively.

The observed time variability is given by Kobayashi et al. [92]; Daigne and Mochkovitch [93]; and Kumar and Zhang [72].

$$\delta t_{obs} \sim \delta t + \frac{R_{int}}{2c^2\gamma_f^2} \sim \left(1 + \frac{\gamma_1}{\gamma_2}\right)\delta t \tag{18}$$

where the first term of the right hand is because of the injection time difference and the second because of the shock propagation. We notice that the variability of lightcurves traces in general the central engine activity, and as a result, the high variability of the prompt emission can be ascribed to the intrinsic variability of the source (BH-torus for short bursts, BH-torus plus the propagation inside the star for the long ones).

The biggest problem for the internal shock model is the efficiency of the collisions. The efficiency of the thermal energy production is easily obtained

$$\varepsilon_{therm} = 1 - \frac{m_1 + m_2}{\sqrt{m_1^2 + m_2^2 + 2m_1m_2\gamma_r}} \tag{19}$$

and is maximized for a given γ_r when the two cells are of equal mass $\varepsilon_{therm,\max} = 1 - \sqrt{2/(1+\gamma_r)}$, e.g., if $\gamma_r = 10$, $\varepsilon_{therm,\max} = 0.28$. Detailed analysis by the number of authors increases this limit up to 40% for thermally dominated outflows, but most of the times the corresponding efficiency is in the range $(1-10)\%$, contrary to the observations that suggest efficiencies exceeding 50% (see Kumar and Zhang [72] and references therein).

Despite the great progress in the interpretation of the prompt GRB radiation, crucial issues still remain open and especially on how the mildly relativistic shocks accelerate particles. As a result, today no model that describes self consistently the whole process exists and most of the approach still uses the fractions ε_B, ε_e of the internal energy that is dissipated on an enhanced magnetic field of the shocked gas and on some fraction of electrons accelerated to a non-thermal energetic distribution. Sequentially to the approximation of the shocked regime, the radiation models can be applied and used to examine all the intervening radiative and kinetic processes. An interesting point to notice is that the cell high magnetization, $\sigma \gg 1$, leads to inefficient collisions preventing the dissipation of the energy [94, 95]. In such a case, the acceleration of the electron can be obtained through the reconnection process. Such a process can occur before or after the photospheric radius [96–98] and despite the extensive outgoing study of the process there are still even bigger ambiguities than the other two just mentioned [99]. For a review on the issue, the reader can refer Kagan et al. [100].

6. Multimessanger discoveries of electromagnetic and gravitational wave counterparts

The assembly of black hole binaries detected in gravitational waves by the LIGO interferometer was established since the discovery of GW150914 [101]. These systems contain very massive black holes, whose origin poses a puzzle for the stellar evolution models [102]. One of the possible scenarios for the formation of such a black hole is a process of direct collapse of massive stars. Here, no spectacular hypernova explosion is proposed, and hence no gamma ray burst should have occured during the formation of a very massive black hole neither for the first nor for the second component in the binary. An additional issue is the feedback from a rotationally supported innermost parts of the star during the collapse. It is rather natural that the star at its final stages of evolution should posses some non-negligible angular momentum in the envelope. This angular momentum may, however, help unbind the outer layers and halt accretion (Ramirez-Ruiz 2017, private communication). This will have a consequence for both the ultimate mass of the black hole, and its resultant spin, to be independently verified by the values obtained for these parameters from gravitational waveform constraints.

One of the possibilities when the gravitational wave signal would be found in relation to the rotating massive star collapse, and coincident with a gamma ray burst, was proposed by Janiuk et al. [103]. In this scenatio, the collapse of a massive rotating star in a close binary system with a companion black hole. The primary BH which forms during the core collapse is first being spun up and increases its mass during the fall back of the stellar envelope. As the companion BH enters the outer envelope, it provides an additional angular momentum to the gas. After the infall and spiral-in toward the primary, the two BHs merge inside the circumbinary disk. The second episode of mass accretion and high final spin of the postmerger BH feeds the gamma ray burst.

In the above framework, it is in principle possible that the observed events have two distinct peaks in the electromagnetic signal, separated by the gravitational wave emission. The reorientation of spin vector of the black holes and gravitational recoil of the burst engine is, however, possible. Therefore, the probability of observing two electromagnetic counterparts of the gravitational wave source would be extremely low.

The electromagnetic signal is in general not expected from a BH-BH merger. However, the weak transient detected by Fermi GBM detector 0.4 s after GW 150914 has been generating much speculation [104, 105]. Despite the fact that other gamma ray missions claimed non-detection of the signal, several theoretical scenarios aimed to account for such a coincidence, whether detected, or to be found in the future events [106–110].

Finally, the binary neutron star merger GW170817, detected in gravitational waves, was connected with the gamma ray emission observed as a weak short burst [111]. Its peculiar properties pose constraints for the progenitor model [112]). Moreover, at lower frequencies, the follow-up surveys have shown the presence of a kilonova emission from the merger’s dynamical ejecta. These ejecta masses are broadly consistent with the estimated r-process production rates, required before to explain the Milky Way isotopes abundances. It is possible that the magnetically driven winds launched due to the accretion in the GRB engine may also contribute to the kilonova emission from NS-NS merger.

7. Summary

Gamma ray bursts are known since almost 50 years now and are still an exciting field of research for both observers and theoretitians. Their energetic requirements proved the fundamental role of the stellar mass black hole formation and mass accretion in the production of ultrarelativistic jets.

The details of this process are, however, far from being fully understood. In short GRBs, the process of black hole birth after the neutron star merger may proceed through different channels, with the possible presence of a transient hypermassive neutron star, depending on the EOS and rotation of the progenitors. In long GRBs, the properties of progenitor star, its envelope rotation, metallicity, etc., as well as the binarity of the whole system, may affect the core collapse in an even greater way. The question of binarity is of a great interest in the context of the fate of high mass X-ray binaries, such as Cygnus X-3, which in addition to the pre-hypernova star contains a companion which is most probably a black hole.

Such fundamental questions are now being attacked with the modern tools of numerical astrophysics, which involve relativistic magnetohydrodynamics and nuclear physics. With the discovery of gravitational waves, a new window has also opened from the observational point of view, especially since the gamma ray signal has been identified in connection with the compact object merger. The identification of the additional electromagnetic signal from the radioactive decay of the GRB ejecta provided a completely new way to probe the whole process and hopefully build a comprehensive picture in the near future.

Acknowledgments

We acknowledge the financial support from the Polish National Science Center through the Grant Sonata-Bis No DEC-2012/05/E/ST9/03914. We also thank the Interdisciplinary Center for Mathematical and Computational Modeling of the Warsaw University for the access to their supercomputing resources, under the grant GB 70-4. Finally, AJ would like to thank the Kavli Summer Program in Astrophysics 2017, and the Center for Transient Astrophysics at the Niels Bohr Institute, for great hospitality and inspiring environment.

Author details

Agnieszka Janiuk* and Konstantinos Sapountzis

*Address all correspondence to: agnes@cft.edu.pl

Centrum Fizyki Teoretycznej PAN, Warsaw, Poland

References

[1] Fishman GJ, Meegan CA. Gamma-Ray Bursts. Annual Review of Astronomy and Astrophysics. 1995;**33**:415

[2] Klebesadel RW, Strong IB, Olson RA. Observations of Gamma-Ray Bursts of Cosmic Origin. The Astrophysical Journal. 1973;**182**:(L85)

[3] Colgate SA. Prompt gamma rays and X-rays from supernovae. Canadian Journal of Physics. 1968;**46**:S476

[4] Kouveliotou C et al. Identification of two classes of gamma-ray bursts. The Astrophysical Journal. 1993;**413**:L101

[5] Costa E et al. Discovery of an X-ray afterglow associated with the γ-ray burst of 28 February 1997. Nature 1997;**387**:783. astro-ph/9706065

[6] Metzger MR et al. Spectral constraints on the redshift of the optical counterpart to the γ-ray burst of 8 May 1997. Nature. 1997;**387**:878

[7] Sahu KC et al. The optical counterpart to γ-ray burst GRB970228 observed using the Hubble Space Telescope. Nature. 1997;**387**(476). astro-ph/9705184

[8] Djorgovski, SG et al. The cosmic gamma-ray bursts and their host galaxies in a cosmological context. In: Guhathakurta P, editor. Discoveries and Research Prospects from 6-to 10-Meter-Class Telescopes II, Proc. SPIE. 2003;**4834**:238-247. astroph/0301342

[9] Frail DA et al. GRB 010222: A Burst within a Starburst. The Astrophysical Journal. 2002; **565**:829. astroph/0108436

[10] Porciani C, Madau P. On the Association of Gamma-Ray Bursts with Massive Stars: Implications for Number Counts and Lensing Statistics. The Astrophysical Journal. 2001;**548**:522. astroph/0008294

[11] Piran T. The physics of gamma-ray bursts. Reviews of Modern Physics. 2004;**76**:1143. astro-ph/0405503

[12] Hjorth J et al. A very energetic supernova associated with the γ-ray burst of 29 March 2003. Nature 2003;**423**:847. astro-ph/0306347

[13] Stanek KZ et al. Spectroscopic Discovery of the Supernova 2003dh Associated with GRB 030329. The Astrophysical Journal. 2003;**591**(L17). astro-ph/0304173

[14] Bloom JS et al. The unusual afterglow of the γ-ray burst of 26 March 1998 as evidence for a supernova connection. Nature. 1999;**401**:453. astro-ph/9905301

[15] Salvaterra R et al. GRB090423 at a redshift of $z{\sim}8.1$. Nature. 2009;**461**:1258. 0906.1578

[16] Guetta D, Piran T. The BATSE-Swift luminosity and redshift distributions of short-duration GRBs. Astronomy and Astrophysics. 2006;**453**:823. astro-ph/0511239

[17] Natarajan P et al. The redshift distribution of gamma-ray bursts revisited. Monthly Notices of the Royal Astronomical Society. 2005;**364**:L8. astro-ph/0505496

[18] Achterberg A et al., Search for Neutrino-induced Cascades from Gamma-Ray Bursts with AMANDA. The Astrophysical Journal. 2007;**664**(397). astro-ph/0702265

[19] Kimura SS, Murase K. Mészáros, P., Kiuchi, K., High-energy Neutrino Emission from Short Gamma-Ray Bursts: Prospects for Coincident Detection with Gravitational Waves. The Astrophysical Journal. 2017;**848**:L4. 1708.07075

[20] Paczynski B, Xu G. Neutrino bursts from gamma-ray bursts. The Astrophysical Journal. 1994;**427**:708

[21] Eichler D, Livio M, Piran T, Schramm DN. Nucleosynthesis, neutrino bursts and gamma-rays from coalescing neutron stars. Nature. 1989;**340**:126

[22] Paczynski B. Gamma-ray bursters at cosmological distances. The Astrophysical Journal. 1986;**308**:(L43)

[23] Paczyński B. Are Gamma-Ray Bursts in Star-Forming Regions? The Astrophysical Journal. 1998;**494**:L45. astro-ph9710086

[24] Woosley SE. Gamma-ray bursts from stellar mass accretion disks around black holes. The Astrophysical Journal. 1993;**405**:273

[25] MacFadyen AI, Woosley SE. Collapsars: Gamma-Ray Bursts and Explosions in "Failed Supernovae". The Astrophysical Journal. 1999;**524**(262). astro-ph/9810274

[26] Fryer CL et al. Constraints on Type Ib/c Supernovae and Gamma-Ray Burst Progenitors. Publications of the Astronomical Society of the Pacific. 2007;**119**;1211. astro-ph/0702338

[27] Woosley SE, Bloom JS. The Supernova Gamma-Ray Burst Connection. Annual Review of Astronomy and Astrophysics. 2006;**44**:507. astro-ph/0609142

[28] Podsiadlowski P et al. The Rates of Hypernovae and Gamma-Ray Bursts: Implications for Their Progenitors. The Astrophysical Journal. 2004;**607**(L17). astro-ph/0403399

[29] Zhang B. Gamma-Ray Bursts in the Swift Era. Chinese J. Astronomy and Astrophysics. 2007;**7**:1. astro-ph/0701520

[30] Narayan R, Piran T, Kumar P. Accretion Models of Gamma-Ray Bursts. The Astrophysical Journal. 2001;**557**:949. astro-ph/0103360

[31] Usov VV. Millisecond pulsars with extremely strong magnetic fields as a cosmological source of gamma-ray bursts. Nature. 1992;**357**:472

[32] Janiuk A. Microphysics in the Gamma-Ray Burst Central Engine. The Astrophysical Journal. 2017;**837**(39):1609.09361

[33] Wallerstein G et al. Synthesis of the elements in stars: forty years of progress. Reviews of Modern Physics. 1997;**69**:995

[34] Janiuk A. Nucleosynthesis of elements in gamma-ray burst engines, Astronomy and Astrophysics 2014;**568**:A105. 1406.4440

[35] Hix WR, Meyer BS. Thermonuclear kinetics in astrophysics. Nuclear Physics A. 2006;**777**: 188. astro-ph/0509698

[36] Meyer BS. The r-, s-, and p-Processes in Nucleosynthesis. Annual Review of Astronomy and Astrophysics. 1994;**32**:153

[37] Banerjee I, Mukhopadhyay B. Nucleosynthesis in the Outflows Associated with Accretion Disks of Type II Collapsars. The Astrophysical Journal. 2013;**778**(8):1309.0954

[38] Wu M-R, Fernández R, Martínez-Pinedo G, Metzger BD. Production of the entire range of r-process nuclides by black hole accretion disc outflows from neutron star mergers. Monthly Notices of the Royal Astronomical Society. 2016;**463**(3):2323

[39] Tanvir NR et al. A 'kilonova' associated with the short-duration γ-ray burst GRB 130603B. Nature 2013;**500**:(547). 1306.4971

[40] Tanaka M. Kilonova/Macronova Emission from Compact Binary Mergers. Advances in Astronomy. 2016;**2016**:634197. 1605.07235

[41] Siegel DM, Metzger BD. Three-Dimensional General-Relativistic Magnetohydrodynamic Simulations of Remnant Accretion Disks from Neutron Star Mergers: Outflows and r-Process Nucleosynthesis. Physical Review Letters. 2017;**119**(23):231102. 1705.05473

[42] Zrake J, MacFadyen AI. Magnetic Energy Production by Turbulence in Binary Neutron Star Mergers. The Astrophysical Journal. 2013;**769**(L29). 1303.1450

[43] Kiuchi K et al. Efficient magnetic-field amplification due to the Kelvin-Helmholtz instability in binary neutron star mergers. Physical Review D. 2015;**92**(12):124034. 1509.09205

[44] Hawley JF, Guan X, Krolik JH. Assessing Quantitative Results in Accretion Simulations: From Local to Global. The Astrophysical Journal. 2011;**738**(84):1103.5987

[45] Tchekhovskoy A, McKinney JC, Narayan R. Simulations of ultrarelativistic magnetodynamic jets from gamma-ray burst engines. Monthly Notices of the Royal Astronomical Society. 2008;**388**(551):0803.3807

[46] Paschalidis V. General relativistic simulations of compact binary mergers as engines for short gamma-ray bursts. Classical and Quantum Gravity. 2017;**34**(8):084002. 1611.01519

[47] Foucart F. Black-hole-neutron-star mergers: Disk mass predictions. Physical Review D. 2012;**86**(12):124007. 1207.6304

[48] Lovelace G et al. Massive disc formation in the tidal disruption of a neutron star by a nearly extremal black hole. Classical and Quantum Gravity 2013;**30**(13):135004. 1302.6297

[49] Shibata M, Taniguchi K. Merger of binary neutron stars to a black hole: Disk mass, short gamma-ray bursts, and quasinormal mode ringing. Physical Review D. 2006;**73**(6) 064027. astro-ph/0603145

[50] Rezzolla L et al. The Missing Link: Merging Neutron Stars Naturally Produce Jet-like Structures and Can Power Short Gamma-ray Bursts. The Astrophysical Journal. 2011;**732** (L6). 1101.4298

[51] Kiuchi K et al. High resolution magnetohydrodynamic simulation of black hole-neutron star merger: Mass ejection and short gamma ray bursts. Physical Review D. 2015b;**92**(6): 064034. 1506.06811

[52] Blandford RD, Payne DG. Hydromagnetic flows from accretion discs and the production of radio jets. Monthly Notices of the Royal Astronomical Society. 1982;**199**:883

[53] Paschalidis V, Ruiz M, Shapiro SL. Relativistic Simulations of Black Hole-Neutron Star Coalescence: The Jet Emerges. The Astrophysical Journal. 2015;**806**(L14):1410.7392

[54] Ruiz M, Lang RN, Paschalidis V, Shapiro SL. Binary Neutron Star Mergers: A Jet Engine for Short Gamma-Ray Bursts. The Astrophysical Journal. 2016;**824**(L6):1604.02455

[55] Blandford RD, Znajek RL. Electromagnetic extraction of energy from Kerr black holes. Monthly Notices of the Royal Astronomical Society. 1977;**179**:433

[56] Morsony BJ, Lazzati D, Begelman MC. The Origin and Propagation of Variability in the Outflows of Long-duration Gamma-ray Bursts. The Astrophysical Journal. 2010; **723**(267):1002.0361

[57] Zhang B, Yan H. The Internal-collision-induced Magnetic Reconnection and Turbulence (ICMART) Model of Gamma-ray Bursts. The Astrophysical Journal. 2011;**726**(90):1011.1197

[58] MacLachlan GA et al. Minimum variability time-scales of long and short GRBs. Monthly Notices of the Royal Astronomical Society. 2013;**432**:857. 1201.4431

[59] Shakura NI, Sunyaev RA. Black holes in binary systems. Observational appearance. Astronomy and Astrophysics. 1973;**24**:337

[60] Chen, W-X, Beloborodov AM. Neutrino-cooled Accretion Disks around Spinning Black Holes, The Astrophysical Journal. 2007;**657**:383. astro-ph/0607145

[61] Zalamea I, Beloborodov AM. Neutrino heating near hyper-accreting black holes. Monthly Notices of the Royal Astronomical Society. 2011;**410**(2302):1003.0710

[62] Globus N, Levinson A. Loaded magnetohydrodynamic flows in Kerr spacetime. Physical Review D. 2013;**88**(084046):1310.0360

[63] Kawanaka N, Piran T, Krolik JH. Jet Luminosity from Neutrino-dominated Accretion Flows in Gamma-Ray Bursts. The Astrophysical Journal. 2013;**766**(31):1211.5110

[64] Lindner CC, Milosavljevíc M, Couch SM, Kumar P. Collapsar Accretion and the Gamma-Ray Burst X-Ray Light Curve. The Astrophysical Journal. 2010;**713**(2):800

[65] Just O et al. Neutron-star Merger Ejecta as Obstacles to Neutrino-powered Jets of Gamma-Ray Bursts, The Astrophysical Journal. 2016;**816**:L30. 1510.04288

[66] Fong W, Berger E, Margutti R, Zauderer BA. A Decade of Short-duration Gamma-Ray Burst Broadband Afterglows: Energetics, Circumburst Densities, and Jet Opening Angles. The Astrophysical Journal. 2015;**815**(102):1509.02922

[67] Levinson A, Globus N. Ultra-relativistic, Neutrino-driven Flows in Gamma-Ray Bursts: A Double Transonic Flow Solution in a Schwarzschild Spacetime. The Astrophysical Journal. 2013;**770**(159). 1303.4261

[68] Komissarov SS. Blandford-Znajek Mechanism versus Penrose Process. Journal of Korean Physical Society. 2009;**54**(2503):0804.1912

[69] Lee HK, Wijers RAMJ, Brown GE. The Blandford-Znajek process as a central engine for a gamma-ray burst. Physics Reports. 2000;**325**(83). astro-ph/9906213

[70] Wang DX, Xiao K, Lei WH. Evolution characteristics of the central black hole of a magnetized accretion disc. Monthly Notices of the Royal Astronomical Society. 2002;**335** (655). astro-ph/0209368

[71] Tchekhovskoy A, McKinney JC. Prograde and retrograde black holes: Whose jet is more powerful? Monthly Notices of the Royal Astronomical Society. 2012;**423**(L55):1201.4385

[72] Kumar P, Zhang B. The physics of gamma-ray bursts relativistic jets. Phys. Rep. 2015; **561**(1):1410.0679

[73] McKinney JC, Tchekhovskoy A, Blandford RD. General relativistic magnetohydrodynamic simulations of magnetically choked accretion flows around black holes. Monthly Notices of the Royal Astronomical Society. 2012;**423**(3083):1201.4163

[74] Bisnovatyi-Kogan GS, Ruzmaikin AA. The Accretion of Matter by a Collapsing Star in the Presence of a Magnetic Field. Astrophysics and Space Science. 1974;**28**:45

[75] Narayan R, Igumenshchev IV, Abramowicz MA. Magnetically Arrested Disk: An Energetically Efficient Accretion Flow. Publications of the Astronomical Society of Japan. 2003;**55**:L69. astro-ph/0305029

[76] Heyvaerts J, Norman C. The collimation of magnetized winds. The Astrophysical Journal. 1989;**347**:1055

[77] Begelman MC, Li Z-Y. Asymptotic domination of cold relativistic MHD winds by kinetic energy flux. The Astrophysical Journal. 1994;**426**:269

[78] Beskin VS, Kuznetsova IV, Rafikov RR. On the MHD effects on the force-free monopole outflow. Monthly Notices of the Royal Astronomical Society. 1998;**299**:341

[79] Tomimatsu A. Asymptotic collimation of magnetized winds far outside the light cylinder. Publications of the Astronomical Society of Japan. 1994;**46**:123

[80] Mizuta A, Aloy MA. Angular Energy Distribution of Collapsar-Jets. The Astrophysical Journal. 2009;**699**(1261):0812.4813

[81] Lazzati D, Morsony BJ, Begelman MC. Very High Efficiency Photospheric Emission in Long-Duration γ-Ray Bursts. The Astrophysical Journal. 2009;**700**(L47):0904.2779

[82] Bromberg O, Tchekhovskoy A. Relativistic MHD simulations of core-collapse GRB jets: 3D instabilities and magnetic dissipation. Monthly Notices of the Royal Astronomical Society. 2016;**456**(1739):1508.02721

[83] Bromberg O, Granot J, Lyubarsky Y, Piran T. The dynamics of a highly magnetized jet propagating inside a star. Monthly Notices of the Royal Astronomical Society. 2014; **443**(1532):1402.4142

[84] Globus N, Levinson A. The collimation of magnetic jets by disc winds. Monthly Notices of the Royal Astronomical Society. 2016;**461**(2605):1604.07408

[85] Granot J et al. Gamma-Ray Bursts as Sources of Strong Magnetic Fields. Space Science Reviews. 191. 1507;**471**(2015):08671

[86] Bromberg O, Granot J, Piran T. On the composition of GRBs' Collapsar jets. Monthly Notices of the Royal Astronomical Society. 2015;**450**(1077):1407.0123

[87] Goodman J. Are gamma-ray bursts optically thick? The Astrophysical Journal. 1986;**308**:L47

[88] Hascöet R, Daigne F, Mochkovitch R. Prompt thermal emission in gamma-ray bursts. Astronomy and Astrophysics. 2013;**551**:A124. 1302.0235

[89] Thompson C. A Model of Gamma-Ray Bursts. Monthly Notices of the Royal Astronomical Society. 1994;**270**:480

[90] Giannios D, Spruit HC. Spectral and timing properties of a dissipative γ-ray burst photosphere. Astronomy and Astrophysics. 2007;**469**:1. astro-ph/0611385

[91] Rees MJ, Meszaros P. Unsteady outflow models for cosmological gamma-ray bursts. The Astrophysical Journal. 1994;**430**(L93). astro-ph/9404038

[92] Kobayashi S, Piran T, Sari R. Can Internal Shocks Produce the Variability in Gamma-Ray Bursts? The Astrophysical Journal. 1997;**490**(92). astro-ph/9705013

[93] Daigne F, Mochkovitch R. The expected thermal precursors of gamma-ray bursts in the internal shock model. Monthly Notices of the Royal Astronomical Society. 2002;**336**:1271. astro-ph/0207456

[94] Mimica P, Giannios D, Aloy MA. Deceleration of arbitrarily magnetized GRB ejecta: The complete evolution. Astronomy and Astrophysics. 2009;**494**(879):0810.2961

[95] Narayan R, Kumar P, Tchekhovskoy A. Constraints on cold magnetized shocks in gamma-ray bursts. Monthly Notices of the Royal Astronomical Society. 2011;**416**(2193): 1105.0003

[96] Drenkhahn G, Spruit, HC. Efficient acceleration and radiation in Poynting flux powered GRB outflows. Astronomy and Astrophysics. 2002;**391**:1141. astro-ph/0202387

[97] Giannios D. Prompt GRB emission from gradual energy dissipation. Astronomy and Astrophysics. 2008;**480**:305. 0711.2632

[98] McKinney JC, Uzdensky DA. A reconnection switch to trigger gamma-ray burst jet dissipation. Monthly Notices of the Royal Astronomical Society. 2012;**419**(573):1011.1904

[99] Sapountzis K, Vlahakis N. Rarefaction acceleration in magnetized gamma-ray burst jets. Monthly Notices of the Royal Astronomical Society. 2013;**434**(1779):1407.4966

[100] Kagan D, Sironi L, Cerutti B, Giannios D. Relativistic Magnetic Reconnection in Pair Plasmas and Its Astrophysical Applications. Space Science Reviews. 2015;**191**(1-4):545

[101] Abbott, BP et al., Observation of Gravitational Waves from a Binary Black Hole Merger. Physical Review Letters. 2016;**116**(6). 061102, 1602.03837

[102] Spera M, Mapelli M, Bressan A. The mass spectrum of compact remnants from the PARSEC stellar evolution tracks. Monthly Notices of the Royal Astronomical Society. 2015;**451**(4086):1505.05201

[103] Janiuk A, Charzýnski S, Bejger M. Long gamma ray bursts from binary black holes. Astronomy and Astrophysics. 560, A25 (2013), 1310.4869

[104] Connaughton V et al. Fermi GBM Observations of LIGO Gravitational-wave Event GW150914, The Astrophysical Journal. 2016;**826**(L6): 1602.03920

[105] Connaughton V et al. On the Interpretation of the Fermi-GBM Transient Observed in Coincidence with LIGO Gravitational-wave Event GW150914, The Astrophysical Journal. 2018;**853**(L9):1801.02305

[106] Janiuk A, Bejger M, Charzýnski S, Sukova P. On the possible gamma-ray burst-gravitational wave association in GW150914, New A 51, 7 (2017), 1604.07132

[107] Loeb A. Electromagnetic Counterparts to Black Hole Mergers Detected by LIGO. The Astrophysical Journal. 2016;**819**(L21):1602.04735

[108] Perna, R, Lazzati D, Giacomazzo B. Short Gamma-Ray Bursts from the Merger of Two Black Holes. The Astrophysical Journal. 2016;**821**(L18):1602.05140

[109] Woosley SE. The Progenitor of GW150914. The Astrophysical Journal. 2016;**824**(L10): 1603.00511

[110] Zhang B. Mergers of Charged Black Holes: Gravitational-wave Events, Short Gamma-Ray Bursts, and Fast Radio Bursts. The Astrophysical Journal. 2016;**827**(L31):1602.04542

[111] Abbott BP et al. Gravitational Waves and Gamma-Rays from a Binary Neutron Star Merger: GW170817 and GRB 170817A. The Astrophysical Journal. 2017:**848**(L13): 1710.05834

[112] Granot J, Guetta D, Gill R. Lessons from the Short GRB 170817A: The First Gravitational-wave Detection of a Binary Neutron Star Merger. The Astrophysical Journal. 2017;**850** (L24):1710.06407

Section 2

Galactic Cosmic Rays

Cosmic Ray Muons as Penetrating Probes to Explore the World around Us

Paola La Rocca, Domenico Lo Presti and
Francesco Riggi

Additional information is available at the end of the chapter

http://dx.doi.org/10.5772/intechopen.75426

Abstract

Secondary cosmic muons provide a powerful probe to explore various aspects of the world around us. Various physical processes have been employed over the last years for such applications. Muon absorption was used to probe the interior of natural and man-made structures, from the Egypt pyramids to big volcanoes, contributing to interdisciplinary studies. Multiple scattering was employed to reconstruct the location of scattering centres, producing 2D and 3D images of the interior of hidden volumes (muon tomography). Additional possibilities of cosmic muons have been exploited even for the alignment of large civil structures and in the study of their stability. All these applications benefit from the development of advanced detection techniques and improvement in software algorithms. This contribution surveys the state of the art of these applications, with special emphasis on their possibilities and limitations.

Keywords: muon tomography, muon imaging, muon absorption, muon scattering, tracking detectors

1. Introduction

Since the early attempts to use cosmic muons as a probe to explore the inner part of solid structures [1], a variety of developments in muon tomography have been achieved, also exploiting new detection techniques and numerical algorithms for reconstruction and imaging. Correspondingly, the use of muons from the secondary cosmic radiation has found applications in many different fields, and an impressive list of documents, papers, projects related to such applications may be now easily found on the Web. From an historical point

IntechOpen

© 2018 The Author(s). Licensee IntechOpen. This chapter is distributed under the terms of the Creative Commons Attribution License (http://creativecommons.org/licenses/by/3.0), which permits unrestricted use, distribution, and reproduction in any medium, provided the original work is properly cited.

of view, an important application of the muon absorption technique dates back to the work of Alvarez et al. [2], concerning the search for hidden chambers in one of the Egyptian pyramids. Nowadays, the applications of muon tomography to various aspects of everyday life include the study of large structures such as mountains and volcanoes, the inspection of large volumes to search for hidden, high-Z materials, such as for fissile illicit elements in containers, the monitoring of civil structures as large buildings or bridges, the control of nuclear reactors and their waste products, and many others.

It is usual to distinguish, from an experimental point of view, between those applications where the absorption of muons is employed to have information about the amount of material traversed by the particles and other applications where the multiple scattering effect is used instead, especially sensitive to the atomic number of the traversed material. Many examples of the two approaches have been given over the last two decades, and this review, although quoting many of these, is in no way a complete listing of what is available in the literature. Moreover, the field is rapidly expanding, with new detector prototypes being designed and tested, and many additional examples reported. After a brief introduction on the basic properties of the primary and secondary cosmic radiation, especially concerning the aspects which are relevant for muon tomography, a review of the problems and applications making use of the muon absorption technique is given in Section 3. Applications of the muon scattering are described in Section 4. Additional examples of applications of the muon interaction in matter are briefly reported in Section 5, while Section 6 reports a naïve discussion of the possible use of this technique outside our planet. Due to the importance of numerical algorithms for track reconstruction, and image processing, some of the relevant problems in this field are recalled in Section 7. Some concluding remarks are finally discussed in Section 8.

2. Basic properties of the primary and secondary cosmic radiation

Since its very beginning, our Earth is continuously bombarded by energetic particles—cosmic rays—which enter the Earth atmosphere from outer space. Most of them are charged nuclei, with H nuclei (protons) being dominant, and other, heavier nuclei, which reflect, with some difference, the nuclear abundance found in nature. Their energy may vary over many orders of magnitude, from a few hundred MeV to 10^{20}eV, with an energy spectrum roughly described by a power law, $dN/dE = \text{const}\ E^{-\gamma}$, with $\gamma = 2.7$ up to 3×10^{15}eV. At higher energies, up to 10^{19}eV, the spectrum steepens, with γ approximately equal to 3.1 (the so-called knee), flattening again above this energy. While a small fraction of the lowest energy particles come from our Sun, most of the primary cosmic rays originate from within the Milky Way, and the most energetic ones have an extra-galactic origin. Apart from the lowest energy component, which is subjected to space and time variations, due to the Sun and to the interplanetary environment, the majority of cosmic rays exhibit a homogeneous distribution, with very small anisotropies investigated, of the order of 10^{-4} to 10^{-3}.

The existence of the Earth atmosphere has a peculiar effect on the arrival of a primary cosmic ray, since an extensive air shower (EAS) is created following the first interaction of a high energy primary particle with the atmospheric nuclei. This interaction produces a cascade of secondary particles, which may produce in turn additional particles or may decay, constituting a shower with hadronic and electromagnetic components. While a single detector may reveal the passage of individual particles in the shower, the coincidence detection between several particles in the shower allows the identification and reconstruction of the primary particle. This is the way in which extended arrays of detectors are able to measure even the largest energy primary particles. The lateral profile of extensive air showers depends on the initial energy and may reach hundreds of metres or even kilometres.

Apart from neutrinos, which are hardly detected, muons are the most penetrating part of the shower. Relativistic effects increase their lifetime (about 2.2 μs at rest), allowing a large fraction of them to reach the Earth surface. Even though detailed measurements of the energy, angular distributions and charge ratio of cosmic muons at different altitudes and locations on the Earth surface are still pursued, especially for the high energy component, the basic properties of the muon flux are well known and many compilations exist concerning the distributions of these particles [3].

Several parameterizations exist for the angular and energy distributions of cosmic muons at the sea level or moderate altitudes. As a result of the muon absorption in the Earth atmosphere, the dependence on the zenithal angle θ at sea level is often expressed as

$$\frac{dN}{d\Omega} \sim \cos\theta^2 \tag{1}$$

while the momentum distribution of vertical muons roughly follows a power law. A reasonable parametrization of the vertical muon flux as a function of the momentum is given by [4].

$$C\,p^{-[c_0 + c_1 lnp + c_2 (ln\,p)^2 + c_3 (lnp)^3]} \tag{2}$$

where the values of the c_i coefficients are given for selected ranges of the muon momentum. As an example, **Figure 1** shows a plot of the muon momentum distribution extracted from the above formula, for momenta up to about 1 TeV/c.

A semi-empirical parametrization of the muon flux at sea level as a function of both the zenithal angle and muon energy, especially valid for high energy muons (E > 100 GeV/cosθ) is the following:

$$\frac{dN}{dEd\Omega} = \frac{0.14\,E^{-2.7}}{cm^2\,s\,GeV\,sr}\left(\frac{1}{1+\frac{1.1\,E\cos\theta}{115\,GeV}} + \frac{0.054}{1+\frac{1.1\,E\cos\theta}{850\,GeV}}\right) \tag{3}$$

The mean energy of muons arriving at the sea level is ~4 GeV and the mean number of particles traversing a horizontal detector is of the order of 1 per cm^2 per minute. For detailed calculations one has to take into account the variations in these quantities which are due to the altitude and geographical location (especially latitude). On a large time scale, solar effects may also modify the numerical values of the measured flux.

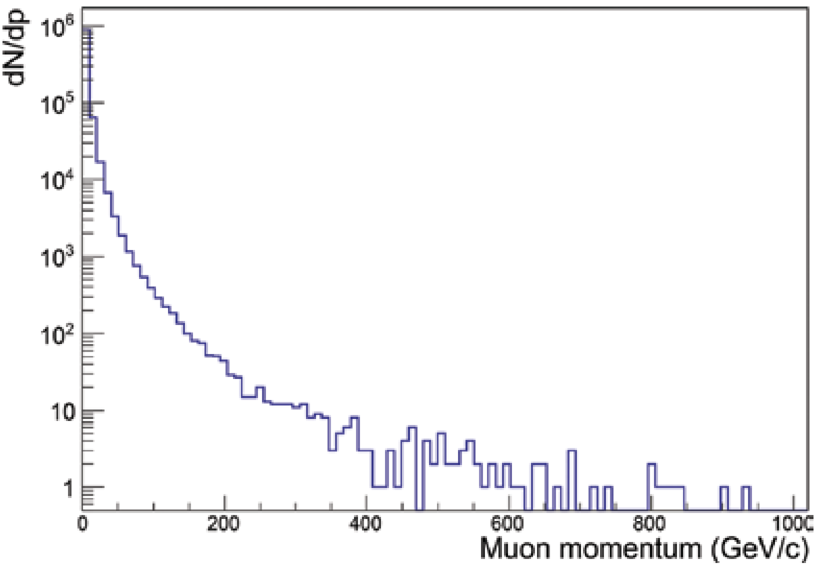

Figure 1. Momentum spectrum of cosmic muons, parametrized by Eq. (2).

3. Applications of the muon absorption technique

The exploration of heavy structures requires penetrating probes, in order to convey information concerning the interior of the structure and its details. For objects having sizes of the order of 1 m or less, X-rays or neutrons may constitute a valid alternative. For instance, typical mass attenuation coefficients of X-rays (30 keV) are of the order of μ/ϱ = 30 cm^2/g for Lead, so that a nonnegligible fraction of X-ray photons may penetrate several cm of Lead. **Figure 2** shows a plot of the mass attenuation coefficient for photons of various energies (from about 0.1 to 10 MeV) in Lead, as derived from the NIST standard data [5].

For larger size objects, the attenuation of such probes would be too high, and more penetrating particles, such as high energy muons, are required to traverse larger thicknesses. The basic properties of muon interaction in matter are known since a long time. However, their potential as a penetrating probe to give information on the interior of large structures is more recent, and only in the last years the literature has seen a large body of applications in this field, also related to the corresponding development of appropriate detectors, electronics, reconstruction and simulation algorithms.

The muon energy loss is usually expressed through its average value

$$-\frac{dE}{dx} = a(E) + b(E)E \tag{4}$$

where $a(E)$ takes into account the energy loss due to ionization, and $b(E)$ the energy loss due to other processes (e^+e^- pair production, Bremmstrahlung and photonuclear processes). The ionization term may be described by the Bethe-Bloch formula as a continuous process. At very high muon energies however, radiative processes become more important than the ionization processes. In case of muons, the value of the critical energy, where the two contributions are comparable, is of the order of several hundred GeV for medium-Z materials like the Iron. Radiative processes then dominate the energy loss of highly energetic cosmic muons, and should be taken into account when considering muons which have to traverse hundred metres solid rock. As an example, **Figure 3** shows the muon energy loss in Lead as a function of the muon energy [6]. The relative contribution of the individual terms due to pair production, Bremmstrahlung and photonuclear processes depends on the muon energy, with the last one being much smaller than the other two for increasing muon energies.

Considering a realistic momentum distribution of muons, GEANT simulations of the interaction of muons with solid rock may be performed. As an example, **Figure 4** shows the fraction of surviving muons after traversing a given thickness of volcano rock, modelled by a realistic chemical composition of the lava from Etna, mainly including SiO_2, Al_2O_3, FeO, MgO, and CaO. As it is seen from **Figure 4**, about 1% of the muon flux is still emerging after traversing 100 m thickness.

Due to the energy loss of muons in a solid material (such as the rock of a mountain), which for a thin layer is proportional to the quantity $\rho\, dx$, where ρ is the density of the material, the fraction of muons which survive after traversing a finite thickness x of material is given, to first order, by the integrated density over the path length L

$$\int_0^L \rho(x)dx \tag{5}$$

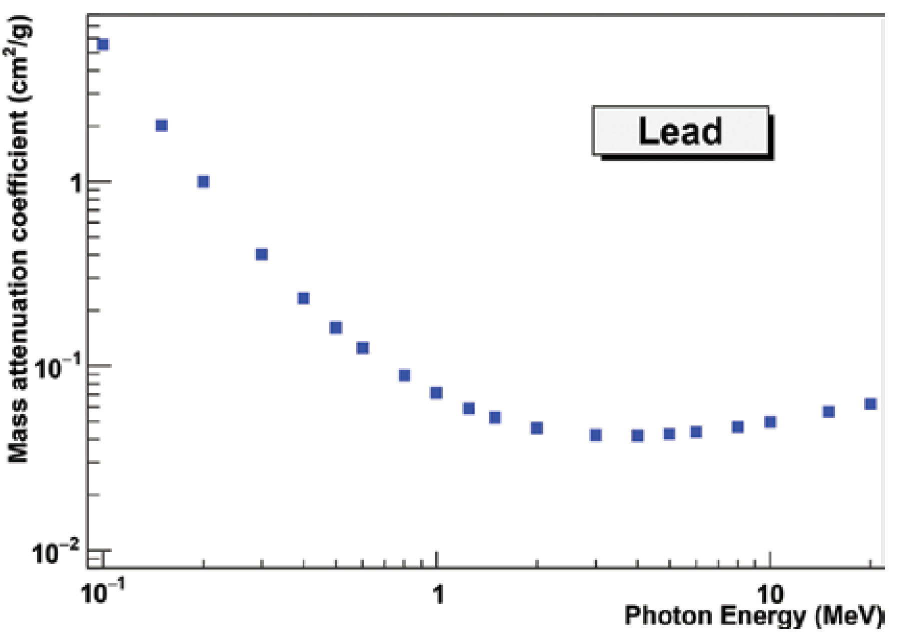

Figure 2. Mass attenuation coefficient of X- or γ-rays of various energies in lead, derived from the NIST standard data [5].

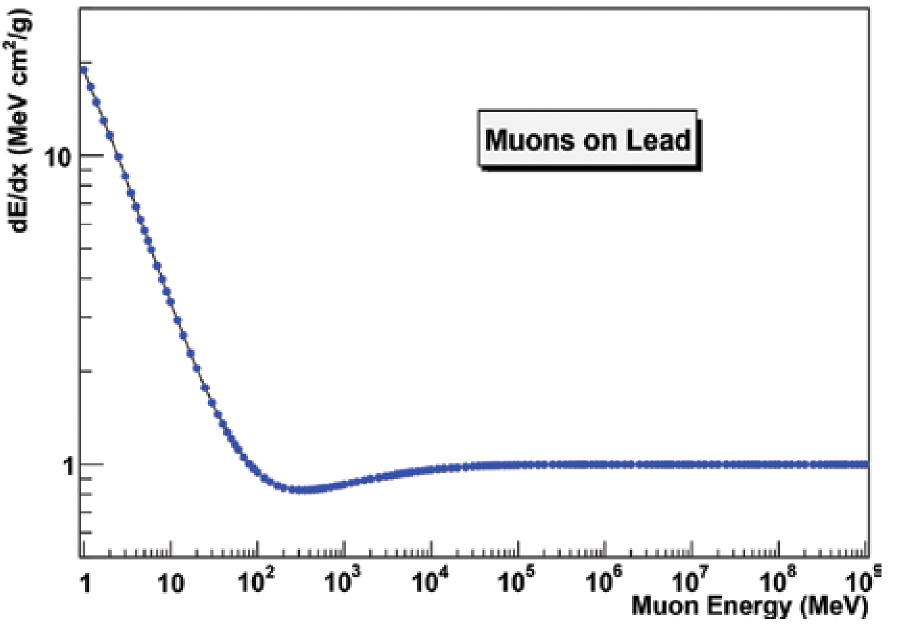

Figure 3. Muon energy loss in lead as a function of the muon energy, as derived from data reported in Ref. [6].

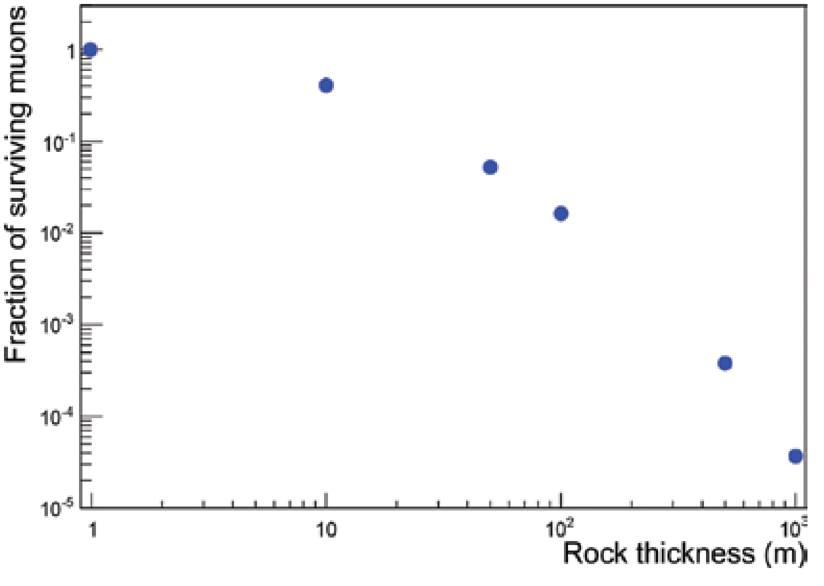

Figure 4. Transmission factor of cosmic muons as a function of the rock thickness traversed, as extracted from GEANT simulations for a realistic lava scenario from Mt. Etna.

Such quantity is sometimes called the opacity. A muon tracking detector, able to measure the number of muons arriving to it from any given direction, provides an experimental measurement of the opacity along different directions. The knowledge of the path length L for any muon direction provides a density map, i.e. a map of the average density along that direction. A density map—once the actual traversed thickness is known and inserted for any specific orientation—may then reveal differences in the density evaluated along different directions. This is the basic principle of the muon absorption tomography. Although the muon absorption tomography may only provide two-dimensional density maps, in principle the combined use of several detectors, pointing to the object from different orientations may produce a 3D map of the object. The construction and use of a set of identical detectors, placed in different locations and working with comparable performance is not a trivial task and the real use of this opportunity is still to be exploited.

A standard setup for muon absorption experiments requires a muon tracking detector (telescope), usually employed in transmission mode (i.e. with the object being located between the open sky and the telescope). The reconstruction of a large number of tracks in the telescope allows for a 2D tomographic map, with a resolution which depends on the telescope tracking performance and on experimental disturbances such as multiple scattering effects in the material surrounding the object to be explored, as well as in the air. Many other aspects of the detector performance, such as its overall detection efficiency, response uniformity, sensitive area, alignment properties, duty cycle, cost and transportability, … influence the real capability of the instrument.

Considering the possibilities offered by muon absorption tomography, several applications have been proposed, with many experimental results obtained so far. Here a brief review of these fields is given.

3.1. Vulcanology

A large interest in absorption muon tomography is related to the possibility of exploring the hidden part of mountains, especially active or potentially active volcanoes, by means of cosmic muons traversing part of their solid structure and being partially absorbed with respect to those coming from the open sky (**Figure 5**). This idea, exploited for the first time by Nagamine et al. in [7] and Tanaka et al. [8], has received an increasing attention in recent years, and a variety of projects, detector prototypes and operational activities have been reported. Important contributions to the field have been given by the Japanese collaboration leaded by H.K.M.Tanaka [8–12], which has employed a muon telescope made by several detection planes with scintillators with PMTs separated by Lead plates, by the Diaphane Collaboration [13–16], which carried out various measurement campaigns in several locations of the world (in France, Italy and Philippines) with scintillator-based muon telescopes, by the TOMUVOL Collaboration [17], employing resistive plate chambers detectors, and by the MU-RAY Project [18, 19], which has employed a muon telescope based on scintillator strips with SiPM photosensors for the exploration of Mt. Vesuvius in Italy.

A recent project has been developed also by our group in Catania, devoted to the study of the top craters of Mt. Etna, the highest active volcano in Europe, with a telescope equipped with three 1 m^2 segmented planes of scintillator strips with multianode PMT readout, already installed since last year close to the top of the mountain. Preliminary tomographic images of such craters have been already obtained by a comparison between the map produced by

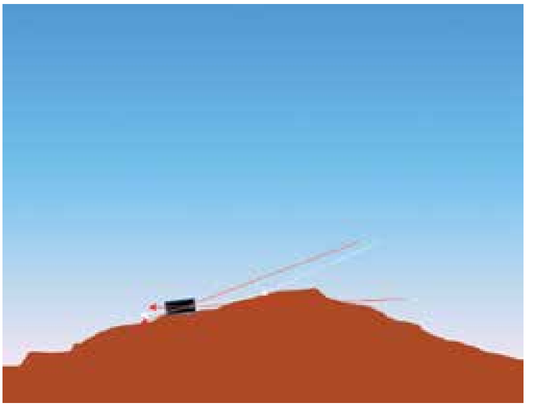

Figure 5. A simple geometrical sketch showing the principle of muon tomography applied to the study of mountain structures. A tracking telescope is placed downstream of the structure being explored, reconstructing muon tracks which ideally have traversed a thickness of solid rock. A comparison with the tracks coming from the open sky or from the backside is used to provide a 2D density map of the structure. A nonnegligible background however may originate from muons which are scattered either from the solid rock or from the air.

muons originating from the front side and the corresponding map produced by the muons coming from the back side.

It must be remembered that other Projects [20, 21] are exploiting the possibility to employ the Cerenkov light produced by the muons in the air after traversing the large thickness of the rock by a Cerenkov detector prototype (ASTRI), originally devised for astrophysical investigation in view of the large Cerenkov Telescope Array (CTA) Project.

The interest in this field is twofold: from one side methods based on muon tomography may complement and sometimes even surpass the potential offered by traditional methods in the understanding the inner part of these structures, revealing empty spaces, or different density profiles inside the mountain. On the other side there is the hope to reach the resolution and capability to monitor in real time the time evolution of the subsurface structures, in order to control potential activities giving rise to explosions and lava eruptions. This last possibility at the moment is still far from being fully reached, while static investigations have offered beautiful pictures of the interior of mountains and volcanoes in several parts of the world.

An important aspect of the technique, which in some cases offers a better figure of merit in comparison to geological and geophysics methods, is the spatial resolution, which can be expressed as

$$\Delta x = L \, \Delta\theta \tag{6}$$

where L is the distance between the detector and the structure being probed, and $\Delta\theta$ is the angular resolution of the tracking device. As an example, for a distance L = 500 m, and an angular resolution of $\Delta\theta$ = 1°, a spatial resolution of the order of 10 m is obtained, which is better than typical values of other geophysical methods.

3.2. Underground measurements

The use of absorption muon tomography is of course not only limited to the study of large mountain structures, but proves much more useful for the investigation of smaller geological locations, underground cavities, caverns, mines and tunnels, due to the reduced thickness to be explored, hence to the large flux being measured. There are several examples of the use of this technique for these applications [21–25]. As a recent example, in one of these investigations [22], carried out to explore underground cavities in the Naples area, a muon detector similar to that employed for volcano muography was employed, with size 1 m x 1 m, and segmented into 32 scintillator strips.

The vertical rock thickness above the detector was in the previous case about 40 m, which did not reduce too much the muon count rate, allowing for a significant result to be obtained in less than one month of data taking. Actually, for many of these applications, the range of rock thickness usually amounts to a few tens metres, which is a value much less than the values of interest for large volcanic structures. The possibility to install the detector in places which are not so prohibitive as for volcanic explorations gives larger opportunities to use this technique, which will likely be employed more and more in the near future to investigate underground environments.

3.3. Archaeology

As recalled at the beginning of this Chapter, one of the first examples of muon absorption tomography is represented by the well-known work by Alvarez and collaborators [2], who employed a muon detector inside an Egyptian pyramid to search for possible hidden chambers. The interest in the study of these very old structures is still very large, and in 2017 a recent study [26] was reported by the ScanPyramid Project, supported by many Institutions, who succeeded to find a very large (~ 30 m) unknown chamber in the Great or Khufu's Pyramid. Such void was first explored by nuclear emulsions and then confirmed by measurements carried out with scintillation hodoscopes and gas detectors; hence, it represents a beautiful example of interrelations between different observation techniques pointing to the same body of evidence. Additional examples of the use of the muon absorption technique for archaeological studies have been reported over the last years [27–29], among which is a study of the cavities in the Teotihuacan Pyramid of the Sun [27].

4. Muon scattering and tomography

The first investigation concerned with the use of the muon scattering process to obtain a radiography of the hidden content in a volume dates back to the work by Borozdin et al. [30], who employed a set of drift chambers (60 × 60 cm) to get radiographic images of tungsten blocks. This technique proved to be very promising for several reasons: it does not introduce any additional radiation, as it is for instance for X-rays; moreover, most of the scattered muons contribute to build the image, contrary to absorption, where a large fraction of muons is absorbed by the material itself. In the scattering mode, the muon tomography technique makes use of this process, which strongly depends on the properties of the material, especially its atomic number Z, thus allowing to discriminate between low- and medium-Z elements with respect to high-Z elements.

The projected scattering angle distribution follows in a first approximation a Gaussian shape, with a width given by:

$$\theta_0 = \frac{13.6MeV}{\beta cp} \cdot Z \cdot \sqrt{\frac{x}{X_0}} \cdot \left[1 + 0.038\, ln\left(\frac{x}{X_0}\right)\right] \tag{7}$$

where p is the muon momentum, β is its speed, X the traversed thickness and X_0 the radiation length of the material, which in turn depends on the properties (Z, A) of the material roughly as

$$X_0 \approx \frac{\frac{716.4\, g}{cm^2}}{\rho} \frac{A}{Z(Z+1)\log\left(\frac{287}{\sqrt{Z}}\right)} \tag{8}$$

4.1. Homeland security

Due to the possibility that illicit fissile elements (Uranium or Plutonium) could be transported inside containers, this technique was suggested as a viable alternative to other traditional methods to inspect and scan a large volume. A muontomograph employing the scattering process basically requires two good muon tracking detectors, one placed above and the other placed below the volume to be inspected. Reconstruction of the muon track above and below the volume allows to evaluate the amount of scattering suffered by the muon, and in the simplest approach (where a single scattering centre is assumed), the so-called POCA (Point of Closest Approach) algorithm determines the 3D coordinates of the scattering centre (**Figure 6**). A sufficiently large number of individual tracks, traversing from any direction of the volume, allow to build 2D and 3D tomographic images. The performance of a muontomograph may be evaluated in terms of its spatial and angular resolution (depending on the tracking detectors), of the overall detection efficiency (which is the result of the detection efficiency of each tracking plane), which in turn determines the required scan time, of the capability to identify high-Z elements and discriminate them with respect to lighter elements, of the sensitivity to false-positive events, which would require an alarm and the opening of the container for a detailed control.

Several applications were oriented to the problem of scanning the content of a cargo container, searching for hidden high-Z materials, which is an important aspect of homeland security. Due to the large amount of containers travelling over the world, which is estimated to be larger than 200 M container/year, controlling the content of any of these volumes is a challenging task. At present, only a small fraction of them are checked, while laws under discussion might require more detailed procedures to be followed over the world. Following this approach, several small-scale prototypes have been built over the last years, employing a variety of detection technologies, from gas chambers to segmented strip scintillators,

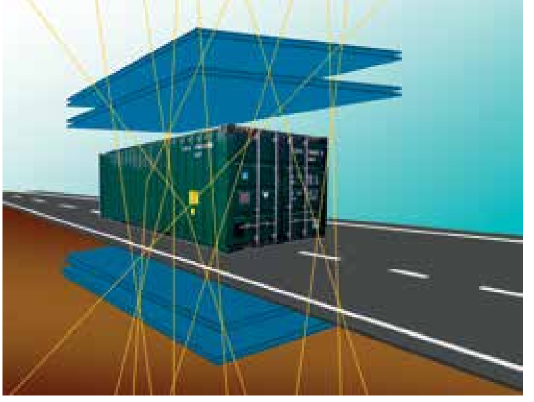

Figure 6. An artist view of the experimental setup being employed for muon tomography applications of cargo containers. Two muon tracking detectors, one placed above and the other placed below the container, are used to reconstruct muon tracks before and after traversing the container content.

Resistive Plate Chambers and GEM. Several contributions in this field have been reported by various groups [31–39], who have designed small scale as well as large and full-size scale detectors for muon tomography.

4.2. Nuclear reactors and waste imaging

For many decades, an impressive amount of used fuel has been produced, and most of this material is stored either in spent fuel pools or in dry storage casks. Such containers are sealed after filling them with the spent fuel, with no possibility to open and visually check their content. Monitoring nuclear waste is then an important aspect of the safety control in nuclear sites. Muon radiography, either in muon absorption or scattering mode, has proven to be a useful tool even for the exploration of nuclear waste storage silos, and many investigations have been already reported in this respect [40–45]. The integrity of nuclear reactors, especially after possible failures, is also a very demanding application for muon tomography [46–48] and following the Fukushima accident, it has been demonstrated that the muon scattering technique may be an answer to the problem of controlling the amount of material inside the reactor core [48].

Also the problem of detecting the presence of orphan sources in metal scraps container has received attention by muon tomography techniques [49, 50], since it is a potential source of large industrial accidents. Blast furnaces have been also explored by cosmic muons [51].

5. Other applications

In principle, dense structures may be explored by muon tomography, either by using the muon absorption or the scattering process, even if they are placed on the Earth surface. As an example, water towers were imaged by muon telescopes [52, 53], calibrating the response of the detector as a function of the water content inside the tower. Post-injection monitoring of CO_2 stored in subsurface locations was investigated by several authors [54–56] by means of muon tomography. Industrial applications have also seen contribution from muon tomography [57, 58]. Finally, another application for the monitoring of civil buildings and structures which employs cosmic muons as a useful probe is the study of the angular distribution of muons detected in coincidence between a tracking detector on the ground and a set of additional detectors mechanically linked to the structure being monitored. Any movement of the structure with respect to the ground will result in a small modification of the distribution of the orientations of cosmic muons detected in coincidence, provided a good reconstruction of tracks and stable working conditions are achieved during long measurements [59, 60].

6. Muon tomography outside the Earth?

Since cosmic rays originate from any direction and permeate all the known Universe, the question whether the same concepts discussed so far apply also to other places outside our terrestrial environment is intriguing. Limiting ourselves to the nearest environment outside the Earth, namely the Solar System, the interaction of the primary cosmics with other planets and celestial bodies produces different results depending on the presence of an atmosphere around the solid structure of the body. For planets or satellites where no atmosphere at all exists, such for instance the Moon, energetic primary particles interact with the surface without producing an extensive air shower. In other situations, where a massive atmosphere exists, much deeper and dense than the Earth atmosphere, as for instance on Venus or Jupiter, air showers may be created but most of the secondary particles are subsequently absorbed by the atmosphere itself, so that only a very small fraction of particles is able to arrive to the surface. Monte Carlo calculations of the interaction of energetic particles with the detailed structure of these bodies should be carried out for any specific situation in order to understand their peculiarities. In case of Mars, where the atmospheric pressure near the surface is only 1/100 with respect to Earth, the development of air showers has been studied in some detail by Tanaka [61], allowing to understand how the proportion between primary protons and secondary pions or muons is very much different than on Earth. In particular, due to the reduced thickness of the Martian atmosphere, the vertical flux of muons is much smaller with respect to the values obtained on the Earth; however, for inclined muons, close to the horizontal, the situation is reversed, and a larger flux of muons would be observed. In any case, contamination from the primary protons is a challenge, and some way to discriminate between the two species should be devised. It is interesting that such concepts have been discussed with relation to realistic Martian exploration missions, trying to understand even the practical aspects and problems which would be required to solve to carry out tomographic measurements on the Red Planet [62, 63].

7. Imaging and simulation methods and algorithms

Muon tomography has offered over the last years also a good environment for the development of mathematical and statistical algorithms, numerical simulation and procedures, to understand and analyze the experimental data being collected, improve the reconstruction and imaging techniques and help to design new apparatus and evaluate their performance.

One of the items that has been long discussed in the muon scattering technique is the reconstruction of the distribution of the scattering centres, leading to a 2D or 3D tomographic image. While the simplest approach employs the POCA method, as discussed in Section 4, better algorithms and methods have been introduced, especially to deal with situations where multiple scattering centres exist. The Maximum Likelihood/Expectation Maximization (EL/EM) iterative method [64] is employed as a valid alternative for processing muon scattering data and reconstruct tomographic images.

Clustering algorithms, which are a set of multivariate data analysis techniques, have been also used to group homogeneous items in a dataset. One of the most known clustering algorithms is the Friends-of-Friends. Applied to muon tomography, clustering analysis helps to detect objects within a spatial domain [65].

Another important aspect of the development of numerical methods in muon tomography is concerned with physics simulations. The importance of numerical simulations in the design of an experimental setup, as well as in the correct interpretation of the effects observed, has been long recognized in nuclear and particle physics and it is nowadays a routine aspect of any quantitative experimental investigation. This is also the case for any tomographic study carried out with cosmic muons. Very frequently, reconstruction and imaging algorithms are tested against simulated data, to compare the merits of different approaches and evaluate their inherent performance. In other cases, only a detailed simulation of the physics processes taking place in the experimental setup and in the surrounding environment may help to understand important aspects of the problem. As an example, the study of the background contribution to the direct flux of muons arriving to the detector through the rock is very important, since in some cases this contribution may be even larger than the direct flux [66], thus leading to an overestimation. In many cases a detailed simulation of the initial energy and angular cosmic particle distributions, coupled to a transport study of these particles along the mountain profile may help to disentangle some of these aspects and provide a quantitative estimate of the role of the background in the corresponding measurements.

8. Conclusions

The list of possible applications provided by this short review is not at all exhaustive, and many other examples of the use of cosmic-ray muons to explore various aspects of our environment are available in the literature [67]. Since the first quantitative investigations at the end of 1990s, in about 20 years, the use of cosmic-ray muons for imaging has grown in interest and this technique is now enough consolidated to be proposed even for commercial use. The variety of possible applications in the field has promoted interdisciplinary studies, with the contribution of experts from different areas, and has already given interesting results in many practical situations. The number of papers, articles, technical reports and conference contributions is more and more large, and specialized conferences and workshop have been organized in the last few years to promote exchange of opinions and results, new collaborations and efforts. Even though many promising results have been reported in various fields of interest, there is still a wide territory where to improve the existing techniques. One important aspect is the detection technology, which has been object of several possible choices, and it is still a point of discussion in terms of the optimization of the performance (especially efficiency and resolution) and cost. Also the existing algorithms and methods may be largely improved to arrive to a better reconstruction and imaging processing of experimental data. The years to come are then a promising period for the development of all such aspects, in view of new applications, only limited by the creativity of interested people, or of large improvements in the existing ones.

Acknowledgements

The authors gratefully acknowledge the fruitful collaboration with many colleagues, students and technicians of the Department of Physics and Astronomy of the University of Catania, of the National Institute for Nuclear Physics (INFN) and National Institute for Astrophysics (INAF), while carrying out various projects concerned with muon tomography.

Author details

Paola La Rocca, Domenico Lo Presti and Francesco Riggi*

*Address all correspondence to: Francesco.Riggi@ct.infn.it

Department of Physics and Astronomy, University of Catania, Catania, Italy

References

[1] George EP. Cosmic rays measure overburden of tunnel. Commonwealth Engineer. 1955:455-457

[2] Alvarez LW et al. Search for hidden chambers in the pyramids. Science. 1970;**167**:832-839. DOI: 10.1126/science.167.3919.832

[3] See e.g. Grieder PKF. Cosmic Rays at Earth. 1st ed. Amsterdam: Elsevier Science; 2001. 1112 p. ISBN: 9780444507105

[4] Bugaev EV et al. Atmospheric muon flux at sea level, underground and underwater. Physical Review D. 1998;**58**:054001. DOI: 10.1103/PhysRevD.58.054001

[5] National Institute of Standards and Technology. https://www.nist.gov/

[6] Data taken from http://pdg.lbl.gov/AtomicNuclearProperties/

[7] Nagamine K et al. Method of probing inner structure of geophysical substance with the horizontal cosmic ray muons and possible application to volcanic eruption prediction. Nuclear Instruments and Methods A. 1995;**356**:585-595. DOI: 1016/0168-9002(94)01169-9

[8] Tanaka HKM et al. Development of the cosmic-ray muon detection system for probing the internal structure of a volcano. Hyperfine Interactions. 2001;**138**:521-526. DOI: 10.1023/A:1020843100008

[9] Tanaka HKM et al. Radiographic visualization of magma dynamics in an erupting volcano. Nature Communications. 2014;**5**:3381. DOI: 10.1038/ncomms4381

[10] Tanaka HKM. Visualization of the internal structure of volcanoes with cosmic-ray muons. Journal of the Physical Society of Japan. 2016;**85**:091016. DOI: 10.7566/JPSJ.85.091016

[11] Tanaka HKM. Instant snapshot of the internal structure of Unzen lava dome, Japan with airborne muography. Scientific Reports. 2016;**6**:39741. DOI: 10.1038/srep39741

[12] Kusagaya T, Tanaka HKM. Muographic imaging with a multi-layered telescope and its application to the study of the subsurface structure of a volcano. Proceedings of the Japan Academy, Series B, Physical and Biological Sciences. 2015;**91**:501-510. DOI: 10.2183/pjab.91.501

[13] Gibert D et al. Muon tomography: Plans for observations in the lesser Antilles. Earth, Planets and Space. 2010;**62**:153-165. DOI: 10.5047/eps.2009.07.003

[14] Lesparre N et al. Geophysical muon imaging: Feasibility and limits. Geophysical Journal International. 2010;**183**:1348-1361. DOI: 10.1111/j.1365-246X.2010.04790.x

[15] Marteau J et al. Muons tomography applied to geosciences and volcanology. Nuclear Instruments and Methods A. 2012;**695**:23. DOI: 10.1016/j.nima.2011.11.061

[16] Carbone D et al. An experiment of muon radiography at Mt Etna (Italy). Geophysical Journal International. 2014;**196**:633-643. DOI: 10.1093/gji/ggt403

[17] Carloganu C. Density imaging of volcanoes with atmospheric Muons using GRPCs. In: Proceedings of Science 055 (POS EPS-HEP2011). 2011

[18] Ambrosi G et al. The MU-RAY project: Volcano radiography with cosmic-ray muons. Nuclear Instruments and Methods A. 2011;**628**:120-123. DOI: 10.1016/j.nima.2010.06.299

[19] Ambrosino F et al. The MU-RAY project: Detector technology and first data from Mt. Vesuvius or silicon detectors. Journal of Instrumentation. 2014;**9**:C02029. DOI: 10.1088/1748-0221/9/02/C02029

[20] Catalano O et al. Volcanoes muon imaging using Cherenkov telescopes. Nuclear Instruments and Methods A. 2016;**807**:5-12. DOI: 10.1016/j.nima.2015.10.065

[21] Del Santo M et al. Looking inside volcanoes with the imaging atmospheric Cherenkov telescopes. Nuclear Instruments and Methods A. 2017;**876**:111-114. DOI: 10.1016/j.nima.2017.02.029

[22] Caffau E et al. Underground cosmic-ray measurement for morphological reconstruction of the GrottaGigante natural cave. Nuclear Instruments and Methods A. 1997;**385**:480-488. DOI: 10.1016/S0168-9002(96)01041-8

[23] Saracino G et al. Imaging of underground cavities with cosmic-ray muons from observations at Mt. Echia (Naples). Nature Scientific Reports. 2017;**7**:1181. DOI: 10.1038/s41598-017-01277-3

[24] Malmqvist L et al. Theoretical studies of *in-situ* rock density determinations using underground cosmic-ray muon intensity measurements with application in mining geophysics. Geophysics. 1979;**44**:1549. DOI: 10.1190/1.1441026

[25] Fujii H et al. Detection of on-surface objects with an underground radiography detector system using cosmic-ray muons. Progress of Theoretical and Experimental Physics. 2017;**5**:053C01. DOI: 10.1093/ptep/ptx061

[26] Barnafoldi GG et al. Portable cosmic muon telescope for environmental applications. Nuclear Instruments and Methods A. 2012;**689**:60-69. DOI: 10.1016/j.nima.2012.06.015

[27] Morishima K et al. Discovery of a big void in Khufu's pyramid by observation of cosmic-ray muons. Nature. 2017;**552**:386-390. DOI: 10.1038/nature24647

[28] Menchaca-Rocha A. Searching for cavities in the Teotihuacan Pyramid of the Sun using cosmic muons experiments and instrumentation. In: Proceedings of the 32nd International Cosmic Ray Conference (ICRC2011); 11-18 August 2011; Beijing, China. 2011;**4**:325-328. DOI: 10.7529/ICRC2011/V04/1117

[29] Gòmez H et al. Studies in muon tomography for archaelogical internal structures scanning. Journal of Physics Conference Series. 2016;**718**:052016. DOI: 10.1088/1742-6596/718/5/052016

[30] Gòmez H et al. Feasibility study of archaeological structures scanning by muon tomography. AIP Conference Proceedings. 2015;**1672**:140004. DOI: 10.1063/1.4928020

[31] Borozdin KN et al. Radiographic imaging with cosmic-ray muons. Nature. 2003;**422**:277. DOI: 10.1038/422277a

[32] Schultz LJ et al. Image reconstruction and material Z discrimination via cosmic ray muon radiography. Nuclear Instruments and Methods A. 2004;**519**:687-694. DOI: 10.1016/j.nima.2003.11.035

[33] Gnanvo K et al. Imaging of high-Z material for nuclear contraband detection with a minimal prototype of a muon tomography station based on GEM detectors. Nuclear Instruments and Methods A. 2011;**652**:16-20. DOI: 10.1016/j.nima.2011.01.163

[34] Baesso P et al. Towards a RPC-based muon tomography system for cargo containers. Journal of Instrumentation. 2014;**9**:C10041. DOI: 10.1088/1748-0221/9/10/C10041

[35] Pesente S et al. First results on material identification and imaging with a large volume muon tomography prototype. Nuclear Instruments and Methods A. 2009;**604**:738-746. DOI: 10.1016/j.nima.2009.03.017

[36] Anghel V et al. A plastic scintillator-based muon tomography system with an integrated muon spectrometer. Nuclear Instruments and Methods A. 2015;**789**:12-23. DOI: 10.1016/j.nima.2015.06.054

[37] Riggi S et al. A large area cosmic ray detector for the inspection of hidden high-Z materials inside containers. Journal of Physics: Conference Series. 2013;**409**:012046. DOI: 10.1088/1742-6596/409/1/012046

[38] Riggi F et al. The Muon portal project: A large-area tracking detector for muon tomography. EPJ Web of Conferences. 2016;**117**:05003. DOI: 10.1051/epjconf/201611705003

[39] Antonuccio V et al. The Muon portal project: Design and construction of a scanning portal based on muon tomography. Nuclear Instruments and Methods A. 2017;**845**:322-325. DOI: 10.1016/j.nima.2016.05.006

[40] Wang X et al. The cosmic ray muon tomography facility based on large scale MRPC detectors. Nuclear Instruments and Methods A. 2015;**784**:390-393. DOI: 10.1016/j.nima.2015.01.024

[41] Clarkson A et al. Characterising encapsulated nuclear waste using cosmic-ray muon tomography. Journal of Instrumentation. 2015;**10**:P03020. DOI: 10.1088/1748-0221/10/03/P03020

[42] Clarkson A et al. The design and performance of a scintillating-fibre tracker for the cosmic-ray Muon tomography of legacy nuclear waste containers. Nuclear Instruments and Methods A. 2014;**745**:138-149. DOI: 10.1016/j.nima.2014.01.062

[43] Poulson D et al. Cosmic ray muon computed tomography of spent nuclear fuel in dry storage casks. Nuclear Instruments and Methods A. 2017;**842**:48-53. DOI: 10.1016/j.nima.2016.10.040

[44] Chatzidakis S et al. Interaction of cosmic ray muons with spent nuclear fuel dry casks and determination of lower detection limit. Nuclear Instruments and Methods A. 2016;**828**:37-45. DOI: 10.1016/j.nima.2016.03.084

[45] Jonkmans G et al. Nuclear waste imaging and spent fuel verification by muon tomography. Annals of Nuclear Energy. 2013;**53**:267-273. DOI: 10.1016/j.anucene.2012.09.011

[46] Ambrosino F et al. Assessing the feasibility of interrogating nuclear waste storage silos using cosmic-ray muons. Journal of Instrumentation. 2015;**10**:T06005. DOI: 10.1088/1748-0221/10/06/T06005

[47] Fujii H et al. Performance of a remotely located muon radiography system to identify the inner structure of a nuclear plant. Progress of Theoretical and Experimental Physics. 2013;**7**:073C01. DOI: 10.1093/ptep/ptt046

[48] Perry J et al. Imaging a nuclear reactor using cosmic ray muons. Journal of Applied Physics. 2013;**113**:184909. DOI: 10.1063/1.4804660

[49] Borozdin K et al. Cosmic ray radiography of the damaged cores of the Fukushima reactors. Physical Review Letters. 2012;**109**:152501. DOI: 10.1103/PhysRevLett.109.152501

[50] Bonomi G et al. Muon tomography as a tool to detect radioactive source shielding in scrap metal containers. International Journal of Modern Physics: Conference Series. 2014;**27**:1460157. DOI: 10.1142/S2010194514601574

[51] Furlan M et al. Application of muon tomography to detect radioactive sources hidden in scrap metal containers. IEEE Transaction on Nuclear Science. 2014;**61**:2204. DOI: 10.1109/ANIMMA.2013.6728043

[52] Nagamine K et al. Probing the inner structure of blast furnaces by cosmic-ray muon radiography. Proceedings of the Japan Academy, Series B. 2005;**81**:257-260. DOI: 10.2183/pjab.81.257

[53] Bouteille S et al. A Micromegas-based telescope for muon tomography: The WatTo experiment. Nuclear Instruments and Methods A. 2016;**834**:223-228. DOI:10.1016/j.nima.2016.08.002

[54] Jourde K et al. Monitoring temporal opacity fluctuations of large structures with muon tomography: A calibration experiment using a water tower tank. Scientific Reports. 2016;**6**:23054. DOI: 10.1038/srep23054

[55] Kudryvtsev A et al. Monitoring subsurface CO_2 injection and security of storage using muon tomography. International Journal of Greenhouse Gas Control. 2012;**11**:21-24. DOI: 10.1016/j.ijggc.2012.07.023

[56] Klinger J et al. Simulation of muon radiography for monitoring CO_2 stored in a geological reservoir. International Journal of Greenhouse Gas Control. 2015;**42**:644

[57] Pal S et al. Muon tomography for carbon storage and monitoring. In: Bhuyan B, editors. XXI DAE-BRNS High Energy Physics Symposium. Springer Proceedings in Physics, Vol. 174; 2016. pp. 479-485. DOI: 10.1007/978-3-319-25619-1_73

[58] Gilboy WB et al. Industrial thickness gauging with cosmic-ray muons. Radiation Physics and Chemistry. 2005;**74**:454-458. DOI: 10.1016/j.radphyschem.2005.08.007

[59] Durham JM et al. Tests of cosmic ray radiography for power industry applications. AIP Advances. 2015;**5**:067111. DOI: 10.1063/1.4922006

[60] Bodini I et al. Cosmic ray detection based measurement systems. Measurement Science and Technology. 2007;**18**:3537. DOI: 10.1088/0957-0233/18/11/038

[61] Donzella A et al. Historical building stability monitoring by means of a cosmic ray tracking system. NuovoCimento C. 2014;**37**:223-232. DOI: 10.1393/ncc/i2014-11806-3

[62] Tanaka H. Monte-Carlo simulations of atmospheric muon production: Implication of the past martian environment. Icarus. 2007;**19**:603-615. DOI: 10.1016/j.icarus.2007.05.014

[63] Kedar S et al. Low cost, low power, passive muon telescope for interrogating martian subsurface. Concepts and Approach for Mars Exploration. 2012;**1679**:4150

[64] Kedar S et al. Muon radiography for exploration of Mars geology. Geoscientific Instrumentation, Methods and Data Systems. 2013;**2**:157-164. DOI: 10.5194/gi-2-157-2013

[65] Schultz LJ et al. Statistical reconstruction for cosmic ray muon tomography. IEEE Transactions on Image Processing. 2007;**16**:1985-1993. DOI: 10.1109/TIP.2007.901239

[66] Bandieramonte M et al. Clustering analysis for muon tomography data elaboration in the muon portal project. Journal of Physics Conference Series. 2015;**608**:012046. DOI: 10.1088/1742-6596/608/1/012046

[67] Nishiyama R et al. Monte Carlo simulation for background study of geophysical inspection with cosmic-ray muons. Geophysical Journal International. 2016;**206**:1039-1050. DOI: 10.1093/gji/ggw191

Galactic Cosmic Rays from 1 MeV to 1 GeV as Measured by Voyager beyond the Heliopause

William R. Webber

Additional information is available at the end of the chapter

http://dx.doi.org/10.5772/intechopen.75877

Abstract

Voyager 1 has now been beyond the heliopause for over 5 years since its seminal crossing of this boundary in August of 2012. During its epic 40 year journey of ~122 AU out to this boundary and beyond this spacecraft has passed through several regions of the heliosphere including the heliosheath of extent ~30 AU just inside the heliopause (HP), where extremely large and variable intensities of protons, helium and oxygen nuclei as well as electrons between 1 and 100 MeV were observed. Then, suddenly these particles completely vanished and new and completely different spectra of particles between 1 MeV up to ~1 GeV and beyond, instantly recognizable as those for galactic cosmic rays were observed. These spectra and intensities at all energies have remained constant to within ±1% for 5 years corresponding to 20 AU beyond the HP.

Keywords: cosmic rays, dark matter, heliosphere, acceleration

1. Introduction

Voyager 1 has now been beyond the heliopause for over 5 years since its seminal crossing of this boundary in August of 2012. During its epic 40 year journey of ~122 AU out to this boundary and beyond this spacecraft has passed through several regions of the heliosphere including the heliosheath of extent ~30 AU just inside the heliopause (HP) where extremely large and variable intensities of protons, helium and oxygen nuclei as well as electrons between 1 and 100 MeV were observed. See earlier article in Astrophysics [1] showing and discussing these intensity time profiles.

IntechOpen

© 2018 The Author(s). Licensee IntechOpen. This chapter is distributed under the terms of the Creative Commons Attribution License (http://creativecommons.org/licenses/by/3.0), which permits unrestricted use, distribution, and reproduction in any medium, provided the original work is properly cited.

Then, suddenly these particles completely vanished and new and completely different spectra of particles between 1 MeV up to ~1 GeV, instantly recognizable as those for galactic cosmic rays, were observed. These LIS intensities at all energies have remained constant to within ±1% for 5 years corresponding to 20 AU beyond the HP. These low energy galactic spectra and their relation to higher energy measurements such as those made by AMS-2 will be discussed in this paper in terms of the acceleration, source distribution and propagation of cosmic rays in the galaxy.

We begin in this paper by discussing the radial intensity profiles outward from the Earth through the heliosphere and beyond into interstellar space. We will compare these intensity profiles for electrons and protons, from the lowest energies, ~1 MeV, to the higher energies of a few hundred MeV which are normally considered as cosmic rays. The profiles provide a graphic view of the scale of the various regions of the heliosphere and the entrance into the uncharted regions of interstellar space and the realm of galactic cosmic rays.

We will then discuss the spectra of galactic cosmic ray electrons, protons, helium and heavier nuclei that are measured for the 1st time by Voyager. Every step in this process provides a new insight into the features of these galactic cosmic rays that could never be studied previously because of our location within the heliosphere.

2. The radial intensity vs. time profiles

Figure 1 shows radial intensity profiles for the two lowest energy electron channels, the HET A1-A2 stop channel at ~0.7 ± 0.3 MeV and the HET B1-B2-C4 stop channel with a peak response

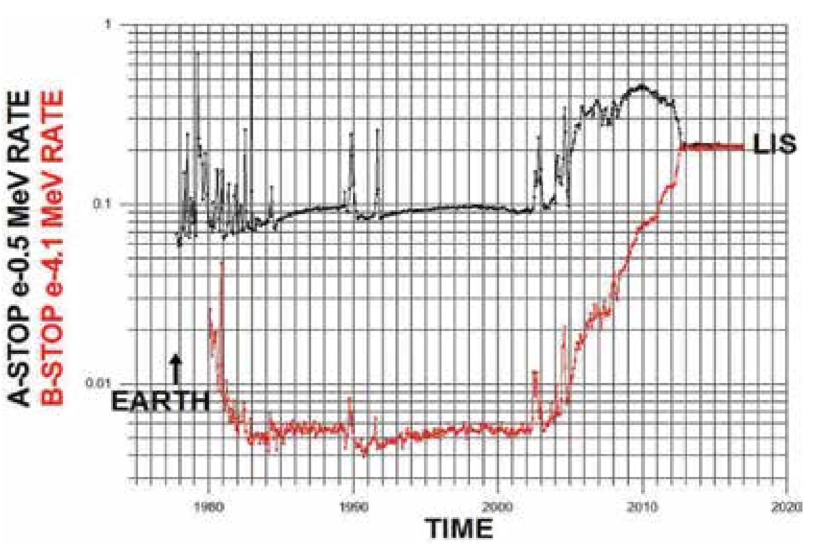

Figure 1. Time history of 26 day average intensities of A-stop 0.7 MeV (in black) and 4 MeV B stop electrons (in red) from launch at earth 1977 to the end of data in 2017, at ~140 AU. These rates provide radial and temporal intensity profiles. The B-stop rate is normalized to A-stop rate of 0.21 c· s^{-1} in LIS using the factor 0.75.

between 3.0 and 4.0 MeV, from the time of launch (1977) to the present time (2018). These energy responses are determined by extensive GEANT-4 calculations. These telescopes are described in [2, 3]. The two intensities are normalized to those observed in local interstellar space (LIS).

One can define from **Figure 1** four temporal or spatial regions that apply to all the components and energies discussed here. The 1st region is from launch in 1977 to 1983.0 when V1 was at about 20 AU and also near its maximum latitude of +30°. This region (nearest the Sun) is punctuated by many abrupt increases related to interplanetary propagating electron events of energy <1 MeV of solar origin. These are closely coordinated with observations inside the Earth's orbit from HELIOS during the 1977–1978 time period. The individual events are separated temporally at Voyager and HELIOS. Also included is the Jupiter encounter occurring at ~1979.2.

The second region (time period) is from 1983.0 to 2005.0 at which time V1 crossed the HTS and entered the heliosheath at ~95.0 AU and at +30°. The effects of the solar 11 year modulation cycle are rather weakly seen in this region. These variations are similar temporally to what was observed for higher energy protons [4] and shown later in **Figure 3**. Two massive solar induced interplanetary electron events are seen in the A stop rate in 1989 and 1991 when V1 was at between 40 and 50 AU. These events are related to large shocks moving outward in the heliosphere with speeds close to 1000 km/s.

During the time V1 is in the heliosheath region from 2005.0 to 2012.65 between 95 and 121.7 AU (Region 3) there is a factor of 3–4 increase in the sub-MeV electron intensities which, during most of this time period, have even higher intensities than those observed beyond the HP, in the local interstellar medium. These are electrons accelerated in the heliosheath. Meanwhile the intensity of the 4 MeV electrons increases in the heliosheath from the HTS crossing to the HP by a factor ~30. This is believed to be a result of modulation effects in the heliosheath which reduce the LIS intensity of these higher energy electrons.

Beyond the heliopause (HP) in LIS the electron intensities have remained constant to within ±1% at both energies for 5 years (~18 AU of outward travel for V1). Notice that the intensities of these electrons in LIS are higher than those at the Earth by a factor ~4 at 0.7 MeV and by a factor ~20 at 4 MeV. These differences are due in part to solar modulation effects and in part to the local acceleration of 0.7 MeV electrons.

In **Figure 2** we show the 1.8–2.6 MeV proton intensity, again normalized to the LIS value that is measured for 0.7 MeV electrons. This is the lowest energy part of the interstellar proton spectrum that can be measured on Voyager in a 2-D, dE/dx, telescope mode. It represents a limit to the characteristics of the lower energy proton propagation in the galaxy from the nearest sources in the galaxy since it corresponds to only ~35μ of equivalent Si traversed during the galactic propagation.

In region 1, between launch and 1983 and inside ~20 AU, the Earth and the inner heliosphere are bathed in an almost continuous flux of 2 MeV protons which exceeds the possible background galactic cosmic rays at this energy and location by a factor ~1000 and is comparable to the intensities observed further out in the heliosheath. This continuously high intensity results from the 1.8 to 2.6 MeV protons from many individual solar events, with the intensities piling up due to the large longitudinal diffusion.

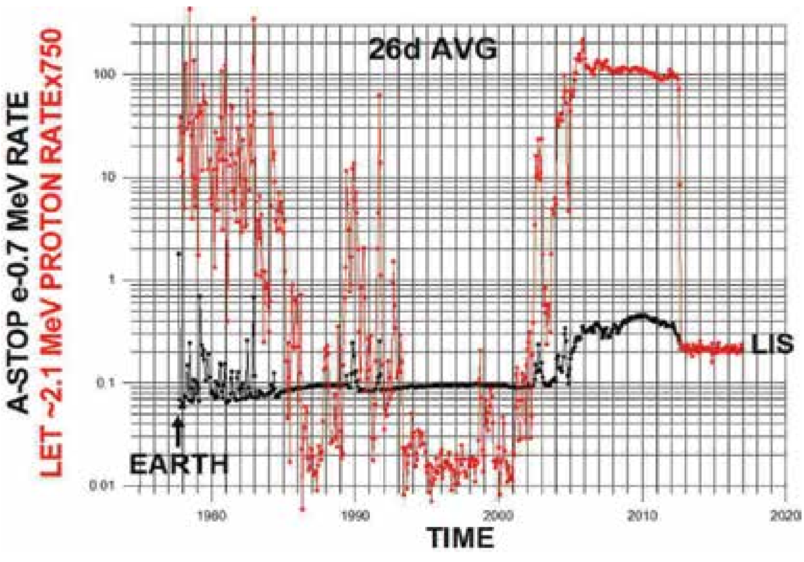

Figure 2. Same as **Figure 1**. The L1-L2 stop 1.8–2.6 MeV proton rate (in red) is normalized to the A-stop 0.7 MeV LIS electron rate using the factor ×750.

In region 2, between ~20 AU and the HTS at 95 AU, these 2 MeV proton intensities reach a level which is less than that in LIS. This corresponds to a solar activity minimum and also to solar modulation minimum. This intensity, which is up to a factor ~12 times less than the LIS intensity, could be a representation of the level of solar modulation of these particles at this low energy of ~2 MeV.

In region 3, the intensity of these low energy protons increases by a factor 1000 beyond the HTS. It remains at this high level for a distance ~30 AU as a result of heliosheath accelerated protons. Then suddenly the intensity decreases by a factor ~500 corresponding to a distance of ~0.1 AU near the HP. This intensity change over such a small radial interval requires a remarkably effective particle barrier at the HP.

In region 4, beyond the HP, the proton intensity represents the low energy tail of the galactic proton spectrum with an intensity ~0.5 of that at the intensity peak of the differential spectrum which occurs at ~30 MeV.

In **Figure 3** we show the higher energy proton (250 MeV) intensity time profile from the solar modulation study in [4]. This proton intensity is also normalized to the 0.7 MeV A1-A2 stop LIS electron intensity beyond the HP. The solar modulation effects are seen in region 1 inside 20 AU where the Voyager observations for 250 MeV protons blend in well with spacecraft observations of this modulation near the Earth and also neutron monitor observations [5–7] at the same time. The intensity at the Earth at this energy is a factor ~8 below the LIS values.

In region 2, between about 20 and 95 AU, solar 11 year modulation effects are observed at 250 MeV which are in synch in both time and magnitude with those observed at the Earth, but with a time delay corresponding to outward moving structural features with a speed ~600 km·s^{-1}.

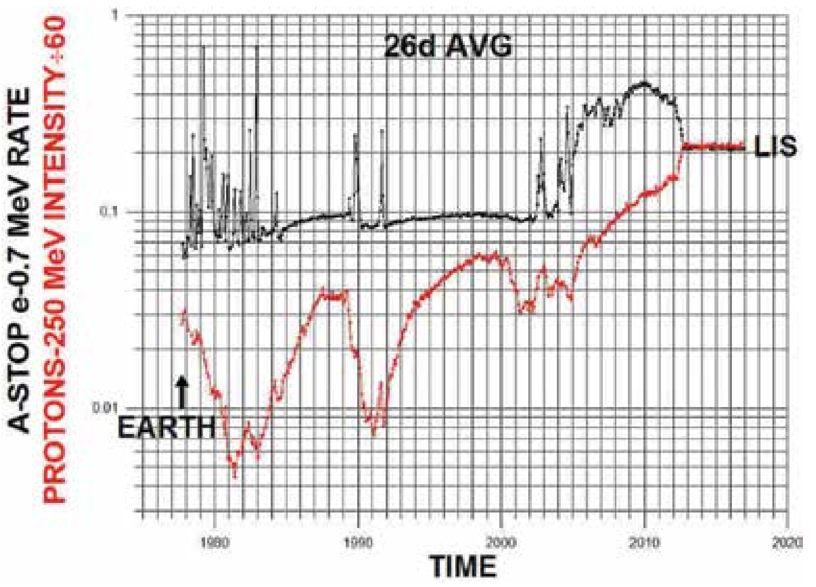

Figure 3. Same as **Figure 1**. The 250 MeV proton intensity in p/m^2·sr·s·MeV (in red) is normalized to A-stop 0.7 MeV LIS electron rate using the factor ÷60.

Moving outward into region 3, we find that the intensity of these 250 MeV protons increases by a factor ~4 in the heliosheath. The large modulation beyond the HTS at this higher energy was previously unrecognized and amounts to ~1/3 of the total solar modulation of these particles in the heliosphere.

This solar modulation of these higher energy protons can be well described with a single modulation parameter ϕ corresponding to an energy loss resulting from a potential difference, ϕ in MV, between the observation point and the LIS spectrum [8]. This simple description arises from the fact that the overall spherically symmetric solar modulation in the heliosphere appears to follow the description provided by Louville's Theorem relating to the constancy for the particle density and momentum in phase space. Of course there are deviations from this simple picture due to structural features in the heliosphere such as the heliospheric current sheet, and also for the solar polarity changes which induce a 22 year cycle in the solar modulation process, but these other processes do not appear to dominate at these energies and above, where, in fact, the same value of ϕ derived from these protons also gives a good description of the historical neutron monitor observations of cosmic ray modulation effects at the Earth that have been carried out over the last 70 years.

Here we summarize the most general features of all of the radial intensity profiles. The most prominent feature is the sharpness and effectiveness of the heliospheric boundary, the heliopause. For low energy protons the reduction of intensity is a factor ~500, taking place in only 1–26 day interval corresponding to less than 0.1 AU in distance.

The effects of this boundary on electrons are even more astounding. A radial intensity gradient ~130%/AU just inside the HP for 4 MeV electrons changes to a 0.1%/AU radial gradient in the LIM in just 1–26 day interval of ~0.1 AU in radius. Essentially whatever intensities exist in the heliosphere apparently stay in the heliosphere as a result of an almost impenetrable heliopause at these lower energies. As far as energetic particles go, the interstellar medium at this location has little recognition of the nearby heliosphere.

Other features of the heliosphere newly recognized from this study include: (1) The heliosheath is a very interesting and important region both in terms of accelerating protons and also (more weakly) electrons as well as for large solar modulation effects. The solar modulation effects on the intensity in this region range from a factor ~4 for ~1 GV protons to a factor ~100 for 15 MV electrons and then decrease to a factor ~30 for 4 MV electrons and much less for 1 MeV electrons which appear to be mostly locally produced.

The massive acceleration of nuclei, e.g., protons and He and O nuclei in the heliosheath, extending down to ~1 MeV and up to ~100 MeV/nuc, which was previously known and believed to be fueled by high ionization potential IS ions, is joined by the newly found acceleration of sub-MeV electrons.

The 11 year and longer solar activity cycles studied now for over 70 years using neutron monitors, balloon and spacecraft borne instruments at higher energies, and so important for geophysical studies [9], are still significant beyond the HTS. Even for protons at 250 MeV the intensity increase in the heliosheath region is a factor ~4; for electrons, this increase due to solar modulation reaches a maximum of a factor ~100 at ~15 MeV. These effects were previously unrecognized.

And finally the new observations reported here have also extended the V1 measurements of the local interstellar electron spectrum by a factor ~10 lower in energy (e.g., down to 0.5 MeV) as compared with even the initial Voyager measurements of [2] beyond the HP. For protons the minimum energy measured is now ~1.8 MeV, a factor ~2 times lower than the initial measurement for these particles. The intensities obtained at these lowest energies appear to be consistent with a smooth extension of those measured at higher energies as would be expected from propagation calculations. The range of the lowest energy electrons and protons is only ~50 μ of Si. This places severe constraints on the distribution of nearby sources of these particles but illustrates that, even at these lower energies, the spectra are still a compendium of many sources with an individuality obscured by diffusion in the galactic magnetic fields.

3. The galactic electron spectrum

Voyager has now measured the true LIS electron spectrum from ~1 to 60 MeV. When compared with simultaneous measurements of electrons by the PAMELA spacecraft near the Earth they indicate a solar modulation factor ~500 between the LIS spectrum and that measured at the Earth between about 10–100 MeV (**Figure 4**). At higher energies this modulation decreases. It is believed to be only a factor ~3–4 at 1 GeV, decreasing to perhaps 20% at 10–20 GeV where high precision electron measurements are available from both PAMELA and AMS-2 [10, 11].

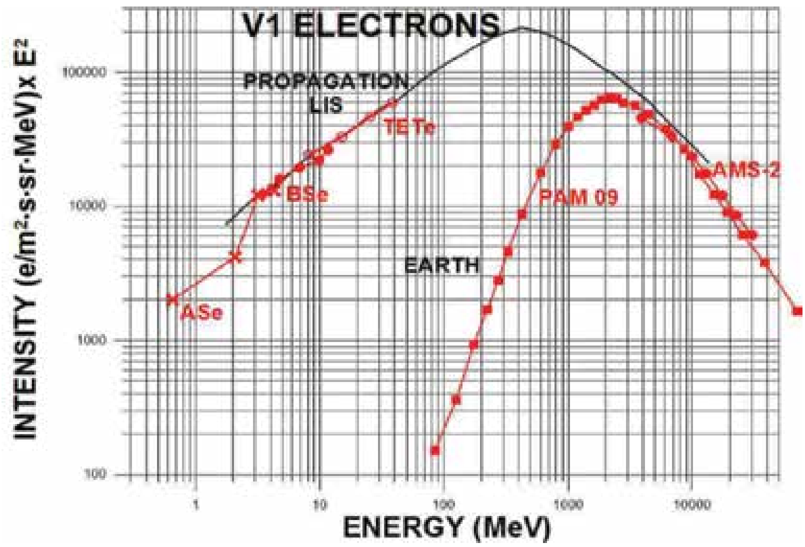

Figure 4. The electron spectrum measured at Voyager using the TET, B stop and A stop telescopes and the measurements of PAMELA and AMS-2 at higher energies. The figure is in a x E^2 format. Note the severe solar modulation of electrons which amounts to a factor ~500 below 100 MeV and is still ~20% between10–20 GeV/nuc. Also note the V1 spectrum which is ~$E^{-1.3}$ between about 1–60 MeV. The black curve shows a Monte Carlo calculation with an electron source spectrum ~$E^{-2.25}$ and a path length ~20.6 β $P^{-0.45}$ above 0.562 GV and with a diffusion coefficient ~$P^{-1.0}$ below 0.562 GV.

Figure 4 shows the electron spectrum measured at Voyager and also in the higher energies where solar modulation effects are small. The plot is a x E^2 presentation which shows both low and high energy differences. There is a large gap in the intermediate energy range for LIS electrons from ~100 MeV to several GeV. At energies above a few GeV the electron spectrum measured by PAMELA and AMS-2 steepens rapidly. Part of this increase in spectral index is due to synchrotron and inverse Compton energy loss which are ~E^2. This high energy region is shown in **Figure 5** in a x E^3 format. The AMS-2 data on electrons [11] is shown along with Monte Carlo propagation calculations of the electron spectrum using various source spectral indices [12, 13].

We have shown from these calculations that, in order to fit both low energy and high energy data, the source spectral exponent for electrons changes from being ~$P^{-2.24}$ below about 8 GV to one ~$P^{-2.4}$ at higher energies extending up to ~1 TV [12, 13].

At ~400 MeV, which is ~1.0 GV for protons there are corresponding measurements of the proton and electron intensities at the Earth by PAMELA and also at Voyager. The ratio of Voyager to PAMELA proton intensities at the two locations is ~4.0 which is caused by the amount of solar modulation between the LIS and the Earth at 1 GV. The electron intensity is also measured at this time by PAMELA and at 1 GV it is 2.5×10^{-2} × the proton intensity. We believe from solar modulation theory [8] that at 1 GV the total modulation of electrons and protons should be nearly the same. So the LIS electron intensity at 1 GV could be estimated from this approach to be 1.4–1.6 × 10^{-1}e/m^2·s·sr/MeV. This intensity is very close to the value

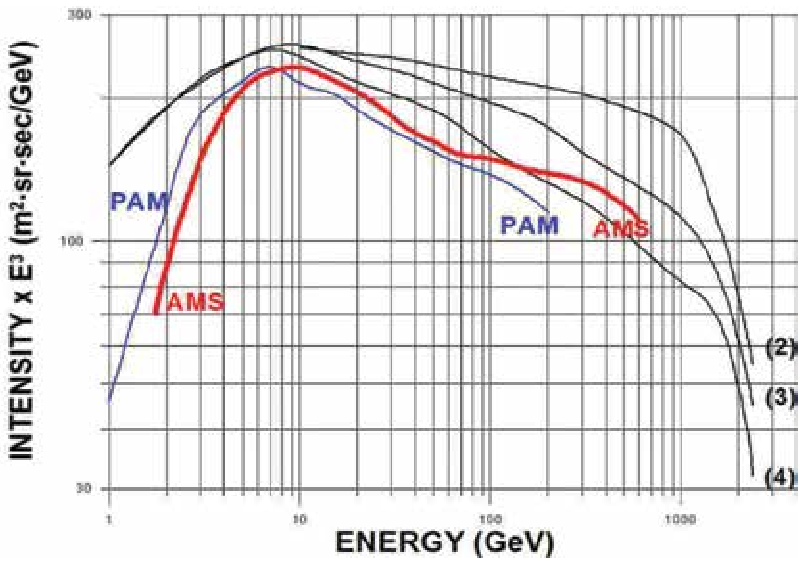

Figure 5. The electron spectrum above 1 GeV measured by AMS-2 [11] and PAMELA [10]. The black solid curves are for (1) a source electron spectrum ~$E^{-2.25}$ at all energies and (2, 3 and 4) for electron source spectra ~$E^{-2.25}$ below ~6 GeV and $P^{-2.30}$, $P^{-2.35}$ and $P^{2.40}$ respectively above 6 GeV.

at 1 GV obtained in the Monte Carlo diffusion propagation models that fit the LIS at the low Voyager energies and the high energies measured by PAMELA or AMS-2 [12, 13].

In **Figure 6** we show the e/H (E) interstellar ratios of intensities measured at both Voyager and at AMS-2 from a few MeV to 1 TeV. These ratios, in intensity/MeV, range from ~10^2 at 2 MeV to ~3×10^{-3} at 1 TeV, a difference of 3×10^5 and include the ratio between electron and proton intensities of 3.0×10^{-2} at 1 GV estimated above. This difference in low energy and high energy e/H (E) ratios is mainly caused by propagation effects.

At lower rigidities this source ratio as a function of energy increases for a number of reasons. First of all there is the conversion between a differential energy and rigidity which depends on the different β of the particles. Then there is the dependence of the diffusion coefficient on $P^{-1.0}$ below 0.5 GV which affects only the electrons and decreases the $P^{-2.25}$ source index to ~$P^{-1.3}$. And also there is the energy loss by ionization which eventually reduces the source spectral index for protons from a negative one to a positive value. At the higher energies the synchrotron and inverse Compton losses increase the source spectral index of electrons by almost 1.0 power thus reducing the e/H ratio.

Recall that we have assumed for electrons, that to fit the data at both low and high energies up to 1 TeV, source spectra of the form dj/dE ~$P^{-2.24}$, below ~6–8 GV are needed with the exponent becoming ~2.40 at high rigidities [12, 13]. Very similar rigidity spectra with almost the same exponents and a break at ~6–8 GeV are required to simultaneously fit the Voyager low energy proton data and the high energy AMS-2 proton data, again from ~2 MeV to 1 TeV [15] (see following sections).

So in view of the above similarity of rigidity spectra for electrons and protons, the e/H ratio itself as a function of rigidity should be almost constant. This almost constant value of the e/H ratio occurs between 0.5 and 1.0 GV where loss processes for electrons and protons in the galaxy are about equal. This value of the ratio is about 3–10 × 10^{-2} as shown in **Figure 6**.

This source ratio of e/H for galactic cosmic rays as a function of rigidity which has previously been hidden from measurements at the Earth and is related to the acceleration of the galactic cosmic rays, now provides a crucial measurement along with the possible spectral break at ~8 GV. If there are no other selection effects, this ratio could indicate the degree of ionization in the acceleration region.

And last but certainly not least, still regarding electrons, we should point out that the electron spectrum ~$E^{-1.3}$ at low energies, just about 1.0 power less than the assumed source spectrum with exponent = −2.25, may have profound significance. Unless the source spectrum has a 2nd break at ~0.3 GV, which seems unlikely, this flattening of the spectrum is caused by a break in the diffusion coefficient which becomes ~$P^{-1.0}$ below ~0.5 GV. This break has been predicted [14]. As a result the diffusion coefficient becomes large and these lower energy electrons rapidly flow out of the extended disk of the galaxy [12, 13]. This fraction that escape the disk, calculated in a Monte Carlo diffusion model, becomes ~90% below ~100 MeV and is shown as a function of energy in **Figure 7** of [12]. These electrons, with a spectrum ~E^{-2} above ~1 MeV, flow outward through the halo and into the local intergalactic medium at essentially the speed of light. They populate the region with a negative charge. Because of their relatively low energy they are undetectable by radio emissions and could be considered a form of non-baryonic dark matter and energy. Perhaps more sobering is the thought that this process of charge

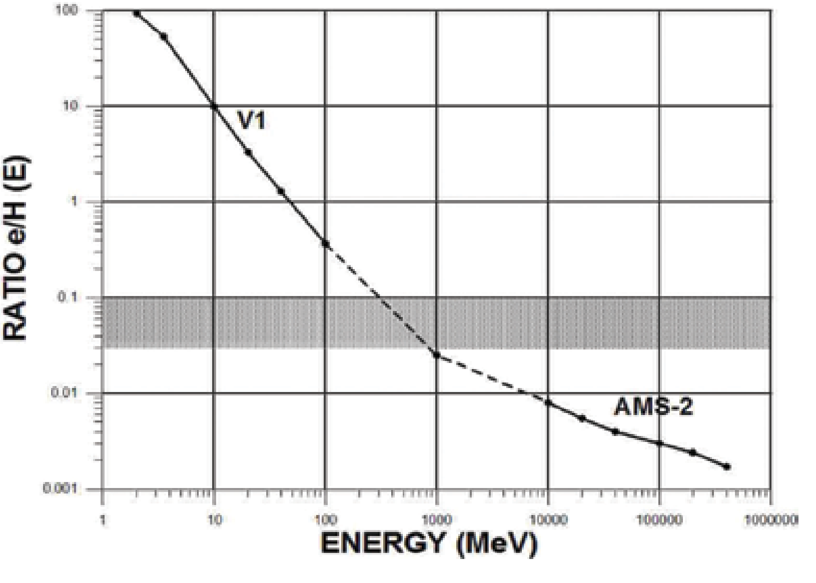

Figure 6. Ratios of intensity of electrons to protons as a function of energy, e/H (E), measured by voyager and AMS-2 [10, 15] from 2 MeV to ~1 TeV. The estimated LIS value of the ratio at ~1 GeV as described below in the text is also shown.

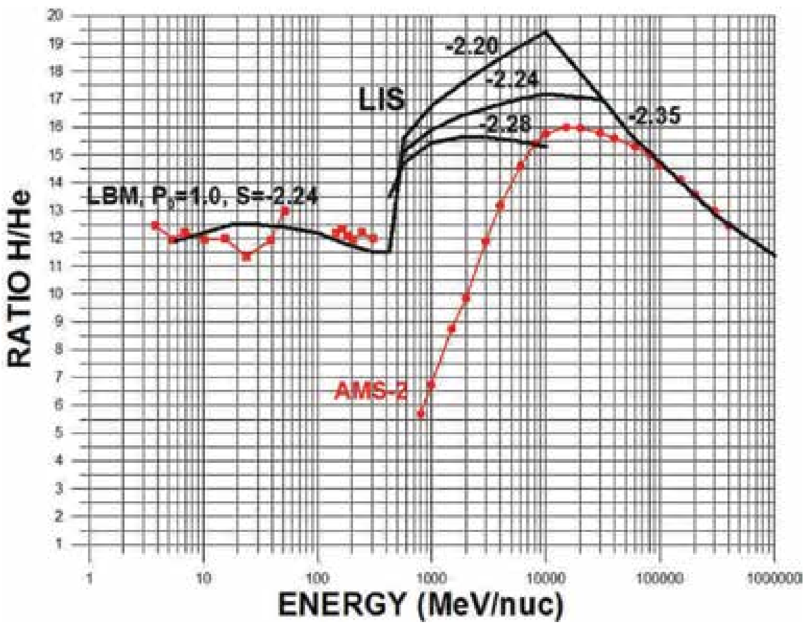

Figure 7. Ratios of hydrogen to helium nuclei intensities as a function of E/nuc as measured by Voyager between 10 and 350 MeV/nuc and by AMS2 [10, 15] above 1 GeV/nuc.

separation of leptons and protons could be going on throughout cosmic time, even stronger at earlier times, and as a result influence our interpretation of the expansion of the Universe.

4. The galactic hydrogen, helium and heavier nuclei spectra

As is the case for electrons, the interpretation of the Voyager measured LIS intensities of hydrogen, helium and heavier nuclei at low energies, and with no solar modulation, may be compared with the higher energy measurements from PAMELA or AMS-2 where the modulation becomes small. This provides a fulcrum of ~10^5 in energy to examine the spectra of the various nuclei. This is best done by examining the intensity ratios such as H/He, He/C, etc., along with the intensities themselves. Most of the measurements are in E/nuc, whereas the source spectra appear to be rigidity spectra so there is always a factor of at least β in converting from one representation to the other.

We begin this section by examining the spectra of H and He nuclei. **Figure 7** shows the ratio of intensities of H and He nuclei measured at Voyager at energies less than a few hundred MeV/nuc [3] and those at AMS-2 [15, 16] at energies from ~1 GeV/nuc up to 1 TeV/nuc. The Voyager measurements are consistent with a constant ratio ~12.5, for H/He from ~10 MeV/nuc to ~350 MeV/nuc. This might suggest very similar H and He spectra in this energy range. The AMS-2 measurements obtain an E/nuc ratio ~16 at ~10 GeV/nuc, decreasing at both high and low energies. The decrease in this ratio at high energies where solar modulation effects are small, indicates different spectra for H and He nuclei, with a spectral index difference of between −0.10 and − 0.12 for either E/nuc or P spectra since at these high energies $\beta \rightarrow 1.0$. At lower energies the AMS-2 H/He (E) ratio decreases and reaches a value ~8 at 1 GeV/nuc. This is due to solar modulation effects. So the main goal of this study is to match the nearly constant LIS H/He (E) ratio of 12.5 measured by Voyager below ~300 MeV/nuc to the ratio of 16 measured at ~10–20 GeV/nuc by AMS-2.

These differences in ratios per E/nuc between a few hundred MeV/nuc and a few GeV/nuc immediately suggest a β dependence is involved and therefore when comparing ratios, source spectra as a function of rigidity is the appropriate parameter. We have found this to be the case in most comparisons of spectra of nuclei, particularly with different A/Z. So we now consider how the differences described above could be understood more simply in terms of source rigidity spectra. We assume that the source spectra of H and He nuclei are the same at rigidities below ~10 GV and can be represented by the formula.

$$dj/dP \sim P^{-S} \tag{1}$$

where we let S vary from −2.20 to −2.28 noting that we have already found that lower rigidity electrons are well described with a spectral index ~ − 2.25 below ~10 GV.

The three solid black curves on **Figure 7** show the calculated H/He ratios after propagation in a LBM using source rigidity spectra for protons with S = −2.20, 2.24 and 2.28 all normalized to the Voyager measured value of 12.5 at 100 MeV/nuc. For the calculated curves above ~10 GV, we use a normalization to the AMS-2 measured ratios and with a source spectra index = −2.36 for

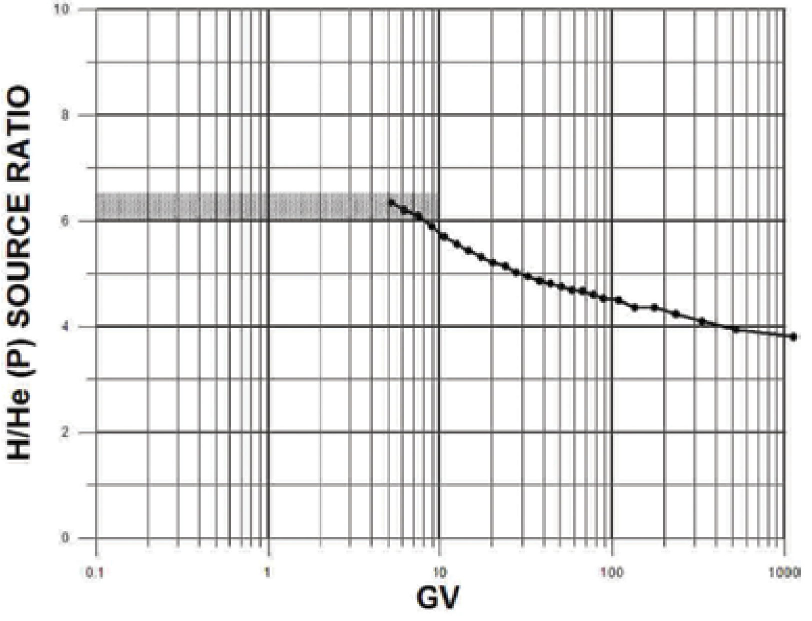

Figure 8. The LIS H/He (P) ratio as a function of rigidity. The data above ~8 GV where the solar modulation of this ratio is small is from AMS-2 [16].

protons, keeping the source spectral index at −2.24 for He nuclei. When a solar modulation of 10–20% in the H/He ratio at about 10 GV is included, a spectral index of −2.24 for both H and He nuclei gives the best fit at low energies along with that for a proton index of −2.36 at high energies and with a spectral break between 6 and 12 GV for protons.

The resulting H/He source ratio as a function of rigidity is very interesting. For this ratio we use the directly measured AMS-2 H/He (P) ratio above ~8 GV [16] as is shown in **Figure 8**. This ratio is ~3.5 at the highest rigidities increasing to ~6.0 at 8 GV. At lower rigidities the source ratio must become a constant because both H and He nuclei have identical rigidity spectra. This constant value depends on the exact details of the break, but we estimate the constant ratio of intensities at low rigidities to be between 6.0 and 6.5.

This ratio has important implications for the relative H and He abundances in the region where the main cosmic ray acceleration occurs. In terms of nucleons the ratio of 6.5 gives 63% protons and 37% Helium nucleons. The cosmological value in the case of big bang nucleosynthesis is usually taken to be ~76% protons and 24% Helium nucleons. Certainly interesting.

We now turn our attention to the comparison of the He and C spectra, again using a comparison of Voyager data on this ratio [3], which in this case extends up 1.5 GeV/nuc [4] and the AMS-2 data above 10 GeV/nuc [16, 17] where the solar modulation is small. The observed He/C (E) ratio from a few MeV/nuc to ~1 TeV/nuc is shown in **Figure 9**. It is seen to vary from

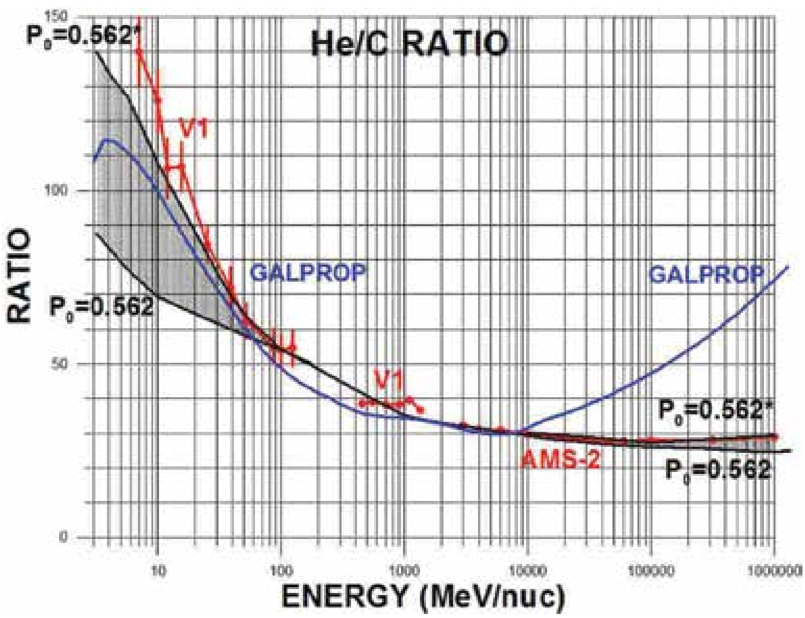

Figure 9. Observations and measurements of the He/C ratio between 3 MeV/nuc and 10^3 GeV/nuc. Errors on individual GeV/nuc voyager measurements are ±5%. Errors on AMS-2 measurements are less than ±2%. Black curve, labeled $P_0 = 0.562$*, is for a truncated exponential PLD with mean path length = $\lambda = 20.6\,\beta\,P^{-0.45}$ Above $P_0 = 0.562$ and with truncation parameters = 0.04 for He and 0.12 for C. The curve labeled $P_0 = 0.562$ is for a simple LBM with a PLD = exponential at all path lengths for $P_0 = 0.562$ GV. Dashed blue line is GALPROP calculation of the He/C ratio from [3].

http://dx.doi.org/10.5772/intechopen.75877

~130 at low energies to about 27 at the highest energies. One might think that this observed ratio would be more or less constant if these nuclei had the same spectra, since they have the same A/Z ratio, etc., but it turns out that, when the actual intensities and spectral shapes are obtained from LBM propagation calculations [10], the observed He/C (E) ratios are reproduced with He and C rigidity spectra with a source spectral index ~ − 2.24 for both components, extending throughout the rigidity range from ~100 MV to ~1.0 TV and with a source abundance He/C ratio = 23.7.

The reason for this is much like the case for electrons and protons, described earlier; it is mostly in the details of the LBM propagation, again in an overall simple LBM but with certain modifications at small matter path lengths, due possibly to the local distribution of the cosmic ray sources themselves. This modification (truncation) is perhaps the only significant departure from the incredible symmetry imposed by the LBM that is yet discerned from the Voyager studies to date. The details of the He/C ratio study are found in [18].

5. Spectral shapes of different nuclei at low energies

It has been possible to extend the earlier Voyager intensity and spectral measurements which were generally in the range 10–200 MeV/nuc [3] up to the GeV/nuc range and above [4]. This technique uses the precision measurement of ionization loss for particles that penetrate the 3 element total energy counters. The spectra of He, C, O, Mg, Si and Fe are obtained in this way up to 1.5 GeV/nuc, with an integral intensity at higher energies [4].

Spectra for these nuclei, including the lower energy Voyager measurements [3], are shown in **Figure 10**. The intensities are all normalized at 1.5 GeV/nuc. There is a dramatic charge dependence of the spectral shape that becomes more obvious at the lower energies. It is believed that these different charges have very similar and possibly identical source rigidity spectra. This identity of source spectra has been determined in the above section for He and C nuclei. In spite of the large dependence of the He and C ratio on energy which, changes from a value ~130 at 10 MeV/nuc to 27 at 1 TeV/nuc where AMS-2 measurements are available, the source spectra of both He and C nuclei are found to be ~$P^{-2.24}$.

Most of the changes in the measured intensity ratios in **Figure 10** are due to the effects of propagation in the galaxy. The curves in **Figure 10** show these effects vividly. There is a Z dependent effect which becomes more prominent at the lower energies. Two sources of these effects are, (1) ionization energy loss in interstellar matter which is Z^2/β^2, and (2) fragmentation collisions which are proportional to a $A^{1/3}$ dependence of these cross sections.

The ionization energy loss is particularly important at the lower energies because of the $1/\beta^2$ dependence, but even these ionization loss effects cannot account fully for the Z dependent turnovers of the differential spectra at lower energies. These differential spectra are observed to have maxima which systematically increase from ~30 MeV/nuc for He to ~100 MeV/nuc for Fe. The explanation for this large Z dependence in the maximum energies includes ionization energy loss but also includes the effect described as truncation (see below).

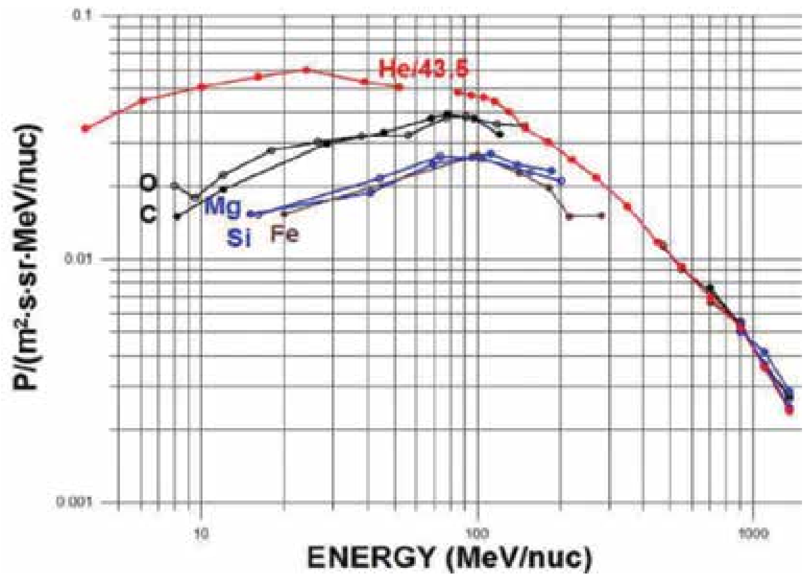

Figure 10. Observed relative intensities of He, C, O, Mg, Si and Fe nuclei between 100 and 1000 MeV/nuc. These intensities are normalized to the values of j at 1000 MeV/nuc for carbon nuclei. The figure includes lower energy intensities from [3].

In a perfect LBM for propagation in the galaxy where the sources are uniform and the propagation is effectively isotropic, the distribution of matter path length is an exponential at all path lengths with a mean path length which is ~ to the amount of matter traversed, e.g., in g/cm^2. At low energies where this ionization loss is large enough so that the particles cannot reach us from the nearest sources, the path length distribution becomes non-exponential or truncated at small path lengths. We believe that the different shapes of these spectra at the lowest energies are the best signature of this effect. A real example of this and other low energy propagation effects have been hidden from us previously by the solar modulation effects. The impenetrable fog of almost isotropic propagation on the study of the origin and acceleration of these particles and their role in the Universe in general may, in some small way, have been lifted by these new Voyager observations.

6. Secondary cosmic rays and the mean path length in g/cm^2 in the galaxy

Isotopes such as ^{2}H and ^{3}He and charges such as Li, Be, B and so called Fe secondaries, Z = 21–23, are believed to have zero abundance in any possible cosmic ray source. They are therefore produced by interactions of primary cosmic rays such as He, C, O, Mg, Si and Fe, to name the most prominent, either by nuclear fragmentations the interstellar medium, or perhaps partly in or near the acceleration region itself. The presence of the radioactive decay secondary isotope ^{10}Be with a half-life of only 1.5×10^6 years as compared with the average cosmic ray life-time of 1.5×10^7 years as determined from the observed ^{10}Be abundance using

LBM diffusion [19, 20], suggests the correct scenario is one in which most of these secondary particles are produced during the extended time of a galactic diffusion process.

The isotopes ^{2}H and ^{3}He and the charge B are the most abundant and well measured of the secondary nuclei. Their cross sections for production when the primary cosmic ray nuclei interact with atoms of H and He that are part of the interstellar medium are also quite well known after years of systematic measurement.

With this as a background we show in **Figure 11** the Voyager measurements of the intensities and spectra of these three secondary nuclei. The calculated abundance for each nuclei is based on a LBM where the mean path length, $\lambda = 20.6\ \beta\ P^{-0.45}$ above P = 1.0 GV and a constant path length = 9.0 g/cm^2 below 1.0 GV, and with a truncation parameter = 0.04.

These measurements make a convincing argument that the primary cosmic rays have gone through ~9 g/cm^2 of interstellar matter between ~10 and 100 MeV/nuc (~0.3 to 0.9 GV). At higher energies the measured B/C ratio may be used to determine the amount of matter traversed as a function of energy or rigidity. We have the V1 determination of the B/C ratio with zero solar modulation below ~1.5 GeV/nuc [4] and the AMS-2 determination of the ratio above ~3 GeV/nuc [17]. These measurements are shown in **Figure 12** along with the LBM propagation prediction using the parameters described in the above paragraph. The agreement is within ±10% from the lowest to the highest energies. Since this is a simple pure diffusion model, this high level of agreement at all energies implies that energy gain (reacceleration)

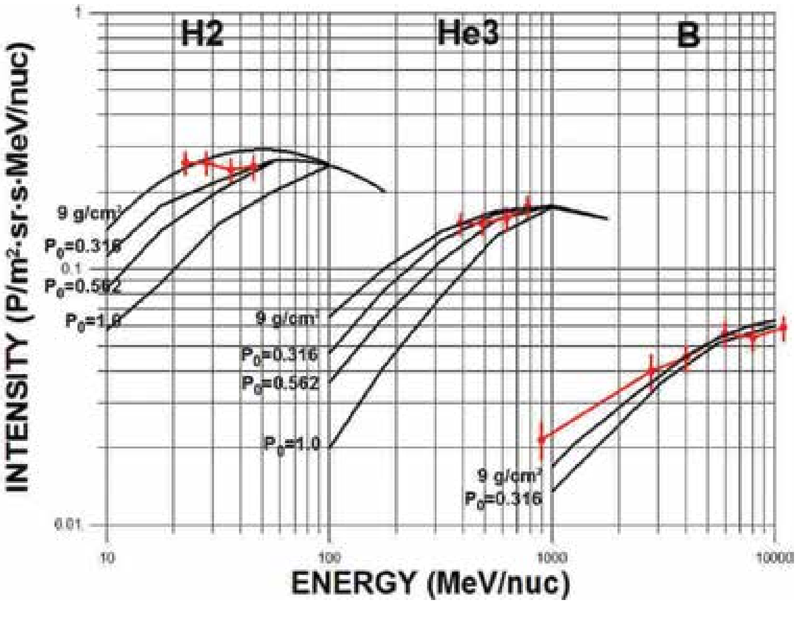

Figure 11. A comparison of the measurements of ^{2}H, ^{3}He and B nuclei intensities measured by the CRS experiment on V1 and the predictions of the LBM for values of P_0 = 0.316, 0.562, 1.0 GV and a constant path length = 9 g/cm^2 below 1.0 GV as described in the text. All three secondary isotopes are consistent with the predictions of a path length, λ, between 7 and 9 g/cm^2 at energies from ~20 to 100 MeV/nuc.

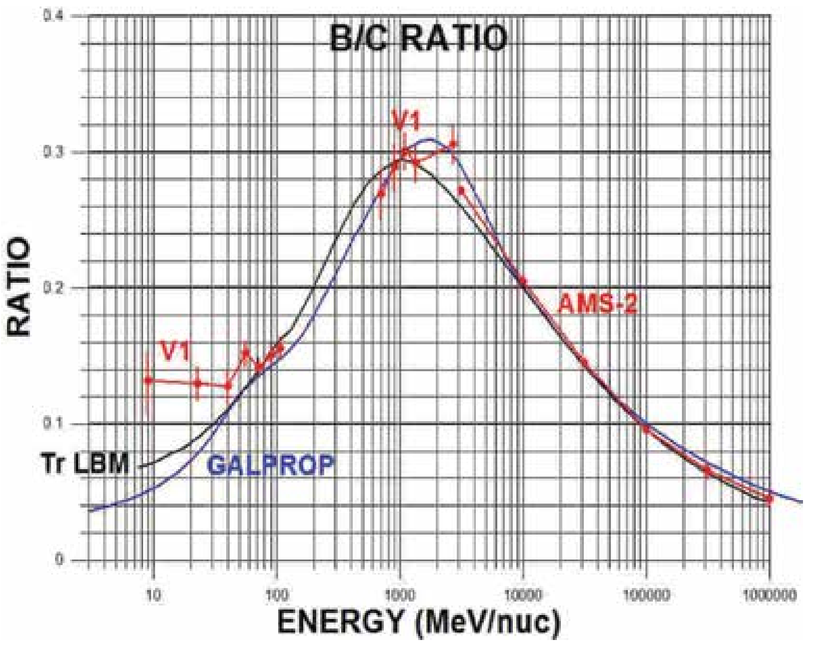

Figure 12 . The B/C ratio as a function of energy. The measurements of this ratio below ~2.4 GeV/nuc are from Voyager 1 beyond the heliopause [3, 4]. The higher energy measurements are from AMS-2 [17]. The calculated ratios are from the truncated LBM model described in the text and the GALPROP-DR model [3].

cannot be significant. The effects of truncation of the path length distributions at small path lengths (where the path length becomes ~0.6 g/cm^2 at the highest energies) are predicted in this model and are observed in the flattening of the B/C ratio at the highest energies [21].

7. Conclusions

So near the end of its 40 plus year mission Voyager has crossed the heliopause and sampled the interstellar energetic particle background for the 1st time. No one who has been involved in this mission from the beginning would have dreamt that this was possible. The goal of this chapter has been to attempt to convey some of the remarkable features of this data. Perhaps Voyager has saved its best for last, but only a few of us who could understand it are still around. The mission did not end with pictures of the planets but perhaps in the experience of the limits of humans in the eternal universe.

Acknowledgements

The author wishes to acknowledge his colleagues for over a generation now on the Voyager CRS team. First is Ed Stone, truly a captain of the “Starship Voyager” in the Captain Kirk tradition. Not to be outdone is Frank McDonald, our most senior advisor who sadly is no

longer with us. In fact the original "team of three" is without doubt the oldest scientifically productive team in history for a major experiment with an average age of 87.0 years. And Alan Cummings would have been part of the original team, except that he was a graduate student at the time of the 1st proposal. Now he is ready to retire, but, of course, nobody working on Voyager data would even think of that. And Nand Lal, the guru of the data system, has been around almost as long (have you ever tried the Voyager web site, http://voyager.gsfc.nasa.gov). There is no better one for any space experiment. And Bryant Heikkila, my former student, who can provide any data you need usually within 48-72 h real time, including the ~20 h light travel time to Earth. And last but not least, Tina Villa, who made this chapter possible.

Author details

William R. Webber

Address all correspondence to: bwebber@nmsu.edu

Department of Astronomy, New Mexico State University, Las Cruces, NM, USA

References

[1] Webber WR. Energetic charged particles in the heliosphere from 1-120 AU measured by the Voyager spacecraft. Astrophysics. InTech; 2012. p. 309

[2] Stone EC, Cummings AC, McDonald FB, et al. Voyager 1 observes low-energy galactic cosmic rays in a region depleted of heliospheric ions. Science. 2013;**341**:150

[3] Cummings AC, Stone EC, Heikkila BC, et al. Galactic cosmic rays in the local interstellar medium: Voyager 1 observations and model results. Astrophysics Journal. 2016;**831**:19

[4] Webber WR, Lal N, Stone EC, et al. Voyager 1 Measurements Beyond the Heliopause of Galactic Cosmic Ray Helium, Boron, Carbon, Oxygen, Magnesium, Silicon and Iron Nuclei with Energies 0.5 to >1.5 GeV/nuc. http://arXiv.org/abs/1712.02818; 2017

[5] Mewaldt RA, Davis AJ, Lave KA, et al. Record-setting cosmic-ray intensities in 2009 and 2010. Astrophysics Journal. 2010;**723**:L1

[6] Lave KA, Wiedenbeck ME, Binns WR, et al. Galactic cosmic-ray energy spectra and composition during the 2009-2010 solar minimum period. Astrophysics Journal. 2013;**770**:117

[7] Usoskin IG, Bazilevskaya GA, Kovaltson GA. Solar modulation parameter for cosmic rays since 1936 reconstructed from ground-based neutron monitors and ionization chambers. Journal of Geophysical Research. 2011;**116**:A02104

[8] Gleeson LJ, Axford WI. Solar modulation of galactic cosmic rays. Astrophysics Journal. 1968;**154**:1012

[9] Beer J, McCracken K, van Steiger. Pysics of earth and space environments cosmogenic radionuclides. Springer-Verlag; 2012;**19**

[10] Adriani O, Barbarino GC, Bazilevskaya R, et al. Time dependence of the proton flux measured by PAMELA during the 2006 july-2009 december solar minimum. Astrophysics Journal. 2013;**765**:91

[11] Aguilar M, Aisa D, Alvino A, et al. Precision measurement of the (e^++e^-) flux in primary cosmic rays from 0.5 GeV to 1 TeV with the alpha magnetic spectrometer on the international space station. Physical Review Letters. 2014;**113**:121102

[12] Webber WR, Villa TL. The Galactic Cosmic Ray Electron Spectrum from 3 to 70 MeV Measured by Voyager 1 Beyond the Heliopause, What This Tells Us About the Propagation of Electrons and Nuclei In and Out of the Galaxy at Low Energies. http://arXiv.org/abs/1703.10688; 2017

[13] Webber WR, Villa TL. A Comparison of the Galactic Cosmic Ray Electron and Proton Intensities From ~1 MeV/nuc to 1 TeV/nuc Using Voyager and Higher Energy Magnetic Spectrometer Measurements – Are There Differences in the Source Spectra of These Particles? To be submitted to arXiv

[14] Ptuskin V, Moskalenko IV, Jones FC, et al. Dissipation of magnetohydrodynamic waves on energetic particles: Impact on interstellar turbulence and cosmic-ray transport. Astrophysics Journal. 2006;**642**:902

[15] Aguilar M, Aisa D, Alvino A, et al. Precision measurement of the proton flux in primary cosmic rays from rigidity 1 GV to 1.8 TV with the alpha magnetic spectrometer on the international space station. Physical Review Letters. 2015;**114**:171103

[16] Aguilar M, Aisa D, Alvino A, et al. Precision measurement of the helium flux in primary cosmic rays of rigidities 1.9 GV to 3 TV with the alpha magnetic spectrometer on the international space station. Physical Review Letters. 2015;**115**:211101

[17] Aguilar M, Ali Cavasonza L, Ambrosi G, et al. Precision measurement of the boron to carbon flux ratio in cosmic rays from 1.9 GV to 2.6 TV with the alpha magnetic spectrometer on the international space station. Physical Review Letters. 2016;**117**:231102

[18] Webber WR. The Different Shapes of the LIS Energy Spectra of Cosmic Ray He and C Nuclei Below ~1 GeV/nuc and The Cosmic Ray He/C Nuclei Ratio vs. Energy-V1 Measurements and LBM Propagation Predictions. 2017. http://arXiv.org/abs/1711311584

[19] Garcia-Munoz M, Simpson JA, Guzik TG, et al. Cosmic-ray propagation in the Galaxy and in the heliosphere-The path-length distribution at low energy. Astrophysics Journal. 1987;**64**:269

[20] Yanasuk NE, Wiedenbeck ME, Mewaldt RA, et al. Measurement of the Secondary Radionuclides ^{10}Be, ^{26}Al, ^{36}Cl, ^{54}Mn, and ^{14}C and Implications for the Galactic Cosmic-Ray Age. Astrophysics Journal. 2001;**563**:768

[21] Webber WR, Villa TL. The Cosmic Ray Boron/Carbon Ratio Measured at Voyager and at AMS-2 from 10 MeV/nuc up to ~1 TeV/nuc and a Comparison With Propagation Calculations. http://arXiv.org/abs/1711.08015;2017

Galactic Cosmic Rays and Low Clouds: Possible Reasons for Correlation Reversal

Svetlana Veretenenko, Maxim Ogurtsov,
Markus Lindholm and Risto Jalkanen

Additional information is available at the end of the chapter

http://dx.doi.org/10.5772/intechopen.75428

Abstract

Influence of galactic cosmic rays (GCRs) on cloud formation is suggested to be an important part of the mechanism of solar activity influence on weather and climate. A high positive correlation between low cloud amount and GCR fluxes was observed in the 1980s–1990s; however, in the early 2000s, it was violated. In this work, we consider a nature of long-term correlation links between cloud cover at middle latitudes and GCRs, as well as possible reasons for this correlation reversal. It was shown that the GCR-cloud links observed on the decadal time scale are indirect and caused by GCR effects on cyclonic activity which depend on epochs of the large-scale atmospheric circulation. The reversal of GCR-cloud correlation in the 2000s seems to be due to a sharp weakening of the Arctic and Antarctic stratospheric polar vortices, which results in the change of the troposphere-stratosphere coupling and, then, of GCR contribution to the development of extratropical cyclogenesis.

Keywords: solar-atmospheric links, space weather, galactic cosmic rays, low clouds, cyclonic activity, polar vortex

1. Introduction

Studying the influence of solar activity and related phenomena on the lower atmosphere state, weather and climate is one of most actual tasks of solar-terrestrial physics, which is due to an important part of climatic changes for different aspects of human activity. One of the possible mechanisms of this influence suggests an impact of galactic cosmic rays (GCRs) on the cloud cover allowing amplifying noticeably a weak signal of solar variability in the Earth's

IntechOpen

© 2018 The Author(s). Licensee IntechOpen. This chapter is distributed under the terms of the Creative Commons Attribution License (http://creativecommons.org/licenses/by/3.0), which permits unrestricted use, distribution, and reproduction in any medium, provided the original work is properly cited.

atmosphere. Indeed, cloudiness changes can strongly modulate fluxes of both incoming short-wave solar radiation and outgoing long-wave radiation of the Earth and the atmosphere and, thus, influence significantly the radiative-thermal balance of the atmosphere. High-level clouds contribute to the warming of the atmosphere, whereas low-level clouds contribute, as a rule, to its cooling. A net influx of radiation coming to the Earth's surface under cloudy conditions depends on latitude, season and underlying surface. According to the data obtained from spaceborne experiments [Nimbus 7 Earth Radiation Budget experiment (N7ERB) and Earth Radiation Budget Experiment (ERBE)], when averaged over the globe, cloudiness reduces the input of solar radiation by 44.5–54.3 $W \cdot m^{-2}$ (depending on the season) and the emission of long-wave radiation to space by 23.6–34.7 $W \cdot m^{-2}$ [1, 2]. As a result, cloudiness decreases the global radiative heating of the atmosphere by 17.3–26.8 $W \cdot m^{-2}$.

The hypothesis about GCR influence on the cloudiness state was first put forward in 1975 by Dickinson [3]. He suggested that ionization changes due to GCR variations affect the formation of stratospheric aerosols, the main component being a water solution of sulfuric acid H_2SO_4. Such aerosol particles of ~100 nm in size are effective cloud condensation nuclei (CCN) due to a high solubility of sulfuric acid in water which greatly lowers the saturated vapor pressure over these particles compared with homogenous water nuclei. According to Dickinson's suggestions, the formation of aerosol particles is more probable on positively charged water clusters $H_3O^+(H_2O)_n$ (n = 5–7), the concentration of such clusters depending on ionization in the atmosphere. So, changes in ionization may influence the rate of nucleation processes and, thus, contribute to the formation of high-level (cirrus) clouds.

At present, we can note two possible ways of GCR influence on cloud formation: the ion-mediated (or induced) nucleation [3–7] and the mechanisms including changes in Global Electric Circuit (for example, see [8, 9]). Ion-mediated nucleation (IMN) is the nucleation of aerosol particles (which under certain conditions may later grow up to cloud condensation nuclei) taking place in the presence of ions. An important source of new aerosols in the atmosphere is molecular clusters forming from water and sulfuric acid. However, clusters of subcritical sizes (<1–2 nm) are unstable and easily destroyed by evaporation. When a cluster reaches a critical size of ~1–2 nm, surface tension forces start dominating and it gets stable. Such clusters represent aerosol nuclei which may grow due to condensation and coagulation up to ~100 nm which allows turning into a cloud condensation nucleus and take part in the formation of cloud particles (~10–20 μm). Charged molecular clusters forming around ions are more stable due to Coulomb attraction and can grow faster than neutral ones. Then, when ionization increases, a probability of the formation of charged, more stable clusters becomes higher and this results in the increase of the nucleation rate. According to model calculations by Yu and Turco [5], a 25% increase of the ionization rate in the lower atmosphere could lead to an increase of the concentration of aerosol particles capable for the further growth, with the diameter being >3 and >10 nm, by 16.5 and 9%, respectively, in several hours after the nucleation start.

Another way of GCR influence on clouds, which suggests changes in the Global Electric Circuit caused by variation of atmospheric conductivity and ionospheric potential, has been developed by Tinsley and colleagues [8–11]. It is suggested that changes of conductivity due to GCR variations, along with changes of ionospheric potential due to variations of interplanetary magnetic fields influence a density J_z of downward ionosphere-Earth currents. In turn, these currents, when flowing through high gradients of conductivity at cloud boundaries, contribute to a separation of positive and negative ions which quickly attach to droplets and aerosol particles, including both cloud condensation nuclei and ice-forming nuclei. Electric charges on these particles influence microphysical processes in clouds, enhancing their collision rate and 'sticking' due to Coulomb attraction. In particular, this may result in more intensive freezing of thermodynamically unstable super-cooled water droplets in high-level clouds ('electrofreezing') [10]. An increase of charge on aerosol particles also enhances the rate of their scavenging by larger droplets due to the electric attraction between the charge on a particle and the image charge which it creates on a droplet ('electroscavenging') [11]. Thus, charging cloud particles associated with J_z variations results in a number of microphysical processes in clouds affecting particle concentration and their size distribution.

First experimental data providing evidence for a possible influence of GCRs on the cloudiness formation were obtained by Pudovkin and Veretenenko [12]. They detected a decrease in cloud cover and an increase in the frequency of occurrence of clear-sky days at middle and high latitudes in the course of short-term decreases of GCR intensity (Forbush decreases), with the data at the network of actinometric stations of the U.S.S.R. being used. The decrease of cloud cover associated with Forbush decreases at the stations under study was also confirmed by an increase of the input of total radiation which includes both direct and scattered solar radiation [13]. Later a remarkable result showing cloud-GCR links on the decadal time scale was obtained by Svensmark and Friis-Christensen [14] basing on the satellite data ISCCP (International Satellite Cloud Climatology Project). The authors detected a variation of 3–4% in global cloud amount which was strongly correlated with GCR intensity (the correlation coefficient ~0.9) for the period 1984–1991. As a change of global cloud cover by 1% corresponds to a net radiation change by 0.5 W.m^{-2} according to the estimates by Rossow and Cairns [15], Svensmark [16] concluded that the radiative forcing of the detected decrease of global cloud cover by ~3% from 1987 to 1990 (i.e. from a minimum to a maximum of solar activity) may amount to ~1.5 W.m^{-2}. He suggested that cloud forcing associated with long-term GCR variations might explain most part of the temperature changes in the period 1975–1989. The results gave rise to a lively discussion of GCR effects on the formation of clouds, as well as their role in the mechanism of solar-atmospheric links (for example, see [17–19]).

The further studies by Marsh and Svensmark [20, 21] revealed that only low-level cloud amount correlates significantly with GCR intensity. The correlation coefficients between globally averaged values of low cloud anomalies (LCA) according to the ISCCP-D2 satellite data and the counting rate of the Huancayo neutron monitor amount to 0.63 and 0.92 for unsmoothed values and 12-month running averages, respectively, for the period 1984–1994. However, in the second part of the 1990s the positive correlation LCA-GCR started weakening and broke down completely near 2000 [22, 23]. The observed violation of LCA-GCR correlation caused doubts in a possible influence of cosmic rays on cloud formation, as well as their important role in the physical mechanism of solar-atmospheric links [22, 24, 25].

Thus, at the moment cloud-GCR relationship remains a rather controversial question. In different studies, we can find the data both confirming and rebutting a possibility of GCR influence on cloud formation. Svensmark et al. [26] found a significant decrease of liquid water in low clouds, as well as in fine aerosol concentration associated with strong GCR Forbush decreases. A decrease of high-level clouds over the Antarctic in the course of Forbush decreases of GCR intensity was revealed by Todd and Kniveton [27, 28] as well as Laken and Kniveton [29] on the base of the ISCCP cloud data. Laken et al. [30] detected changes in cloud cover over middle latitudes (30–60°) of both hemispheres associated with short-term changes in GCR intensity, using also the ISCCP data. However, no responses of cloudiness to Forbush decreases were revealed by Čalogović et al. [31], Krissansen-Totton and Davies [32].

As to the decadal time scale, the problem of GCR-cloud relations is complicated because of a number of other solar activity phenomena affecting the atmosphere and conditions for cloudiness formation simultaneously with cosmic rays. Kristjánsson et al. [33, 34] concluded that low cloud cover correlates better with total solar irradiance (TSI) variations than with those of GCRs, the suggested mechanism involving variations in sea surface temperature and their impact on low clouds. In the works by Voiculescu and colleagues [35–37], variations of ultraviolet radiation and solar wind disturbances are considered as possible factors influencing cloudiness state. In particular, it was noted that the effects of GCR and UV variations on cloudiness state are characterized by regional and altitudinal dependencies [36]. In this work the areas of positive and negative correlations were revealed for low cloud amount and GCRs. For middle and high clouds the areas of statistically significant correlations with GCRs and UV radiation were also detected. The data in [37] provide evidence for a possible influence of interplanetary electric fields (IEE) modulated by solar wind speed and interplanetary magnetic fields on cloud formation. The detected cloud-IEE correlations seem to indicate an important part of downward atmospheric currents in the Global Electric Circuit for cloud particle formation, as described in [8–11].

For an experimental verification of a possible influence of cosmic rays on the rate of nucleation and subsequent growth of clusters an experiment CLOUD (Cosmics Leaving OUtdoor Droplets) was carried out at CERN (the European Organization for Nuclear Research) [38]. In this experiment there were investigated processes of cluster formation on the base of sulfuric acid, ammonia and water vapor, as well as ionization influence on these processes. The results of the experiment CLOUD confirmed that in the presence of ions the nucleation rate does really increase by a factor of ~10 under conditions typical for the middle troposphere (~5 km), the sulfuric acid and water being involved in nucleation. However, under conditions in the lower part of the atmosphere the rate of the formation of clusters with the diameter ~1.4 nm was found to be less by a factor of 10–10,000 than in the real atmosphere [38]. To reach nucleation rates corresponding to those measured in the lower atmosphere, the content of ammonia had to be substantially increased and the temperature had to be lowered to ~250°C [38, 39]. Another way to enhance nucleation was to add biogenic amines (dimethylamine), as it was reported by Almeida et al. [40]. The results of this study carried out on the base of the CLOUD chamber at CERN showed that dimethylamine can influence significantly nucleation rates and account for the rates observed in the real atmosphere. These results indicate that in the lower atmosphere a ternary nucleation seems to take place, with sulfuric acid, water and bioorganic compounds being involved. However, the rate of the ternary nucleation was found to depend weakly on ionization [40]. On the other hand, the experiments by Svensmark et al. [41] revealed a noticeable link between the formation of CCN particles ~50 nm and ionization. Thus, the question of GCR influence on the intensity of nucleation and subsequent growth of clusters to CCN sizes remains open and further experiments are needed.

Concerning observations in the real atmosphere, one should stress that direct effects of GCRs and corresponding changes of ionization on microphysical processes in clouds seem to be detectable only on rather short time scales (about several hours or days). On longer time scales dynamic processes developing as a response to GCR variations (or to some other solar activity phenomena) should be taken into account. Indeed, cloud enhancement according to any suggested mechanism (ion-mediated nucleation or mechanisms including atmosphere electricity changes) results in changing radiative-thermal balance in the lower atmosphere and, consequently, in some changes in the structure of thermo-baric fields of the troposphere which, in turn, influence atmospheric circulation and the evolution of baric systems. If changes of the thermo-baric field contribute to the deepening of low-pressure systems (cyclones and troughs), cloud fields of these systems will be enhanced. Thus, monthly averaged cloud amount will include not only direct (microphysical) effects of GCR variations on cloud particle formation, but also indirect effects due to the circulation changes influencing cloudiness. So, when considering cloud data on longer time scales, we cannot distinguish between primary (microphysical) GCR effects on clouds and secondary ones, resulting from circulation changes associated with GCRs. Moreover, direct effects of GCRs on cloud characteristics seem to be weaker than those associated with long-term circulation disturbances. This point seems to be of importance to understand the nature of cloud-GCR correlation on longer time scales.

An important point to be understood concerns the violation of correlations between cloudiness and GCR intensity occurred near 2000. As it was said above, this violation gave rise to doubt the role of GCRs in the mechanism of solar-atmospheric links. However, temporal variability of correlation links between the lower atmosphere characteristics and solar activity characteristics is a rather typical feature of these links. The observed correlations may enhance, weaken or even change the sign depending on time period. Veretenenko and Ogurtsov [42, 43] suggested that this variability may be due to changes of the epochs of the large-scale atmospheric circulation associated, in turn, with changes in the strength of the stratospheric polar vortex. So, the question arises whether the observed violation of cloud-GCR links is a result of a change in the character of helio-geophysical effects on tropospheric circulation. The aim of this study is to consider the nature of correlation links detected between low clouds and GCRs on the decadal time scale, as well as possible reasons for the violation of these links near 2000.

2. CGR effects on atmosphere dynamics and cloud fields

It is well known that the main reason for cloud formation is a vertical transport of water vapor which results in its cooling and condensation (for example, see [44]). So, the formation of cloud fields in the troposphere is determined by upward air movements which, in turn, are closely related to atmospheric circulation.

At extratropical latitudes most large-scale upward movements, with the horizontal extent being from several hundred to several thousand kilometers, are associated with low-pressure systems, cyclones and troughs. They result from a convergence of air flows near the Earth's surface to the cyclone center or to the trough axis. Upward movements in the atmosphere are also associated with atmospheric fronts which are narrow transition zones between cold and warm air masses. A front is called 'warm', if a warm air mass moves toward a cold one shifting it. Warm fronts are characterized by regular ascending movements of air sliding slowly along a frontal surface. These movements produce strong systems of frontal stratiform clouds Ns-As-Cs (nimbostratus Ns, altostratus As and cirrostratus Cs) with continuous precipitation. Cold fronts arise when a cold air mass moves toward a warm one. Cloud systems of slowly moving cold fronts are similar to those of warm ones. If a cold front is fast moving, vertical velocity of air movements before this front is higher than before a warm one; this contributes to the development of convective clouds, such as cumulonimbus (Cb) with storm precipitation and lightening (for example, [44]). A merging of the cold and warm fronts (so-called 'occlusion') in the process of cyclone evolution results in the formation of an occluded front with the most complex cloud systems. A cloud field of an atmospheric front is seen from satellites as a long band, with the width being usually less than 1000 km and the length reaching several thousand kilometers.

An extratropical cyclone is usually a frontal one, all its evolution being closely related to fronts. First, a cyclone arises as a wave at cold front; then, it passes to the stage of a young cyclone characterized by an existence of a warm sector, i.e. the area of warm air between its cold and warm fronts. At the stage of the maximum development of a cyclone the occlusion starts and an occluded front is formed. At the final stage of cyclone evolution the occlusion continues, a cyclone gets cold and slow and starts filling. A well-developed cyclone can be seen from a satellite as a cloud vortex with a spiral structure, the cloud field dimensions being comparable with those of a cyclone (see **Figure 1**). Thus, frontal cloudiness develops at all the stages of cyclone evolution. This results in a close connection between cloud fields and baric fields of the atmosphere, with baric field changes being accompanied by the evolution of cloud systems.

Figure 1. Cloud system of an extratropical cyclone over Alaska gulf (NASA Earth Observatory, photo by Jessy Allen and Robert Simon [45]). The center of the vortex is marked by A.

http://dx.doi.org/10.5772/intechopen.75428

Let us consider variations of cloud cover at middle latitudes where the intensive cyclonic activity takes place and compare them with pressure variations. As experimental base for this study the cloud data from ISCCP (International Satellite Cloud Climatology Project) [46] available for the period from July 1983 to December 2009 were used. At present it is the most comprehensive and the longest archive of different cloud characteristics. According to ISCCP classification clouds are divided into three types depending on pressure at cloud top (CP): low (CP > 680 hPa), middle (440 hPa < CP < 680 hPa) and high (CP < 440 hPa) clouds. Cloud amount is defined as a fraction of the area covered by clouds of a definite type and is expressed as a percentage of the total area. Anomalies of cloud amount are determined as the difference between monthly values of cloud amount of the studied type and the climatic mean, i.e. cloud amount for a given month averaged over the whole period of observation.

In this study we consider monthly values of low cloud anomalies (LCA) from the ISCCP-D2 archive based on infrared (11 μm) radiance measurements [47]. Low-level cloudiness involves stratus (St), nimbostratus (Ns) and stratocumulus (Sc), it may also involve convective cumulus (Cu). The data were taken for the mid-latitudinal belts 30–60° of both hemispheres which are regions of intensive extratropical cyclogenesis. At these latitudes the ISCCP data are in a rather good agreement with other satellite data (MODIS, UW HIRS), unlike polar ones [48].

In **Figure 2a** and **b**, temporal variations of LCA for the Northern and Southern hemispheres are presented. One can see a gradual decrease of low cloudiness from the early 1980s to 2009,

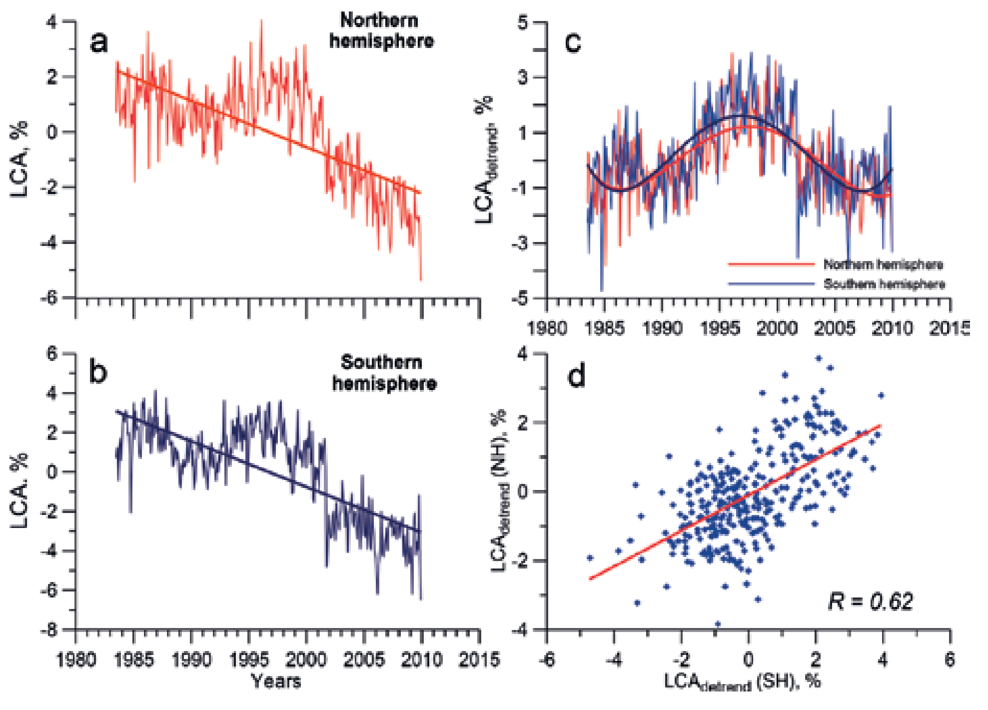

Figure 2. *Left*: Temporal variations of LCA (monthly values) at the latitudes 30–60° in the Northern (a) and Southern (b) hemispheres. *Right*: Temporal variations of detrended values of LCA in the Northern and Southern hemispheres (c) and detrended values of LCA in the Northern hemisphere versus those in the Southern one. Thick lines show linear (a, b) and polynomial (c) trends in LCA variations.

a reason for this decrease being not quite clear. According to [49], the trends may be due to some changes in the satellite view angles. However, as it will be shown later, this decrease of cloudiness may be also associated with long-term weakening of cyclonic activity in the belts under study. In any case, for our analysis of cloud-GCR links, we detrend values of LCA and GCR intensity.

Removal of linear trend in LCA reveals (**Figure 2c**) that low cloud anomalies in the Northern and Southern hemispheres have a rather high similarity. The correlation coefficient between these values amounts to 0.62 (**Figure 2d**), the statistical significance being 0.95 according to the random-phase test [50]. LCA variations in both hemispheres seem to be also characterized by a roughly 20-year periodicity. This periodicity, which is close to the magnetic Hale cycle on the Sun, was detected in many climatic parameters (for example, see [51, 52]), including the intensity of extratropical cyclogenesis in the North Atlantic [53]. Thus, the ~20-year periodicity indicates a link between cloudiness and the evolution of dynamic processes in the lower atmosphere.

Let us now compare temporal variations of LCA and GCR intensity. To characterize GCR intensity we used monthly values of charged particle fluxes F_{CR} measured in the stratosphere at ~15–20 km (in the maximum of the transition curve) at the mid-latitudinal station Dolgoprudny (geomagnetic cutoff rigidity R_c = 2.35 GV) near Moscow [54]. Variations of LCA and F_{CR} monthly values, the linear trends being subtracted, are presented in **Figure 3**. We can see that till ~2000 LCA and GCR intensity varied in a similar way, but then this similarity was violated. Indeed, the correlation coefficients between yearly values of LCA and GCR fluxes for sliding 11-year intervals (**Figure 4**) show that cloud-GCR links were the closest in both hemispheres from the middle 1980s to the middle 1990s, the correlation coefficients amounting to ~0.6–0.8. The statistical significance levels (dotted lines in **Figure 4**) for the correlation coefficients were estimated on the base of Monte-Carlo simulations of sliding coefficients for surrogate time series obtained by a randomization of initial ones. In the indicated period the cloud-GCR correlations were most significant (the significance level 0.95–0.99), but since ~2000 they started to decrease sharply and in the early 2000s correlation became negative in both hemispheres.

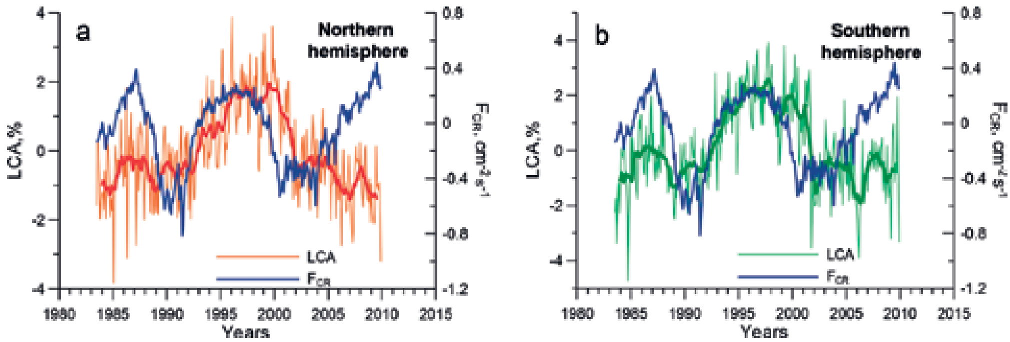

Figure 3. Temporal variations of detrended monthly values of LCA and GCR fluxes in the Northern (a) and Southern (b) hemispheres. Thick lines show 12-month running averages of LCA.

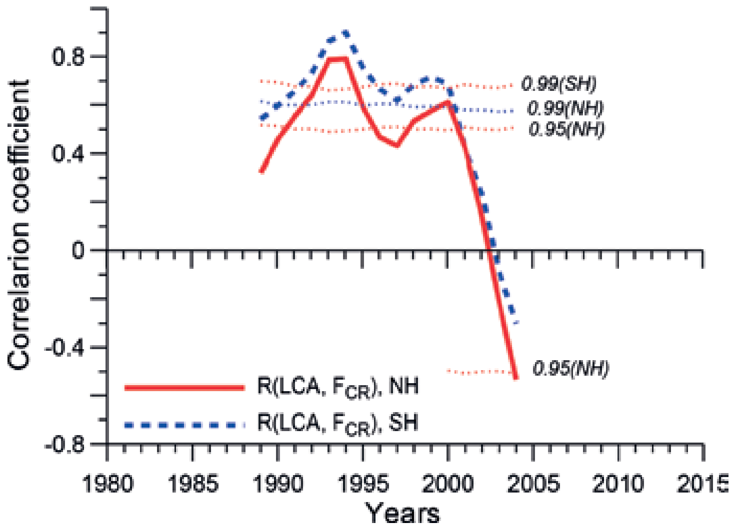

Figure 4. Correlation coefficients between yearly values of LCA and GCR fluxes for sliding 11-year intervals in the Northern (solid red line) and Southern (dashed blue line) hemispheres. Dotted lines show the significance levels of the correlation coefficients.

Taking into account a close link between cloudiness and dynamic processes in the atmosphere, let us consider pressure variations at middle latitudes. As a characteristic of pressure we used geopotential heights of the pressure level 700 hPa (GPH700), taken from NCEP/NCAR reanalysis archive [55]. The indicated level is related to the free atmosphere where effects of Earth's surface friction on air motion are negligible, and its heights correlate well with surface pressure. Temporal variations of 12-month running averages of GPH700 values area-averaged over the belts 30–60° in both hemispheres are shown in **Figure 5** for the period 1948–2013. One can see that long-term variations of pressure differ noticeably in these belts, which implies that cyclonic processes at middle latitudes of the Northern and Southern hemispheres develop to a great extent independently. However, during the period of ISCCP observations (1983–2009) pressure in the studied belts was gradually increasing, i.e. cyclonic processes were weakening. As cloud fields are produced by upward air movements closely associated with large-scale low-pressure areas, a weakening of cyclonic processes had to result in a decrease of cloud cover. Thus, LCA decrease during the period 1983–2009 is consistent with observed pressure changes.

In **Figure 6a** and **b**, pressure (GPH700) anomalies in the belts 30–60°N (S), calculated similarly to low cloud anomalies, are compared with GCR variations, with the data being averaged over a year and the linear trends being removed. From the early 1980s to ~2000 pressure at middle latitudes of the Northern hemisphere and GCR variations developed in the opposite phases, i.e. GCR increases were accompanied by cyclone intensification and pressure decrease, which agrees well with the effects detected in [42]. However, this link was destroyed near 2000. A similar situation took place in the Southern hemisphere. However, unlike the Northern one, where GCR effects are pronounced in almost all the belt 30–60°, GCR effects on cyclone evolution in the Southern hemisphere are restricted by the areas of climatic lows near

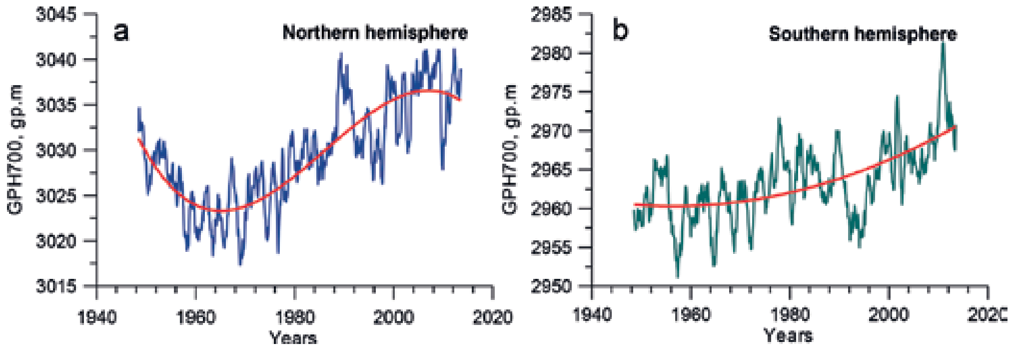

Figure 5. Long-term variations of tropospheric pressure (12-month running averages of GPH700) in the belts 30–60° of the Northern (a) and Southern (b) hemispheres. Red lines show polynomial trends.

Antarctic coasts in the South Atlantic and the Indian ocean, as well at climatic Polar fronts over the South Pacific [42]. So, GPH700 anomalies for the Southern hemisphere (**Figure 6b**) were calculated for these cyclonic areas.

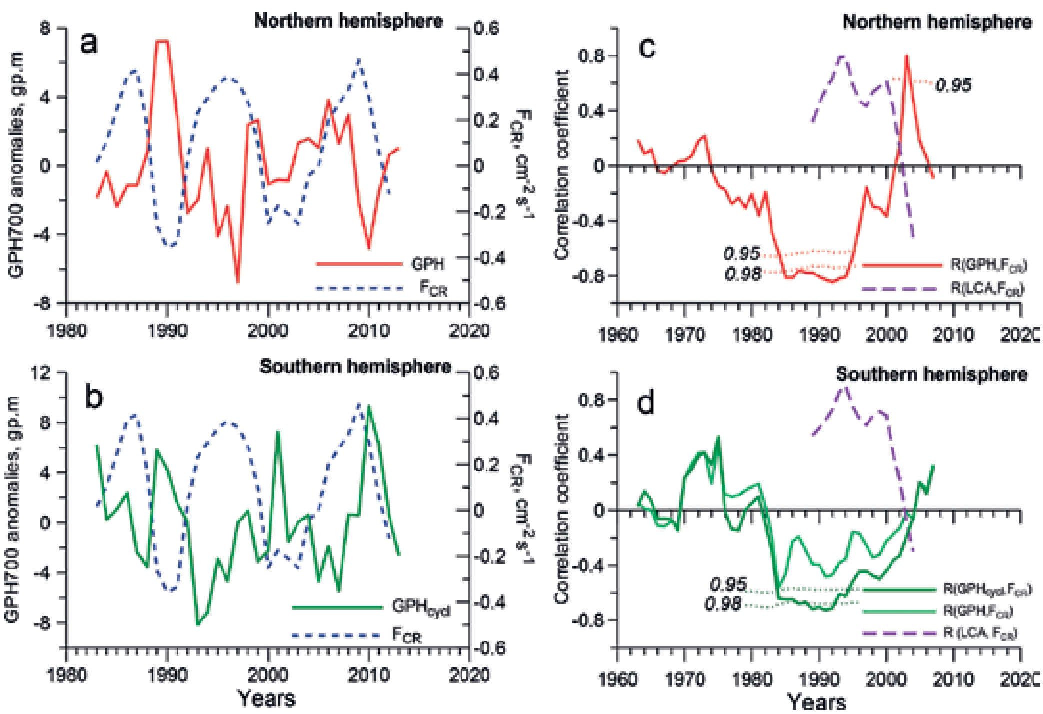

Figure 6. *Left*: Temporal variations of GPH700 anomalies in the belts 30–60° and GCR fluxes (detrended yearly values) in the Northern (a) and Southern (b) hemispheres. *Right*: Correlation coefficients for sliding 11-year intervals between LCA and GCR fluxes (dashed lines), GPH700 anomalies and GCR fluxes (solid lines) in the Northern (c) and Southern (d) hemispheres. In the Southern hemisphere, the correlation coefficients are shown for the whole belt 30–60°S (light green line) and for the cyclonic areas (dark green line). Dotted lines show the significance levels of the correlations coefficients between GPH700 and GCR fluxes.

Thus, the data presented in **Figure 6** (left) show that before ~2000 GCR increases in the solar minima contributed to extratropical cyclone intensification at middle latitudes of both hemispheres, but near 2000 the character of the pressure-GCR link was abruptly changed. This is confirmed by the temporal behavior of correlation coefficients for sliding 11-year intervals between detrended yearly values of GPH700 anomalies and GCR fluxes shown in **Figure 6** (right). From the middle 1980s to the middle 1990s, the strongest negative correlation, with R(GPH, F_{CR}) reaching approximately −0.8 and statistically significant at the level 0.98 according to Monte-Carlo estimates, was observed throughout the mid-latitudinal belt of the Northern hemisphere and in the cyclonic areas of the Southern one. In this period we can see the most pronounced positive correlation between low clouds and GCR fluxes which is consistent with GCR effects on cyclone development. Then, a negative correlation between pressure and GCR fluxes started weakening and its sign reversal took place in the early 2000s. Simultaneously with the weakening of the pressure-GCR correlation, we observe the corresponding weakening of a positive correlation between low clouds and GCR variations, as well as this correlation turning negative in the early 2000s. Thus, the obtained results suggest that cloud-GCR correlation links at middle latitudes observed on the decadal time scale are closely related to GCR effects on the development of cyclonic processes.

3. Polar vortex as a possible reason for the variability of GCR effects on the lower atmosphere

It is well known that temporal variability is a characteristic feature of solar-atmospheric links (see, for example, [56]). Correlation links observed between lower atmosphere characteristics and phenomena related to solar activity may weaken, disappear and even change sign depending on time period. So, a violation of the cloud-GCR link in the 2000s is not an extraordinary event. Herman and Goldberg [56] suggested that a reason for temporal variability of solar-atmospheric links may be long-term processes of the Sun which do not influence sunspot numbers and/or some changes of atmospheric conditions. Veretenenko and Ogurtsov [42, 43] showed that temporal behavior of correlation links between surface pressure at extratropical latitudes and sunspot numbers is characterized by a roughly 60-year periodicity caused by changes in the epochs of the large-scale atmospheric circulation. The reversals of the correlation signs were found in the end of the nineteenth century, in the early 1920s, the 1950s and the early 1980s coinciding with climatic regime shifts at middle latitudes [57], as well as with the transitions between cold and warm epochs in the Arctic [58]. So, a violation of the cloud-GCR link in the 2000s seems not to be unexpected and may be associated with the next change of the circulation epochs resulting in the change of GCR contribution to extratropical cyclonic activity and, then, to cloud field formation.

According to the suggestions in [58], the changes of the circulation epochs are closely related to the state of the polar vortex. The polar vortex is a cyclonic circulation forming in a cold air mass in the polar region of the Northern and Southern hemispheres and spreading from the middle troposphere to the upper stratosphere. A circular air motion in the vortex results in a decrease of heat exchange between polar and middle latitudes and this contributes to a temperature drop inside the vortex and an increase of temperature gradients at its edges (see **Figure 7**). The vortex can also be seen as a region of enhanced velocity of zonal winds in the stratosphere during cold months for the given hemisphere, the highest values being observed at latitudes 50–80° at the pressure levels above 50 hPa.

The polar vortex is an important factor of the large-scale atmospheric circulation and climate variability. Gudkovich et al. [58] showed that the rotation of cold and warm epochs in the Arctic are caused by changes of the vortex intensity, warm and cold epochs being associated with a strong and weak vortex, respectively. Indeed, under strong vortex conditions cyclone tracks are shifted to the north [59] and more North-Atlantic cyclones arrive in the polar region bringing warm air. An important feature of the polar vortex is its influence on the troposphere-stratosphere coupling via planetary waves. Propagation of planetary waves upward depends on stratospheric circulation (for example, [60, 61]). If the vortex is strong and a velocity of western winds in the stratosphere exceeds some critical value, these waves are reflected back to the troposphere. If the vortex is weak, planetary waves propagate freely upward. So, the stratosphere may influence the troposphere under a strong vortex regime. Under a weak vortex, only the troposphere may influence the stratosphere. This point seems to be of importance to understand the observed temporal variability of solar activity/GCR effects on tropospheric circulation.

Let us consider variations of the polar vortex intensity and compare them with temporal behavior of GCR effects on cyclonic activity and clouds. To characterize the vortex strength, we used zonally averaged velocity of western winds (i.e. the U-component of wind velocity directed from west to east from [55]) at the level 50 hPa (~20 km). In **Figure 8** (top panel) there are presented variations (detrended values) of mean zonal wind velocity in the belts 60–80° in both hemispheres averaged for six cold months (October-March in the Northern hemisphere and April-September in the Southern one). The correlation coefficients R(GPH, F_{CR}) and R(LCA,F_{CR}) for sliding 11-year intervals are shown in **Figure 8** (bottom panel).

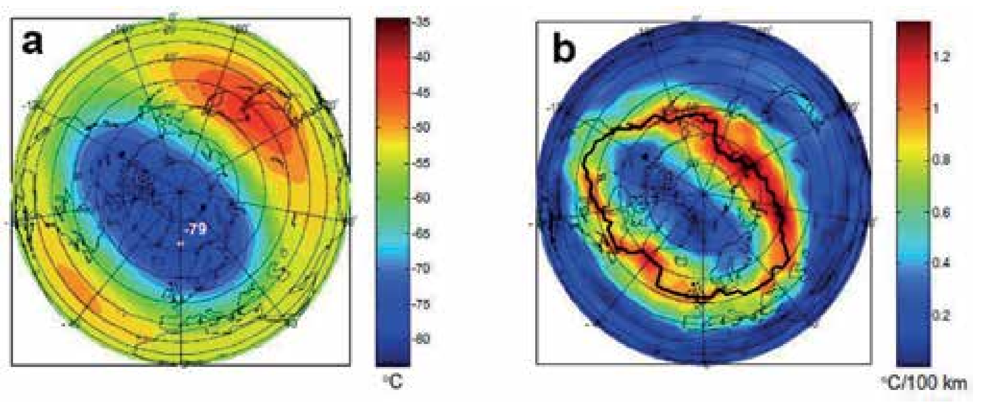

Figure 7. Distribution of mean monthly temperature at the pressure level 20 hPa (a) and of magnitude of horizontal temperature gradients (b) in the Northern hemisphere in January 2005. White asterisk indicates a minimum of temperature in the vortex; thick black line connects the points of maximal values of the temperature gradient at given latitude.

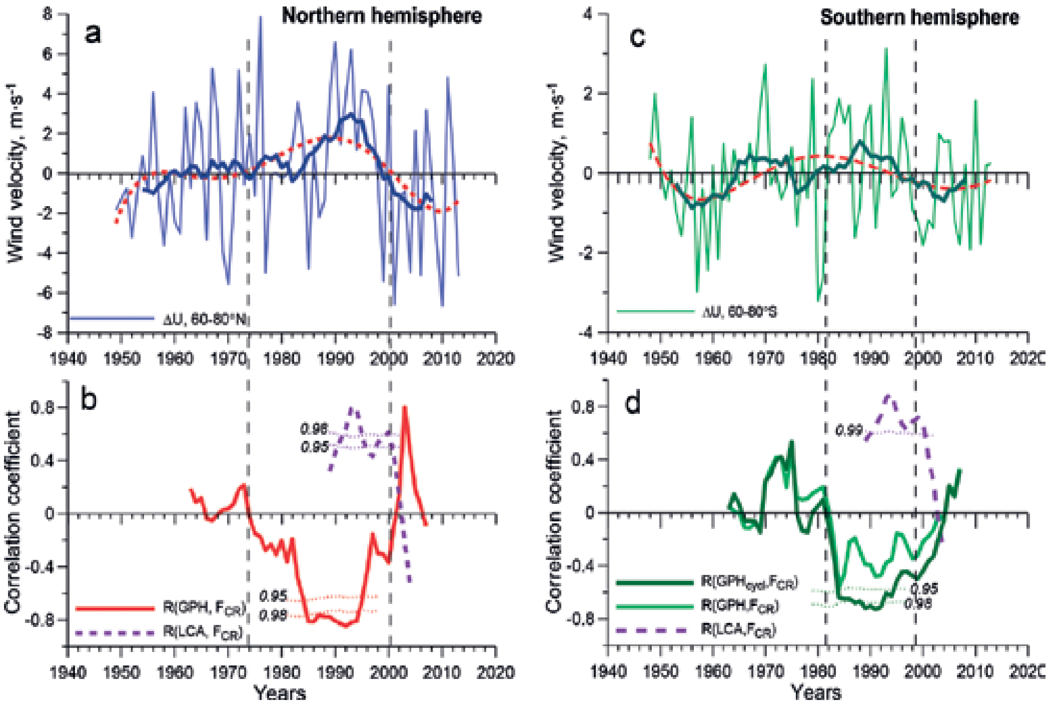

Figure 8. *Top*: Variations of mean zonal velocity of western winds (the U-component) at the stratospheric level 50 hPa in the belt 60–80° for cold months in the Northern (a) and Southern (c) hemispheres. Thick lines show 11-year running averages and polynomial fits. *Bottom*: Correlation coefficients for sliding 11-year intervals between LCA and GCR fluxes (dashed lines), GPH700 anomalies and GCR fluxes (solid lines) in the Northern (b) and Southern (d) hemispheres. Dotted lines show the significance levels of the correlation coefficients. The period of an enhanced vortex is marked by vertical dashed lines.

From the middle 1980s to the middle 1990s the polar vortices in both hemispheres were enhanced. The vortex enhancement was the most prominent in the Northern hemisphere, the wind velocity increasing up to 4–7 m.s^{-1} relative to the trend values. This agrees well with the data [62] showing no strong sudden stratospheric warming destroying the vortex in the indicated period. The vortex in the Southern hemisphere is more stable than that in the Northern one; however, we can also see a noticeable increase in wind velocity. The data in **Figure 8** show that in the period of the vortex enhancement most statistically significant correlations between pressure (cyclonic intensity) and GCR fluxes, as well as between low clouds and GCR fluxes take place. In the late 1990s both the vortices and the correlations GPH–GCR and LCA–GCR in both hemispheres started weakening. A sharp decrease of the wind velocities resulting in the vortex transition to its weak state occurred near 2000 in both hemispheres. The reversal of correlation coefficients under study coincided well with the transition of the vortices to a weak state. Thus, the presented data allow suggesting that the violation of the correlation between low cloudiness and GCR intensity detected on the decadal scale is closely related to the change of the polar vortex strength.

The results of this study confirm that the changes of the atmosphere state, in particular, of the intensity of the stratospheric polar vortex, may be a real reason for the observed temporal variability of solar-atmospheric links. Indeed, sign reversals of correlation links between troposphere pressure in the Northern hemisphere and sunspot numbers during the twentieth century coincided with the changes in the evolution of the large-scale circulation, which, in turn, were associated with the polar vortex transitions from one state to another [42, 43]. A roughly 60-year periodicity was revealed in the vortex strength, the phases of the Arctic Oscillation being used as a proxy of the vortex intensity [43], which is consistent with a similar periodicity found earlier in correlation links between pressure at extratropical latitudes and sunspot numbers [42]. Thus, the data presented in this study revealed the next change of the vortex state, which resulted in the reversal of correlation links between atmosphere characteristics and phenomena associated with solar activity.

The detected modulation of long-term solar activity/GCR effects on troposphere dynamics by the polar vortex state seems to be due to its role in troposphere-stratosphere coupling via planetary waves. As it was said above, the stratosphere may influence the troposphere only under a strong vortex regime when planetary waves are reflected back to the troposphere. Hence, a strong vortex regime seems to be more favorable to transfer a signal produced in the polar stratosphere by GCRs (or other solar activity phenomena) to the troposphere, as changes in the vortex formation region may influence its intensity and, then, conditions for propagation of planetary waves. Indeed, we can see that GCR effects on cyclonic activity are most pronounced under a strong vortex (see **Figures 6** and **8**) that agrees well with the previous data [42]. Thus, the results of this study provide new evidence for an important part of the polar vortex in the mechanism of solar activity/GCR influence on the troposphere dynamics on the decadal and longer time scales.

Let us note a favorable location of the vortex for GCR effects on the lower atmosphere. The vortex is formed in the region of low geomagnetic cutoff rigidities (R_c < 2–3 GV) that allows particles with a broad energy range to precipitate, including low-energy GCR component which is strongly modulated by solar activity. Wind velocities in the vortex reach maximal values at the heights ~20–30 km where the maximum of the transition curve is observed [63]. This height range also involves the layer of stratospheric aerosols consisting mainly of water solution of sulfuric acid (the Junge layer) (for example, [64]). This creates conditions for influence of ionization changes on aerosol formation which, in turn, may influence the radiative-thermal balance and temperature in the stratosphere and, as a result, the vortex characteristics.

We should also stress that the data presented above do not imply a lack of GCR influence on microphysical processes in clouds. However, they suggest that the formation of cloud-GCR correlation links differs depending on the time scale. GCR variations may influence nucleation rates and growth of particles in clouds according to IMN and/or electric mechanisms [3–11], but this influence may be detected only on rather short time scales (from hours to several days) until the response of atmosphere dynamics to radiative forcing of cloud changes enhances or weakens initial microphysical effects. On longer time scale direct effects of GCRs on cloud formation are masked by more powerful indirect effects through circulation changes associated with GCR variations, these indirect effects depending on the polar vortex state. Taking into account this suggestion, the violation of cloud-GCR correlation links detected near 2000 may be explained.

http://dx.doi.org/10.5772/intechopen.75428

4. Conclusion

The question of cloud-GCR links remains controversial and requires new studies, both experimental and theoretical, to evaluate a real contribution of galactic cosmic rays to solar activity influence on the Earth's climate. The data presented in this chapter show that possible links between clouds and GCR variations on the decadal and longer time scales could involve not only direct (microphysical) effects, but mostly indirect ones mediated by circulation changes. This should be taken into account when considering long-term GCR effects on the cloudiness state.

An important part in the formation of long-term GCR effects on cloud cover at extratropical latitudes seems to be played by the stratospheric polar vortex. The state of the vortex controls the stratosphere-troposphere coupling creating more favorable conditions for GCR influence on extratropical cyclonic activity and, consequently, on cloud cover under a strong vortex regime. In this connection, a high positive correlation of low cloudiness and GCR variations in the 1980s–1990s, which was the period of a strong vortex, may be explained by a pronounced intensification of extratropical cyclones associated with GCR increases in the minima of the 11-year solar cycle. A sharp change of the vortex state near 2000 both in the Northern and Southern hemispheres altered the character of GCR effects on cyclone evolution and, thus, resulted in a violation of cloud-GCR correlation links observed earlier under strong vortex conditions.

Author details

Svetlana Veretenenko[1]*, Maxim Ogurtsov[1], Markus Lindholm[2] and Risto Jalkanen[2]

*Address all correspondence to: s.veretenenko@mail.ioffe.ru

1 Ioffe Institute, Sankt-Petersburg, Russia

2 Natural Resources Institute, Finland

References

[1] Harrison EF, Minnis P, Barkstrom BR, Ramanathan V, Cess RD, Gibson GG. Seasonal variation of cloud radiative forcing derived from the earth radiation budget experiment. Journal of Geophysical Research. 1990;**95**:18687-18703. DOI: 10.1029/JD095iD11p18687

[2] Ardanuy PE, Stowe LL, Gruber A, Weiss M. Shortwave, longwave, and net cloud-radiative forcing as determined from Nimbus 7 observations. Journal of Geophysical Research. 1991;**96**:18537-18549. DOI: 10.1029/91JD01992

[3] Dickinson RE. Solar variability and the lower atmosphere. Bulletin of the American Meteorological Society. 1975;**56**:1240-1248. DOI: 10.1175/1520-0477(1975)056<1240:SVATLA>2.0.CO;2

[4] Yu F, Turco RP. Ultrafine aerosol formation via ion-mediated nucleation. Geophysical Research Letters. 2000;**27**:883-886. DOI: 10.1029/1999GL011151

[5] Yu F, Turco RP. From molecular clusters to nanoparticles: The role of ambient ionization in tropospheric aerosol formation. Journal of Geophysical Research. 2001;**106**:4797-4814. DOI: 10.1029/2000JD900539

[6] Carslaw KS, Harrison RG, Kirkby J. Cosmic rays, clouds and climate. Science. 2002;**298**: 1732-1737. DOI: 10.1126/science.1076964

[7] Kazil J, Lovejoi ER. Tropospheric ionization and aerosol production: A model study. Journal of Geophysical Research. 2004;**109**:D19206. DOI: 10.1029/2004JD004852

[8] Tinsley BA. The global atmospheric electric circuit and its effects on cloud microphysics. Reports on Progress in Physics. 2008;**71**:66801-66900. DOI: 10.1088/0034-4885/71/6/066801

[9] Tinsley BA. A working hypothesis for connections between electrically-induced changes in cloud microphysics and storm vorticity, with possible effects on circulation. Advances in Space Research. 2012;**50**:791-805. DOI: 10.1016/j.asr.2012.04.008

[10] Tinsley BA, Deen GW. Apparent tropospheric response to MeV-GeV particle flux variations: A connection via electrofreezing of supercooled water in high-level clouds? Journal of Geophysical Research. 1991;**96**:22283-22296. DOI: 10.1029/91JD02473

[11] Tinsley BA. Influence of solar wind on the global electric circuit, and inferred effects on cloud microphysics, temperature, and dynamics in the troposphere. Space Science Reviews. 2000;**94**:231-258. DOI: 10.1023/A:1026775408875

[12] Pudovkin MI, Veretenenko SV. Cloudiness decreases associated with Forbush-decreases of galactic cosmic rays. Journal of Atmospheric and Solar-Terrestrial Physics. 1995;**57**: 1349-1355. DOI: 10.1016/0021-9169(94)00109-2

[13] Veretenenko SV, Pudovkin MI. Effects of the galactic cosmic ray variations on the solar radiation input in the lower atmosphere. Journal of Atmospheric and Solar-Terrestrial Physics. 1997;**59**:1739-1746. DOI: 10.1016/S1364-6826(96)00183-6

[14] Svensmark H, Friis-Christensen E. Variations of cosmic ray flux and global cloud coverage – A missing link in solar–climate relationships. Journal of Atmospheric and Solar-Terrestrial Physics. 1997;**59**:1225-1232. DOI: 10.1016/S1364-6826(97)00001-1

[15] Rossow WB, Cairns B. Monitoring changes of clouds. Climatic change. 1995;**31**:175-217. DOI: 10.1007/BF01095151

[16] Svensmark H. Influence of cosmic rays on Earth's climate. Physical Review Letters.1998; **81**:5027-5030. DOI: 10.1103/PhysRevLett.81.5027

[17] Kernthaler SC, Toumi R, Haigh JD. Some doubts concerning a link between cosmic ray fluxes and global cloudiness. Geophysical Research Letters. 1999;**26**:863-865. DOI: 10.1029/1999GL900121

[18] Gierens K, Ponater M. Comment on "Variations of cosmic ray flux and global cloud coverage – A missing link in solar–climate relationships" by H. Svensmark, E. Friis-Christensen (1997). Journal of Atmospheric and Solar-Terrestrial Physics. 1999;**61**:795-797. DOI: 10.1016/S1364-6826(99)00040-1

[19] Jørgensen TS, Hansen AW. Comments on "Variation of cosmic ray flux and global cloud coverage – A missing link in solar-climate relationships" by Henrik Svensmark and Eigil Friis-Christensen. Journal of Atmospheric and Solar-Terrestrial Physics. 2000;**62**:73-77. DOI: 10.1016/S1364-6826(99)00106-6

[20] Marsh N, Svensmark H. Low cloud properties influenced by cosmic rays. Physical Review Letters. 2000;**85**:5004-5007. DOI: 10.1103/PhysRevLett.85.5004

[21] Marsh N, Svensmark H. Cosmic rays, clouds, and climate. Space Science Reviews. 2000;**94**:215-230. DOI: 10.1023/A:1026723423896

[22] Gray LJ, Beer J, Geller M, Haigh JD, Lockwood M, Matthes K, et al. Solar influences on climate. Reviews in Geophysics. 2010;**48**:RG4001. DOI: 10.1029/2009RG000282

[23] Ogurtsov M, Lindholm M, Jalkanen R. Global warming – Scientific facts, problems and possible scenarios. In: Tarhule A, editor. Climate Variability – Regional and Thematic Patterns. Croatia, Rijeka: InTech; 2013. pp. 75-103. DOI: 10.5777/56077

[24] Sloan T, Wolfendale AW. Testing the proposed causal link between cosmic rays and cloud cover. Environmental Research Letters. 2008;**3**:024001. DOI: 10.1088/1748-9326/3/2/024001

[25] Erlykin AD, Wolfendale AW. Cosmic ray effects on cloud cover and their relevance to climate change. Journal of Atmospheric and Solar-Terrestrial Physics. 2011;**73**:1681-1686. DOI: 10.1016/j.jastp2011.03.001

[26] Svensmark H, Bondo T, Svensmark J. Cosmic ray decreases affect atmospheric aerosols and clouds. Geophysical Research Letters. 2009;**36**:L15101. DOI: 10.1029/2009GL038429

[27] Todd M, Kniveton DR. Changes of cloud cover associated with Forbush decreases of galactic cosmic rays. Journal of Geophysical Research. 2001;**106**:32031-32042. DOI: 10.1029/2001JD000405

[28] Todd M, Kniveton DR. Short-term variability in satellite-derived cloud cover and galactic cosmic rays: An update. Journal of Atmospheric and Solar-Terrestrial Physics. 2004;**66**:1205-1211. DOI: 10.1016/j.jastp.2004.05.002

[29] Laken BA, Kniveton DR. Forbush decreases and Antarctic cloud anomalies in the upper troposphere. Journal of Atmospheric and Solar-Terrestrial Physics. 2011;**73**:371-376. DOI: 10.1016/j.jastp.2010.03.008

[30] Laken BA, Kniveton DR, Frogley MR. Cosmic rays linked to rapid mid-latitude cloud changes. Atmospheric Chemistry and Physics. 2010;**10**:10941-10948. DOI: 10.5194/acp-10-10941-2010

[31] Čalogović J, Albert C, Arnold F, et al. Sudden cosmic ray decreases: No change of global cloud cover. Geophysical Research Letters. 2010;**37**:L03802. DOI: 10.1029/2009GL041327

[32] Krissansen-Totton J, Davies R. Investigation of cosmic ray–cloud connections using MISR. Geophysical Research Letters. 2013;**40**:5240-5245. DOI: 10.1002/grl.50996

[33] Kristjánsson JE, Staple A, Kristiansen J, Kaas E. A new look at possible connections between solar activity, clouds and climate. Geophysical Research Letters. 2002;**29**:2107-2111. DOI: 10.1029/2002GL015646

[34] Kristjánsson JE, Kristiansen J, Kaas E. Solar activity, cosmic rays, clouds and climate – An update. Advances in Space Research. 2004;**34**:407-415. DOI: 10.1016/j.asr.2003.02.040

[35] Voiculescu M, Usoskin I, Mursula K. Different response of clouds at the solar input. Geophysical Research Letters. 2006;**33**:L21802. DOI: 10.1029/2006GL027820

[36] Voiculescu M, Usoskin I. Persistent solar signatures in cloud cover: Spatial and temporal analysis. Environmental Research Letters. 2012;**7**:044004. DOI: 10.1088/1748-9326/7/4/044004

[37] Voiculescu M, Usoskin I, Condurache-Bota S. Clouds blown by the solar wind. Environmental Research Letters. 2013;**8**:045032. DOI: 10.1088/1748-9326/8/4/045032

[38] Kirkby J, Curtius J, Almeida J, et al. Role of sulfuric acid, ammonia and galactic cosmic rays in atmospheric aerosol nucleation. Nature. 2011;**476**:429-435. DOI: 10.1038/nature10343

[39] Dunne EM, Gordon H, Kurten A, et al. Global atmospheric particle formation from CERN CLOUD measurements. Science. 2016;**354**:1119-1124. DOI: 10.1126/science.aaf2649

[40] Almeida J, Schobesberger S, Kurten A, et al. Molecular understanding of sulphuric acid-amine particle nucleation in the atmosphere. Nature. 2013;**502**:359-363. DOI: 10.1038/nature12663

[41] Svensmark H, Enghoff MB, Pedersen JOP. Response of cloud condensation nuclei (>50 nm) to changes in ion-nucleation. Physics Letters A. 2013;**377**:2343-2347. DOI: 10.1016/j.physleta.2013.07.004

[42] Veretenenko S, Ogurtsov M. Regional and temporal variability of solar activity and galactic cosmic ray effects on the lower atmosphere circulation. Advances in Space Research. 2012;**49**:770-783. DOI: 10.1016/j.asr.2011.11.020

[43] Veretenenko S, Ogurtsov M. Stratospheric polar vortex as a possible reason for temporal variations of solar activity and galactic cosmic ray effects on the lower atmosphere circulation. Advances in Space Research. 2014;**54**:2467-2477. DOI: 10.1016/j.asr.2013.09.001

[44] Vorobjev VI. Synoptic Meteorology. Leningrad: Gidrometeoizdat; 1991 (in Russian) 616 p

[45] NASA Earth Observatory. Available from: https://earthobservatory.nasa.gov

[46] Rossow WB, Walker AW, Beuschel DE, Roiter MD, et al. International Satellite Cloud Climatology Project (ISCCP): Documentation of New Cloud Datasets. WMO/TD-737. Geneva: World Meteorological Organization; 1996. 115 p

[47] ISCCP: International Satellite Cloud Climatology Project. Available from: https://isccp.giss.nasa.gov/pub/data/D2CLOUDTYPES/

[48] Chernokulsky AV, Mokhov II. Intercomparison of global and zonal cloudiness characteristics from different satellite and ground-based data. Earth's Research from Space. 2010;**3**:12-29 (in Russian)

[49] Evan AT, Heidinger AK, Vimont DJ. Arguments against a physical long-term trend in global ISCCP cloud amounts. Geophysical Research Letters. 2007;**34**:L04701. DOI: 10.1029/2006GL028083

[50] Ebisuzaki W. A method to estimate the statistical significance of a correlation when the data are serially correlated. Journal of Climate. 1997;**10**:2147-2153. DOI: 10.1175/1520-0442(1997)010<2147:AMTETS>2.0.CO;2

[51] Mitchell Jr JM, Stockton CW, Meko DM. Evidence of a 22-year rhythm of drought in the western United States related to the Hale solar cycle since the 17th century. In: McCormac BM, Seliga TA, editors. Solar–Terrestrial Influences on Weather and Climate. New York: D. Reidel; 1979. pp. 125-143. DOI: 10.1007/978-94-009-9428-7

[52] Raspopov OM, Dergachev VA, Kolström T. Hale cyclicity of solar activity and its relation to climate variability. Solar Physics. 2004;**224**:445-463. DOI: 10.1007/s11207-005-5251-8

[53] Veretenenko SV, Dergachev VA, Dmitriev PB. Solar activity and cosmic ray variations as a factor of intensity of cyclonic processes at midlatitudes. Geomagnetism and Aeronomy. 2007;**47**:375-382. DOI: 10.1134/S0016793207030152

[54] Stozhkov YI, Svirzhevsky NS, Bazilevskaya GA, Kvashnin AN, Makhmutov VS, Svirzhevskaya AK. Long-term (50 years) measurements of cosmic ray fluxes in the atmosphere. Advances in Space Research. 2009;**44**:1124-1137. DOI: 10.1016/j.asr.2008.10.038

[55] Kalnay E, Kanamitsu M, Kistler R, et al. The NCEP/NCAR 40-year reanalysis project. Bulletin of the American Meteorological Society. 1996;**77**:437-472. DOI: 10.1175/1520-0477(1996)077<0437:TNYRP>2.0.CO;2

[56] Herman JR, Goldberg RA. Sun, Weather, and Climate. Washington, DC: NASA Scientific and Technical Information Branch; 1978. 360 p

[57] Minobe SA. 50-70 year oscillation over the North Pacific and North America. Geophysical Research Letters. 1997;**24**:683-686. DOI: 10.1029/97GL00504

[58] Gudkovich ZM, Karklin VP, Smolyanitskii VM, Frolov IE. On the character and causes of the Earth's climate change.Problems of the Arctic and Antarctic. 2009;**81**(1):15-23 (in Russian)

[59] Baldwin MP, Dunkerton TJ. Stratospheric harbingers of anomalous weather regimes. Science. 2001;**294**:581-584. DOI: 10.1126/science.1063315

[60] Avdushin SI, Danilov AD. The sun, weather and climate: A present-day view of the problem (review). Geomagnetism and Aeronomy. 2000;**40**:545-555

[61] Perlwitz J, Graf H-F. Troposphere-stratosphere dynamic coupling under strong and weak polar vortex conditions? Geophysical Research Letters. 2001;**28**:271-274. DOI: 10.1029/2000GL012405

[62] Ivy DJ, Solomon S, Thompson DW. On the identification of the downward propagation of Arctic stratospheric climate change over recent decades. Journal of Climate. 2004;**27**:2789-2799. DOI: 10.1175/JCLI-D-13-00445.s1

[63] Bazilevskaya GA, Krainev MB, Makhmutov VS. Effects of cosmic rays on the Earth's environment. Journal of Atmospheric and Solar-Terrestrial Physics. 2000;**62**:1577-1586. DOI: 10.1016/S1364-6826(00)00113-9

[64] Pruppacher HR, Klett JD. Microphysics of Clouds and Precipitation. 2nd ed. Dordrecht: Springer; 2010. 954 p. DOI 10.1007/978-0-306-48100-0

Chapter 6

Cosmic Ray Cradles in the Galaxy

Mehmet Guenduez, Julia Becker Tjus,
Björn Eichmann and Francis Halzen

Additional information is available at the end of the chapter

http://dx.doi.org/10.5772/intechopen.75429

Abstract

The search for the origin of high-energy cosmic rays has made significant progress in the past decade. By including multi-messenger methods, the general picture of the presence of a galactic component at low energies and an extragalactic one at the highest energies has been strengthened. Yet, unambiguous proof of the exact origins of cosmic rays is still missing. This chapter will review localized regions in the galaxy, which, due to their high nonthermal emission, are likely cosmic ray cradles. What we can learn from combining theoretical modeling with multi-messenger observations of regions like the Cygnus X complex, the Eta Carinae, and the Galactic Center region will be discussed. How the investigation of such localized regions in the Milky Way will help to resolve the more than 100-year-old question: *what is the origin of cosmic rays?* will be reviewed.

Keywords: cosmic rays, supernova remnants, Cygnus X complex, Galactic Center

1. Introduction

Galactic cosmic rays (GCRs) are defined as originating from outside our solar system but inside of the Milky Way. The cosmic ray (CR) spectrum in the range of ~ 10 GeV and 10^{15} eV and possibly beyond is believed to originate from the Milky Way. One of the main arguments for this hypothesis concerns the energy budget needed to produce the CR spectrum above $\sim$GeV energies, which cannot be reproduced by extragalactic sources but in particular by supernova remnants (SNRs) in the Milky Way [1]. The shock fronts of SNRs are well suited to accelerate charged particles via diffusive shock acceleration, which is another indication that SNRs work well as a particle accelerator. However, it is not clear yet how SNRs can reach the 10^{15} eV that is needed to reach the first kink in the CR spectrum, the so-called *cosmic ray knee*. Other sources like binary systems or pulsars could accelerate to even higher energies than

IntechOpen

© 2018 The Author(s). Licensee IntechOpen. This chapter is distributed under the terms of the Creative Commons Attribution License (http://creativecommons.org/licenses/by/3.0), which permits unrestricted use, distribution, and reproduction in any medium, provided the original work is properly cited.

10^{15} eV. On the other hand, their total energy budget does not suffice to reproduce the intensity of the CR spectrum at Earth. In order to resolve the question of the origin of GCRs, nonthermal emission of photons and neutrinos can be investigated. Low-energy photons (in the radio to X-ray regime) comes from acceleration of electrons that suffer from synchrotron radiation and can thus be used to estimate the electron spectrum in dependence on the local magnetic field of the sources (see, e.g., [2] and references therein). High-energy photons can come from hadronic interactions via the production of neutral pions or leptonic processes like inverse Compton scattering or bremsstrahlung. This makes the interpretation of the signatures a challenge. The identification of galactic sources in neutrinos would help to identify the hadronic parts of the gamma spectrum, as neutrinos are co-produced with hadronic gamma rays via the decay of charged pions that are created in hadronic interactions. While a flux of astrophysical high-energy neutrinos has been detected for the first time in 2012 by IceCube [3], due to the low statistic of neutrinos, it is not resolved at the moment in which sources contribute to this diffuse flux. Thus, a combination of theoretical models with multi-messenger observations—also taking into account thermal and line emission signatures—is crucial to deduce information about the CRs and thus their formation process. It is advantageous to consider as much various measurements as possible to constrict the space of variation of the theoretical models. Once the various spectra and the ambient conditions from a potential CR object are known, we can constrict the source geometry, the radiating processes, and the properties of the attended CRs. In the next decades, as soon as we achieve the desired sensitivity for measuring neutrinos, the revelation of the origin of CRs is only a question of time. Theoretical predictions can lead the way to the first identification of the origin of GCRs. In this context, star-forming regions are crucial for the understanding of cosmic ray cradles, as all potential sources are correlated with star formation (or rather the dead of massive stars, which correlates with star formation). In this review, we therefore focus on recent results that could be achieved from the measurement and theoretical modeling of extended regions of CR emission and interaction. We will focus on the Cygnus region, the Galactic Center region, and the Eta Carinae region. In order to understand the connection between star formation and CRs, different correlations between wavelength bands can be investigated. In particular, such regions reveal a correlation between radio and far-infrared emission, as well as between radio and gamma-ray emission. In the introduction, we will review these correlations that are best established for starburst galaxies but exist locally in star-forming regions as well. Hereafter, Chapter 2 will focus on the general ansatz to describe CR transport and interaction in these extended regions. Chapter 3 will review the state of the art concerning measurements and modeling of the nonthermal emission regions Cygnus X, Eta Carinae, and Galactic Center.

1.1. FIR-radio, radio-gamma, and gamma-neutrino correlations

The first FIR-radio correlation was discovered in Seyfert galaxy nuclei by van der Kruit (1971). A general linear correlation for starburst galaxies was first discussed by Helou et al. [4]. Many attempts have been made to understand the proportionality between radio and far infrared. On the basis of rather simple modeling of galactic evolution, a strong correlation is actually expected, since both supernova remnants and the dominant heating by ultraviolet light from massive stars derive from the same stellar population [5, 6]. Using such models, the far-infrared

http://dx.doi.org/10.5772/intechopen.75429

luminosity of NGC2146 was predicted by [7], which is now observationally supported by IRAS observations [8]. The correlation as seen in the data was first clearly stated by [9] and subsequently discussed at some length by many authors; see, e.g., [10–12].

An extensive attempt to interpret the correlation was made by Völk and collaborators [13]. Here, the electrons lose all energy and therefore, the correlation is calorimetric. The model works quite well when considering the total energy budget, but it has some difficulties in explaining the observation of flat radio spectra also holding on small scales, which is not in concordance with the loss-dominated model. The solution of a spatial mixture of cutoffs would still allow for a locally loss-dominated scenario. Most recently, it was discussed that the nonthermal electrons that produce the synchrotron signatures are not those primarily co-accelerated with the hadrons but that they dominantly come from charged pion decays, which change the energetics of the problem [14].

Independent on the exact interpretation of the FIR-radio correlation, it indicates the coupling of particle acceleration (visible in the radio band) to star formation, seen via FIR emission.

The different formation processes and their connection are illustrated in the following **Figure 1**.

As the CR electrons also interact with the ambient photons and lose energy due to inverse Compton scattering, the FIR-radio correlation mainly depends on the average photon and magnetic field according to $q = 1 + U_R/U_B$ where $U_{R,B}$ denotes the averaged energy density of the magnetic field and photon field, respectively [13]. **Figure 2** demonstrates such a correlation.

1.1.1. Radio-gamma correlation

A correlation between radio and gamma emission has been found for a small number of objects that are detected by Fermi and that are expected to be dominated by signatures of star formation [16, 17]. Those objects that form the correlation are M 82, NGC 253, 1068, 4945, the Milky Way, and the Large Magellanic Cloud. Such a linear correlation is striking. First of all,

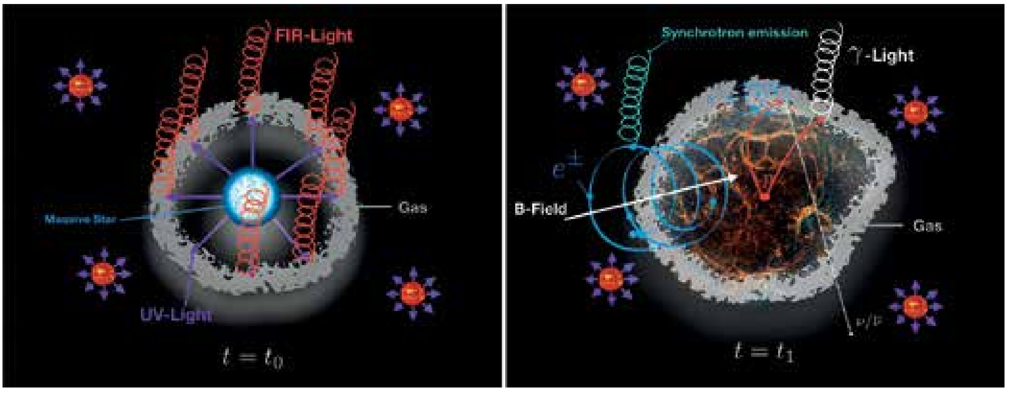

Figure 1. At $t = t_0$: A massive star emits UV radiation which is absorbed by the ambient gas; after that, it releases FIR radiation. At $t = t_1$: The massive star forms into a supernova remnant. The CRs from the SNR interact with the ambient medium and fields. As a result, γ-rays, neutrinos, and synchrotron radiation are produced.

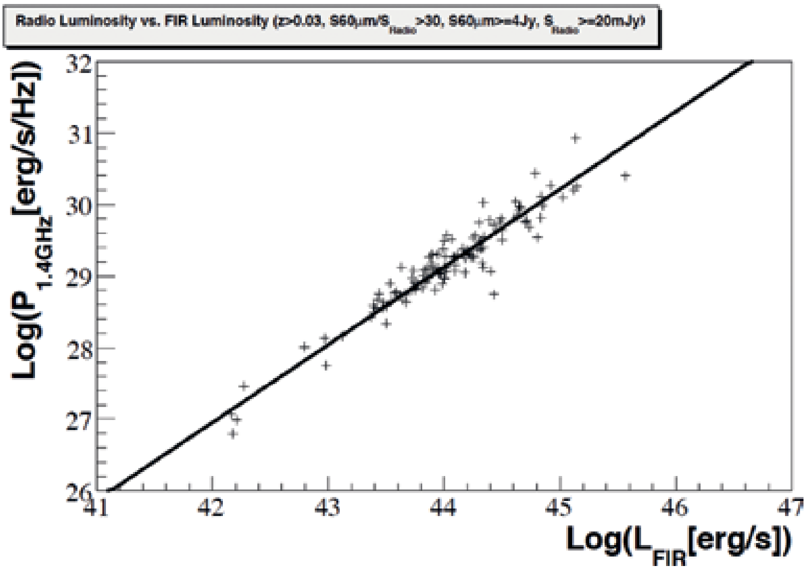

Figure 2. Correlation of L_{FIR} and $L_{\mathrm{Radio,\,1.4GHz}}$. Data from [15].

these are all objects of different sizes and level of star-forming activity. Secondly, gamma-ray emission is expected to be produced via hadronic interactions. Thus, the intensity should scale with the density of the ambient medium. On the other hand, radio emission is due to synchrotron radiation and thus depends on the magnetic field strength. It is therefore not necessarily natural that a linear correlation is established. A correlation between gas density and magnetic field strength, as established for different systems, could account for such an effect. This correlation has been investigated in detail for starburst galaxies by [18, 19].

1.1.2. Gamma-neutrino correlation

A source that is dominated by hadronically produced gamma rays should correlate with the neutrino strength of a source. However, for most regions in the sky, it is not clear if the detected gamma rays are of hadronic or leptonic nature.

The relevance of each process has to be restricted by considering reasonable arguments such as measurements at different energy ranges or neutrino spectra that accompany the γ-ray production due to the hadronic pion production. CR protons generate γ-rays due to the interaction with the ambient gas and CR electrons due to the interaction with an ambient photon field (inverse Compton) and the electromagnetic field of the ambient nucleus (nonthermal bremsstrahlung). All these processes can be formulated stochastically as energy spectra which are included in the integrand formulations of a specific flux. For clarification, all relevant processes for γ production and useful correlations are illustrated in **Figure 3**. As CR electrons and protons from a unique source, they can be correlated according to a quasi-neutral plasma, or in our galaxy (see [20] for a discussion), the relation of nonthermal radio and γ-ray emission is

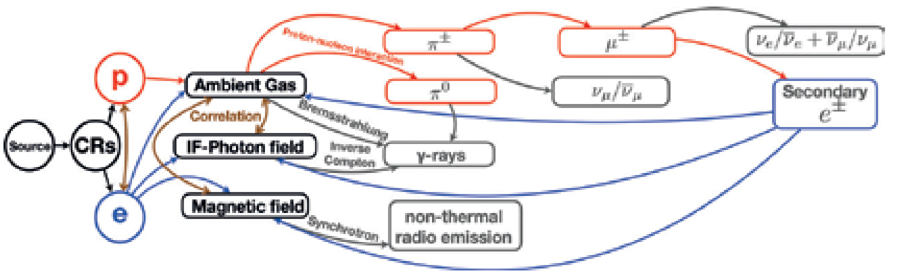

Figure 3. An illustration of the relation in star-forming regions and all relevant astrophysical processes in our galaxy: The red arrow represents the hadronic, the blue arrow the leptonic, and the gray arrow all processes which lead to the generation of radiations that can be measured and correlated. Lastly, the brown arrow illustrates the correlation of different physical quantities.

just a question of completeness of the considered processes which generate γ-rays and synchrotron radiation.

Thus, a gamma-neutrino correlation is based on all generation processes. Though neutrinos can be generated by CR protons, the consideration of leptonic processes is just as well important. Assuming that neutrinos are only produced in the processes illustrated in **Figure 3**, the γ-rays and neutrinos from the same source can easily be correlated. They can be correlated by considering the relevant energy spectra of neutrinos produced at proton-proton interaction following to [21] and by using the same normalization factor as for the γ-ray flux.

1.1.3. Conclusions for nonthermal emission from star-forming regions

In star-forming regions in the Milky Way, it has become obvious in the past decades through detections by Fermi, H.E.S.S., MAGIC, VERITAS, Milagro, and others that high energetic processes are omnipresent. The content of many massive stars leads to a high rate of a supernova explosion which releases high-energy CRs. On the one hand, the UV radiation of the massive stars collides with the high-density dust and generates FIR radiation. On the other hand, the released CR electrons are deflected by the ambient magnetic field which is related to the column density [22] and produce synchrotron radiation. Moreover, the released CR can cause γ-rays according to the processes in **Figure 3**. **Figure 3** illustrated all crucial relations and processes in star-forming region in our galaxy. Considering this relation, it is possible to correlate the FIR emission with synchrotron radiation as well as with γ-ray and neutrino emission. The procedure mentioned above is also illustrated in **Figure 1** (left) where the massive star at time $t = t_0$ sends out UV light that heats the ambient medium, which emits FIR radiation. **Figure 1** (right) exhibits the processes at $t = t_1$, after a supernova explosion, where synchrotron radiation dominates at low energies and hadronic emission together with IC and bremsstrahlung makes up the high-energy part of the energy spectrum.

Therefore, the star-forming regions such as starburst galaxies are natural laboratories for studying the FIR-radio and even radio-gamma or gamma-neutrino correlation as high-energy processes occur in these areas. Also, a correlation between the column density, IF photon field, and the magnetic field has been observed [22]. In total, γ-rays, synchrotron, and FIR emission are reinforced by the high ambient gas density, amount of massive stars, and thus also SNRs. Due to their relation with CRs, the role of star-forming regions becomes of prime importance for the understanding of the origin and propagation of CRs.

2. Modeling nonthermal emission from star-forming regions

The dynamics in a star-forming region can be very complicated. It is therefore often necessary to work by simplifying assumptions which are reasonable and convenient to the relevant conditions. The ability to describe particle transport phenomena is indispensable for predicting processes in star-forming regions. The generic transport equation of the differential cosmic density $n(t, \mathbf{r}, \gamma)$ at a given time t, location $\vec{r}$, and particle Lorentz factor γ is given by [23]:

$$\underbrace{\frac{\partial n(\mathbf{r},\gamma,t)}{\partial t}}_{\text{Temporal Evolution}} \underbrace{-\nabla D(\mathbf{r},\gamma)\nabla n(\mathbf{r},\gamma,t)}_{\text{Spatial Diffusion}} \underbrace{-\frac{\partial}{\partial \gamma} b(\mathbf{r},\gamma) n(\mathbf{r},\gamma,t)}_{\text{Continuous Loss}} + \underbrace{\mathbf{v}\nabla n(\mathbf{r},\gamma,t)}_{\text{Advective Wind}} = \underbrace{Q(\mathbf{r},\gamma,t)}_{\text{CR Source Rate}} \tag{1}$$

Here, $\mathbf{v}$ is the advection velocity; in consideration, it represents the local wind structure that can be created through the density gradient which is present if a star-forming region of high density sits in a lower-density region of the galaxy. The diffusion tensor is denoted by $D(\mathbf{r}, \gamma)$, the continuous momentum loss by $b(\mathbf{r}, \gamma)$, and the source rate by $Q(\mathbf{r}, \gamma, t)$. Depending on the problem under investigation, the range of Eq. (1) can be extended by terms which consider a network of losses of the nuclei via spallation and by collision and decay.

Numerical approaches are helpful and are already performed for the investigation of our galaxy, e.g., by [24] or [25]. From the solution of the transport equation, Eq. (1), the differential cosmic ray density can be calculated. This can be done for hadrons and/or electrons, where different loss processes and source rates need to be considered depending on the species under investigation. The source rate can then be used to model the interaction with the ambient gas, magnetic field, or photon field. From the electron density, synchrotron radiation, inverse Compton emission, and nonthermal bremsstrahlung can be calculated. Focusing on high-energy hadronic processes (π^0, $\pi^\pm$, secondary $e^\pm$, ν; see red lines in **Figure 3**), the resulting fluxes Φ_{p_3} of the generated messenger particle of type p_3 at a distance d to the source are generally given by:

$$\begin{aligned}\Phi_{p_3}\left(E_{p_3}\right) = & \frac{c}{4\pi \cdot d^2} \int_{r_{min}}^{r_{max}} \int_0^{\pi} \int_0^{2\pi} \int_{E_{p3}}^{\infty} N_{p_2}\left(r,\phi,\Theta\right) n_{p_1}\left(E_{p_1}, r, \phi, \Theta\right) \\ & \cdot \frac{\mathrm{d}\sigma_{p_1,p_2}\left(E_{p_1}\right)}{\mathrm{d}E} \cdot F_{p_3}\left(\frac{E_{p_3}}{E_{p_2}}, E_{p_1}\right) \frac{\mathrm{d}E_{p_1}}{E_{p_2}} \ \sin(\Theta) \ d\Theta \ \ \mathrm{d}\phi \ \ r^2 \ \ \mathrm{d}r.\end{aligned} \tag{2}$$

Here, the specification is done by considering the cross sections σ_{p_1,p_2}, the energy spectra, F_{p_3}, e.g., from [21], and the reactant distribution N_{p_2}, where p_1 is an index that indicates the primary particle species (CRs, either protons or electrons) and the index p_2 relates to properties connected to the ambient reactant (photon field, magnetic field, or matter). Note that we suppose that all generated particles can escape free from the region of interest, i.e.:

$$1 \gg \tau_{p_1,p_2}\left(E_{p_1}\right) = \int_{r_{min}}^{r_{max}} \int_{f\left(E_{p_1}\right)}^{\infty} \sigma_{p_1,p_2}\left(E_{p_1}, E_{p_2}\right) \cdot n_{p_1}\left(E_{p_2}, r\right) \mathrm{d}r \, \mathrm{d}E_{p_2}, \tag{3}$$

with the minimum energy $f\left(E_{p_1}\right)$ of particle p_1 to interact inelastically with particle p_2. For the nonthermal Bremsstrahlung production, the flux simplifies and is given by:

$$\begin{aligned} \Phi_{\mathrm{BR}}\left(E_\gamma\right) = \frac{\left(m_p \cdot c\right)^{-1}}{4\pi \cdot d^2} \int_{r_{min}}^{r_{max}} \int_0^{\pi} \int_0^{2\pi} \int_{E_\gamma}^{\infty} N_t(r, \phi, \Theta) \, \frac{\sigma_{Br}}{E_\gamma} \\ \cdot n_e\left(E_e, r, \phi, \Theta\right) \mathrm{d}E_e \sin(\Theta) \; d\Theta \;\; \mathrm{d}\phi \;\; r^2 \;\; \mathrm{d}r \end{aligned} \tag{4}$$

with the bremsstrahlung cross section $\sigma_{Br} \simeq 3.38 \cdot 10^{-26}$ cm^2 and the proton target density N_t. The flux contributed by the inverse Compton (IC) process can be written as:

$$\begin{aligned} \Phi_{\mathrm{IC}}\left(E_\gamma\right) = \frac{3}{4} \frac{c \cdot \left(m_p \cdot c^2\right)}{4\pi \cdot d^2} \int_{r_{min}}^{r_{max}} \int_0^{\pi} \int_0^{2\pi} \int_{E_{min}}^{\infty} \int_0^{\infty} \frac{N_{IR}\left(\varepsilon, r, \phi, \Theta\right)}{\varepsilon} \\ \cdot \sigma_T \cdot n_e\left(E_e, r, \phi, \Theta\right) \frac{F\left(E_e, E_\gamma\right)}{E_e^2} \mathrm{d}E_e \, \mathrm{d}\varepsilon \sin(\Theta) \, d\Theta \;\; \mathrm{d}\phi \;\; r^2 \;\; \mathrm{d}r \end{aligned} \tag{5}$$

Here, σ_T denotes the Thomson cross section, N_{IR} the differential photon density, $F\left(E_e, E_\gamma\right)$ the Klein-Nishina related function, and $E_{min} = E_\gamma / \left(2m_e \cdot c^2\right) + \left(E_\gamma / (4\varepsilon)\right)^{1/2}$ the lower integration limit [26].

For the low-energy photon emission, the spectrum of synchrotron radiation can be derived by considering the total radiated power, which is performed isotropically; see [27] and references therein:

$$\begin{aligned} \Phi_{syn}(\nu) = \frac{P_0}{4\pi d^2} \left(\frac{\nu}{\nu_s}\right)^{1/3} \int_{r_{min}}^{r_{max}} \int_0^{\pi} \int_0^{2\pi} \int_{\gamma_{min}^e}^{\gamma_{max}^e} d\gamma \, \gamma^{-\frac{2}{3}} \\ \cdot n_e(\gamma, r, \phi, \Theta) \exp\left(-\frac{\nu}{\gamma^2 \nu_s}\right) \; \sin(\Theta) \;\; d\Theta \;\; \mathrm{d}\phi \;\; r^2 \;\; \mathrm{d}r, \end{aligned} \tag{6}$$

with $P_0 = 2.65 \cdot 10^{-10} \cdot \left(\frac{B}{1\,G}\right) \mathrm{eVs}^{-1} \mathrm{Hz}^{-1}$ and $\nu_s \simeq 4.2 \cdot 10^6 \left(\frac{B}{1\,G}\right)$ Hz as the characteristic frequency; see [18] and the references therein for the explicit mathematical derivation. While the above equations are in principle valid for an arbitrary region of cosmic ray emission, the adaption of the parameters in the equations, in particular the ambient conditions of the region of interest, is crucial to find a sufficiently accurate solution for the problem of consideration.

One simplifying approach to solve the transport equation, Eq. (1), is the consideration of a contained volume, the so-called leaky box model, where particles leak the volume due to diffusion and advection on the characteristic timescales τ_{diff} and τ_{adv}, respectively. Hence, the diffusion term can be replaced by $-n(\gamma, t)/\tau_{\mathrm{diff}}$ and the advection term by $n(\gamma, t)/\tau_{\mathrm{adv}}$. In doing so, the solution just depends on the complexity of the source function and the continuous losses. Numerical approaches can treat the problem in a higher complexity; the analytical solutions have the advantage of being able to analyze the behavior of the source in more detail.

In the following, we will present three localized regions, which are star-forming regions and deserve an adapted formulation of the CR density.

3. Star-forming regions in the Milky Way and the nonthermal emission

3.1. Cygnus X

Cygnus X is a part of the largest star-forming region of the constellation Cygnus in the northern galactic plane and has a distance of 1.4 kpc from the Earth.

There are many reasons why Cygnus X is an excellent region to investigate the origin of CRs:

- The emission is observable from radio to high-energy gamma-ray frequencies [28], at which in the energy range from GeV up to TeV, Cygnus X has the brightest emission in the northern hemisphere [29].
- Many potential accelerators such as supernova remnants,[1] pulsars, and pulsar wind nebulae can be found. The Milagro detections at $>$ TeV energy point toward a possible hadronic emission scenario as leptonic processes cannot easily reach these energies, while they are natural for hadronic scenarios. IceCube has good visibility of the Cygnus region with muon neutrinos and could thus reveal a possible signal in neutrinos from that direction in the near future [31]. Many of these constituents are pictured in **Figure 4**.
- Cygnus X contains a large number of H_{II} regions [32], indicating a high level of ionization —possibly caused by CRs; see, e.g., [33, 34].

All of these characteristics make Cygnus X a suitable natural laboratory for the astronomer to look beyond the usual constrained view.

The supernova remnant γ Cygni was first investigated using Fermi data, which provide information about the interstellar background by subtracting the radiation from γ Cygni. Cygnus X has a cocoon, in which freshly accelerated CRs are expected to be present, as its thermal emission exceeds 100 GeV. The SNR γ Cygni, which is in the cocoon, could cause the acceleration of protons even up to $80 - 300\,\text{TeV}$ and electrons up to $6 - 30\,\text{TeV}$ [35]. The accelerated particles could fill the whole cocoon if it is assumed that the main transport mechanism is diffusion [35]. Thus, γ Cygni has the potential to be the only accelerator in the cocoon. On the other hand, advection could dominate the transport mechanism, if an anisotropic emission of γ Cygni was observed [35]. Yet, there is still no final proof for this scenario. The cocoon could give hints about the transport mechanism and escape of CRs from their source.

---

[1]For example: γ Cygni J2021.0 + 4031e, which Milagro also detected at very high energies [30].

http://dx.doi.org/10.5772/intechopen.75429

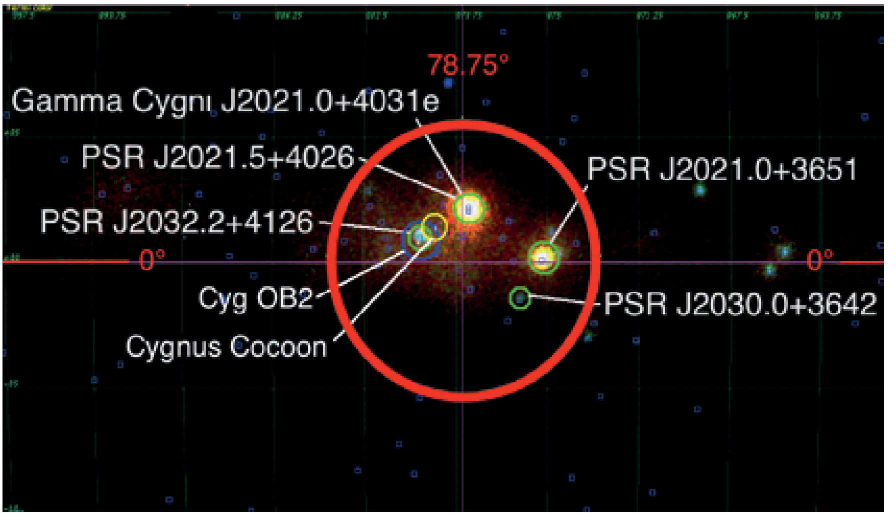

Figure 4. Fermi's color map of Cygnus X (red cycle) distributed by Skyview HEASARC—HEALPixed by CDS; the map was edited with Aladin v9.0. Additionally Cygnus X is pictured by a red cycle.

The modeling of the Cygnus region is based on the transport equation, Eq. (1). In order to solve the equation analytically, an emission from an isotropic and spatially homogeneous distributed part of the Cygnus region in its steady state is assumed. Additionally, a spatially independent diffusion of the particles within Cygnus X is applied. This assumption is reasonable since an extended region with a diameter of 77 pc will be considered, emission outside this zone is negligible, the region is very complex, and small inhomogeneities are expected to vanish at scales larger than the gyroradius. By this ansatz of the combination of a homogeneous injection and a leaky box, the variation of $n(\mathbf{r}, \gamma, t)$ only takes place at the scale of the radius of our region of interest. Using the quasi-neutrality of the plasma, the nonthermal radio and γ-ray emission can be correlated. This model has already been used for different starburst galaxies by [18], and details of the calculation can be found there.

As no accurate data about the ambient conditions are known, the spectral index α, the target density N_t, and the magnetic field B are kept as best-fit parameters which lead to a coincidence between nonthermal radio and γ-ray data and the prediction from the model.

The variated parameters as a function of χ are shown in **Figure 5**.

The continuous and catastrophic losses are essential for the transport within Cygnus X. **Figure 6** compares all relevant losses in Cygnus X for electrons and protons separately.

Hereafter, the different γ-ray and neutrino fluxes, which are caused by different processes as explained in **Figure 3**, can be calculated separately according to Eq. (2) and by considering the related CR density distribution in Eq. (1). The agreement between γ-ray, synchrotron emission, and the model can be seen by the following spectra.

The left spectrum of **Figure 7** displays the γ-ray flux considering leptonic as well as hadronic processes where the CR density has been derived for a homogeneous distribution in its steady

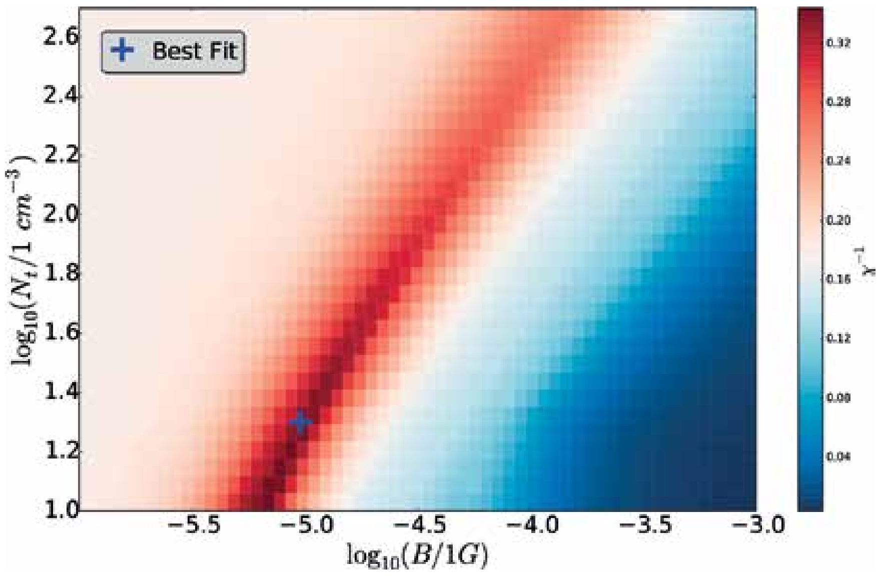

Figure 5. The total deviation χ^2 from the γ-ray and nonthermal radio data as a function of the magnetic field B and target density N_t. The best-fit parameters are represented by "+".

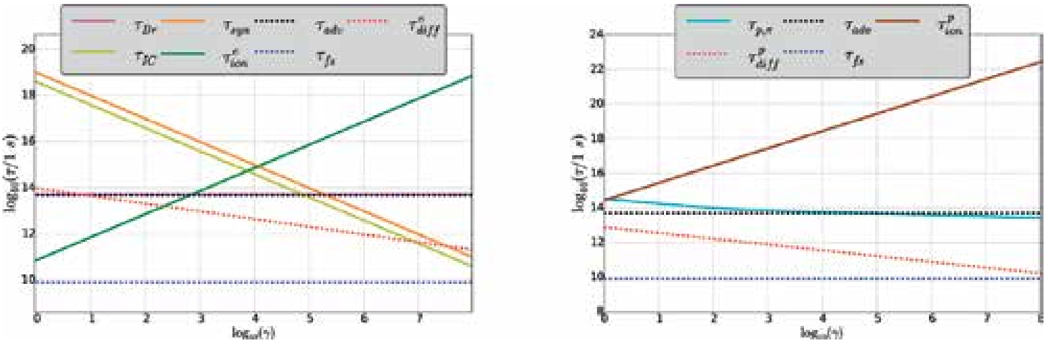

Figure 6. Continuous timescales (solid lines) and catastrophic timescales (dashed lines) for electrons (left) and protons (right) as a function of the Lorentz factor γ considering the best-fit parameters $\alpha = 2.4$, $N_t = 19.4\,\mathrm{cm}^{-3}$, and $B = 9 \times 10^{-6}\,\mathrm{G}$. Here, $\tau_{fs} = R/c$ denotes the timescale of a free-streaming particle with the velocity of light c.

state. Here, data from "Integral," "Fermi-LAT," and "ARGO-YBJ" as well as "Milagro" data, were considered. It is of great importance that data from "Integral" were taken into account, as the measurement at MeV energies strongly constraints the nonthermal bremsstrahlung and therefore the leptonic processes. Considering the synchrotron spectrum on the right side, a suitable diffusion coefficient helps to reach the γ-ray flux at 10 MeV and find the desired agreement.

The parameters from these spectra are used to find the neutrino spectrum which is displayed in **Figure 8**.

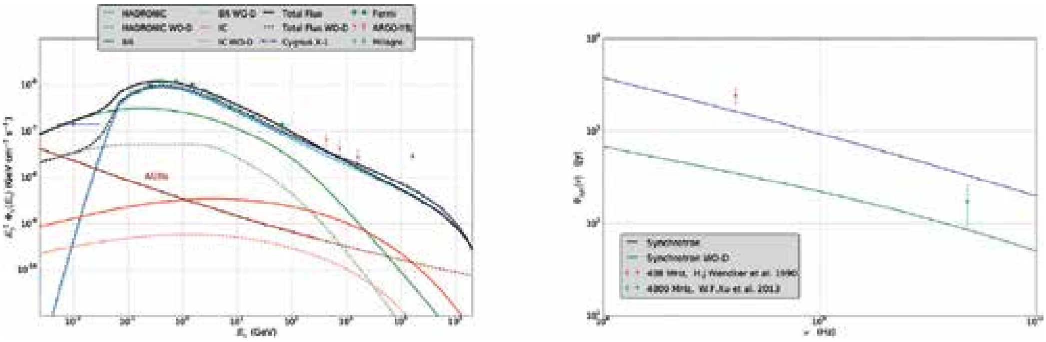

Figure 7. Synchrotron and γ-ray energy spectrum with and without (WO-D) consideration of diffusion; the source rate normalization factor q_0 was fitted on the observed gamma data.

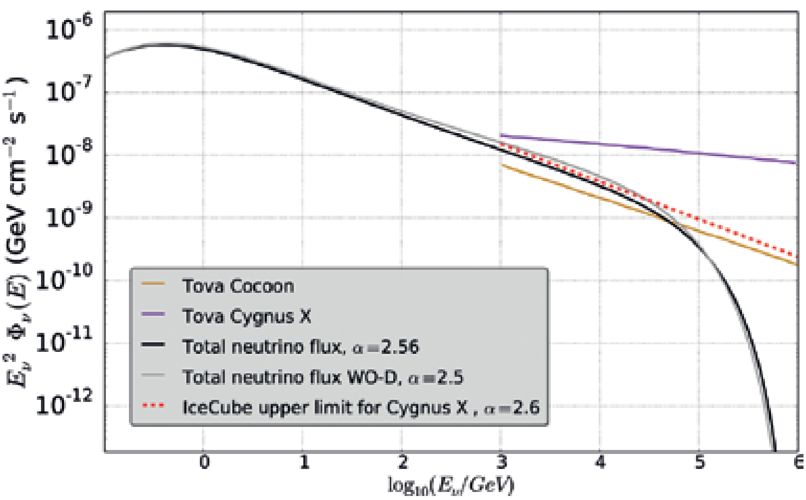

Figure 8. Differential neutrino flux considering new parameters with and without (WO-D) diffusion. A neutrino flux from an alternative model calculated by [36] and IceCube's upper limit calculated for Cygnus X [31] is also displayed.

The influence of the models is evident as Tova et al. [36] suggest a neutrino spectrum from Cygnus X which is most likely not detectable, whereas the model from this work coincides with the limit of IceCube. Additionally, in **Figure 8** the neutrino spectrum from Cygnus Cocoon is displayed, which has relatively a high flux. As IceCube has the highest sensitivity at 100 TeV and the spectral index of the predicted flux and the limit does not differ much from each other, a significant measurement by IceCube or IceCube-Gen2 may be soon possible. In fact, IceCube received already a 2 σ detection from Cygnus X. However, it is still not significant.

Tova et al. (2017) investigated the γ-ray and neutrino spectrum from Cygnus X by assuming that the CR spectrum observed at Earth is also a representative for the Cygnus X. This contribution has been added by emission from the Cygnus Cocoon separately as well as from identified and unidentified point sources. All calculations were carried out for 5 deg. $\times$ 5 deg. region which is subdivided in 0.25 deg. $\times$ 0.25 deg. In contrast to the multiwavelength model in this work, which considered the whole region as one source, and radio and hard γ-ray emission, [36] just calculated and considered γ-ray emission. Here, the validation is only a question of time and just depends on the measurement of IceCube.

3.2. Eta Carinae

η Carinae is a binary system which contains a massive LBV star and an O- or B-type companion star and is located 2.3 kpc from the Earth [37]. Astronomers have recognized it in the past in the 1840s and 1890s due to series of giant outbursts, which now formed into a nebula. The binary system itself is the most prominent source of one of the most active star-forming regions in the Milky Way.

In the astronomically near future, the system is expected to implode into a supernova. It has been already detected from hard X-rays to high-energy γ-rays. It was observed up to 300 GeV by Fermi-LAT during its full orbital period of 5.54 years [37] which is most commonly interpreted as a colliding wind binary. This binary creates a very strong terminal wind velocity of $\sim 500 - 700\,\mathrm{km\,s^{-1}}$ [38]. Thus, the acceleration might be performed at the shock fronts of the extensive wind collision. The interaction between the accelerated CRs and the stellar radiation fields, the magnetic fields, and the surrounding plasma leads to high-energy nonthermal emission due to nonthermal bremsstrahlung, inverse Compton emission, synchrotron radiation, and hadronic pion production [39]. This motivated the H.E.S.S. collaboration in 2012 to observe η Carinae between Fermi and H.E.S.S. energies as only then H.E.S.S. could measure this region of interest. The observations from 2014 to 2015 achieved a 13.6 σ pretrial measurement for the combined data set [40]. These observations indicate that $\eta-$ Carinae could be another cosmic ray cradle in our galaxy.

Roughly, η Carinae can be sectioned into two phases:

1. Periastron passage: from the largest distance between both stars up to the shortest distance
2. Apastron passage: from the shortest distance between both stars up to the largest distance

A fully hadronic interpretation has been presented in [41]. In order to calculate the secondary emission from photons and neutrinos, it has been assumed that a fraction of $\eta < 1$ of the colliding wind luminosity goes into CRs. The wind luminosity is determined by the sum of the kinetic luminosities of the mass loss of the two stellar objects, so that $L_{CR} \approx 1/2 \cdot \eta \cdot \sum_{i=1,2}(\dot{M}_i \cdot V_i^2)$, with M_i as the $i = 1\mathrm{st}, 2\mathrm{nd}$ companion, $\dot{M}_i$ as the mass loss, and V_i as the wind velocity of the two individual objects. The result of this calculation is shown in **Figure 9**. Here, the result for Eta Carinae is compared to other Wolf-Rayet star binary systems, which only have limits from Fermi observations. The neutrino fluxes are calculated by assuming a gamma-ray flux at the Fermi limit and are therefore also to be considered as upper limits to a possible neutrino flux from these heavy binary systems in the Milky Way. The expected emission of these point sources is at low energies for neutrino telescopes, which makes them difficult to detect with IceCube or KM3NeT. An interesting opportunity in the future could be

http://dx.doi.org/10.5772/intechopen.75429

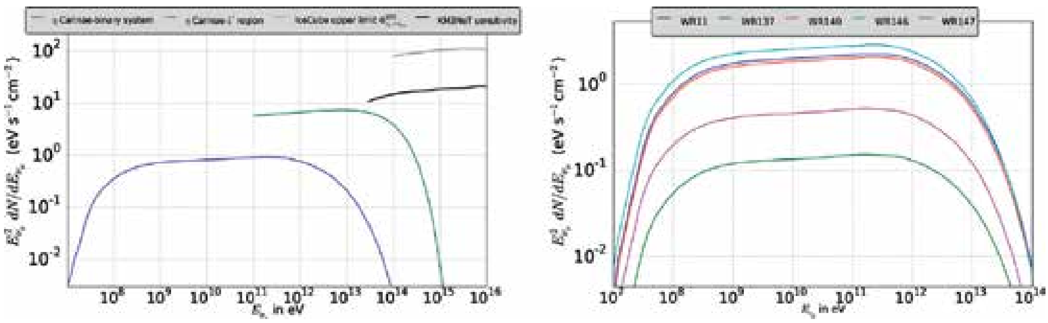

Figure 9. Left figure: neutrino energy spectrum of η Carinae during the 500-day periastron passage from [42] is shown in green, the neutrino spectrum of the binary system η Carinae calculated by [41] in blue, the IceCube upper limit in gray, and the KM3NeT sensitivity for the whole region of 1°. Right figure: neutrino spectrum of different Wolf-Rayet star binary systems.

searches for GeV neutrino sources with PINGU or ORCA. These have effective areas optimized to the GeV range, where atmospheric neutrino oscillations can be studied. At ~ 25 GeV, there is a minimum at which muon neutrinos from the atmosphere are strongly suppressed. This could open a small window in which the sensitivity for galactic GeV sources could be enhanced due to a strongly reduced background of atmospheric neutrinos [41].

A lepto-hadronic model to explain the nonthermal emission from Eta Carinae as an extended region has been presented in [42]. The spectral energy for both the periastron and apastron passage was derived. In this model, the part in the energy spectrum below 100 GeV is explained by inverse Compton emission. A prediction of a synchrotron spectrum is made in the radio to X-ray range. At the highest energies, $E_{\gamma} > 100$ GeV, the spectrum is explained by a hadronic component, with a prediction of the detection potential for H.E.S.S. and CTA. Although the CRs have been described by just a simple power law without any cutoff, the calculation of the flux considered the loss timescale, the maximum energy, ambient conditions, and the source geometry.

Deriving parameters from the comparison of the expected flux, observation data, and gamma-neutrino correlation, the neutrino flux can be predicted. **Figure 9** compares the prediction of the neutrino spectrum of η Carinae as derived from [41] (blue line) with the one in [42] (green line).

Considering the position of η nebulae and the size of $\sim 1^{\circ}$, one obtains an upper flux limit of $E^2\Phi^{90\%}_{\nu_\mu+\bar{\nu}_\mu} \simeq 1 \cdot 10^{-7}\,\mathrm{GeV\,cm^{-2}\,s^{-1}}$ for an E^{-2} unbroken power law of IceCube considering the 7-year data [43] (gray line), as also indicated in **Figure 9**. There is a difference of nearly one order of magnitude which is rather unrealistic to measure. With Eta Carinae in the southern hemisphere, the region is quite difficult to see for IceCube. A future surface array in connection to an IceCube-Gen2 array could change this.

Because of its location, KM3NeT has a better sensitivity to the southern hemisphere. For a 500-day exposure, the number of expected μ-neutrino events at KM3NeT for η Carinae between

10 TeV and 1 PeV amounts to 18 and for the diffuse astrophysical event to 0.03 [42], which could become interesting in the near future with a fully constructed KM3NeT detector.

3.3. Galactic Center

At a distance of 8.5 kpc from the Earth, the prominent supermassive black hole SgrA * represents the center of our galaxy. This central region in the galaxy is peculiar, as it reveals a high molecular density but no strong enhancement in star formation—a phenomenon that is also observed for other centers of galaxies [44]. Thus, it can formally not be considered as a star-forming region. Nevertheless, this region shows enhanced nonthermal emission at a broad energy range, which makes it equally interesting as those star-forming regions in the galaxy that we discuss here. This is linked with the ambient conditions but as well as with the sources within the region. SgrA * is surrounded by a circumnuclear disk (CND) with $R \simeq 3$ pc and a total mass of $10^6 M_\odot$ [45]. SgrA West the "minispiral," respectively, is a thermal radio source with three spiral arms of molecular gas that surrounds SgrA *. In every respect, the Galactic Center is very crowded especially by the stellar population as well as by molecular, atomic, and ionized gas. These characteristics make it rich on red giant stars, massive stars, and hundreds of OB and Wolf-Rayet stars [46]. Some prominent SNRs can be found near the Galactic Center, among those the prominent SNR SgrA East. This SNR is just 2.5 pc far away from the Center, has an elliptical shell along the galactic plane, and is surrounded by ionized gas. A visualization is exemplified in **Figure 10**.

SgrA * is supposed to generate high-energy CRs [47]. In fact, a diffuse γ-ray up to several tens TeV has been observed by H.E.S.S. within a radius of approximately 200 pc around the Center. Considering just a radius of about 8 pc, a large-scale diffuse radio emission, the radio halo, of a

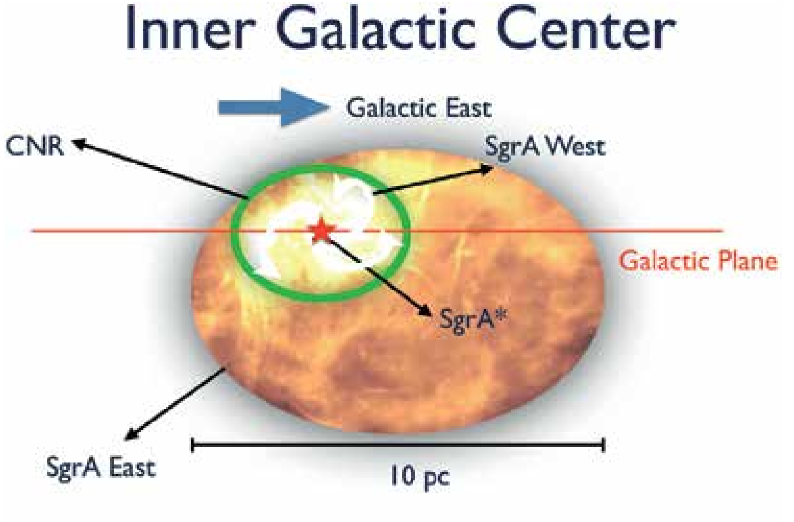

Figure 10. Inner 10 pc Galactic Center at 5 GHz.

synchrotron nature is present [48]. In contrast, a high-energy diffuse γ-ray emission contributed by electrons through the molecular zone is not realistic for various reasons:

- Electrons are susceptible to severe synchrotron and inverse Compton (IC) losses. Assuming a formation of high-energy electrons close to the black hole and a magnetic field strength of 100 μ G, the synchrotron timescale is $\tau_{\text{syn}} \approx 7.7 \cdot \gamma^{-1}$ s, which corresponds to a mean free path of roughly $\lambda_{\text{syn}} \approx 3.9 \cdot 10^9 \gamma$ cm where γ denotes the Lorentz factor. Moreover, the ionization loss timescale yields $\tau_{\text{io}} = 8 \cdot 10^{-10} \cdot \gamma \cdot \left(N_t/5.7 \cdot 10^4\, cm^{-3}\right)$ s. In contrast, the diffusion timescale is given by $\tau_{\text{diff}} = 2.1 \cdot 10^8 \gamma^{1/3} \cdot (R/200pc)^2 \cdot \left(D_0/4.7 \cdot 10^{27}\right)^{-1}$ s.
- The loss timescale inside the dense molecular clouds at the Galactic Center is much shorter than the propagation timescale. Thus, the γ-ray emission contributed by electrons is expected to be focused around a small region around the black hole.
- Therefore, a diffuse flux through the whole molecular zone demands an accelerator that boosts electrons up to ≥ 100 TeV [47] which requires unrealistic assumptions due to the diffusion and magnetic field.

Thus, the calculation of the diffuse γ-ray flux to describe the emission detected by H.E.S.S. [47] requires only proton transport Eq. (1). By maintaining the radial dependency, the γ-ray luminosity as a function of the distance from the center can be calculated. The measurement of this quantity has already been presented at H.E.S.S. energies ($E \geq 1$ TeV) by [47] and at Fermi (10 GeV $\leq E \leq 0.3$ TeV) energies by [49]. [50] also take the radial dependency of the continuous momentum loss rate due to hadronic pion production and the target density into account. This consideration complicates the transport Eq. (1) but gives an insight into the source distribution and reveals the real origin of the diffuse γ-ray emission. In doing so and by considering an isotropic distribution of the CR injection and gas, [50] present a hadronic one-component model (1CM), which considers only SgrA * as the main source, and a two-component model (2CM) which considers SgrA * as well as the SNR SgrA East. **Figure 11** on the left side shows the calculated γ-ray emission from the hadronic pion production with the 1CM and 2CM. The filled blue circle is the measurement of Fermi-LAT PASS8 data [49] and the red filled triangles from H.E.S.S. [47]. The γ-ray fluxes in **Figure 11** denoted by "Gaggero 1 & 2" are calculated by [49] who consider the CR large-scale population and a hard and conventional diffusion. However, the flux denoted by "Gaggero 3" works with a best-fit procedure and does not consider CR large-scale population. Each of the calculations is based on extensive transport equation which is only numerically solvable and takes the general radial dependency and the radial component of the diffusion tensor into account [49].

The 2CM of [50] and the best-fit model of [49] describe the γ-ray data at higher energies sufficiently, though the best-fit model does not seem to consider a cutoff. Therefore, at higher energies, the discrepancies might become larger. The 2CM, which considers an exponential cutoff at 1 PeV, seems to describe Fermi-LAT as well as H.E.S.S. data best. However, only [50] tried to reproduce the γ-ray luminosity by their model. Due to the short distance of SgrA East to SgrA * ($\approx$ 2 pc), the radial distribution of the luminosity of both component models is quite similar and presented in **Figure 12**.

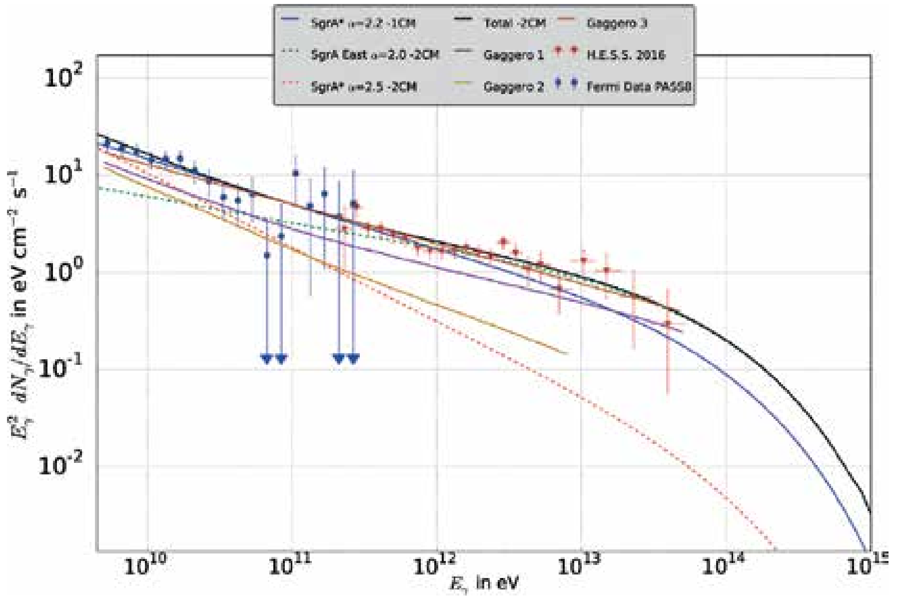

Figure 11. γ-ray emission from the inner 70 pc of the Galactic Center by [50] and by [49].

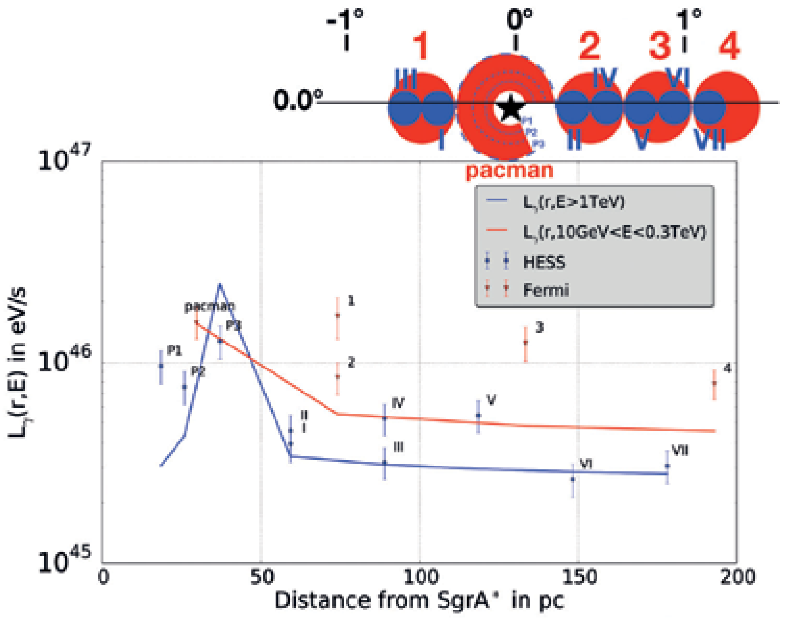

Figure 12. γ-ray luminosity as function of the distance from SgrA * for $E_{\mathrm{cut}} = 1$ PeV.

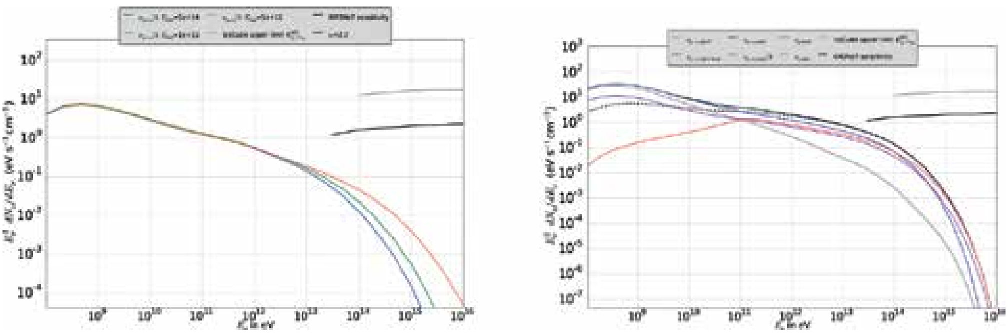

Figure 13. Neutrino spectrum from 1CM (left) and from 2CM (right) for $E_{\text{cut}} = 1$ PeV.

Although the radial distribution of H.E.S.S. is reproduced pretty well, the Fermi distribution exhibits discrepancies. This may be due to the simplification of the model which assumed an isotropic distribution around the Galactic Center or due to additional sources which are not identified or studied yet. The comparison between the expected and the measured luminosity does not suggest an isotropic injection of protons from one centrally located accelerator into the Central Molecular Zone as if it does it would not be able to suffice the observed luminosity. In contrast an additional source or sources could change the distribution in the right way. However, the model reproduces the γ-ray flux and the luminosity satisfactorily.

Accordingly, the neutrino spectrum is derived for the 1CM as well as for the 2CM.

Figure 13 also displays the IceCube's upper flux adapted for the region of interest as well as the sensitivity of KM3NeT. Again, due to atmospheric μ, the capability of KM3NeT is higher to detect neutrinos from the southern hemisphere and thus from the Galactic Center. Both observatories are still not able to detect any neutrinos from the direction of the Galactic Center.

4. Summary and outlook

Star-forming regions are of prime importance for investigating the origin of CRs, as they can be considered as CR birthplaces. During the past decades, a large variety of telescopes went into operation, starting to shed light on the nonthermal multi-messenger picture from star-forming regions in the Milky Way. Of particular interest are three concrete regions in the Milky Way:

1. *The Cygnus complex* is the most interesting star-forming region in the northern sky. It reveals nonthermal emission from diffuse regions and point sources up to $>$ TeV energy, in particular detected by the Milagro detector. This makes it a prime candidate to search for hadronic interaction signatures. The northern location is beneficial for the IceCube experiment, which can detect neutrinos in the TeV range with a spatial resolution of below 1° from the northern sky. The neutrino flux from Cygnus X approaches the IceCube's upper limit and past already the $2\,\sigma$ deviations from background could be detected in the past. Model predictions show that a detection of the region could already be possible with IceCube, certainly with the next-generation array IceCube-Gen2 for a detection threshold in the TeV range.

2. The *Eta Carinae* region is of particular interest because of the binary system η Carinae, detected at energies from radio to gamma rays. It is one of the most energetic binary systems in the galaxy and could have the potential to accelerate hadrons at the shock front forming from the collision of the winds of the two massive stars. Gamma-ray fluxes for such binary systems are in general quite low, i.e., apart from η Carinae they are so far below the detection threshold of Fermi. Thus, even the expected neutrino flux is relatively low, with one more disadvantage of an energy cutoff at relatively low energy. A window of opportunity here could be the detection of astrophysical sources in the $\sim 25\,\mathrm{GeV}$ neutrino energy range, as atmospheric muon neutrinos have an oscillation minimum here, which results in a highly reduced background.

3. The *Galactic Center* itself is no classical star-forming region, as—despite of the high molecular densities—the star formation rate is not increased in the amount expected for a correlation with the gas. It is, nevertheless, a region of high nonthermal emission. The most striking evidence for the existence of PeV CRs comes from H.E.S.S. measurements of the Galactic Center, where the gamma emission suggests a CR spectrum extending up to the knee. The question now is if a large part of the CR energy budget can come from that region or source or if this is a smaller part of the total energy budget. Neutrino measurements in the future by KM3NeT and IceCube-Gen2 will help to disentangle hadronic from leptonic signatures and thereby to quantify the hadronic contribution.

Future developments of telescopes will help to use star-forming regions in our galaxy in order to understand the birthplaces of CRs, i.e., the construction instruments like SKA, CTA, KM3NeT, IceCube-Gen2, and more. At least equally important is the proper modeling of these regions. Here, both plasma aspects, present in the transport equation via the diffusive and convective terms, and particle aspects, defined through the loss terms of leptons and hadrons, need to be considered in detail. Recent developments of numerical tools like CRPropa [25], DRAGON [51], GALPROP [52], and PICARD [53] represent important steps for a proper modeling, in which a diffusion tensor can be applied as well as hadronic and leptonic interactions with state-of-the-art cross sections that combine forward measurements with high-energy collision results at LHC. Thus, the next decade is very promising, as we will now be able to learn from this combination of precision astro- and astroparticle measurements and detailed theoretical modeling of the physics processes involved.

Author details

Mehmet Guenduez[1], Julia Becker Tjus[1]*, Björn Eichmann[1] and Francis Halzen[2]

*Address all correspondence to: julia.tjus@rub.de

1 Fakultät für Physik und Astronomie, RAPP Center, TP IV, Ruhr-Universität Bochum, Germany

2 Department of Physics, WIPAC, University of Wisconsin, Madison, WI, USA

References

[1] Becker Tjus J, Eichmann B, Kroll M, Nierstenhöfer N. Gamma-ray emitting supernova remnants as the origin of galactic cosmic rays? Astroparticle Physics. 2016;**81**:1-11

[2] Mandelartz M, Tjus JB. Prediction of the diffuse neutrino flux from cosmic ray interactions near supernova remnants. Astroparticle Physics. 2015;**65**:80-100

[3] Aartsen MG et al. Evidence for high-energy extraterrestrial neutrinos at the IceCube detector. Science. 2013;**342**:1242856

[4] Helou G, Soifer B, Rowan-Robinson M. Thermal infrared and nonthermal radio: Remarkable correlation in disks of galaxies. Astrophysical Journal Letters (United States). Nov 1985;**298**:2

[5] Biermann PL. On the radio continuum flux from the disks of spiral galaxies. Astronomy and Astrophysics. 1976;**53**:295

[6] Biermann PL, Fricke K. On the origin of the radio and optical radiation from Markarian galaxies. Astronomy and Astrophysics. 1977;**54**:461

[7] Kronberg PP, Biermann P, Schwab FR. The continuum radio structure of the nucleus of M82. The Astrophysical Journal. 1981;**246**:751

[8] Moshir M, Kopan G, et al. The faint source catalog, version 2.0. Bulletin of the American Astronomical Society. 1990;**22**:1325

[9] de Jong T et al. Radio continuum and far-infrared emission from spiral galaxies - A close correlation. Astronomy and Astrophysics. 1985;**147**:L6

[10] Wunderlich E, Klein U. A further study of the radio-far-infrared relation in galaxies. II— The ubiquity of the correlation. Astronomy and Astrophysics. 1988;**206**:47

[11] Wunderlich E, Klein U. The radio-far-infrared relation of interacting and non-interacting spiral galaxies. I - Observations and data collection. Astronomy & Astrophysics, Supplement Series. 1991;**87**:247

[12] Condon JJ et al. Correlations between the far-infrared, radio, and blue luminosities of spiral galaxies. The Astrophysical Journal. 1991;**376**:95x

[13] Völk HJ. The correlation between radio and far-infrared emission for disk galaxies - A calorimeter theory. Astronomy and Astrophysics. 1989;**218**:67

[14] Lacki BC, Beck R. The equipartition magnetic field formula in starburst galaxies: Accounting for pionic secondaries and strong energy losses. Monthly Notices of the Royal Astronomical Society. 2013;**430**:3171

[15] Becker JK, Biermann PL, Dreyer J, Kneiske TM. Cosmic rays VI—Starburst galaxies at multiwavelengths. ArXiv e-prints. Jan 2009

[16] Schöneberg S, Becker Tjus J, Schuppan F. A possible GeV-radio correlation for starburst galaxies. In: Torres DF, Reimer O, editors. Cosmic Rays in Star-Forming Environments. Vol. 34. Astrophysics and Space Science Proceedings. Springer; 2013. p. 299

[17] Becker JK, Schuppan F, Schöneberg S. A multifrequency view of starburst galaxies. Memorie della Societa Astronomica Italiana. 2012;**83**:154

[18] Eichmann B, Tjus JB. The radio-gamma correlation in starburst galaxies. The Astrophysical Journal. 2016;**821**:82

[19] Yoast-Hull TM, Gallagher JS III, Zweibel EG, Everett JE. Active galactic nuclei, neutrinos, and interacting cosmic rays in NGC 253 and NGC 1068. The Astrophysical Journal. Jan. 2014;**780**:137

[20] Merten L, Becker Tjus J, Eichmann B, Dettmar R-J. On the non-thermal electron-to-proton ratio at cosmic ray acceleration sites. Astroparticle Physics. Apr. 2017;**90**:75

[21] Kelner SR, Aharonian FA, Bugayov VV. Energy spectra of gamma-rays, electrons and neutrinos produced at proton-proton interactions in the very high energy regime. Physical Review D. 2006;**74**:034018

[22] Thompson TA, Quataert E, Waxman E, Murray N, Martin CL. Magnetic fields in starburst galaxies and the origin of the fir-radio correlation. The Astrophysical Journal. 2006;**645**(1): 186

[23] Ginzburg V, Syrovatskii S. The Origin of Cosmic Rays. 1st ed. Pergamon Press; 1964; p. 284

[24] Gaggero D et al. The gamma-ray and neutrino sky: A consistent picture of Fermi-LAT, Milagro and IceCube results. The Astrophysical Journal. 2015;**815**:L25

[25] Merten L, Becker Tjus J, Fichtner H, Eichmann B, Sigl G. CRPropa 3.1—A low energy extension based on stochastic differential equations. JCAP. 2017;**1706**(06):046

[26] Schlickeiser R. Cosmic Ray Astrophysics. 1st ed. Springer; 2002; p. 84

[27] Ghisellini G. Radiative Processes in High Energy Astrophysics. 1st ed. Springer; 2013; p. 43

[28] Virginia McSwain M, et al. Multiwavelength observations of gamma-ray binary candidates. Fermi Symposium proceedings—eConf C121028; 2012

[29] Abdo AA et al. Spectrum and morphology of the two brightest Milagro sources in the Cygnus region: MGRO J2019+37 and MGRO J2031+41. The Astrophysical Journal. 2012; **753**:159

[30] Abdo AA et al. Milagro observations of multi-TeV emission from galactic sources in the Fermi bright source list. The Astrophysical Journal. 2009;**700**:L127-L131

[31] Bernhard A. Origin of IceCubes astrophysical neutrinos: Autocorrelation, multi-point-source and time-structured searches [dissertation]. Technische Universität München; 2015

[32] Bartoli B et al. Identification of the TeV gamma-ray source ARGO J2031+4157 with the Cygnus cocoon. The Astrophysical Journal. 2014;**790**:152

[33] Becker JK, Black JH, Safarzadeh M, Schuppan F. Tracing the sources of cosmic rays with molecular ions. The Astrophysical Journal Letters. Oct. 2011;**739**:L43

[34] Schuppan F, Becker JK, Black JH, Casanova S. Cosmic-ray-induced ionization in molecular clouds adjacent to supernova remnants. Tracing the hadronic origin of GeV gamma radiation. Astronomy and Astrophysics. May 2012;**541**:317-324

[35] Tibaldoa L et al. The Fermi LAT view of Cygnus: A laboratory to understand cosmic-ray acceleration and transport. Nuclear Physics B, Proceedings Supplements. 2012;**230–240**:70-75

[36] Yoast-Hull TM, Gallagher JS III, Halzen F, Kheirandish A, Zweibel EG. The γ-ray puzzle in Cygnus X: Implications for high-energy neutrinos. Physics Review. 2017:**D96**(4):043011

[37] Reitberger K, Reimer A, Reimer O, Takahashi H. The first full orbit of η Carinae seen by Fermi. Astronomy and Astrophysics. 2015;**577**:A100

[38] Bednarek W, Pabich J. High-energy radiation from the massive binary system Eta Carinae. AAP. June 2011;**530**:A49

[39] Reimer A, Pohl M, Reimer O. Nonthermal high-energy emission from colliding winds of massive stars. The Astrophysical Journal. 2006;**644**(2):1118

[40] Leser E, Ohm S, Füßling M, de Naurois M, Egberts M, Bordas P, Klepser S, Reimer O, Reimer A, Hinton J. First results of Eta Car observations with H.E.S.S.II Proceedings of Science. 2017;ICRC2017:717

[41] Becker Tjus J. Neutrinos from colliding wind binaries: Future prospects for PINGU and ORCA. ASTRA Proceedings. May 2014;**1**:7

[42] Gupta N, Razzaque S. Lepto-hadronic model of gamma rays from Eta Carinae and prospects for neutrino telescopes. Physics Review. 2017;**D96**(12):123017

[43] Aartsen MG et al. All-sky search for time-integrated neutrino emission from astrophysical sources with 7 years of IceCube data. APJ. 2017;**835**(2):151

[44] Kennicutt RC, Evans NJ. Star formation in the Milky Way and nearby galaxies. ARAA. Sept. 2012;**50**:531-608

[45] Haardt F, Gorini V, Moschella U, Treves A, Colpi M. Astrophysical Black Holes. 2nd ed. Springer; p. 205

[46] Mauerhan JC, Cotera A, Dong H, Morris MR, Wang QD, Stolovy SR, Lang C. Isolated Wolf-Rayet stars and O supergiants in the Galactic Center region identified via Paschen-α excess. APJ. Dec. 2010;**725**:188-199

[47] Abramowski A et al. Acceleration of petaelectronvolt protons in the Galactic Centre. Nature. 2016;**531**:476

[48] Pedlar A, Anantharamaiah KR, Ekers RD, Goss WM, van Gorkom JH, Schwarz UJ, Zhao J-H. Radio studies of the Galactic Center. I—The Sagittarius A complex. APJ. July 1989; **342**:769-784

[49] Gaggero D, Grasso D, Marinelli A, Taoso M, Urbano A. Diffuse cosmic rays shining in the Galactic Center: A novel interpretation of H.E.S.S. and Fermi-LAT γ-ray data. Physical Review Letters. 2017;**119**(3):031101

[50] Guenduez M, Tjus JB. Modeling cosmic ray propagation in the Galactic Center region - Neutrino flux prediction and interpretation of the gamma-ray data from GeV to TeV energies. In preparation. 2018

[51] Evoli C, Gaggero D, Vittino A, Di Bernardo G, Di Mauro M, Ligorini A, Ullio P, Grasso D. Cosmic-ray propagation with *DRAGON*2: I. Numerical solver and astrophysical ingredients. JCAP. 2017;**1702**(02):015

[52] Moskalenko I. Modeling cosmic ray propagation and associated interstellar emissions. In: 39th COSPAR Scientific Assembly, Vol. 39 of COSPAR Meeting; July 2012. p. 1281

[53] Kissmann R. PICARD: A novel code for the Galactic Cosmic Ray propagation problem. Astroparticle Physics. 2014;**55**:37-50

Chapter 7

Exploration of Solar Cosmic Ray Sources by Means of Particle Energy Spectra

Jorge Perez-Peraza and Juan C. Márquez-Adame

Additional information is available at the end of the chapter

http://dx.doi.org/10.5772/intechopen.77052

Abstract

Through the analysis of the energy spectrum of 12 ground level enhancements (GLE) of solar protons, a contribution in the understanding of the generation process of flare particles is attempted. Theoretical spectra of protons are derived by considering either they do not lose energy within the acceleration volume or that they are decelerated during the acceleration process. By comparing the theoretical source spectra with the experimental spectra, it is claimed that the generation process of solar particles develops under three main temperature regimes: the efficiency of particles acceleration is relatively high in cold-regimens decreasing while increasing the temperature of the medium. It is shown that in some events energy losses are able to modulate the acceleration spectrum within the source during the short time scale of the phenomenon, whereas in other events energy losses are completely negligible during the acceleration. It is argued that acceleration takes place in closed magnetic field lines and predicted the expansion and compression of the source material in association with the generation process of particles. This study allows us to estimate the range of variation from event to event of several parameters of the source and the acceleration process itself.

Keywords: solar protons, energy spectrum, solar sources, GLE

1. Introduction

Most of the information on solar flares has been generally supplied by the analysis of their electromagnetic spectrum; however, the confrontation of timing synchronization between

IntechOpen

© 2018 The Author(s). Licensee IntechOpen. This chapter is distributed under the terms of the Creative Commons Attribution License (http://creativecommons.org/licenses/by/3.0), which permits unrestricted use, distribution, and reproduction in any medium, provided the original work is properly cited.

electromagnetic flare emissions with those of energetic particles and coronal mass ejections (CME) is the method utilized to explore the physical conditions and processes taking place in the sources of particle generation. For example, results obtained from the SEPS server project and future HESPERIA HORIZON 2020 project. However, the study of the corpuscular radiation emitted in some flares can also provide us with very valuable information about the physical conditions and processes occurring in association with this solar phenomenon. It is known, for instance, that the processes involved in the generation of solar particles are probably of a non-thermal nature, because the intensity of particles usually decays more softly than an exponential of a the thermal type does, and so other properties may be deduced in order to investigate how and where multi-GeV solar protons originate, that means the source parameters and the parameters involved in the generation process of particle [69, 70]. In this chapter, we attempt to draw some inferences concerning solar sources by the analysis of 12 ground level enhancements (GLE) of solar cycles 19 and 20.

It has been shown [40] that the best representation of the energy spectrum of solar protons through the whole energy domain explored experimentally at present is given by an inverse power law with an upper cutoff in its high energy portion. In fact, a good fit of the experimental data can be obtained with an exponential law in a limited energy band; however, a strong deflection is obtained with them as soon as a wider energy domain is involved. Besides, it has been established [11] that the measured differential intensity in solar proton events, as well as the source spectrum (inferred as an inverse power law in energy) are both velocity-dependent. Therefore, we infer that the acceleration rate of particles in the sun must provide the spectral shape and velocity dependence such as suggested by those results. This is the case with an energy gain rate of the form

$$\left(\frac{dW}{dt}\right)_{acc} = \alpha\beta W = \alpha\left(W^2 - \left(Mc^2\right)^2\right)^{1/2} \tag{1}$$

where β is the velocity of the particles in units of light velocity and W the total energy of particles. The parameter $\boldsymbol{\alpha}$ denotes the efficiency of the acceleration mechanism, which in the case of solar sources may be considered as roughly constant when the acceleration process reaches the steady-state in a given event [79, 80]. It has been generally thought that the energy loss processes of solar particles acceleration stage are not important in practice, and have only been taken into account after the acceleration stage in order to explain some features of electromagnetic emissions in solar flares and heating of the chromosphere [87].

In this chapter we shall consider, together with acceleration, energy loss processes occurring in the high density plasma of the solar source. It will be shown that energy losses in some proton flares can modulate the acceleration spectrum, thus implying that if such a small effect compared to the acceleration rate is able to modify the spectrum during the short lapse of the acceleration process, then the source spectrum is actually the result of a strong modulation due to local energy losses during acceleration and not only through interplanetary propagation; thus in Section 2, we discuss the basic equations of the more plausible energy loss processes in particle sources. In Section 3, we present the observational energy spectrum of the concerned GLE as reported by several authors. In Section 4, we deduce theoretical source spectra, without and with energy losses during acceleration, disregarding energy changes of after acceleration while traversing the dense medium of the solar atmosphere to attain the interplanetary medium. In Section 5, we describe the criterion employed to construct integral energy spectra of solar proton (GLE) as well as the methods used in calculations; the results are presented graphically. In Section 6, the interpretation and significance of our results are discussed. In Section 7, the concluding remarks are summarized.

2. Energy losses of protons during acceleration in solar flares

Some researchers who study radiation and secondary particle fluxes consider an acceleration stage followed by a slowing down phase in the solar material once the action of the acceleration mechanism on particles has ceased (e.g. [86–89]); and they generally neglect the simultaneous occurrence of energy loss and acceleration.

However, particle acceleration is not performed in the vacuum but in the high density medium of flare regions; therefore, we shall study the local modulation of the acceleration spectrum as the protons are broken during the short-time scale of solar particle generation. The most important processes occurring in astrophysical plasmas capable of affecting the net energy change rate of particles in the range of kinetic energies of energetic solar protons ($E \sim 10^6$–10^{10} eV) are:

2.1. Collisional energy losses

These depend strongly on the density and temperature of the plasma; thus we assume that the main energy dissipation of particles must occur in the generation region, in the body of the flare itself. The rate of collisional losses in a medium of density $\boldsymbol{n}$ has been given in a simplified expression [37]

$$\left(\frac{dW}{dt}\right)_{ion} = -\frac{7.62 \times 10^{-9} nL}{\beta} \text{ (eV/sec)} \tag{2}$$

where $\beta = v/c$ is the particle velocity in terms of the light velocity, $\boldsymbol{L}$ is a unidimensional factor and logarithmically depending marginally on the particle energy. We shall assume a value of L $\sim$ 27 for solar flare conditions, when the medium concentration is $n \sim 10^{12} - 10^{13}$ cm^3. In **Figure 1**, the behavior of Eq. (2) with energy is shown. The complete description of collisional losses through the entire energy range including losses in the low energy portion (the so called nuclear stopping and electronic stopping) has been given by [10] for fully ionized hydrogen as:

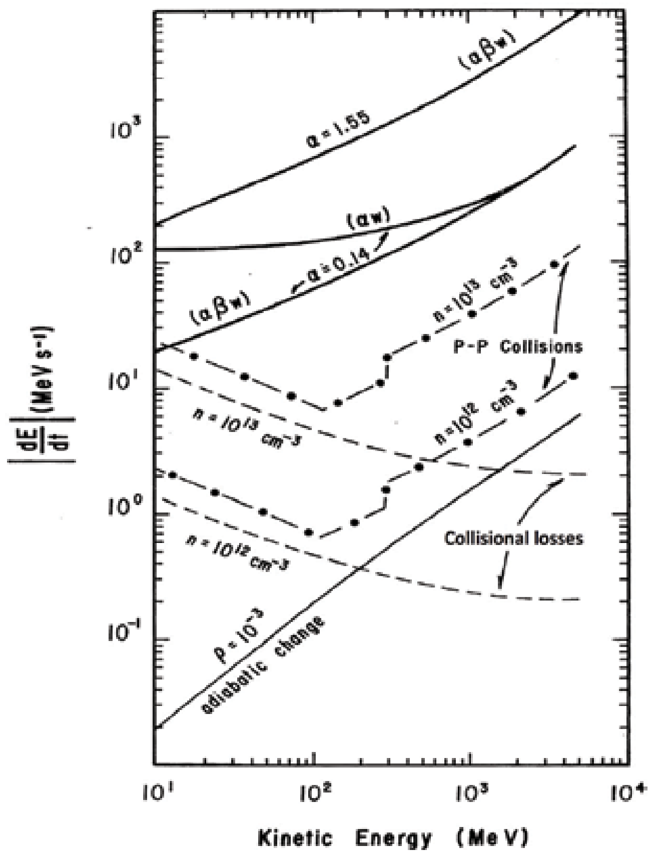

Figure 1. Energy change rates of protons (acceleration for two different rates) and deceleration for collisional losses p–p nuclear collisions and adiabatic cooling in a medium of density n = 10^{12}–10^{13} cm^{-3}.

$$\frac{dE}{dt} = -\frac{1.57 \times 10^{-35} N}{\beta} \frac{Q^2}{A} H(x) ln\Lambda \ \ (\text{eV/ns}) \tag{2.1}$$

where $x = 5.44 \times 10^4 \beta T^{-0.5}$, $H(x) = \xi_1 H_e(x_e) + \xi_2 H_p(x_p)$ with

$H_e(x_e) = 0.88 erf(x_e) - (1 - 5.48 \times 10^{-4}/A) x_e e^{-x_e^2}$ for electrons,

$H_p(x_p) = 0.88 erf(x_p) - (1 + \frac{1}{A}) x_p e^{-x_p^2}$ for protons,

$\xi_1 = 1.097803296 \times 10^{27}$, $\xi_2 = 5.979073244 \times 10^{23} and\ \Lambda = \left[4.47 \times 10^{16} A (T/N)^{0.5} \beta^2\right]/Q$

For the task of simplicity and because we are dealing in this work with GLE (high energy protons), we will use preferentially Eq. (2).

2.2. Energy degradation from proton-proton collisions

At present, there are evidences of the occurrence of nuclear reactions between solar nuclei and solar material, producing high energy gamma rays although is not absolutely clear whether nuclear reactions of solar energetic particles and solar material take place, when protons are injected into the photosphere, or they pass through coronal condensations, or during their acceleration within the dense material of flare regions. We shall assume that nuclear interactions occur at least in the acceleration volume where very likely the motion of energetic particles is completely random with respect to the local solar material. The isotropic motion of the accelerated particles is suggested by an analysis of neutron fluxes [45]. For purposes of energy loss calculations, we do not take into account collisions protons with other nuclear species, because the maximum energy change in elastic scattering occurs when the colliding particles have similar mass. Although the energy dissipation from *p: p* collisions is believed to appear mainly from elastic scattering, however at high energies (>750 MeV), the inelastic cross-section becomes highly important [44] increasing up to a maximum at some GeV, where it remains practically constant. In fact, as pion production initiates at ~ 285 *MeV* and a fraction $\geq 35\%$ of the kinetic energy of the incident proton goes into pion energy, then, energy dissipation from inelastic *p: p* scattering is not negligible in a high density medium ($\boldsymbol{n} \geq 10^{12}$ cm^{-3}). Concerning inelastic *p: p* interactions, the gamma ray line at 2.2 *MeV* due to fast neutron production, seems to be strong evidence of the occurrence of *p: p* collisions in solar flares. All this depends strongly on the production model: The assumed geometry and the spectral shape considered [2]. In fact, the cross-section for the later interactions is 10: 100 times higher, that is, their threshold is ≤ 36 *MeV/nucleon*, while that for inelastic *p: p* scattering are $\sim$ 285 MeV. Nevertheless, it has been known for a long time from [12] that solar abundances of CNO and he are of the order of $\sim$ 1.5: 7% with respect to the local *H*, in such a way that this kind of equilibrium between local abundances and interaction cross-sections states a high probability for the occurrence of *p: p* collisions in the body itself of the solar flare material. The main problem related with these features is that some reactions, as for instance $p(p;\, a\pi^0)p$ and multiple pion yielding at high energies, $p(p;\, a\pi^+)p$ or $p(p;\, a\pi^-,\, b\pi^0)p$ or $p(p;n,\, \pi^+,\, a\pi^+, a\pi^{--},\, b\pi^0)$ by π^0 decay produce high energy solar gamma rays (50 *MeV*) that have neither been detected to our knowledge nor their plausible absorption into the solar material satisfactorily explained. In fact, the predicted wide peak for these gamma rays ranging from $\sim$38.5: 118 *MeV* [6] could probably render their identification difficult due to the presence of high energy photons expected from bremsstrahlung of very high energy solar electrons. In addition, there is the fact that high energy *p: p* reactions must occur more frequently, since the inelastic cross-section rises progressively from 290 *MeV* up to a maximum of about 1 *GeV* where it remains practically constant. Refs. [14, 15] have reviewed the problems connected with secondary products of nuclear interactions in solar flares. Nevertheless we show later in this work that *p: p* collisions are only expected in some few GLE. Hence, although the measured flux of particles does not distinguish whether solar protons have suffered nuclear collisions or not, the modulation of the energy spectrum by their effects furnish available information about their occurrence. The importance of energy degradation from *p: p* collisions in cosmic rays physics has been pointed out for the first time by [129]. The energy loss rate by nuclear interactions is agreement with [38]

$$\frac{dW}{dt} = -\sigma cn\beta W \text{ (eV/sec)} \tag{3}$$

where σ in p–p collisions is composed of $\sigma_{p-p}^{ine} + \sigma_{p-p}^{el}$. As the inelastic cross-section is weakly energy dependent, it may be approximated to its mean value at high energies ($\sigma_{p-p}^{ine} \sim 26$ mb).· Concerning elastic collisions, a reasonable fit of the differential cross-section data by an analytical expression has been given by [91]. As the differential cross-section is highly isotropic, we can assume symmetry around 90°, such that their expression may be rewritten as $\sigma_{p-p}^{el} = hE^{-2} + JE^{-1}$ (if E ≤ 110 MeV) and $\sigma_{p-p}^{el} = hE^{-2}$ + f (if E > 110 MeV), where h = 96.09 mb-MeV^2, $j = 5.497 \times 10^3$ mb MeV and f = 46.49 mb. We have then from Eq. (3):

$$\left(\frac{dW}{dt}\right)_{p-p} = -cn\left(h\overline{E}^2 + j\overline{E}\right)\beta W \text{ (if } E \leq 110 \text{ MeV)}$$

$$\left(\frac{dW}{dt}\right)_{p-p} = -cn\left(h\overline{E}^2 + f\right)\beta W \text{ (If } 110 < E < 290\ MeV)$$

$$\left(\frac{dW}{dt}\right)_{p-p} = -\left[\eta + cn\left(h\overline{E} + f\right)\right]\beta W \text{ (If } E \geq 290 \text{ MeV), where } \eta = cn\sigma_{in}$$

So that the net energy change can be compacted as:

$$\left(\frac{dW}{dt}\right)_{p-p} = -\left(hE^{-2} + jE^{-1} + f + \eta\right)\beta W \text{ (eV/sec)} \tag{4}$$

where $h = 2.88 \times 10^{-15}$ n Me ^{2} s^{-1}, $j = 1.65 \times 10^{-13}$ n MeV s^{-1} (*if E* ≤ 110 MeV), j = 0 and $f = 1.39 \times 10^{-15}$ n s^{-1} (*if E* > 110 MeV), f = 0 (*if E* ≤ 110 MeV), $\eta = cn\sigma_{p-p}^{ine} = 8.1 \times 10^{-16}$ n s^{-1}, (*if E* > 290 MeV) and η = 0 *if* (*E* < 290 MeV). We have plotted Eq. (4) in **Figure 1** for two different values of the density *n*.

2.3. Adiabatic deceleration at the source level

Adiabatic cooling of cosmic particles in the solar wind has been proved long ago (e.g. [34]). However, here we are dealing with adiabatic cooling at the sources of solar energetic protons in GLE and not in the interplanetary or interstellar media medium. It is well-known that great flares are associated with magnetic arches, such as loop prominences and flare nimbuses (e.g. [7, 97, 98]) which occur between regions of opposite-polarity in the photosphere. Observations show that magnetic flux tubes expand from flare regions [23, 66, 107, 109, 117]. These configurations identified as "magnetic bottles" are usually related to the development of flare phenomena (e.g. [14, 83, 84, 96, 104, 110, 123]), therefore, we shall investigate the relationship between these magnetic structures and the phenomenon of particle generation through the study of the energy spectra of solar protons in GLE: We assume the hypothesis that particles are enclosed within those "magnetic bottles", where they are accelerated up to high energies.

Therefore, while the acceleration mechanism is in effect, and a fraction of particles are escaping from the flare region, the bulk of particles lose energy by adiabatic cooling due to the work that protons exert on the expanding material. Mechanisms for the expansion (or compression) of magnetic structures have been widely discussed (e.g. [96, 99]). It has been shown through energetic estimations that when particle kinetic density exceeds magnetic field pressure, the sunspot field lines are transported upward by the accelerated plasma; and thus, owing to the decrease of magnetic field density according to the altitude over the photosphere [1, 101], the magnetic bottles blow open at an altitude lower than 0.6: 1 R_s allowing particles] to escape into the interplanetary medium. Particles that have left the acceleration region before the magnetic bottle blows up may escape due to drift by following the field lines, or they remain stored therein losing energy losing energy until the magnetic structure is opened. We shall not consider this eventual deceleration during particle storage but only energy losses inside the acceleration volume. According to [46, 77], the energy change rate of particles by expansion (or compression) of magnetic fields producing adiabatic cooling or heating of the solar cosmic ray gas, when the non-radial components of the plasma velocity are negligible is given as

$$\left(\frac{dE}{dt}\right)_{ad} = \pm\frac{2}{3}\frac{V_r}{R}\mu E \text{ (eV/sec)} \tag{5}$$

where Vr and R are the velocity and distance of the plasma displacement, respectively, $\mu = 1 + \gamma^{-1}$ and $\gamma = W/Mc^2$. Hence, in terms of total energy W the adiabatic deceleration rate in the expanding magnetic fields may be expressed as

$$\left(\frac{dW}{dt}\right) = -\rho\beta^2 W \text{ (eV/sec)} \tag{6}$$

In order to estimate an approximate value for $\rho = (2/3)\,(V_r/R)$ in flare conditions, we extend the following considerations: it is known that the hydromagnetic velocity of the coronal expansion is in average of the order 400 km s^{-1}) and that in association with proton flares type IV sources systematically appear expanding with velocities in the range of 10^2–10^3 km s^{-1} depending on the direction of the expansion (e.g. [100, 101, 136]). Observations also show displacements with velocities of 650–2600 km s^{-1} in association with type II burst [95] and expansion of flare knots in limb flares with velocities in the range 5.3–110 km s^{-1} [54, 55, 83, 84]. Besides, it is also known that closed magnetic arches have a mean altitude of 0.6 Rs above the photosphere [122]. Therefore, assuming that the average velocity of 400 km s^{-1} is a typical value of magnetic motions in the chromosphere and low corona and an average expanded distance of the source of 0.3 R_s while acceleration is operating, we obtain thus $\rho \approx 10^{-3}$ s^{-1}. On the other hand, if we take into account the results usually associated with multi-Gev proton flares (GLE), then, magnetic loops expand $\sim$ 30,000 km with a velocity of $\sim$45 km s^{-1} at the time of the flare start, thus giving a value for ρ of the same order. We have illustrated Eq. (6) with $\rho = 10^{-3}$ s^{-1} in **Figure 1**.

It is expected that if the physical conditions in the source of multi-GeV solar proton flares and processes acting on solar particles must be similar, the behavior of the theoretical source spectra of solar protons from event to event will be similar, and thus by comparing the rates (1)–(6) the influence of each process on the acceleration spectrum can be established. For instance, it can be seen from **Figure 1** that in the energy range 1–10^3 MeV and medium concentration $n = 10^{13}$ cm^{-3}, the ratio $r_1 = (dW/dt)_{p-p}/(dW/dt)_{coll}$ changes from r_1 = 1.7–16 and the ratio $r_2 = (dW/dt)_{ad}/(dW/dt)_{coll}$ varies from r_2 = 4.6 10^{-5}–0.64; therefore if all processes would act simultaneously in solar flares, the acceleration spectrum is mainly affected by energy degradation from *p–p* collisions, whose effects are stronger in the high energy portion of the spectrum. Collisional losses are more important in the non-relativistic region, whereas adiabatic losses become important in the relativistic region of the spectrum. Using experimental data of several GLE of solar protons, we shall investigate if the same processes occur in all events, and thus similar physical conditions are prevalent at the sources, or if they vary from event to event, in which, case it is interesting to investigate why and how they vary.

3. Experimental integral spectra of multi-GeV solar proton events

The description of the spectral distribution of solar particle fluxes of a given event is concerned, the result is a strong spread of spectral shape representations, according to the different detection methods employed, the energy bands and time intervals studied. The most plausible spectral shapes are described either by inverse power laws in kinetic energy or magnetic rigidity and exponential laws in magnetic rigidity (e.g. [53]). One of the most popular methods was developed by Forman et al, published in Ref. [59].

For example, in the case of the GLE of January 28, 1967, for which experimental measurements of fluxes through a wide energy range are available, several different spectral shapes have been analyzed: from the study of the relativistic portion of the spectrum, [60–62] proposes an exponential rigidity law $\{\sim exp.\,(-P/0.6\,(GV)\}$ and alternatively a differential power law spectrum in rigidity ($\sim P^{-5}$); [8] proposed a differential spectrum of the form ($\sim P^{-4.8}$) for relativistic protons of the event. Taking into consideration data from balloon, polar satellite and neutron monitors (N.M.), [3] gives an integral spectrum of the form ($\sim P^{-4}$); similarly, [40] deduced an integral spectrum as a power law in kinetic energy ($\sim E^{-2}$) with an upper cutoff at E_m = 4.3 GeV or in magnetic rigidity P as ($\sim P^{-3.1}$) with an upper cutoff at P_m = 5.3 GV. These authors have shown that as far as the whole energy spectrum through the different energy bands is concerned, any spectral shape that does not take into an upper cutoff is strongly deflected from the experimental data.

It would seem, therefore, that the description of energy spectra of solar particles is one of the most particular topics connected with solar cosmic ray physics: that is, owing to the lack of global measurements of the whole spectrum at a given time and to the lack of simultaneity in the measurements of differential fluxes, the integral spectra must be constructed with the inhomogeneous data available for each event. Therefore, in order to do so for 12 GLE during solar cycles 19 and 20, we have used low rigidity data (high latitude observations) for the following events: for September 3, 1960 event we have employed the 14:10 U.T. data from Rocket Observations [18] in the (0.1–0. 7) GV band. For November 12 and 15, 1960 GLE's, we have used the 18:40 U.T. and 05:00 U.T. data, respectively, from rocket observations in the (6.16–1.02) GV band [73]. For July 7, 1966 GLE, we have used the 19:06 U.T. data given by [57, 58] in the (0.13–0.19) GV band, and the spectrum given by [118] in the (0.19–0.44) GV band;

for higher rigidities (> 0.44 GV) we have employed the 03:00 U.T. measurements on Balloon and N.M. data given by [39]. In the events of November18, 1968, February 25, 1969, March 30, 1969, November 2, 1969 and September 1, 1971, we have used the peak flux data in the (0.1–0.7) GV band, given by [47] from the IMP4 and IMP5 satellite measurements. For January 24, 1971 GLE, we have employed the 06:05 flux data and at 07:20 U.T. in the (0.28–0.7) GV band from [134] For August 4, 1972 event, we have considered the HEOS2 graphical fluxes in the (0.15–0.45) GV band at 16:00 U.T. by [61] which lie between the 09:57–22:17 U.T. data of [4] and is in good agreement with N.M. measurements; for the (0.6–1.02) GV band we have employed the balloon extrapolated data by [61]. For the high rigidity portion of the spectrum (> 1.02 Gy), we have made use of the measurements given by [41–43] from NM data, in the following form:

$$J(>P) = K\int_{P}^{P_m} P^{-\Phi} dP \tag{7}$$

where K is a constant, P_m the high rigidity cutoff and Φ the spectral slope of the differential fluxes.

The values of P_m and Φ were taken through several hours around the peak flux of the event, as explained by the latter authors. The values of Φ were found to be systematically lower than other values furnished by GLE measurements due to the presence of the high rigidity cutoff parameter. For November 2, 1969 event we have taken the high rigidity power law spectrum as given by [61]; according to this data, we have considered a characteristic upper cutoff at 1.6 GV. In the case of August 4, 1972 event, we have taken the upper bound of Φ given for August 7 event by [43] considering that the particle spectrum became flatter with time during August 1972 events [4]. For the high rigidity cutoff, we have tested that within the error band, the value was essentially the same of that of August 7 event.

The extrapolation of the high rigidity power laws to the integral fluxes of the lower rigidity branches, has allowed us to determine K from Eq. (7) and thus to construct the high rigidity branches of the proton fluxes. By smoothing fluxes of both branches we have obtained the experimental integral spectra, which we have represented in the kinetic energy scale with solid lines through **Figures 2–4**. We have verified the good agreement of the high energy power law shape deduced in this manner, with the corresponding integral slope of the differential power law in kinetic energy $\int_{E}^{E_m} E^{-\Phi} dE$ reported in several works by (e.g. [41–43]). However, although it is systematically true that the best fit for the experimental points is given by such a power law, it is also true that there are some points that do not fit perfectly with that kind of curve; we have attempted to include these points in the experimental curves in the case of some GLE events. For January 28, 1967 event, we employed the integral spectrum deduced by [40] with the previously mentioned characteristics. It must be emphasized that the choice of these 12 multi-GeV proton events (GLE) follows from the fact that they furnish particle fluxes through a large range of energy bands and because of the information of the experimental value of E_m in these cases, which unlike the other parameters of the spectrum is the only one that does not vary through the propagation of particles into the interplanetary space as shown by [40]) and therefore, can be directly related to the acceleration process

An excellent review of solar cosmic ray events has been given in [130].

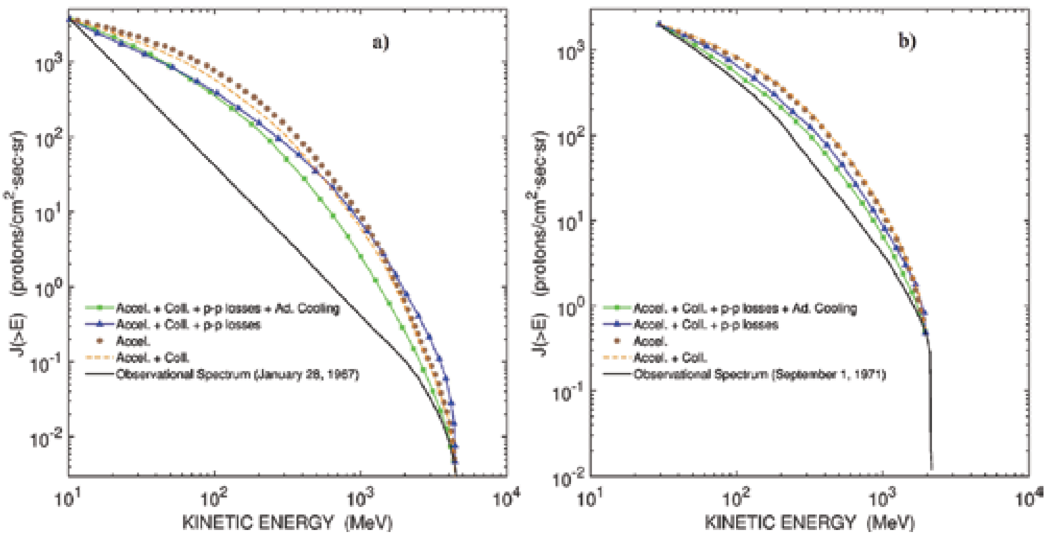

Figure 2. Theoretical and observational integral energy spectrum of *hot* events.

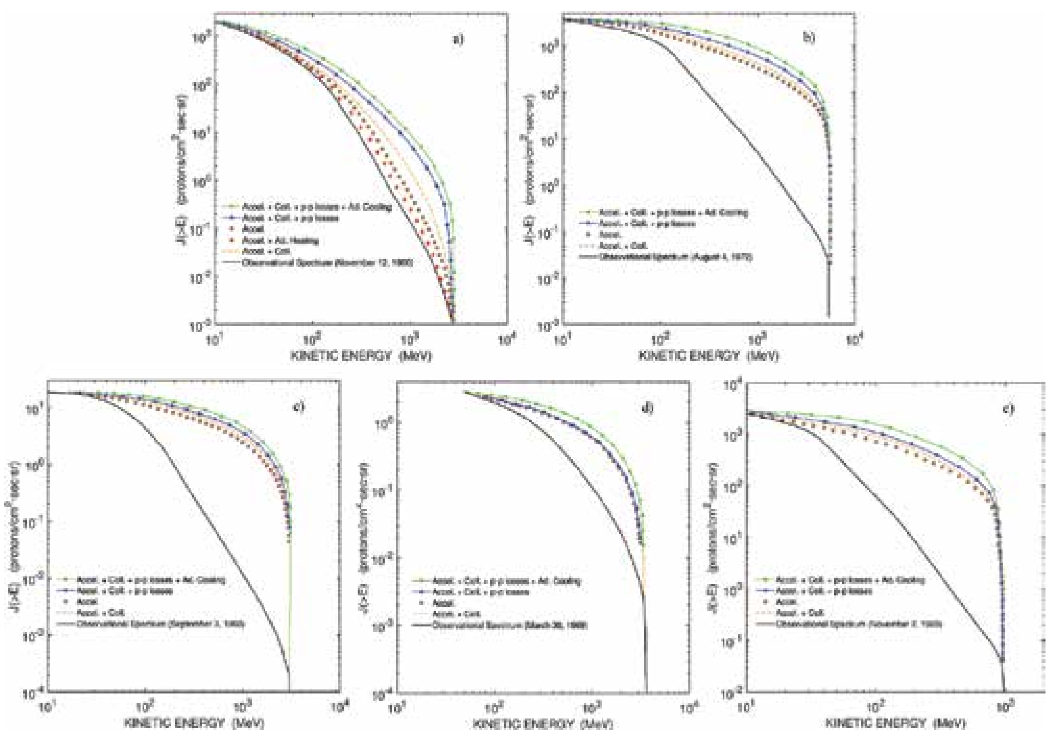

Figure 3. Theoretical and observational integral energy spectrum of *cold* events.

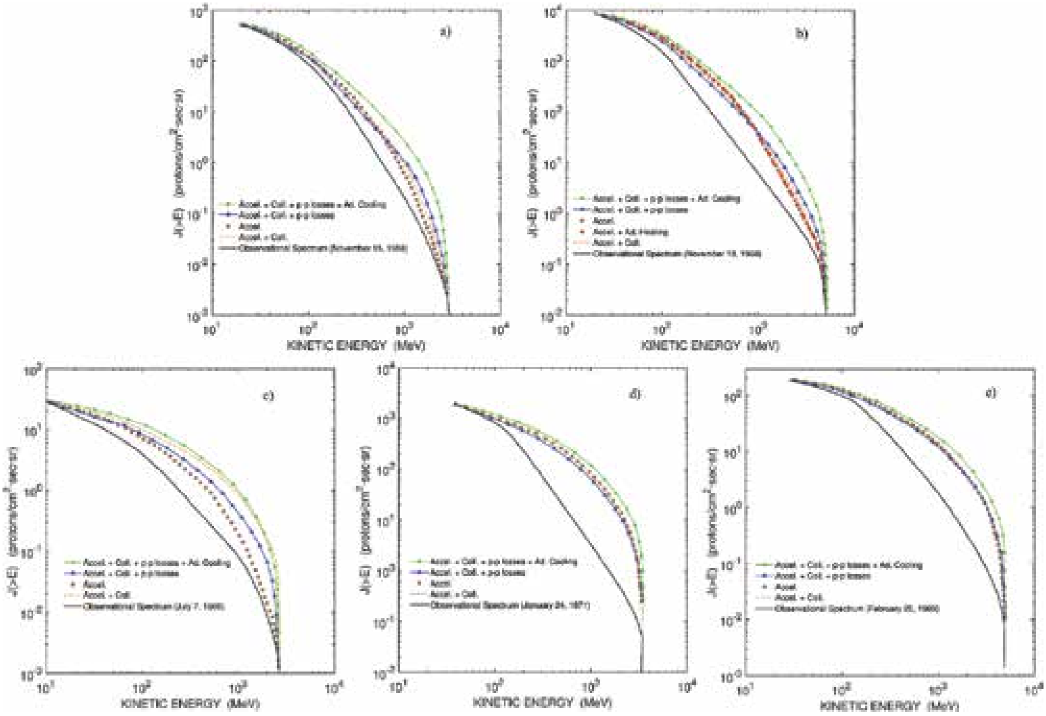

Figure 4. Theoretical and observational integral energy spectrum of *warm* events.

4. Theoretical spectra of solar protons in the source

In order to deduce the velocity and time dependent theoretical spectrum of the accelerated protons, one must take into account the various processes which affect particles during the remaining time within the acceleration volume. The main processes acting on particles during acceleration in a high density plasma are related either to catastrophic changes of particle density from the accelerated flux or to energy losses. Whereas the first kind of processes affect mainly the number density of the spectrum, energy losses entail a shift of the particle distribution toward lower energies, and a certain degradation of the number density due to thermalization of the less energetic particles. The number density changes on the accelerated proton flux may occur from catastrophic particle diffusion out of the flare source or by nuclear disintegration or creation of solar protons by nuclear reactions. Given the lack of knowledge about the exact magnetic field configuration and thus of the confinement efficiency of these fields, we do not consider here the effects of plausible escape mechanisms [26, 27, 104] on the theoretical spectrum. Therefore, to make a clear distinction between the energy loss effects (Section 2) on the spectrum of acceleration, we shall also neglect nuclear transformation during acceleration, local modulation post-acceleration and interplanetary modulation [67, 68] in this approach.

In addition, we shall not take into account spatial spread in the energy change rates within the acceleration process such that energy fluctuations [81, 82] which are considered minor for the purpose of this work.

It must be emphasized that since we are dealing with solar energetic particles, the well-known phenomena of Forbush decreases are rather related with galactic cosmic rays but not necessarily with solar energetic protons (e.g. [20]).

To establish the particle spectrum, we shall follow the assumptions that under the present simplified conditions lead to similar results that are obtained by solving a Fokker-Planck type transport equation on similar conditions [36, 81], that is, when the steady-state is reached in the source: we assume that a suprathermal flux with similar energy or a Maxwellian particle distribution is present in the region where the acceleration process is operating and a fraction $\boldsymbol{N_0}$ of them can be accelerated during the time interval in which the stochastic acceleration mechanism is acting [93]. The selection of particles follows to the fact that their energy must be ≥ than a critical energy, E_c, determined by the competition of acceleration and by local energy losses. By analogy with radioactive decay the energy distribution of cosmic ray particles is assumed as an exponential distribution in age of the form

$$N(E)dE = N(t)dt = \frac{N_0}{\tau} \exp\left(-t/\tau\right)dt \tag{8}$$

which in terms of the Lorentz factor is expressed as

$$N(\gamma)d\gamma = \left(1/Mc^2\right)N(t)\mathrm{dt} \tag{8.1}$$

where $\boldsymbol{t}$ is the necessary time to accelerate particles up to the energy E and $\boldsymbol{\tau}$ is considered as a mean confinement time of particles in the acceleration process. Eq. (8) represents hence the differential spectrum of the accelerated particles; to obtain the integral spectrum we take the integration of (8) up to the maximum energy of the accelerated protons, E_m (corresponding to the upper cutoff in the particle spectrum) the existence of which has been shown by [43] as discussed before.

$$J(>E) = \int_E^{E_m} N(E)dE = \int_t^{t_m} N(t)dt = N_0 \int_t^{t_m} \frac{e^{-t/\tau}}{\tau} dt = N_0\left[e^{-t/\tau} - e^{-t_m/\tau}\right] \tag{9}$$

where t_m is the acceleration time up to the high energy cutoff. Because the acceleration process is competing with energy loss processes, the net energy gain rate is effectively fixed on particles, only beginning at a certain threshold value, E_c defined by $(dE/dt) = 0$, such that only particles with $E > E_c$ are able to participate in the acceleration process (the flux N_0). Thus the acceleration time $\boldsymbol{t}$ is defined as

$$t = \int_{E_c}^{E} \left(\frac{dE}{dt}\right) dt = t(E) - t(E_c) \tag{10}$$

Similarly the constant value t_m, representing the acceleration time up to the high energy cutoff, E_m defined as $t_m = t(E_m) - t(E_c)$, where $t(E_c)$ denotes the time of the acceleration onset. Therefore, Eq. (9) can be rewritten as

$$J(>E) = N_0 e^{t(E_c)/\tau}\left[e^{-t(E)/\tau} - e^{-t(E_m)/\tau}\right] \tag{11}$$

4.1. The spectrum of acceleration

For the case in·which energy losses are completely unimportant within the acceleration time scale, the net energy change rate is determined by the acceleration rate, Eq.(1), which for simplicity's sake, we shall represent hereafter in terms of the Lorentz factor γ as

$$\left(\frac{d\gamma}{dt}\right) = \alpha\left(\gamma^2 - 1\right)^{1/2} \tag{12}$$

the condition $(d\gamma/dt) = (d\gamma/dt)_{acc} - (d\gamma/dt)_{loss} = 0$ gives $\boldsymbol{\gamma_c} = 1$ (and hence $E_c = 0$), such that by integration of (12) we obtain the acceleration time up to the energy $E = Mc(\gamma-1)$ as

$$t = \frac{1}{\alpha}\ln\left[\gamma + \left(\gamma^2 - 1\right)^{1/2}\right] \tag{13}$$

Now, by substitution of (13) in Eq. (8.1), we obtain the following differential spectrum

$$N(\gamma) = \frac{N_0}{\alpha\tau Mc^2}\left(\gamma^2 - 1\right)^{-1/2}\left[\gamma + \left(\gamma^2 + 1\right)^{1/2}\right]^{-1/\alpha\tau} \tag{14}$$

which in terms of total energy W is expressed as

$$N(W) = \frac{N_0}{\alpha\tau}\left(Mc^2\right)^{1/\alpha\tau}\frac{(1+\beta)^{-1/\alpha\tau}}{\beta}W^{-(1+1/\alpha\tau)} = \frac{N_0}{\alpha\tau}\left(Mc^2\right)^{1/\alpha\tau}\frac{\left\{W + \left(W^2 - \left(Mc^2\right)^{1/2}\right)\right\}^{1/\alpha\tau}}{\left(W^2 - \left(Mc^2\right)^2\right)^{1/2}} \tag{14.1}$$

When the parameter β is considered outside of the integrating equations a somewhat different expression is obtained:

$$N(W) = \frac{N_0}{\alpha\beta\tau}\left(Mc^2\right)^{1/\alpha\beta\tau}W^{-\left(1+1/\alpha\beta\tau\right)}$$

The corresponding integral spectrum of the accelerated particles appears from Eqs. (11)–(13) as

$$J(>E) = N_0\left[\left[\gamma + \left(\gamma^2 - 1\right)^{1/2}\right]^{-1/\alpha\tau} - \left[\gamma_m + \left(\gamma_m^2 - 1\right)^{1/2}\right]^{-1/\alpha\tau}\right] \tag{15}$$

(where) $\gamma_m = \left(E_m + Mc^2\right)/Mc^2$

the integral spectrum expressed in terms of kinetic energy becomes,

$$J(>E) = N_0\left(Mc^2\right)^{1/\alpha\tau}\left\{\left[E + Mc^2 + \sqrt{E^2 + 2Mc^2E}\right]^{-I/\alpha\tau} - \left[E_m + Mc^2 + \sqrt{E_m^2 + 2Mc^2E_m}\right]^{-I/\alpha\tau}\right\} \tag{15.1}$$

4.2. The modulated spectrum in the acceleration region

In order to study local modulation of spectrum (14) or (15) during acceleration, we shall proceed to consider energy loss processes together with the energy gain rate (12), according to the processes discussed in Section 2.

4.2.1. Modulation by collisional losses

When collisional losses are not negligible during acceleration, the net energy change rate is determined by (2) and (12) as

$$\frac{d\gamma}{dt} = \alpha\left(\gamma^2 - 1\right)^{1/2} - \left(b/Mc^2\right)\gamma\left(\gamma^2 - 1\right)^{-1/2} \tag{16}$$

where $b = 7.62 \times 10^{-9}$ nL, then, the solution of (16) is easily performed by employing a change of variable of the form $x = [(\gamma - 1)/(\gamma + 1)]$ [90], such that the acceleration time from the critical energy E_c up to the energy E, in terms of the Lorentz factor is

$$t = \ln\left|\frac{1+x}{1-x}\right|^{1/\alpha}\left|\frac{\phi^{1/2}x - (-Y_2)^{1/2}}{\phi^{1/2}x - (-Y_2)^{1/2}}\right|^{p} + \xi\tan^{-1}\left[x\left(\phi/Y_1\right)^{1/2}\right]\Big|\begin{matrix} x \\ x_c \end{matrix} = t(x) - t(x_c) \tag{17}$$

with $\varphi = b/Mc^2$, $Y_1 = 2\alpha + (4\alpha^2 + \varphi^2)^{1/2}$, $Y_2 = 2\alpha - (4\alpha^2 + \varphi^2)^{1/2}$, $p = Y_3/[2(-Y_2)^{1/2}\varphi^{1/2}]$, $Y_3 = (2\varphi/\alpha)[(\varphi\text{-}Y_2)/(Y_1\text{-}Y_2)]$, $Y_4 = (2\varphi/\alpha)[(Y_1\text{-}\varphi)/(Y_1\text{-}Y_2)]$, $\zeta = Y_4/(\varphi Y_1)^{1/2}$ and $x_c = [(\gamma_c\text{-}1)/(\gamma_c + 1)]^{1/2}$, where $\gamma_c = (b/2\alpha Mc^2) + 1$ is the critical value for acceleration determined by $(d\gamma/dt) = 0$, and the constant value $t(x_c)$ corresponds to the value of $t(E_c)$ appearing in Eq. (10). The differential spectrum of particles is obtained by substituting of (Eq. 17) in Eq. (8′) as follows

$$N(\gamma) = \frac{N_0}{\tau Mc^2}e^{t(x_c)/\tau}\frac{\left(\gamma^2 - 1\right)^{1/2}}{\left[\alpha(\gamma^2 - 1) - \phi\gamma\right]}\left(\frac{1+x}{1-x}\right)^{-1/\alpha\tau}\left[\frac{\phi^{1/2}x - (-Y_2)^{1/2}}{\phi^{1/2}x + (-Y_2)^{1/2}}\right]^{-\varnothing/2}\exp\left[(-q/\tau)\tan^{-1}\left[x\left(\phi/Y_1\right)^{1/2}\right]\right] \tag{18}$$

The integral spectrum is then from Eq. (11) and Eq. (17)

$$J(>E) = N_0\exp\left(t(x_c)/\tau\right)\left\{\left(\tfrac{1+x}{1-x}\right)^{-1/\alpha\tau}\left(\frac{\phi^{1/2}x - (Y_2)^{1/2}}{\phi^{1/2}x + (Y_2)^{1/2}}\right)^{-p/2}\exp\left[\left(-\frac{q}{\tau}\right)\tan^{-1}\left[x\left(\phi(Y_1)^{1/2}\right]\right]\right.$$
$$\left. - \exp\left(-t(x_m)/\tau\right)\right\} \tag{19}$$

where $t(x_m)$ corresponding to $t(E_m)$ in Eq. (11), appearing from the evaluation of Eq. (17) in the constant value $x_m = \left[\left(\gamma_m - 1\right)/\left(\gamma_m + 1\right)\right]^{1/2}$. It can be seen that spectra (18) or (19)reduces to (14) or (15) when b = 0. The integral spectrum in terms of kinetic energy is expressed as

$$J(>E) = N_0 \exp\left(\frac{t(E_i)}{\tau}\right)\left\{\left[\left|\frac{\varepsilon+E+Mc^2}{Mc^2}\right|^{-1/\alpha\tau}\left|\frac{(E-E_1)-\varepsilon+\left[E_1\left(E_1+2Mc^2\right)\right]^{\frac{1}{2}}}{(E-E_1)-\varepsilon-\left[E_1(E_1+2Mc^2)\right]^{\frac{1}{2}}}\right|^{-p}\right.\right.$$
$$\left.\left.\times \exp\left(\frac{-\left[E_2\left(-E_2-2Mc^2\right)\right]^{\frac{1}{2}}}{\alpha\tau(E_1-E_2)}\tan^{-1}\left(\frac{E\left(E_2+Mc^2\right)+Mc^2E_2}{\varepsilon E_2(-E_2-2Mc^2)}\right)\right)\right] - \exp\left(\frac{-t(E_m)}{\tau}\right)\right\} \tag{19.1}$$

with $p = \frac{\left[E_1\left(E_1+2Mc^2\right)\right]^{1/2}}{\alpha\tau(E_1-E_2)}, = \left(E^2+2Mc^2E\right)^{1/2}$, $E_i = b/2\,\alpha$ is the threshold value for effective acceleration and E_1, E_2 correspond respectively to $\left\{\left[b \pm \left(b^2+4\alpha^2\left(Mc^2\right)^2\right)^{1/2}\right]/2\alpha\right\}$. It can be seen that spectrum (19.1) reduces a spectrum (15.1) when $b = 0$.

The corresponding particle energy spectrum to Eq. (2′) is developed in the Appendix.

4.3. Modulation by proton-proton nuclear collisions

In the event that proton-proton collisions are important during the acceleration process. By adding Eq. (4), the net energy rate (16) turns into the following expression

$$\frac{d\gamma}{dt} = \alpha\left(\gamma^2-1\right)^{1/2} - \left(b/Mc^2\right)\gamma\left(\gamma^2-1\right)^{-1/2} - \left[h\left[Mc^2(\gamma-1)^{-2} + j\left[Mc^2(\gamma-1)\right]^{-1} + f + \eta\right]\right](\gamma-1)^{1/2} \tag{20}$$

The critical value γc for acceleration resulting when $(d\gamma/dt) = 0$ is obtained by solving a cubic equation of the form $A\gamma^3 + B\gamma^2 + C\gamma + D = 0$ with $A = \alpha(Mc^2)^2$, $B = -A-(b+j)Mc^2$, $C = -A + bMc^2 - h$, $D = A + jMc^2 - h$ if $E \leq 110$ MeV, or, $A = (\alpha - f)(Mc^2)^2$, $B = -A - bMc^2$, $C = -A + bMc^2 - h$, $D = A - h$ if $110 < E \leq 290$ MeV and for the range $E > 290$ MeV similar to the last one but with $A = (\alpha - f - \eta)(Mc^2)^2$. Therefore, the roots a_1, a_2 and a_3 depend on α, b, h, j, f and η, such than when a medium concentration n is fixed, the basic dependence remains on α. Given that for the bulk of the involved parameters the conditions $a_1 > 1$, $a_2 \leq -1$ and $0 < a_3 \leq 1$ are systematically satisfied through all the energy ranges the relation $E_c = Mc^2\,(\gamma_c - 1)$ states a_1 as the critical value for effective acceleration. The acceleration time of particles beginning with this critical value up to the energy E is obtained from Eq. (20) as

$$t = \frac{1}{\lambda}\left\{\ln\left[\left|2\left(\gamma^2-1\right)^{1/2}+2\gamma\right|^{A_1a_1+A_2a_2+A_3a_3}\left|\frac{\gamma-a_1}{2\left(a_1^2-1\right)^{1/2}\left(\gamma^2-1\right)^{1/2}+2a_1\gamma-2}\right|^{A_1\left(a_1^2-1\right)^{1/2}}\right]\right.$$
$$\left. -\left[A_2\left(1-a_2^2\right)^{1/2}\sin^{-1}\left(\frac{a_2\gamma-1}{|\gamma-a_2|}\right) + A_3\left(1-a_3^2\right)^{1/2}\sin^{-1}\left(\frac{a_3\gamma-1}{|\gamma-a_3|}\right)\right] - t\left(\gamma_c\right)\right\} \tag{21}$$

where the constants. $A_1 = (a_1-1)(a_2-a_3)/\xi$, $A_2 = (a_2-1)(a_3-a_1)/\xi$ and $A_3 = (a_3-1)\,(a_1-a_2)/\xi$ emerge from the integration by partial fractions of Eq. (20), with $\xi = {a_1}^2(a_2-a_3) + {a_2}^2(a_3-a_1) + {a_3}^2(a_1-a_2)$, and take on different values according to the energy range concerned;

$\lambda = \alpha$ (if E ≤ 110 MeV), $\lambda = \alpha - f$ (if 110 < E ≤ 290 MeV) and $\lambda = \alpha - f - \eta$ (if E > 290 MeV). The differential spectrum in this case follows from Eqs. (8.1) and (20) as

$$N(\gamma) = \frac{N_0 Mc^2}{\tau} e^{t(\gamma_c)/\tau} \left|2\left(\gamma^2-1\right)^{1/2} + 2\gamma\right|^{-\delta} \left|\frac{\gamma - a_1}{2(a_1\gamma - 1) + 2\left(a_1^2 - 1\right)^{1/2}\left(\gamma^2-1\right)^{1/2}}\right|^{-\delta_1}$$
$$\exp\left[-\delta_2 \sin^{-1}\left(\frac{a_2\gamma - 1}{|\gamma - a_2|}\right) - \delta_3 \sin^{-1}\left(\frac{a_3\gamma - 1}{|\gamma - a_3|}\right)\right] \frac{(\gamma - 1)\left(\gamma^2-1\right)^{1/2}}{A\gamma^3 + B\gamma^2 + C\gamma + D} \tag{22}$$

where $\delta = (A_1a_1 + A_2a_2 + A_3a_3)/\lambda\tau$, $\delta_1 = A_1(a_1{}^2-1)^{1/2}\lambda\tau$, $\delta_2 = A_2(1 - a_2{}^2)^{1/22}/\lambda\tau$ and $\delta = A_3(1-a_3{}^2)^{1/2}/\lambda\tau$; therefore, the integral spectrum is given from (Eq. 11) and Eq. (21) as

$$J(>E) = N_0\left(Mc^2\right)^2 \left\{ e^{t(\gamma_c)/\tau}\left|2\left(\gamma^2-1\right)^{\frac{1}{2}} + 2\gamma\right|^{-\delta} \left|\frac{\gamma - a_1}{2(a_1\gamma-1) + 2\left(a_1^2-1\right)^{\frac{1}{2}}\left(\gamma^2-1\right)^{\frac{1}{2}}}\right|^{-\delta_1} \right.$$
$$\left. \times \exp\left[-\delta_2 \sin^{-1}\left(\frac{a_2\gamma - 1}{|\gamma - a_2|}\right) - \delta_3 \sin^{-1}\left(\frac{a_3\gamma - 1}{|\gamma - a_3|}\right)\right] exp\left[-t\left(\gamma_m\right)/\tau\right] \right\} \tag{23}$$

which in terms of kinetic energy becomes,

$$J(>E) = N_0 \exp\left(\frac{t(E_i)}{\tau}\right)\left\{\left[\left|\frac{2}{Mc^2}\left[\left(E^2 + 2Mc^2E\right)^{1/2} + E + Mc^2\right]\right|^{-\delta_1} \left|\frac{2\left(a_1^2-1\right)\left(E^2+2Mc^2E\right)^{1/2} + 2a_1E + 2Mc^2(a_1-1)}{E + Mc^2(1-a_1)}\right|^{\delta_2}\right.\right.$$
$$\left.\left. \cdot\left(\exp\left[A_2\left(1-a_2^2\right)^{1/2}\sin^{-1}\left(\frac{a_2E + (a_2-1)Mc^2}{|E + (1-a_2)Mc^2|}\right) + A_3\left(1-a_3^2\right)^{1/2}\sin^{-1}\left(\frac{a_3E + (a_3-1)Mc^2}{|E + (1-a_3)Mc^2|}\right)\right]\right)^{\delta_3}\right] - \exp\left(\frac{-t(E_m)}{\tau}\right)\right\} \tag{23.1}$$

where
$\delta_1 = \left[\left(Mc^2\right)^2/Q\tau\right](a_1A_1 + a_2A_2 + a_3A_3 +)$, $\delta_2 = \left[\left(Mc^2\right)^2/Q\tau\right]A_1(a_2-1)^{1/2}$, $\delta_3 = \left(Mc^2\right)^2/Q\tau$
and Q, A_1, A_2, A_3, a_1, a_2, a_3, are constants that depend on α, b, η, h, j and f which emerge from the integration by partial fractions and take different values throughout the three different range considered.

4.4. Modulation by adiabatic processes

Under the consideration of adiabatic deceleration of protons while the acceleration mechanism is acting, the net energy change rate Eq. (20), is transformed by addition of Eq. (6) in

$$\frac{d\gamma}{dt} = \alpha\left(\gamma^2-1\right)^{1/2} - \left(Mc^2\right)\gamma\left(\gamma^2-1\right)^{-1/2} - \left\{h\left[Mc^2(\gamma-1)\right]^{-2} + j\left[Mc^2(\gamma-1)^{-1} + f + \eta\right]\right\}$$
$$\times\left(\gamma^2-1\right)^{1/2} - \rho\left(\gamma^2-1\right)\gamma^{-1} \tag{24}$$

The condition $(d\gamma/dt) = 0$ for determining γ_c in this case, leads to a transcendental equation of the form $E\gamma^4 + F\gamma^3 + G\gamma^2 + H\gamma + I(\gamma-1)(\gamma^2-1)^{3/2} = 0$, whose solution depends only on $\boldsymbol{\alpha}$, $\boldsymbol{n}$ and very weakly on ρ, and where $E = \alpha(Mc^2)^2$, $F = -E-(b+j)Mc^2$, $G = -E-h+bMc^2$, $H = E-h+jMc^2$ and $I = -\rho(Mc^2)^2$ in the range $E \leq 110$ MeV. Therefore, since critical energy for acceleration is defined in the low energy range, the wide interval $1.0 \leq \gamma \leq 1.1$ states a unique value of γ_c for any acceleration parameter α when the values of n and ρ are fixed. In order to deduce the particle spectrum, we have simplified Eq. (24) by changing variable $Z = \gamma-(\gamma^2-1)^{1/2}$, thus, obtaining in this way a rational function which integration by partial fractions gives the following acceleration time

$$t = \frac{1}{k}\left\{\left[ln\left(\left|z^2+R_1z+R_2\right|^{c_{1/2}}\left|z^2+R_3z+R_4\right|^{c_{3/2}}\left|z^2+R_5z+R_6\right|^{c_{5/2}}\left|z^2+R_7z+R_8\right|^{c_{7/2}}z^{c_9}\left|\frac{2z+R_1-(\Delta_1)^{1/2}}{2z+R_1+(\Delta_1)^{1/2}}\right|^{k_1}\right)\right.\right.$$
$$\left.\left.+k_2\,tan^{-1}\left(\frac{2z+R_3}{(-\Delta_2)^{1/2}}\right)+k_3\,tan^{-1}\left(\frac{2z+R_5}{(-\Delta_3)^{1/2}}\right)+k_4\,tan^{-1}\left(\frac{2z+R_7}{(-\Delta_4)^{1/2}}\right)\right]-t(z_c)\right\} \tag{25}$$

where $K_1 = (2C_2 - R_1C_1)/2\Delta_1^{1/2}$, $K_2 = (2C_4 - R_3C_3)/(-\Delta_2)^{1/2}$, $K_3 = (2C_6 - R_5C_5)/(-\Delta_3)^{1/2}\mathrm{K}_1$

$K_4 = (2C_8 - R_7C_7)/(-\Delta_4)^{1/2}$; R_1, R_2, … R_8 are the coefficients of the quadratic factors Δ_1, Δ_2, Δ_3 and Δ_4 their discriminants, corresponding to two real and six complex roots of the nine roots of the rational function denominator, and C_1, C_2,. C_9 are the coefficients of the linear factors. For a given value of the acceleration efficiency $\boldsymbol{\alpha}$ all the quantities involved in (25) become constants and take on different values according to the three energy intervals studied. The factor κ is give as $\kappa = \alpha + \rho$ (if $E \leq 110$ MeV), $\kappa = \alpha-f-\eta$ (if $110 < E \leq 290$ MeV) and $\kappa = \alpha-f-\eta+\rho$ (if $E > 290$ MeV). As in the preceding cases, the substitution of Eq. (25) in (8′) furnishes us with a differential spectrum of the form

$$N(\gamma) = \frac{N_0}{Mc^2k\tau}e^{t(z_c)/\tau}\left(\frac{-z^8+2z^7-2z^5+2z^4-2z^3+2z-1}{z^8+Jz^7+Mz^6+Nz^5+Pz^4+Qz^3+Rz^2+Sz+V}\right)$$
$$\times\left\{\left(\left|z^2+R_1z+R_2\right|^{-\theta_1}\left|z^2+R_3z+R_4\right|^{-\theta_2}\left|z^2+R_5z+R_6\right|^{-\theta_3}\left|z^2+R_7z+R_8\right|^{-\theta_4}\right.\right.$$
$$\left.\left.\times\left|\frac{2z+R_1-(\Delta_1)^{1/2}}{2z+R_1+(\Delta_1)^{1/2}}\right|^{-\theta_5}z^{-\theta_6}\right)exp\left[\theta_7\,tan^{-1}\left(\frac{2z+R_3}{(-\Delta_2)^{1/2}}\right)+\theta_8\,tan^{-1}\left(\frac{2z+R_5}{(-\Delta_3)^{1/2}}\right)+\theta_9\,tan^{-1}\left(\frac{2z+R_7}{(-\Delta_4)^{1/2}}\right)\right]\right\} \tag{26}$$

$\Theta_1 = c_1/2\kappa\tau$, $\Theta_2 = c_3/2\kappa\tau$, $\Theta_3 = c_5/2\kappa\tau$, $\Theta_4 = c_7/2\kappa\tau$, $\Theta_5 = K_1/2\kappa\tau$, $\Theta_6 = c_9/2\kappa\tau$, $\Theta_7 = (-K_2)/\kappa\tau$, $\Theta_8 = (-K_3)/\kappa\tau$ *and* $\Theta_9 = (-K_4)/\kappa\tau$, $J = 2(F+I)/V$, $M = (4E+4G+2I)/V$, $N = (6F+8H-GI)/V$, $P = (GE+8G)/V$, $Q = (GP+8H+GI)/V$, $R = (4E+4c-2I)/I$, $S = 2(F-I)/V$, $V = (E+I)/V$ and $V = E-I$. The values of E, F, G, H, I in the range $E < 110$ MeV are the values given above; in the range $110 < E \leq 290$ MeV, $\mathrm{E} = (\alpha-\mathrm{f})(\mathrm{Mc}^2)^2$, $\mathrm{F} = \mathrm{E}-\mathrm{bMc}^2$, $\mathrm{G} = -\mathrm{E}+\mathrm{bMc}^2$, $\mathrm{H} = \mathrm{E}-\mathrm{h}$ and $\mathrm{I} = \rho(\mathrm{Mc}^2)^2$. In the range $E > 290$ MeV the only difference with the precedent range is $E = (\alpha-f-\eta)(Mc^2)^2$. The constant $t(Z_c)$ is the evaluation of (25) in the threshold value $Z_c = \gamma_c-({\gamma_c}^2-1)^{1/2}$. The integral spectrum according Eq. (11) is,

$$J(>E) = N_0 e^{t(z_c)/\tau}\Big\{\Big(\left|z^2+R_1z+R_2\right|^{-\theta_1}\left|z^2+R_3z+R_4\right|^{-\theta_2}\left|z^2+R_5z+R_6\right|^{-\theta_3}\big|z^2+R_7z$$
$$+R_8\big|^{-\theta_4}\left|\tfrac{2z+R_1-(\Delta_1)^{1/2}}{2z+R_1+(\Delta_1)^{1/2}}\right|^{-\theta_5}\left|z^{-\theta_6}\right|\Big)\, exp\left[\theta_7\, tan^{-1}\left(\frac{2z+R_3}{(-\Delta_2)^{1/2}}\right)+\theta_8\, tan^{-1}\left(\frac{2z+R_5}{(-\Delta_3)^{1/2}}\right)\right. \tag{27}$$
$$\left.+\theta_9\, tan^{-1}\left(\frac{2z+R_7}{(-\Delta_4)^{1/2}}\right)\right] - \exp\left(-t(z_m)/\tau\right)\Big\}$$

where $t(Z_m)$ is the evaluation of Eq. (25) in $Z=\gamma_m-\left(\gamma_m^2-1\right)^{1/2}$ corresponding to the high energy cutoff value in the acceleration process.

In order to express the previous equation as a function of the kinetic energy E, the variable Z should be written as $Z(E)=\left(E+Mc^2\right)-\left(E^2+2EMc^2\right)^{1/2}$ and $Z(E)_m=\left(E_m+Mc^2\right)-\left(E_m^2+2E_mMc^2\right)^{1/2}$.

It is also interesting to analyze the opposite case, when instead of an expansion of the source materials, there is a compression of the source medium (e.g. [101–103]) with a consequent adiabatic acceleration of the flare particles, which entail a change of sign in the last term of the net energy change rate (24). Let us develop the situation for which energy losses are completely negligible in relation to the acceleration rate during the stochastic particle acceleration and compression of the local material

$$(d\gamma/dt)=\alpha\left(\gamma^2-1\right)^{-1/2}+\rho\left(\gamma^2-1\right)\gamma^{-1} \tag{28}$$

As in the case of Eq. (12) the threshold for acceleration is meaningless, and thus the acceleration time up to the energy E is given as

$$t=ln\left(\left|\frac{\gamma}{\alpha\gamma+\rho(\gamma^2-1)^{\frac{1}{2}}}\right|^{\chi}\left|\frac{\gamma+\left(\gamma^2-1\right)^{\frac{1}{2}}}{\gamma-\left(\gamma^2-1\right)^{\frac{1}{2}}}\right|^{\psi}\gamma^{\omega}|\alpha|^{\chi}\right) \tag{29}$$

where $=\frac{\rho}{(\alpha^2-\rho^2)}$, $\psi=\frac{\alpha}{2(\alpha^2-\rho^2)}$ *and* $\omega=\frac{\rho}{\rho^2-\alpha^2}$, consequently, the differential spectrum of particles is

$$N(\gamma)d\gamma=\frac{N_0}{mc^2\tau|\alpha|^{\chi/2}}\left|\frac{\gamma}{\alpha\gamma+\rho(\gamma^2-1)^{\frac{1}{2}}}\right|^{-\chi/\tau}\left|\frac{\gamma+\left(\gamma^2-1\right)^{\frac{1}{2}}}{\gamma-\left(\gamma^2-1\right)^{\frac{1}{2}}}\right|^{-\psi/\tau}\frac{\gamma^{(1-\omega/\tau)}d\gamma}{(\gamma^2-1)^{\frac{1}{2}}\left[\alpha\gamma+\rho(\gamma^2-1)^{\frac{1}{2}}\right]} \tag{30}$$

and then the integral spectrum is simply given as

$$J(>E)=\frac{N_0}{|\alpha|^{\chi/2}}\left(\left|\frac{\gamma}{\alpha\gamma+\rho(\gamma^2-1)^{\frac{1}{2}}}\right|^{-\chi/\tau}\left|\frac{\gamma+\left(\gamma^2-1\right)^{\frac{1}{2}}}{\gamma-\left(\gamma^2-1\right)^{\frac{1}{2}}}\right|^{-\psi/\tau}\gamma^{-\omega/\tau}-e^{-t\left(\gamma_m\right)/\tau}\right) \tag{31}$$

which in terms of kinetic energy becomes,

$$J(>E) = \frac{N_0}{|\alpha|^{\chi/2}} \left(\left| \frac{E + Mc^2}{\alpha(E + Mc^2) + \rho\left(E^2 + 2EMc^2\right)^{1/2}} \right|^{-\chi/\tau} \left| \frac{\left(E + Mc^2\right) + \left(E^2 + 2EMc^2\right)^{1/2}}{\left(E + Mc^2\right) - \left(E^2 + 2EMc^2\right)^{1/2}} \right|^{-\psi/\tau} \right.$$
$$\left. \left[\left(E + Mc^2\right)/Mc^2\right]^{-\omega/\tau} - e^{-t\left[\left(E_m + Mc^2\right)/Mc^2\right]/\tau} \right) \tag{31.1}$$

It is worth mentioning that although it is expected that the critical energy for acceleration E_c increases while adding energy loss process to the net energy charge rate, nevertheless, the value of E_c resulting from Eq. (24) is essentially the same as that obtained from Eq. (20). This can be understood from **Figure 1**, because adiabatic cooling is practically negligible at low energies.

5. Procedure and results

As seen in the preceding section, the calculation of our theoretical spectra, Eqs. (15),(19), (23), (27) and (31) requires three fundamental parameters, one of them directly related to the physical state of flare regions, that is, the medium concentration n, and the others concerning the acceleration mechanism itself, that is, the acceleration efficiency α and the mean confinement time τ. These last two depend of course on some of the physical parameters of the source, which we attempt to estimate from the appropriate values of α and τ. In the case of the solar source, we have considered the mean value of the electron density and a conservative value for the proton population as $n_e \approx n_H = 10^{13}$ cm^{-3} (e.g. [19, 35, 56, 113, 114, 116, 118]).

This assumption locates the acceleration region in chromospheric densities in agreement with some analysis of the charge spectrum of solar cosmic rays [64, 92].

Besides, since our expressions contain the acceleration parameter as the product $\alpha\tau$ and since we are dealing with particles of the same species, for the sake of simplicity we have adopted the assumption $\tau = 1 \cdot s$ which allows us to separate the behavior of the acceleration efficient α in order to analyze it through several events and several source conditions. In any event, this value falls within the generally accepted range (e.g. [130, 131]); we shall discuss the implications of this assumption in the next section.

The determination of $\boldsymbol{\alpha}$ has been carried out through the following procedure: in order to represent the theoretical spectrum within the same scale as that of the experimental curve, we have normalized both fluxes at the minimum energy for which available experimental data are effectively trustworthy, in such a way as to state the maximum flux of particles at the normalization energy, E_{nor}

$$\left[J(>E)_{acc}\right]_{E_{nor}} = q\left[J(>E)_{earth}\right]_{E_{nor}} \tag{32}$$

where q is the normalization factor. Since our expressions do not directly furnish the source integral spectrum but rather $J(>E)/N_0$, we have deduced in this way a normalization flux K_0, keeping the same proportion with the differential flux N_0 appearing in our expressions

$$N_0 = qk_0 = protons/4\pi R_{SE}^2 s \quad \left(\text{protons}/\text{cm}^2 \text{ str } s\right) \tag{33}$$

where $R_{SE} = 1.5 \times 10^{13} cm$ = sun-earth distance. We have listed E_{nor} for every event on columns 8 of **Tables 1–3**.

The value of N_0 for every event is tabulated on columns 10 of **Tables 1–3**.

Assuming that the theoretical curve among Eqs. (15), (19), (23), (27) and (31) is near the experimental curve in a given event, describes the kind of phenomena occurring at the source better, we have proceeded to perform this intercomparison according to the following criterion: first, the condition stated by Eq. (32) at the normalization energy and, second, that $J(>E) \approx 0$ at the high energy cutoff E_m. In order to compare each one of the theoretical spectra with an

Hot Events		Specrum (31)	Spectum (15)	Specrum (19)	Specrum (23)	Specrum (27)	E_m (GeV)	E_n (MeV)	N_0(protons/cm^2 s str)
28/01/1967	$\alpha(s^{-1})$	0.18	0.18	0.19	0.23	0.21	4.30	10.00	$2.1\text{x}10^{-12}$
	E_c(MeV)	*****	*****	5.26	11.57	12.67			
01/09/1971	$\alpha(s^{-1})$	0.21	0.21	0.22	0.24	0.23	2.30	30.00	$9.9\text{x}10^{-13}$
	E_c(MeV)	*****	*****	4.54	11.09	11.57			

Table 1. Characteristic parameters of the acceleration process in solar protons ***hot*** events: acceleration efficiency α, high energy cutoff E_m, normalization energy E_n, flux of accelerated particles in the source N_0 and heliographic coordinates of the flare according to different reports.

Hot Events		Specrum (31)	Spectum (15)	Specrum (19)	Specrum (23)	Specrum (27)	E_m (GeV)	E_n (MeV)	N_0(protons/cm^2 s str MeV)
12/11/1960	$\alpha(s^{-1})$	0.13	0.14	0.17	0.26	0.26	2.600	15.000	3.891x10-11
	E_c(MeV)	15.32	14.30	13.45	9.67	10.58			
04/08/1972	$\alpha(s^{-1})$	0.59	0.60	0.70	0.90	0.93	4.280	15.000	1.979x10-11
	E_c(MeV)	4.28	4.21	3.87	3.06	2.97			
03/09/1960	$\alpha(s^{-1})$	0.72	0.73	0.83	0.98	0.99	2.960	10.000	4.704x10-16
	E_c(MeV)	2.96	2.92	2.77	2.40	2.39			
30/03/1969	$\alpha(s^{-1})$	0.91	0.92	0.95	0.99	1.08	2.340	50.000	1.449x10-15
	E_c(MeV)	2.34	1.18	2.42	2.38	2.48			
02/11/1969	$\alpha(s^{-1})$	1.54	1.55	1.76	2.10	2.59	0.915	10.000	2.342x10-11
	E_c(MeV)	0.84	0.84	0.81	0.66	1.05			

Table 2. Characteristic parameters of the acceleration process in solar protons ***cold*** events: acceleration efficiency α, high energy cutoff E_m, normalization energy E_n, flux of accelerated particles in the source N_0 and heliographic coordinates of the flare according to different reports.

Hot Events		Specrum (31)	Spectum (15)	Specrum (19)	Specrum (23)	Specrum (27)	E_m (GeV)	E_n (MeV)	N_0(protons/ cm^2 s str MeV)
15/11/1968	α(s^{-1})	0.16	0.16	0.18	0.23	0.25	2.60	20.00	4.550x10-13
	E_c(MeV)	*****	*****	12.68	11.22	11.03			
18/11/1968	α(s^{-1})	0.20	0.20	0.21	0.26	0.28	4.80	20.00	6.400x10-11
	E_c(MeV)	*****	*****	13.17	11.62	10.84			
07/07/1966	α(s^{-1})	0.23	0.23	0.35	0.36	0.39	2.70	10.00	1.376x10-16
	E_c(MeV)	*****	*****	2.85	7.40	6.83			
24/01/1971	α(s^{-1})	0.34	0.34	0.35	0.39	0.41	6.90	40.00	1.365x10-12
	E_c(MeV)	*****	*****	6.90	6.62	6.56			
25/02/1969	α(s^{-1})	0.40	0.40	0.41	0.46	0.48	6.57	30.00	6.300x10-15
	E_c(MeV)	*****	*****	6.57	6.18	6.14			

Table 3. Characteristic parameters of the acceleration process in solar protons ***warm*** events: acceleration efficiency α, high energy cutoff E_m, normalization energy E_n, flux of accelerated particles in the source N_0 and heliographic coordinates of the flare according to different reports.

experimental curve under the same conditions, we could proceed to fix the value of the acceleration parameters in advance, which would entails making a priori inferences about the physical parameters of the source involved in the acceleration process of a given solar event; furthermore, this would result in a bias for the interpretation of the phenomenology involved in each event depending on the selected value of the efficiency α; that is, high values would give systematically the best fit with spectrum (27), whereas low values would show a systematically better fit with spectrum (15). Therefore, we proceeded conversely by determining the appropriate parameters of the source from the value of α in the theoretical spectra that best represents the experimental curve. The optimum values of α, obtained for each of the theoretical curves allows us to determine the critical energy E_c and the normalization flux K_o appropriate to each case. We have tabulated the values of α, E_c and K_o obtained for every event through calculations of the spectra (15) (19), (23), (27) and (31) in **Tables 1–3**. We have illustrated the optimum theoretical curves on **Figures 2–4**. From an examination of these results, it can be observed that no general conclusion can be drawn about the behavior of our theoretical spectra by the simple comparison of energy change rates (1), (2), (4) or (6) at different energy values 7 as if the medium density n were the only important parameter in determining the processes occurring at the source. Other factors must intervene, as can be seen from the fact that spectra behavior changes from event to event. Nevertheless, according to the behavior of particle spectra, we can group the solar events in three groups of similar characteristics: those illustrated in **Figure 2**, which we shall denominate *hot events*, where it can be seen that theoretical spectra progressively approach the experimental curves while adding energy loss processes to the acceleration rate. Therefore, the physical processes taking place at the source in those events are described by spectrum (27) indicating that adiabatic cooling of protons together with energy degradation from p–p collisions and collisional losses may have taken place. In this case spectrum (31) (illustrated only in the January 28, 1967 event) is systematically the more deflected curve, showing the absence of adiabatic compression, at least during the acceleration period. **Figure 3** shows the second group which we will call *cold events*, and where it can be seen that energy losses are not important within the time scale of the acceleration process because theoretical curves get progressively separate from the experimental one while adding energy loss processes. Actually the best systematic approach in these cases is obtained with spectrum (31) (illustrated only for November 12, 1960 event) indicating that acceleration of protons by adiabatic compression could have taken took place. The third group that we shall distinguish as *warm* events is represented in **Figure 4**, where we can observe that there is no systematic tendency as compared to the previous groups. Nevertheless, it can be seen that at least at low energies the best approach to the experimental curve is described by spectrum (23), whereas at high energies the best fit is obtained with spectrum (15), thus indicating that to greater or lesser degree energy losses by collisional losses and proton-proton collisions may be important on low energy protons but they become negligible in relation to the acceleration rate in high energy particles. The point where this change may occur varies from very low energies in some events (July 7, 1966) to very high energies in others (January 24, 1971). The larger deflection from the experimental curve in these cases is obtained with spectrum (27), indicating that adiabatic expansion do not take place; furthermore, the fact that spectrum (31) (illustrated only for the November 18, 1968 event) is systematically deflected in relation to the acceleration spectrum (15) indicates that there is no adiabatic compression either. The values of the parameters describing the most adequate theoretical spectrum of events of **Figures 2–4** are tabulated on columns 7, 3 and 6 of **Tables 1–3**, respectively.

In order to estimate the amount of local plasma particles that must be picked up by the acceleration process to produce the observed spectrum, are must know the value of N_o in (8) when t = 0. Therefore, roughly assuming that at least for events of (**Figure 3**, **Table 2**), the picked up protons originate in a thermal plasma where the velocities distribution is of a Maxwellian-type, or that they appear from a preliminary heating related to turbulent thermal motions, then, it can be inferred that the primary differential flux is given as, related with the flux defined in Eq. (33).

$$N_0 = \left[9/(2\pi)^{3/2}\right](k/M)^{1/2}e^{3/2}nT^{1/2} \tag{34}$$

where M is the mass of protons and k the of Boltzman's constant. Then, by assuming that K_o is related to the flux of protons involved in the acceleration process and the flux N_o related to the original concentration of the medium, we have estimated from Eq. (33) the fraction of the local plasma particles that were accelerated in each event and tabulated them on columns 10 of **Tables 1–3**. In evaluating (34), we have assumed a different value of temperature T for each one of the 3 groups of events, before discussing them in the next section.

Now let us summarize the results which emerge from **Figures 2–4** and **Tables 1–3**, before extending their interpretation in next section:

1. The events illustrated in **Figure 2**, show the following features:

   i. In September 1, 1971 event, the best fit of the experimental spectrum is obtained with (27) whereas the worst fit is given by (15) and (31).

ii. The January 28, 1967 event follows the same tendency as the preceding event up to ∼800 MeV, with an exception at very low energies (≤ 30 MeV) where it can be seen that spectrum (23) is slightly better than (27). Beyond ∼800 MeV spectrum (23) becomes the more deflected curve. The low particle energy flux tail is noticeably similar to the minimum theoretical energy for effective acceleration ($E_c \sim 12$ MeV).

2. The events of **Figure 3** show that:

The best fit of the experimental curve is systematically given by spectrum (31) and (15) (e.g. the November 12, 1960 event), whereas spectrum (27) is systematically the most deflected one.

3. The events of **Figure 4** show the following characteristics

a. The theoretical curve which best approximates the experimental one at low energies is spectrum (23) followed by spectrum (19).

b. At given energy (from ∼500 to ∼3000 MeV) the previous tendency is abandoned, such that spectrum (15) interchanges sequential order with spectrum (23).

c. Spectrum (27) is systematically the most deflected curve at all energies.

d. Spectrum (31) is systematically deflected in relation to spectrum (15) (e.g. November 18, 1968 event).

e. The July 7, 1966 event, however, by following the feature (a) at E ≤ 25 MeV, beyond this energy spectrum (15) comes nearer to the experimental curve than spectrum (23), whereas spectrum (19) through a progressive, separation becomes the most deflected curve beyond ∼2000 MeV.

4. Examination of **Tables 1–3** shows the following features:

a. For a given event the obtained value of acceleration efficiency α is the same with spectrum (31) and (15) (columns 3 and 4 of **Tables 1** and **3**) contrary to the events of **Table 2**, in which case α is lower with spectrum (31) than with (15).

b. Examination of a given spectrum (same column 5, or, 6 or 7) shows that α and E_c behave in an inversely proportional manner.

c. For a given event, the values of α in the events of **Tables 2** and **3** (columns 4, 5, 6, and 7) increase monotonically while adding energy loss processes to the acceleration rate, with the exception of the events of **Table 1**, in which case the obtained values of α with spectrum (27) decrease in relation to the value of α from spectrum (23).

d. For a given event of **Table 1**, the value of E_c increases monotonically with the addition of an energy loss process to the net energy change rate, whereas in the events of **Tables 2** and **3** the value of E_c obtained from (27) (column 7) decreases in relation to the values obtained from spectrum (23).

e. The obtained value of K_0, (column 10) is related only to the magnitude of the event (i.e. the value of $J(>E)$ at E_n).

f. There is no correlation between E_m and the other parameters of the tables α, E_c, K_0, or heliographic coordinate; neither is there any correlation between the maximum flux at E_n and α or E_c.

g. If we ignore the fact that the assumed heliographic position of the flare associated to the January 28, 1967 event is relatively uncertain, it can be noted that there is a south asymmetry in the what we designate as *hot events* (**Table 1**), a north asymmetry in *cold* and *warm events* (**Table 2**) and a certain west and north asymmetry among the events of **Table 3**.

h. The critical energy E_c from *cold* and *warm* events is correlated with the temperature of the source in the sense that their values increase from *cold* to *warm* and from *warm* to *hot* events. The significance of the association of the parameter temperature to solar proton events will be discussed in Section 6.

6. Discussion

It has been said that we cannot give a general interpretation of our theoretical source spectra behavior on the sole basis of the relationships between the energy change rates (1)–(6) since their behavior in the events of **Figure 2** is different from that in **Figure 3** and both differ from that in **Figure 4**, implying that the kind of processes, their sequence of occurrence and their importance is not the same from event to event To interpret this behavior we cannot remit ourselves to the amount of traversed material, positing that particles originated in the invisible side of the sun or in the eastern hemisphere have lost more energy, because in that case events as such as the March 30, 1969 or February 2, 1969 ones would behave like the events of **Table 1**. Moreover, our hypothesis does not consider deceleration of particles after acceleration, while they traverse the solar atmosphere. Therefore, we believe that the explanation is on the basis of the parameter temperature: that is, we argue that solar proton flares develop under three main different temperature regimes, a low one that we shall denominate *cold* events ($T{\approx}10^3$–$10^{5\circ}$K) (**Table 3**), an intermediate regime that we shall call *warm* events (≈10^5–$l0^{7\circ}$K) (**Table 4**), and a high temperature regime that we shall call hereafter *hot* events (T > 107°K) (**Table 3**). On the basis of this conjecture, let us discuss the main results of the preceding section:

Concerning points 1(a), 1(b) and 1(c), we can comment that as the medium was very hot, collisional losses were very high, making spectrum (18) better than spectrum (15); due to the high temperature and high density in the source nuclear reactions took place and thus spectrum (23) is even closer than (18) to the experimental curve.

Furthermore, the fact that the best fit is given by (27) seems to indicate that beyond a certain temperature, the source material is able to expand and consequently particles which have not escaped the source are adiabatically cooled. In addition, since spectrum (15) is better than (31) it is assumed that compression of the medium did not take place in high temperature regions, and so neither did adiabatic heating of protons. The irregular behavior of spectrum (23) at $E \leq 30$ MeV and $E \geq 800$ MeV in the January 28, 1967 event in relation to the tendency outlined in the last section, may be interpreted as indicating that the low energy protons observed in this event did not originate in. the same process, which explains why the observations show a high flux of protons at energy lower than the threshold acceleration value for in a medium of density $n{\approx}10^{13}\text{cm}^{-3}$• Therefore, these particles may form part of the high energy tail of a preliminary heating process which were not transported by the expanding material. This

http://dx.doi.org/10.5772/intechopen.77052

would mean that only deceleration by collisional losses and p–p collisions took place during the acceleratory process. At high energies, although energy losses from p–p collisions are stronger than collisional losses (**Figure 1**), it can be speculated that the low flux of high energy protons escape very fast from the acceleration region, so that the contribution of this process at high energies was not very important during the time scale of the acceleration.

Concerning point 2 of the last section, we assume that the acceleration process in the events of **Figure 3** was carried out in a low temperature regime so that collisional losses were completely unimportant in relation to the acceleration rate, and nuclear reactions did not take place, at least within the acceleration phase. Furthermore, a compression of the local material is associated with low temperature regimes as indicated by the fact that spectrum (31) systematically gives the best fit to the experimental curves (e.g. November 12, 1960 event).

Points 3(a)–3(d) are interpreted as follows: the temperature and density associated with the acceleration region was high enough to favor nuclear reactions, but not the expansion of source material; consequently, collisional losses of low energy protons were important in the events of **Figure 4**, providing spectrum (23) with a better description of the experimental curve. Also, because the higher temperature does not allow for a compression of the material, spectrum (31) is systematically deflected in relation to spectrum (15). Furthermore, the sudden change in the order of the sequence of curves (15) (19) and (23) is the combined effect of the temperature associated to each event and the importance of the accelerated flux of high energy protons as discussed above with respect to the January 28, 1967 event; the lower the temperature the faster spectrum (19) deflects in relation to (15) (e.g. the November 15, 1960 and November 18, 1968 events); and the higher the flux of the accelerated high energy protons, the later spectrum (23) deflects in relation to (19) (e.g. the February 25, 1969 and January 24, 1971 events).

Related to point 3(e) of last section, it would appeal that the temperature associated with this event was not very high, so that collisional losses were significant only on the low energy protons. Because of the low flux of the accelerated protons in this event, the effect of *p–p* collisions diminishes as energy increases. This event behaves almost like the cold events of **Figure 3**, since energy losses are negligible in relation to the acceleration rate of high energy protons. The reason why beyond 2 GeV spectrum (19) is more deflected than (27) is that the latter includes the *p–p* contribution to this event and collisional losses are unimportant on high energy particles (**Figure 1**). Interpretation of 3(b) and 3(e) must also consider the fact that high energy particles escape faster from the acceleration volume, and so, they are subject to energy degradation by *p–p* collisions during the acceleration time.

The interpretation of 4(a) follows from the fact that in cold events the contribution of the adiabatic heating is translated into a lower effort of the acceleration mechanism; however, in the hot and warm events (**Tables 1** and **3**) adiabatic heating did not occur, and so no effect was produced.

In relation to the interpretation of 4(b) to 4(d) it must be pointed out that the inverse proportionality between $\boldsymbol{\alpha}$ and $\boldsymbol{E_c}$ follows from the fact that for a given situation the requirement for effective acceleration is lowered while the acceleration efficiency becomes progressively higher. On the other hand, the addition of energy losses to a given situation (same row in the

Tables) generally entails an increase in the requirement of energy E_c, and thus an increase of $\boldsymbol{\alpha}$ in order to exceed the new barrier. However, the irregularities synthetized in points 4(c) and 4 (d) of last section, which can be seen on **Tables 1–3**, that may be explained in the following manner: the critical energy, $\boldsymbol{E_c}$, is defined at low energies where the effect of adiabatic deceleration is negligible in relation to the other processes involved (**Figure 1**), and thus for a same value of $\boldsymbol{\alpha}$ the values of E_c from (19) and (23) are remarkably similar. Nevertheless, the decrease of the values of $\boldsymbol{\alpha}$ in column 7 of **Table 1** may be explained by the fact that although the requirement for acceleration is the same, as in column (6), a supplementary process is acting on the particles, and efficiency of the process is being lowered. Since E_c and α behave inversely, the value of $\boldsymbol{E_c}$ appears to increase; but in fact the real value of E_c in this event was $\sim$11.6 MeV. Besides, we see from columns 6 and 7 of **Tables 2** and **3** that under the hypothetical situation of the presence of adiabatic cooling in these events, the efficiency α appears higher in relation to that of column 6, given that there is an additional barrier to overtake. The value of $\boldsymbol{E_c}$ should behave similarly, but since the value of E_c in (13) is the same as that in (19), then, this hypothetical increase of α shown in column 7 in relation to that of column (6) implies a decrease of the value of $\boldsymbol{E_c}$ in column 7; this in fact does not occur because adiabatic cooling did not take place and thus the real values of $\boldsymbol{\alpha}$ and $\boldsymbol{E_c}$ in events of **Tables 1** and **3** were those of columns 3 and 6 respectively. The interpretation of 4 (e) follows from the definitions of Eqs. (31) and (32), whereas points 4(f) and 4 (g) cannot have a coherent interpretation, what can be attributed to the complexity and variability of conditions from flare to flare (e.g. the medium density, temperature, conductivity, magnetic field strength, magnetic topologies, etc.). In relation to point 4(h) it must be mentioned that deduce the same result by discussing three main different temperature regimes in the acceleration region of solar particles [105]; they estimate threshold values for proton acceleration of 1, 2.7 and 5.5 MeV for a cold region, an intermediate one and a hot region. These values are slightly lower than ours, since they do not take into account all the energy loss processes we·did. In any event, as we discussed previously, the threshold value E_c increases with the temperature because energy loss processes are increased with this parameter.

In addition to the suggestion of three temperature regions in acceleration regions extended by [105], several other suggestions have been presented in this direction: the author in [78] has discussed temperatures of $10^{4\circ}$K suggested by the central peak of hydrogen emission lines, up to more than $10^{8\circ}$K suggested by thermal emissions of X-rays. Furthermore, the flare phenomenon has usually been interpreted on basis of a dual character): the optical flare of $T\sim10^{4\circ}$K and high electron density, and on the other hand, the high energy flare plasma of $T\sim10^{7}$–$10^{9\circ}$K and relatively low electron density. The existence of several temperature regimes during a given flare has also been evoked by suggesting that the emitting regions have a filamentary and intermingling structure with hot filaments about 1 km. of diameter imbedded in cooler material [113, 115], or by suggesting a cooling of a hot region during the flare development [17, 135]. Some other models for explaining the flare energy output suggest several phases of the phenomenon, each associated with a different temperature; for example, a of relatively low temperature thermal phase followed by an explosive high temperature phase [13, 50–52, 111] posit similar models. We have not attempted to place our results into the framework of what of any of these interpretations of the flare phenomenon, but rather only to demonstrate that the generation of solar particles is accompanied by, several processes whose occurrence is narrowly related to, the temperature of the medium, and to suggest that the acceleration regions must be associated alternately with the hot and cold aspects present during a flare or even in a pre-flare state, but certainly under very different temperature regimes from flare to flare.

Related with the expansion and compression of the source medium, there are some observational indications [84] which propose a minimum value of $\sim 3 \times 10^{7^\circ}$K for expansion. The author in [102, 103] has studied hydromagnetic criteria for expansion and compression of the sunspot magnetic lines, which he distinguishes as two different phases of the flare development; although he shows that sometimes the expansion phase may not present itself according to our findings such as we found in warm and cold events. However, in Sakurai's model acceleration occurs during the compression phase, whereas our results indicate that expansion of the source material may also occur during the acceleration process; moreover, our analysis does not show indications of expansion and compression during the same event during the phase of particle acceleration. Nevertheless, we see that, with exception of the November 12, 1960 event, the acceleration efficiency is very high where there is a compression (cold event), presumably due to the strong spatial variations of the of the longitudinal and transversal field lines, as suggested by [101, 102].

It must be emphasized that we have taken into account that expansion of closed structures occurs only within a height lower than ~0.6 to 1 solar radius, and thus expansions beyond this distance may be associated with propagation of shock waves generated in relation to type II burst or CME; therefore, our assumptions concern only adiabatic cooling through the local expansion of the source and not in higher the solar envelope.

In the specific case of the November 18, 1968 event, for which our results do not indicate any expansion of the source, observations reported a loop expansion; however s it is usually supported the fact that there is no mass motion but only a traveling excitation front. It must also be mentioned that it is generally accepted that low energy protons are much more likely to be subject to adiabatic cooling since high energy protons are rather dominated by drifts and scattering in field inhomogeneities [27, 33]; Moreover, according to [131, 132, 133] adiabatic deceleration disappears as the density of the accelerated particles decreases, so that when particle velocity is much higher than both the velocity of the medium and the Alfven velocity, the adiabatic cooling is null. This would imply that in the case of our hot events (**Figure 2**) protons of energy much higher than ~670 MeV should not be adiabatically cooled in a medium of $T > 10^{8\circ}$K, however, our results show that even higher energy protons were adiabatically decelerated. Therefore, we claim that at least in these two events, our results support the hypothesis that particles were accelerated in closed magnetic field lines with high confinement efficiency.

Now turning to the problem of *p–p* nuclear collisions in some solar flares: we had mentioned that the value of $N_H \sim 10^{13}$ cm^{-3} was an average value in flare regions, since in fact concentrations as high as 10^{16} cm^{-3} have been reported (e.g. [118]) which implies that Eq. (23) and Eq. (27) will remain near the observational curves. This feature leads us to speculate that some flares have a high proton concentration medium (e.g. January 24, 1971), whereas in others the concentration is much lower (e.g. July 7, 1966), and that a great spread in high energy gamma rays and neutron fluxes is expected from flare to flare. The difference between observational and theoretical fluxes of gamma ray and neutrons is not a matter of discussion here, we only want to note that these fluxes are mainly generated from the most energetic protons which are in fact the first to escape and do not frequently interact with the medium, as discussed previously in relation with some events of **Figures 2** and **4**. This implies that depending on the magnetic confinement efficiency in each flare, the expected flux of the secondary radiation will be of greater or lesser importance. According to **Figures 2** and **4** a high gamma ray flux must be generated in the February 25, 1969, January 24, 1971 and September 1, 1971 events, whereas a lower flux should be expected from the July 7, 1966 event and no gamma-ray fluxes from nuclear collision in the acceleration volume must be expected in the events of **Figure 3**. The variability of the expected high energy gamma-ray fluxes has been previously discussed in [25]. Concerning neutron fluxes we argue that they are strongly absorbed by a neutron capture reaction $(n+ H_e^3 \rightarrow H^3 + p)$.

It must be pointed out that the need of protons for a minimum energy in order to overtake energy losses and to be accelerated upwards, measured energies may not be a strong requirement since the temporal and spatial sequence of phenomena in a flare seem to indicate the occurrence of a two-step acceleration of solar particles (e.g. [19, 16, 123]). A great variety of preliminary acceleration processes capable of accelerating particles up to some MeV has been suggested (e .g. [104, 112], etc.). It ·can be assumed that a certain portion of the low energy tail of the particle spectrum may belong to the first acceleration step. By smoothing the experimental data we have obtained a peculiar shape for this low energy tail of some spectra, although a similar shape is predicted from the theoretical point of view [5]. Moreover, authors in [94] discuss a noticeable deviation of the power spectrum below ≈ 4 MeV in low energy proton events, which they attribute to collisional losses during storage in the ionized medium of the low corona. We are aware of the difficulty of estimating the exact shape of the low energy spectrum, due to the strong modulation of these particles either within or outside of the source. Therefore, we argue that in addition to energy losses, this particular slope change in the low energy tail of some spectra may be due to an upper cutoff in the preliminary acceleration process.

Now let us discuss the assumption made in Section 5 in taking τ as a constant value: although it is expected that the mean confinement time varies according to particle rigidity, it is not clear if the escape mechanism from the source occurs through leakage, by thin or thick scattering, by curvature drifts, by gradient drifts or even by a sudden catastrophic disruption of a closed magnetic structure at the source; therefore, we opted for a mean value τ = 1 sec. Whose implications can be seen as follows: we note from Eq. (11) that if the value of τ increases, then $J(>E)$ increases, whereas if τ decreases, then $J(>E)$ decreases and so the theoretical spectra will approximate the experimental curves. At any rate, what can be deduced is that if τ is either lower or higher than the assumed value, the sequence of theoretical spectra does not change or consequently our conclusions are not altered. In order to evidence that the value of τ is in general of the order assumed, we shall develop the following considerations: if we make the extreme assumption that acceleration of solar protons is performed by a low efficiency process, such as a second-order Fermi-type mechanism then we know that in these cases the acceleration efficiency is given as $\alpha= V_a^2/v\iota$, where v is the velocity of protons, ι the acceleration step within the acceleration volume, and V_a the hydromagnetic velocity of the magnetic field irregularities. Taking into account that our values of α in a given event can be considered as an average value for different energies of protons, we shall estimate the average value of ι for a 50 MeV proton and assume that the value of ι is typical of the acceleration region configuration; hence for a field strength of 500 G and density $n = 10^{13}$ cm^{-3}, the extreme values of α obtained are α = 0.1 and 1.54 s^{-1} leading to the following values: ι =10 Km and 0.84 Km respectively, which are of the same order as the values found by Perez-Peraza (1975) for multi-GeV solar protons. To estimate τ in a magnetic field (H) where the field gradient is ≈H/ι, we use the fact that $\tau = L^2 /v\iota$, where L is the linear size of the acceleration region; an approximate' value of L may be deduced by the fact that the volume of flare regions varies from 10^{25} to 10^{29}cm^3 from flare to flare [19, 54, 55], and hence a linear dimension of $\sim 10^9$ cm may be considered as a typical value [30, 31] Assuming that the acceleration volume cannot be greater, than the flare volume, we shall consider $L = 10^8$ cm as a typical linear dimension for acceleration regions [116]. In such conditions we obtain τ = 1 and 12.6 s. for solar events where $\boldsymbol{\alpha}$**=** 0.13 and 1.54 s^{-1} respectively. We should say that if a shorter length scale L than the assumed one were taken values of τ <1 could be obtained, and hence our theoretical fluxes *J (>E)* would come closer to experimental curve as discussed above. In fact, it can be observed in **Figure 3**, that the theoretical curve corresponding to $\boldsymbol{\alpha}$=0.13 and thus to a low value of τ (the November 12, 1960 event) is nearer the experimental curve than to the theoretical curve corresponding to higher values of α, where it is supposed that τ must be higher. It must be noted that a higher value of α in one event with respect to another event does not imply a shorter escape time for particles in the former with respect to the latter, because the source conditions are not the same from one event to the other, as can be seen from the fact that magnetic inhomogeneities are much closer between them in events of high acceleration efficiency. We have considered a second-order Fermi-type mechanism to illustrate that even in the extreme case of such low efficiency the acceleration process may be performed within the flare time scale and to show that the assumption of τ = 1 s is well justified. If instead of a second-order Fermi mechanism we consider a first-order Fermi-type process in a shock wave, such as is usually attributed to the acceleration of solar particles (e.g. [32, 110]) the resulting value of τ is then lower than 1 s. From the study of heavy nuclei overabundances in solar cosmic rays it can be predicted that the value of τ is comprised between 0.1 and 0.4 s; these values when included in our calculations result in a much better fit of the theoretical spectra to the observational curves that the one illustrated with τ = 1 s.

The acceleration time scale of protons in solar flares, can be estimated from the following expression: $t = \int_{E_c}^{E} \frac{dE}{f(E)}$. In the energy range $10^6 \lesssim E \lesssim 10^{10}$ eV we have according our results discussed in last section that,

$$f(E) = \begin{cases} \alpha\beta W \\ (\alpha\beta + \rho\beta^2)W \end{cases} \text{in low temperature regimens}$$

$$f(E) = \left(d - hE^{-2} - jE^{-1}\right)\beta W - b/\beta \text{ in intermediate temperature regions}$$

$$f(E) = \left[\left(d - hE^{-2} - jE^{-1}\right)\beta - \rho^2\right]W - b/\beta \text{ in high temperature regimens}$$

(where) $d = \alpha - f - \eta$

Therefore, a consideration of the parameters obtained α and E_c for a medium density $n = 10^{13}$ cm^{-3} give acceleration times much lower than the time scale of the explosive phase of the flare phenomenon. For instance, for a low efficiency event ($\alpha = 0.14$) in a high temperature regime, the time necessary to accelerate a proton from 10 MeV to 5000 MeV, is only of the order of 8 sec.

It is interesting to comment on the estimated parameter ι on the basis of our results of the parameter α: as pointed out by [102] the time scale of the explosive phase in solar flares, is $\sim 10^3 s$, and it is believed to be that of the stored magnetic energy dissipation, which is given as

$$\tau_d = 4\pi\sigma l^2/c^2 \tag{35}$$

where l is the characteristic length of the system and σ the electrical conductivity in flare material is of the order of 2.1×10^{12}–2.4×10^{14} s^{-1}. A single calculation with (35) shows us that $l = 1.7 \times 10^4$–1.8×10^5 cm which agrees well with the values estimated in this work and previously deduced by [79].

It worth comment on the discrepancy between the predicted theoretical energy spectra at the source and the experimental spectra measured in the earth environment: first we note that the physical processes that can occur in a medium as dense as the sun's atmosphere are undoubtedly very diverse, and so, we do not claim to have included in our treatment all loss processes for charged particles, but only those of greatest interest that can affect protons within the energy range we are concerned with and during the short time scale of the acceleration durability. In fact, although Cerenkov losses are included in Eq. (2) we have ignored other losses from collective effects, however, some of them, such as energy 10 s by plasma perturbations see to be negligible for protons o f $E > 23$ MeV; also we have not considered energy losses caused by viscosity and Joule dissipation as suggested by [120]. On the other hand, we have not included nuclear transformation within the acceleration volume, as for instance proton production by neutron capture, nor loss of particles from the accelerated flux as leakage from the acceleration volume. Therefore, it is expected that the consideration of these neglected processes, together with a lower value of τ as discussed above and a higher proton concentration of the medium would depress our theoretical fluxes in greater congruency with the experimental curves. Again, local modulation of particles at the source level after acceleration are not examined here, either by an energy degradation step in a closed magnetic structure, or while traversing the dense medium of the solar atmosphere as studied by [121].

In fact, observations of low energy particles indicate the existence of a strong modulation within a small envelope of $\sim$ 0.2–0.3 A.U. (e.g. [34]). Furthermore, studies of relativistic solar flare particles during the May 4,.1960 and November 18, 1968 events have shown that particles diffuse in the solar envelope (< 30 R_s) [9, 21, 22, 63] which entails a modulation of the solar fluxes. Evidences of partic1e storage in the sun, where particles can be strongly decelerated, have been widely mentioned in the literature (e.g. [1, 65, 106]). Modulation in interplanetary space is a complicated process (e.g. [28, 29]) which provokes both the depression in the number density of particles and their strong deceleration: estimations of [74] indicate that particles lose $\sim$ 10–64% of their energy through propagation, while [75, 76] sustains a loss of

$\sim$ a half of their energy before escaping into interstellar space. Moreover, the acceleration of particles in interplanetary space [21, 22, 85] may strongly disturb the spectrum. Given the strong modulation of solar particles at different levels, one cannot expect a good fit between the predicted source spectrum and the experimental one. Nevertheless, we believe that the kind of intercomparison performed here permits the clarification of ideas about the processes related to the generation of solar flare particles.

7. Concluding remarks

In order to provide some answers to the numerous questions associated with the generation of solar particles (e.g. [24, 26, 71, 102, 119]) we have attempted to study the physical processes and physical conditions prevailing in solar cosmic ray sources by separating source level effects from interplanetary and solar atmospheric effects. On this basis, we have drawn some inferences from the intercomparison of the predicted theoretical energy spectra of protons in the acceleration region with the experimental spectra of multi-GeV proton events. Concerning this kind of events a number of modern techniques have been recently developed (e.g. [72]) and the, the PGI group in Apatity, Mursmansk, Russia [124–128]. In some of GLE it has been frequent to discern two particles populations: a prompt component and a delayed one. A new kind of classification has been proposed, *GLE's* and *SubGLE*'s depending the number of station that register the earth level enhancement, location and latitude of NM stations.

We have chosen to study this particular kind of solar events (GLE) because they allow the study of the behavior of local modulation on protons, through the widest range of solar particle energies. Although one should expect that local modulation by particle energy losses at the source should follow the behavior illustrated in **Figure 1**, our results on source energy spectra indicate that is not the general case, but local modulation varies from event to event, depending on the particular phenomena that take place at the source according to the particular physical parameters prevailing in each event, such as density, temperature, magnetic field strength as well as the acceleration efficiency and particle remaining time before they escape from the source.

In drawing conclusions about the physical processes at the source, we have assumed a fixed value of the parameter n, taking into account that although spectroscopic measurements show a variation in the value of n from flare to flare, these fluctuations are nonetheless very near the value $n = 10^{13}$ cm^{-3} [115], and thus our conclusions about energy loss processes in the acceleration region are not significantly altered by small fluctuation on this parameter. Moreover, an analysis of the electromagnetic emission associated with flares indicate a spread of several decades on the medium temperature in flare regions ($\sim 10^4$–$10^{8\circ} K$), hence we have chosen to fix the parameter n in order to concentrate our analysis on the parameter temperature. On the other hand, in drawing conclusions about the physical parameter of the acceleration process we have selected a mechanism with an energy gain rate proportional to particle energy as is the case of stochastic acceleration by MHD turbulence [36]; nevertheless, we believe that our results can in general be considered as valid, in the sense that whatever the acceleration mechanism may be, the physical conditions of the medium (density, temperature, field strength) state undoubtedly state the kind of phenomena occurring at the source. We have shown that even a low efficient mechanism (low values of α) is able to explain the generation process within the observation time scale of the explosive phase of flares, when severe conditions in the density of the medium are assumed.

Finally, let us discuss the global conception of the generation process of solar particles, according to the results obtained in this work: it is first assumed that in association with the development of solar flare conditions for the acceleration of particles may be such that it can take place either in a hot medium or in a cold one; in the first case, as a result of some powerful heating process, the local plasma must be strongly heated and acceleration of particles up to some few MeV must take place. This preliminary heating must follow to a some specific kind of hydromagnetic instability or a magnetic field annihilation process in a magnetic neutral current sheet, so that by means of electron-ion and electron-neutral collisions, Joule dissipation, viscosity, slow and fast Alfven modes or even acoustic and gravity waves, the local plasma attain very high temperature $\geq 10^7$°K. The processes involved in this preliminary process of particle acceleration is not yet completely well understood; several plausible processes capable to accelerate particles up to some MeV have been suggested in the literature (e.g. [112]). Among many possibilities suggested, we believe that the one proposed by [108] presents a very plausible picture: a very select group of fast particles appearing from the preliminary heating can be reaccelerated up to very high energies, probably by a Fermi-type mechanism as proposed by [108]. Because the medium is very hot and dense we propose that collisional and *p–p* nuclear collisions between the fast protons and particles of the medium take place. Besides, we predict that up to some definite temperature the kinetic pressure of the gas is such that it favors the hydromagnetic expansion of a closed field line configuration, and thus adiabatic deceleration of particles takes place during their acceleration in the expanding plasma. Those particles with very low energy with respect a threshold energy E_c (determined by the competition between the acceleration and the deceleration rates) cannot escape from the sunspot magnetic field configuration because of their low rigidity, and thus, by scattering with the atoms, ions and electrons of the turbulent plasma, their energy is rapidly converted into heat to rise the local plasma temperature while the selected particles go into the main acceleration process. As noted by [110] the increase of electron temperature tends to decrease the efficiency of acceleration, such as that obtained in the case of *hot* events (**Table 1**) with regard to the events of **Tables 2** and **3**. This low efficiency is also related to the relatively large characteristic length- scale of the magnetic field, so that the acceleration time of particles up to high energies is relatively long. A second kind of solar event may be distinguished from the previous one, when the temperature is not so high (*warm* events in **Table 3** and **Figure 4**) and thus expansion of the source material does not take place, at least during the time of the particle acceleration process. The temperature being lower and the characteristic magnetic field length shorter than in hot events, the acceleration efficiency is higher and consequently the acce1eration time is relatively shorter. In these events or in *hot* events a low flux of high energy gamma rays generated by nuclear collisions of highly energetic protons is expected, because these fast particles spend very short time in the source before they escape. On the other hand, conditions in solar flares may be such that energy losses of protons are negligible during the acceleration process, because particles are generated by a very efficient process in a shorter acceleration time. This kind of events are assumed to occur when the acceleration region is associated with a relatively cold plasma, such that below a certain critical temperature, a compression of the sunspot field lines takes place and thus particles are more efficiently accelerated because the characteristic magnetic field length scale is reduced. Moreover, adiabatic heating of protons into the compressed plasma may occur within the short acceleration time of these events raising the net energy exchange rate. Since the energy loss rate is negligible by rapport to the energy gain rate in these events, particles may practically be accelerated regardless of their energies, so that a preferential acceleration of heavy nuclei as suggested by [48, 49], must be expected when acceleration occurs in a region of low temperature regime. Either by assuming that in *cold* events particles are picked up from a thermal plasma or that in *warm* and *hot* events the preliminary heating is of quasi-thermal nature, a very small fraction ($N_0{\sim}10^{-11}$-10^{-18}) of plasma particle of the source volume need to be picked up by the acceleration process in order to explain the experimental spectra.

The most important parameters concerning the source and acceleration process of solar particles deduced under the assumptions made in in this work may be summarized as follows: acceleration efficiency $\alpha = 0.1 - 1.5\ \text{s}^{-1}$, characteristic magnetic field length in the acceleration volume $\iota = 3 \times 10^4$–10^6 cm, linear dimension of the acceleration volume $L = 10^9$ cm, field strength of magnetic field inhomogeneities $\sim$500 G, hydromagnetic velocity $Va = 3.5 \times 10^7$cm s^{-1}, medium density $n{\sim}10^{13}$ cm^{-3}, mean confinement time of particles within the acceleration volume $\tau \sim 0.1$–4 s, average acceleration time of individual protons $t = 12$ s, medium temperature $T{\sim}10^4$–$10^{8\circ}$K. Finally, we add that whatever the approach may be in developing flare models, an expansion and compression of the source material (e.g. [96]) local modulation of particles after the acceleration processes and a plausible absorption of secondary radiation from nuclear collisions in the solar environment must be considered.

Epilogue

We would like to emphasize that this work is to some extent with the aim to pay homage to the forefathers-founders of solar cosmic ray physics and space physics.

Acknowledgements

We are very grateful to the B.S. **Alejandro Sánchez Hertz** for his valuable help in the preparation of the figures.

A. Appendix

Energy spectrum of energetic particles accelerated in a plasma by a stochastic type-Fermi acceleration process ($\sim \alpha\beta W$) while losing energy simultaneously by collisional losses according to the general expression of [10], operative throughout all the range from suprathermal to ultrarelativistic energies, given in Eq. (2.1) in Section II. In this case, the equation to be solved when only collisional losses are competing with acceleration is

$$\frac{dW}{dt} = \alpha\beta W - \frac{k}{\beta} ln\left(k_1\beta^2\right)\left[R_4H(\chi_e) + R_5H\left(\chi_p\right)\right] \quad \left(\frac{MeV}{seg}\right) \tag{A.1}$$

where all the factors appearing in (A1) were defined below Eq. (2.1) in Section II

Now we proceed to a variable change, in terms of $\gamma = \frac{1}{\left(1-\beta^2\right)^{\frac{1}{2}}}$ since $W = Mc^2\gamma$, dW= $Mc^2 d\gamma$ and

$$\beta = \frac{\sqrt{\gamma^2 - 1}}{\gamma} \tag{A.2}$$

Hence

$$\alpha\beta W = \alpha\frac{\sqrt{\gamma^2 - 1}}{\gamma} Mc^2\gamma = Mc^2\alpha\sqrt{\gamma^2 - 1} \tag{A.3}$$

Therefore, Ec. (A.1) as a function of γ can be rewritten in the following form

$$\frac{d\gamma}{dt} = \alpha\sqrt{\gamma^2 - 1} - \frac{\kappa}{Mc^2}\frac{\gamma}{\sqrt{\gamma^2 - 1}} \ln\left(\frac{\kappa_1\left(\gamma^2 - 1\right)}{\gamma^2}\right)\left[R_4H(x_e) + R_5H\left(x_p\right)\right] \tag{A.4}$$

From where

$$dt = \frac{d\gamma}{\alpha\sqrt{\gamma^2 - 1} - \frac{\kappa}{\mu c^2}\frac{\gamma}{\sqrt{\gamma^2 - 1}} \ln\left(\frac{\kappa_1\left(\gamma^2 - 1\right)}{\gamma^2}\right)\left[R_4H(x_e) + R_5H\left(x_p\right)\right]} \tag{A.5}$$

and thus

$$t = \frac{1}{\sqrt{b^2 - 4ac}}\left[ln\left|\frac{2a\left(\sqrt{\gamma^2 - 1}/\gamma\right) + b - \sqrt{b^2 - 4ac}}{2a\left(\sqrt{\gamma^2 - 1}/\gamma\right) + b + \sqrt{b^2 - 4ac}}\right|\left|\frac{2a\left(\sqrt{\gamma_c^2 - 1}/\gamma_c\right) + b - \sqrt{b^2 - 4ac}}{2a\left(\sqrt{\gamma_c^2 - 1}/\gamma_c\right) + b + \sqrt{b^2 - 4ac}}\right|\right] \tag{A.6}$$

For integration of (A.5) we have assumed the case when $b^2 > 4ac$

$$\text{(were) } a = -\alpha; b = -f'\left(\gamma_T\right); c = \alpha - f\left(\gamma_T\right) + \frac{\sqrt{\gamma_T^2}}{\gamma_T} f'\left(\gamma_T\right);$$

$$f(\gamma) = \frac{1}{\gamma^3 - \gamma}\frac{\kappa}{mc^2} ln\left(\frac{k_1\left(\gamma^2 - 1\right)}{\gamma^2}\right)\left[R_4H(x_e) + R_5H\left(x_p\right)\right] \text{ (and)}$$

$$f'(\gamma) = \frac{\kappa}{Mc^2}\frac{\left[R_4H(x_e) + R_5H\left(x_p\right)\right]}{\sqrt{\gamma^2 - 1}}\left[\left(-3 - \frac{2}{\gamma^2 - 1}\right) ln\left(\frac{k_1\left(\gamma^2 - 1\right)}{\gamma^2}\right) + \frac{2}{\gamma^2 - 1}\right]$$
$$+ \frac{\kappa}{Mc^2}\frac{1}{\gamma(\gamma^2 - 1)} ln\left(\frac{k_1\left(\gamma^2 - 1\right)}{\gamma^2}\right)\left\{R_4R_2e^{-x_e^2}\left[1 - c_4\left(1 - 2x_e^2\right)\right] + R_5R_3e^{-x_p^2}\left[1 - c_5\left(1 - 2x_p^2\right)\right]\right\}$$

Now, according to Eq. (8.1) in Section IV the differential spectrum in terms of γ is,

$$N(\gamma)d\gamma = \frac{N_0}{\tau Mc^2} e^{-t/\tau} dt \tag{A.7}$$

And from (A.6) we obtain

$$e^{-t/\tau} = \left[\left|\frac{2a\left(\sqrt{\gamma^2-1}/\gamma\right)+b-\sqrt{b^2-4ac}}{2a\left(\sqrt{\gamma^2-1}/\gamma\right)+b+\sqrt{b^2-4ac}}\right|\left|\frac{2a\left(\sqrt{\gamma_c^2-1}/\gamma_c\right)+b-\sqrt{b^2-4ac}}{2a\left(\sqrt{\gamma_c^2-1}/\gamma_c\right)+b+\sqrt{b^2-4ac}}\right|\right]^{\frac{1}{\tau\sqrt{b^2-4ac}}} \tag{A.8}$$

in such a way that Eq. (A.7) can be rewritten

$$N(\gamma)d\gamma = \frac{N_0}{\tau Mc^2}\frac{\left[\left|\frac{2a\left(\sqrt{\gamma^2-1}/\gamma\right)+b-\sqrt{b^2-4ac}}{2a\left(\sqrt{\gamma^2-1}/\gamma\right)+b+\sqrt{b^2-4ac}}\right|\left|\frac{2a\left(\sqrt{\gamma_c^2-1}/\gamma_c\right)+b-\sqrt{b^2-4ac}}{2a\left(\sqrt{\gamma_c^2-1}/\gamma_c\right)+b+\sqrt{b^2-4ac}}\right|\right]^{\frac{1}{\tau\sqrt{b^2-4ac}}}d\gamma}{\alpha\sqrt{\gamma^2-1}-\frac{\kappa}{\mu c^2}\frac{\gamma}{\sqrt{\gamma^2-1}}\ln\left(\frac{\kappa_1(\gamma^2-1)}{\gamma^2}\right)\left[R_4H(x_e)+R_5H\left(x_p\right)\right]} \tag{A.9}$$

which is the differential spectrum as a function of gamma.

To obtain the integral spectrum we resort to Eq. (9) of Section IV,

$$J(>\gamma) = \int_{\gamma}^{\gamma_m} N(\gamma)d\gamma = \frac{N_0}{Mc^2}e^{t\left(\gamma_c\right)/\tau}\left[e^{-t(\gamma)/\tau} - e^{-t\left(\gamma_m\right)/\tau}\right] \tag{A.10}$$

Introducing A.8 in A.10 we obtain the integral spectrum

$$\begin{gathered} J(>\gamma) = \frac{N_0}{Mc^2}\left|\frac{2a\left(\sqrt{\gamma_c^2-1}/\gamma_c\right)+b-\sqrt{b^2-4ac}}{2a\left(\sqrt{\gamma_c^2-1}/\gamma_c\right)+b+\sqrt{b^2-4ac}}\right|^{1/\tau\sqrt{b^2-4ac}} \\ \left[\left|\frac{2a\left(\sqrt{\gamma^2-1}/\gamma\right)+b-\sqrt{b^2-4ac}}{2a\left(\sqrt{\gamma^2-1}/\gamma\right)+b+\sqrt{b^2-4ac}}\right|^{1/\tau\sqrt{b^2-4ac}} - \left|\frac{2a\left(\sqrt{\gamma_M^2-1}/\gamma_M\right)+b-\sqrt{b^2-4ac}}{2a\left(\sqrt{\gamma_M^2-1}/\gamma_M\right)+b+\sqrt{b^2-4ac}}\right|^{1/\tau\sqrt{b^2-4ac}}\right] \end{gathered} \tag{A.11}$$

Eqs. A.9 and A.12 may become very important for the study of all the entire range of particle energy of solar particles, particularly low energy protons measured by satellites in the interplanetary space, that presumably they have been affected in their sources. Eventually this approach could be used at laboratory scale for experiments of particle energization in plasmas.

Author details

Jorge Perez-Peraza* and Juan C. Márquez-Adame

*Address all correspondence to: perperaz@geofisica.unam.mx

Instituto de Geofisica, Universidad Nacional Autonoma de Mexico, D.F. for CDMX, Mexico

References

[1] Alhualia. 12th ICRC, Tasmania, Hobart; 1971. p. 468

[2] Bai T, Ramaty R. Solar Physics. 1976;**49**:343

[3] Barcus JG. Solar Physics. 1969;**8**:186

[4] Bazilevskaya GA, Charakhchyan AN, Charakhchyan TN, Lozutin IL. 12th I.C.R.C., Tasmania. 1971;**5**:1825

[5] Biswas S, Radhakiskshnan B. Solar Physics. 1973;**28**:211

[6] Bland. Nuovo Cimento. 1966;**13**:427

[7] Bruzek A. Solar Physics. 1972;**26**:94

[8] Bukata RP, Gronstal PI, Palmeira RAR, McCracken KG, Rao UR. Solar Physics. 1969;**10**:198

[9] Burlaga. Solar Physics. 1970;**13**:348

[10] Buttler ST, Buckingham MJ. Physical Review. 1962;**126**:1

[11] Bryant DA, Cline TL, Desai VD, McDonald FB. Astrophysical Journal. 1965;**141**:478

[12] Cameron AGW. The Astrophysical Journal Letters. 1967;**1**:35

[13] Cheng C-C. Solar Physics. 1972;**22**:178-188

[14] Chupp EL. Space Science Reviews. 1971;**12**:486

[15] Chupp EL, Forrest DJ, Higbie PR, Suri AN, Tsai C, Dunphy PP. Nature. 1974;**241**:333

[16] Cline T. NASA-X-661-7133, GSFC, Greenbelt, Maryland;1970

[17] Datlowe D. Solar Physics. 1971;**17**:436

[18] Davis L. In: Mackin RJ, Neugebauer M, editors. The Solar Wind. NY: Pergamon Press; 1966

[19] De Jager C. Solar Physics. 1967;**2**:327

[20] Dessai UD. Canadian Journal of Physics. 1971;**49**:265

[21] Duggal SP, Guidi I, Pomerantz MA. Solar Physics. 1971;**18**:234

[22] Duggal SP. Reviews of geophysics. Space Physics. 1979;**17**:1021

[23] Dulk GA, Altschuler MD, Smerd SF. Astrophysical Journal Letters. 1971;**8**:235

[24] Elliot H. In: Wilson JG. Progress in Cosmic Ray Physics, Vol. 1;1952

[25] Elliot H. Planetary and Space Science. 1964;**12**:657

[26] Elliot H. In: De Jager C, Svestka Z, editors. N Solar Flares and Space Research. Amsterdam: North Holand Pub; 1969. p.356

[27] Elliot H. In: De Jager C, editor. Solar-Terrestrial Physics, Part I; 1972. p.134

[28] Englade RC. 12th International Conference on Cosmic Rays. 1971;**2**:502

[29] Englade RC. Journal of Geophysical Research. 1972;**77**:6266

[30] Ellison MA, McKena SMP, Reid. Dunsink Observatory Publications. 1961. 53

[31] Ellison MA, Reid JA. Research in Geophys. 1964 M.I.T. Presstime 1,43

[32] Fichtel CE, McDonald FB. Annual Review of Astronomy and Astrophysics. 1967;**5**:359

[33] Fisk LA, Axford WI. Journal of Geophysical Research. 1968:73. DOI: 10.1029/JA073i013p04396 ISSN 0148-0227

[34] Fisk LA. 14th ICRC; Munich. 1975;**2**:810

[35] Fritzova-Svestkova, Svetska. Solar Physics. 1967;**2**:87

[36] Gallegos-Cruz A, Pérez-Peraza J. Astrophysical Journal. 1995;**446**:669

[37] Ginzburg VL, Syrovatskii SI. The Origin of Cosmic Rays. Oxford: Pergamon Press;1964

[38] Ginzburg VL. Elementary Processes for Cosmic Ray. Astrophys, Gordon & Breach;1969

[39] Heristchi Dj, Kangas J, Kremser G, Legrand JP, Masse P, Palous M, Pfotzer G, Riedler W, Whilhem K. Annals of the International Quiet Year. 1967;**3**:267

[40] Heristchi Dj, Trottet G. Physical Review Letters. 1971;**26**:197

[41] Heristchi DJ, Perez-Peraza J, Trottet G. In: Lincoln V, editor. Bulletin of the World Data Center A, Upper Atmosphere Geophysics, Boulder Colorado. Vol. **24**; 1972. 182

[42] Heristchi Dj, Perez-Peraza J, Trottet G. Paper SP-5.3-9 14th ICRC. 1975;**5**:1841

[43] Heristchi Dj, Trottet G, Perez-Peraza J. Solar Physics. 1976;**49**:141

[44] Hess WN. Reviews of Modern Physics. 1958;**30**:368

[45] Ifedili SO. Solar Physics. 1974**39**:233

[46] Jokipii JR. Reviews of Geophysics and Space Physics. 1971;**9**:1

[47] King JH. J. Spacecraft Rockets. 1974;**11**:40l

[48] Korchak AA, Sirovatskii SI. Soviet Doklady. 1958;**3**:983

[49] Korchak AA, Sirovatskii SI. Proc of the 6th ICRC 3, 216. Moscow: Izd AN SSSR (in Russian); 1960

[50] Korchak AA. Astronomicheskii Zhurnal. 1967a;**11**:258

[51] Korchak AA. Doklady AN SSSR. 1967b;**12**:192

[52] Korchak AA, Platov YV. Astronomicheskii Zhurnal. 1968;**45**(6):1185

[53] Krimigis SM. Journal of Geophysical Research. 1965:70, 2943

[54] Krivsky. Acta Physica Academiae Scientiarum Hungaricae. 1970;**29**:427

[55] Krivsky L. Nuovo Cimento Series. 1965;**10-27**:1017

[56] Kurochka LN. Astronomicheskii Zhurnal. 1970;**47**:111

[57] Lin RP. Journal of Geophysical Research. 1968;**73**:3066

[58] Lin RP, Kahler SW, Roelof EC. Solar Physics. 1960;**4**:338

[59] Lingelfelter RE, Ramaty R. In: Shen BSP, editor. High Energy Nuclear Reactions in Astrophysics. New York: Benjamin WA, Inc; 1967. p. 99

[60] Lockwood JA. Journal of Geophysical Research. 1967;**72**:3395

[61] Lockwood JA. Journal of Geophysical Research. 1968;**73**:4247

[62] Lockwood JA, Webber WR, Hsieh L. Journal of Geophysical Research. 1974;**79**:4149

[63] Lust R, Simson JA. Physical Review. 1957;**108**:1563

[64] McCracken KG. 1969 in Solar Flares and Space Research, Ed. by De Jager, C. and Svetska, Z. North Holland Pub, Amsterdam, p. 202

[65] McDonald FB, Dessai. Journal of Geophysical Research. 1971;**76**:808

[66] Malville JM, Smith SF. Journal of Geophysical Research. 1963;**68**:3181

[67] Miroshnichenko L, Sorokin MO. Geomagn and Aeronomy. 1985;**25**(4):534

[68] Miroshnichenko LI, Sorokin MO. Geomagnetism and Aeronomy. 1986;**26**(4):535

[69] Mirosnichenko LI, Pérez-Peraza J. Astrophysical Aspects in the studies of solar cosmic rays. International Journal of Modern Physics. 2008;**23**:1

[70] Mirosnichenko LI, Vashenyuk EV, Pérez-Peraza J. Bulletin of the Russian Academy of Sciences. 2009;**73**(3):297

[71] Miroshnichenko L. Solar cosmic rays: Fundamental and applications. Astrophysics and Space Science Library. 2015;**405**

[72] Mishev AL, Kocharov LG, Usoskin G. J.G.R.: Space Physics. 2014;**119**:670

[73] Ogilvie KW, Bryant DA, Davis LR. Journal of Geophysical Research. 1962;**67**(3):929

[74] Palmer IA. Reviews of Geophysics and Space Physics. 1982;**20**:335

[75] Parker EN. Interplanetary Dynamical Processes. New York: John Wiley & Sons, Interscience;1963a

[76] Parker EN. ApJ. 1963b. Suppl 77;**8**:177

[77] Parker. Planetary and Space Science. 1965;**13**(1):9

[78] Parker EN. Space Science Reviews. 1969;**9**:325

[79] Perez-Peraza J. Journal of Geophysical Research. 1975;**80**:3535

[80] Perez-Peraza J, Galindo Trejo J. Revista Mexicana De Astronomia Y Astrofisica. 1975;**1**:273

[81] Perez-Peraza J, Gallegos-Cruz A. The Astrophysical Jornal Supplements. 1994a;**669**:90-92

[82] Perez-Peraza J, Gallegos-Cruz A. Geofísica Internacional. 1994b;**33-2**:311

[83] Pinter S. Solar Physics. 1969;**8**:149

[84] Pinter S. Proc. IV Leningrad Cosmic Phys. Seminar, Phys. Techn. Inst., Leningrad; 1972p.63

[85] Pomerantz, Duggal. Journal of Geophysical Research. 1974;**79**:913

[86] Ramaty R, Lingelfetter RE. High Energy Phenomenon on the sun NASA SP-342; 1973. 301

[87] Ramaty R, Lingelfelter RE. Journal of Geophysical Research. 1967;**72**:879

[88] Ramaty R, Stone RG. High Energy Phenomenon on the Sun NASA SP-342;1973. 341

[89] Ramaty R, Lingelfetter RE. In: Kane RS, editor. N Solar Gamma, X and EUV Radiation, IAU Symposium 68. Dordrecht, Holland: Reidel Pub Co; 1975. p. 363

[90] Ramudarai S, Biswas S. 12th International Cosmic Rays Conference. Vol. 21971. p. 793

[91] Ramudarai S, Biswas S. Astrophysics and Space Science. 1974;**30**:187

[92] Reames DF, Fichtel CE. 10th ICRC, CAL. 1967;**2**:546

[93] Reid JH. Dunsink Obs. Publ.1961;53

[94] Rotwell PL. Journal of Geophysical Research. 1976;**81**:709

[95] Sakurai K. Journal of Geomagnetism and Geoelectricity. 1963;**14**:144

[96] Sakurai K. Publications of the Astronomical Society of Japan. 1965;**19**:408

[97] Sakurai K. Publications of the Astronomical Society of Japan. 1966a;**18**:77

[98] Sakurai K. Report of Ionosphere and Space Research in Japan 20 519. 1966b;**20**:233

[99] Sakurai K. Report of Ionosphere and Space Research in Japan 21. 1967;**21**:113, 213

[100] Sakurai K. NASA Report X- 693-71-268 GSFC, Greenbelt Md1971

[101] Sakurai K. Solar Physics. 1973;**31**:483

[102] Sakurai K. Physics of Solar Cosmic Rays. Tokio, Japan: University of Tokyo Press; 1974

[103] Sakurai K. Publications of the Astronomical Society of Japan. 1976;**28**:177

[104] Schatzman E. Solar Physics. 1967;**1**:411

[105] Severnii, Shabanskii. Soviet Astronomy - Astrophysical Journal. 1961;**4**:583

[106] Simnet. Solar Physics. 1971;**20**:448

[107] Smerd SF, Dulk GA. Solar Magnetic Fields, IAU 431971. p. 616

[108] Smith EVP. In: Oman Y, editor. N Mass Motions in Solar Flares and Related Phenomena, Nobel Symposium 9. Stockholm: Almqvistand Wiksell; 1968. p. 137

[109] Smith SF, Ramsay HE. Solar Physics. 1967;**2**:158

[110] Smith DF. Advances in Space Research. 1986;**6**(6):135

[111] Somov BV, Syrovatskii SI. Solar Physics. 1974;**39**:415

[112] Sonnerup. In: Ramaty R, Stone RG, editors. High Energy Phenomena on the Sun, NASA X-693-73-193. 1973. p. 357

[113] Suemoto, Hiei. Publications of the Astronomical Society of Japan. 1959;**11**:185

[114] Suemoto, Hiei. Publications of the Astronomical Society of Japan. 1962;**14**:33

[115] Svestka Z. BAC. 1963;**14**:234

[116] Svetska Z. Bulletin of the Astronomical Institute of Czechoslovakia. 1966;**17**:262

[117] Svetska Z. Solar Physics. 1968;**4**(1):18

[118] Svetska, Z. 1969 in Solar Flares and Space Research (ed. By de Jager, C. and Svestka, Z.) North-Holland Pub., Amsterdam, p. 16.

[119] Svetska Z. Solar Flares Geophysical and Astrophysics Monographs. Dordrecht Holland: Reidel Publishing Company; 1976

[120] Syrovatskii SI. Soviet Physics - Journal of Experimental and Theoretical Physics. 1961;**13**: 1257

[121] Syrovatskii SI, Shmelevae OP. Soviet Astronomy - Astrophysical Journal. 1972;**16**:273

[122] Takakura T. Space Science Reviews. 1966;**5**:80

[123] Takakura T. Solar Physics. 1969;**6**:133

[124] Vashenyuk EV, Balabin YV, Perez-Peraza J, Gallegos-Cruz A, Miroshnichenko LI. Advances in Space Research. 2006;**38**(3):411

[125] Vashenyuk EV, Balabin YV, Miroshnichenko LI, Pérez-Peraza J, Gallegos-Cruz A. 30th Int. Cosmic Ray, Mérida. Vol. 12007a. p. 249

[126] Vashenyuk EV, Miroshnichenko LI, Balabin Y-V, Pérez-Peraza J, Gallegos-Cruz A. 30th Int. Cosmic Ray Conf., Merida. 2007b;**1**:253

[127] Vashenyuk EV, Balabin YV, Miroshnichenko LI. Advances in Space Research. 2008;**41**(6):926

[128] Vashenuyk EV. Bulletin of the Russian Academy of Sciences. 2011;**75**(6):767

[129] Vernov SN, Grigorov NL, Zatespin GT, Chudakov AE. Izvstia Akademii Nauk Sssr, Deriya Series Fizika (English Translation). 1955;**19**:45

[130] Webber WR. In: Hess WW, editor. AAS-NASA SP-50 Symp. On the physics of Solar flares, GSFC. 1964. p. 515

[131] Wentzel DG. Journal of Geophysical Research. 1965;**70**:2716

[132] Wentzel DG. ApJ. 1969a;**156**:303

[133] Wentzel DG. ApJ. 1969b;**157**:545

[134] West HI Jr, Buck RM, Walton JR, D'Arcy RG Jr. Upper Atmosph. Geophys World Data Center A, NOAA, Rep. 241972. p. 113

[135] Widding KG. IAU Symposium. 1975;**68**:153

[136] Wild JP. Journal of the Physical Society of Japan. 1962;**17**(Suppl. A II):249

Edited by Zbigniew Szadkowski

Measurements in present experiments have dramatically advanced our understanding of ultrahigh-energy cosmic rays. The suppression of the flux at the highest energies is now confirmed without any doubt, and strong limits have been placed on the photon and neutrino components. There are indications for a small, large-scale anisotropy both below and above the energy of the angle and for a correlation on smaller angular scales at E > 5.5*1019 eV. Around 3*1018 eV, there is a distinct change of slope with energy, and the shower-to-shower variance decreases. Interpreted with the leading LHC-tuned shower models, this implies a gradual shift to a heavier composition, and a number of fundamentally different astrophysical model scenarios have been developed to describe this evolution.

Published in London, UK
© 2018 IntechOpen
© Shtrunts / iStock

IntechOpen

ISBN 978-1-83881-699-5